Constitutive modelling of composite materials under impact loading

Jens Wiegand

Solid Mechanics and Materials Engineering Group
Department of Engineering Science
University of Oxford

Trinity Term 2008

Constitutive modelling of composite materials under impact loading

Jens Wiegand, Christ Church, University of Oxford
For the degree of D.Phil. in Engineering Science, Trinity Term 2008

In this thesis a constitutive model is developed for the numerical prediction of UD composite material behaviour under impact loading. Impact induced loading usually results in three dimensional stress states which significantly influences the failure behaviour. The heterogeneous nature of composite materials, in particular, results in a complex failure behaviour which manifests itself in various failure modes. Predicting the onset and evolution of these failure modes requires the use of physically based three dimensional theories for the prediction of the onset of damage and subsequent damage evolution. Furthermore, the use of polymeric matrices in continuous fibre reinforced composites results in a distinct directional strain rate dependent material behaviour which needs to be incorporated in constitutive models for the numerical simulation of impact events.

The developed constitutive model relies on the prediction of the onset of damage evolution by the use of physically based three dimensional stress based failure criteria. A special feature of the proposed model is the identification of potential fracture planes. Numerically efficient algorithms for finding such planes are developed thus enabling the implementation into an explicit FE environment which was prohibitive so far. Damage evolution is simulated by degrading the tractions which are acting on the failure mode dependent fracture planes. The damage evolution and consequent energy dissipation is thereby driven by physically based dissipation potentials which consider only stresses which contribute to damage growth. The well known mesh dependent energy dissipation in Continuum Damage Mechanics is reduced by the introduction of an element size dependent parameter into the constitutive equations.

An experimental program is conducted to investigate the compressive behaviour of composites. The focus of the study is on the rate dependent failure behaviour. The experiments are designed such that the failure mechanisms can be studied at varying strain rates with identical boundary conditions. This allows for direct conclusions about the strain rate dependent material behaviour. Novel optical measurement techniques are applied across all investigated strain rates thus ensuring an improved observation of the failure modes.

The proposed constitutive model is finally verified by modelling of three point beam bending experiments which were performed quasi-statically and at impact velocities. The experimental technique for beam bending at impact loading was therefore improved thus yielding significantly more accurate experimental data.

Contents

List of Figures

List of Tables

Acknowledgements

I would like to start my acknowledgements by thanking my supervisor Nik Petrinic for the faith in me. I am very grateful for the chance you gave me by inviting me to Oxford for this work of research which finally found it's place in this thesis. It certainly helped me to grow in confidence both, privately and professionally. I think this is the right place to thank you for all the advice and patience in my supervision.

Having been part of the Impact team in Oxford was a challenging and enriching experience. I would like to thank all of my colleagues who contributed with their own research to the content of this thesis. Many aspects of my work could not have been addressed as professionally without this great team of young and motivated people around me.

Special thanks goes to my former colleagues at the Institut fuer Leichtbau und Kunststofftechnik in Dresden. I am very grateful for the provided material and advice. The exchange of ideas was a constant source of inspiration and certainly improved the quality of my research.

Furthermore, I kindly acknowledge the financial support of the EU within the frame of the VITAL project (FP6-012271) and Rolls Royce plc. Especially, I would like to thank people at Rolls Royce who went through all the troubles related to the use of the early versions of my constitutive model. The feedback was essential for the final outcome!

Finally, I would like to thank my parents, my brother and my sister in law who always encouraged me in my projects even though this meant not having me around. It was always a pleasure and a source of strength to go back home and spend time with you!

Notation

Symbols used in expressions throughout the text are explained in detail immediately after their first appearance. Nevertheless, some generally applied notation rules and common symbols are given below.

General Notation

Regular italic typeface (v, σ, ...): scalars and scalar functions.

Bold italic typeface ($\boldsymbol{P}$, $\boldsymbol{v}$, $\boldsymbol{A}$, $\boldsymbol{s}$, ...): vectors and tensors or vector and tensor functions.

Coordinate systems, angles and rotations

1,2,3	...	material coordinate system with 1-direction indicating the fibre orientation
1,n,t	...	coordinate system of the fracture plane for IFF
1^m,n,t	...	coordinate system of the fracture plane for fibre kinking initiation
$1^k, 2^k, 3^k$	...	kink plane coordinate system
$1^m, 2^m, 3^m$	...	fibre misalignment coordinate system
$1^p, 2^p$	...	kink propagation coordinate system

β	...	kink band inclination angle
θ	...	orientation of possible fracture planes parallel to the fibres for IFF
θ_{fr}	...	fracture plane angle for IFF
θ_{fr}^0	...	inclination of the fracture plane for IFF under uniaxial compression
ψ	...	angle describing the orientation of the kink band
ψ_k	...	orientation of the kink propagation plane
ϕ^0	...	initial fibre misalignment

ϕ^c ... total fibre misalignment at failure

ϕ^e ... fibre misalignment due to elastic deformation

The transformation of stress and strain from one coordinate system to another one is performed by the use of tensor rotation. The rotation matrix $\boldsymbol{R}_x(\alpha)$ is used to rotate an second order tensor about the x-axis by an angle α.

Symbols

$\boldsymbol{\sigma}$ ... stress tensor in material coordinates

$\hat{\boldsymbol{\sigma}}$ ... effective stress tensor

$\boldsymbol{\sigma}^{tr}$ ... stress predictor in explicit FE

$\boldsymbol{\sigma}^{fr}$ ... stress tensor in IFF fracture plane coordinate system

$\boldsymbol{\sigma}^{m}$ ... stress tensor in misalignment coordinate system

$\boldsymbol{\sigma}^{p}$ ... stress tensor in kink propagation coordinate system

$\sigma_n, \tau_{n1}, \tau_{nt}$ ... fracture plane tractions (used for IFF and fibre kinking)

$\boldsymbol{\varepsilon}$ ... strain tensor

$\dot{\boldsymbol{\varepsilon}}$ ... strain rate tensor

$\boldsymbol{C}$ ... fourth order tensor of material constants - stiffness tensor

$\boldsymbol{C}^0$ ... stiffness tensor of initial (undamaged) material constants

$\boldsymbol{C}(\boldsymbol{\omega})$ ... stiffness tensor of current (damaged) material constants

$\boldsymbol{M}$ ... stiffness damage tensor

v_f ... fibre volume fraction

ρ ... density

α, β ... stress waves in thin bars

Z_0 ... characteristic acoustic impedance

Δt ... time step in explicit FE

X_t ... tensile strength in fibre direction

X_c ... compressive strength in fibre direction

Y_t ... tensile strength in transverse direction

Y_c ... compressive strength in transverse direction

Z_t ... tensile strength in through thickness direction

S_{12} ... in-plane shear strength

S_{13}, S_{23}	...	out of plane shear strength
S_d	...	out of plane shear strength for delamination
S_f	...	shear strength for shear failure across the fibres
S_{kink}	...	shear resistance against kink propagation
$R_n^{(+)}$	...	fracture plane resistance against tensile failure
R_{n1}, R_{nt}	...	fracture plane resistance against fracture due to shear stress
p_t, p_c	...	slope parameters for the Puck IFF failure criterion (parabolic formulation)
p_{n1}, p_{nt}	...	slope parameters for the Puck IFF failure criterion (linear formulation)
e	...	material exposure
e_1	...	material exposure for fibre rupture
e_2	...	material exposure for fibre kinking
e_3	...	material exposure for IFF
e_4	...	material exposure for delamination
f^{res}	...	reserve factor for damage initiation
k_{exit}	...	exit criterion for fracture plane angle search algorithm
f_i^1	...	strain rate dependent factor for fibre rupture ($i = 1, 2, 3, 4, 5, 6$)
f_i^2	...	strain rate dependent factor for fibre kinking ($i = 1, 2, 3, 4, 5, 6$)
f_i^3	...	strain rate dependent factor for IFF ($i = 1, 2, 3, 4, 5, 6$)
f_i^4	...	strain rate dependent factor for delamination ($i = 1, 2, 3, 4, 5, 6$)
f_i^s	...	strain rate dependent factor for the elastic properties ($i = 1, 2, 3, 4, 5, 6$)
d_{rate}	...	damping coefficient for rate dependent stiffness

r_i	...	elastic domain threshold for the ith damage mode
g_i	...	damage growth function for the ith damage mode
Δg_i	...	increment of damage growth for the ith damage mode
$\boldsymbol{Y}$	...	conjugated thermodynamical force in CDM models
U	...	dissipated energy per unit volume, strain energy
Γ	...	dissipated energy per unit area
G	...	energy release rate
G_i	...	mode i component of the energy release rate, $i = I, II$
G_c	...	critical energy release rate
G_{ic}	...	mode i component of the critical energy release rate, $i = I, II$
f^e	...	material and FE mesh dependent energy release factor
A_{crack}	...	cracked area in the RVE
α	...	coefficient of the power law for mixed mode damage propagation
η	...	ratio of mode I and mode II in mixed mode situations

δ_1, δ_1, δ_1	...	opening displacement for mode I and mode II

Abbreviations

CFRP	...	Carbon Fibre reinforced polymers
GFRP	...	Glass Fibre reinforced polymers
RVE	...	Representative Volume Element
UD	...	Unidirectional reinforced
IFF	...	Inter Fibre Failure
SHP	...	Split Hopkinson Bar
SHPB	...	Split Hopkinson Pressure Bar
SHTB	...	Split Hopkinson Tension Bar
DSP	...	Digital Speckle Photography

Chapter 1

Introduction

1.1 Motivation and background

The ever growing demand for lighter structures resulted in the increasing replacement of metal parts by composite structures. Especially in the aeronautic industry, composite materials are expected to increase efficiency without compromising safety. For reasons of lack of confidence for safe design, limited technology readiness and the comparatively high cost for the material and manufacturing, in the past, the application of composites remained mainly limited to military applications were extensive testing programs could be undertaken. The reduction in prices within the last decade together with the improved understanding of the material behaviour and rising awareness for environmentally friendly technology have allowed for composites to be employed in civil aerospace applications. A good example of successful substitution of metallic components by composite or hybrid materials is the new Airbus A380 (see Fig 1.1). The intensified use of composites in civil applications requires reliable and cost efficient design tools. Realistic constitutive models for numerical analysis tools like Finite Elements (FE), for instance, can enhance performance and safety by more sophisticated structural design and at the the same time decrease the development costs and time as experimental design verification can be significantly reduced.

The use of composites in aircrafts in general, and aircraft engines in particular, re-

The figure originally presented here cannot be made available via ORA for copyright reasons.

Figure 1.1: CFRP parts in the new Airbus A380

quires a detailed understanding of the material behaviour especially in view of impact events which often mark the critical loading event for design. Impact induced loading poses various difficulties for structural design. First, impact events result often in complex three-dimensional stress states which requires advanced theories for strength and damage prediction. Furthermore, composite materials, especially with polymeric matrices, are well known for their strain rate dependent material behaviour. As a consequence, special constitutive models for the numerical simulation of impact events are required.

The current predictive capability of composite constitutive models is often insufficient to master above mentioned challenges. Many available models are limited to plane stress and the representation of the complex composite failure behaviour often lacks a sound physical basis. It is only very recent that physically based three dimensional failure theories started to emerge. These novel theories aim at representation of the failure mechanisms and enable a more realistic prediction of the various composite failure modes. Predictive modelling of the composite response to impact loading requires constitutive models which incorporate the strain rate dependent material behaviour thus enabling a realistic prediction of the stresses induced due to impact loading. This, in conjunction with physically based theories for strength prediction and subsequent damage evolution and representative energy dissipation are key aspects for predictive modelling of composite material behaviour.

1.2 Objectives

The research which is presented in this thesis was mainly inspired by the desire to introduce composite materials in parts of aircraft engines such as fan blades threatened by impact. The objective of the conducted research program is to enhance the available model capabilities for unidirectionally reinforced continuous Carbon Fibre Reinforced Polymers (CFRP) subjected to impact loading. The proposed constitutive model is developed for explicit FE which has demonstrated to be a powerful tool for the simulation of impact events. The key for successfully modelling of impact events is a strain rate dependent constitutive model which considers three-dimensional stress states for strength prediction and subsequent damage evolution. Reaching this objective requires the following tasks to be addressed within the thesis

- *selection/extension of physically based failure theories which enable improved prediction of the onset of damage*
- *incorporation of strain rate dependent material behaviour into the constitutive equations*
- *development of damage evolution algorithms which predict the propagation of damage evolution and the resulting energy dissipation*
- *implementation of the proposed constitutive model into an explicit FE environment*
- *experimental investigation of rate dependent material behaviour*
- *verification of the proposed model by modelling of conducted experiments*

The current state of research requires novel contribution to each of the tasks stated above. The focus of the constitutive model development lies in the implementation of a physically based model for the prediction of the initiation of damage and the subsequent damage evolution. The approach as followed here, relies on the prediction of planes of critical orientation on which failure is likely to occur. Novel accurate and numerically efficient algorithms for predicting the orientation of such fracture planes need to be developed thus enabling the application of physically based failure criteria within the environment of explicit FE which was prohibitive so far. Considering the identified fracture planes in the damage evolution will enable a novel more realistic modelling of the composite failure mechanisms.

The experimental work will help to improve the understanding of the underlying failure mechanisms and the influence of changing strain rate on them. An important aspect of the experimental work is the improvement of the accuracy of the obtained data by the use of optical measurement systems. Digital high speed and ultra high speed camera equipment, which is available for this study, will enable the investigation of the change of failure mechanisms due to changing strain rates which has not been addressed sufficiently until now. Special focus will be given to the experimental identification and characterisation of failure mode dependent fracture planes.

1.3 Introduction to composite materials

The word composite in the term composite materials signifies that two or more materials are combined on a macroscopic scale to form a useful third material. The advantage of composite materials is that, if well designed, they usually exhibit the best qualities of their constituents and often some qualities that neither constituent possesses. The variable composition of composites enables the engineer not only to design the structure, but the material itself, which gives the design an additional 'degree of freedom'.

Composite materials are typically composed of a reinforcing material and a matrix material. The reinforcing material can be particles, short fibres with a random orientation or continuous fibres. On of the most popular composites are the so called continuous fibre reinforced composite materials (sometimes referred to as long fibre reinforced composites). This type of materials consist of reinforcing continuous fibres of certain orientation which are embedded in a matrix system. In this combination the fibres give the material outstanding strength and stiffness while the matrix allows for the force transmission between fibres. Additionally, the matrix protects the fibre and keeps the composite together. Composites are usually built up of separate thin layers of fibres and matrix, called ply or lamina. A single lamina with only one orientation of the fibres is called unidirectionally (UD) reinforced. Often laminas of different fibre orientations are stuck together to form a laminate. The stacking sequence of laminas is optimised thus giving the laminate the desired stiffness and strength for a given application. The continuous fibre reinforced composite materials are the focus of this study. Especially the combination of carbon fibre and epoxy resin will be investigated due to the high relevance in industrial applications.

The heterogeneous composition of composites leads to direction dependent material properties. In order to distinguish the different material directions, a material coordinate system (1,2,3) is introduced. Commonly, 1-direction indicates the orientation of the reinforcing fibres, while the 2-direction is the transverse direction in the plane of the fibre reinforcement. The 3-direction usually points in the through thickness direction if the lamina is embedded in a laminate. The material coordinate system and the corresponding components of the stress tensor used within this thesis is displayed in Fig 1.2.

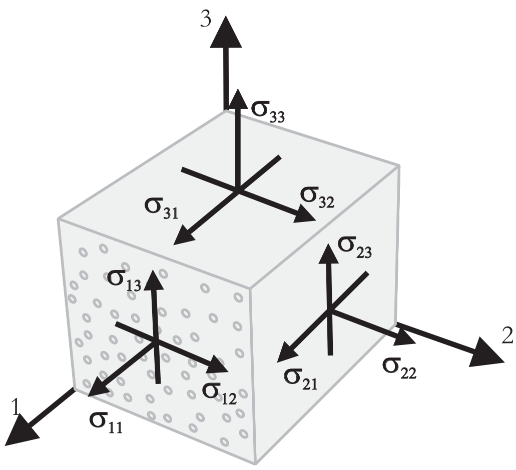

Figure 1.2: The definition of the material coordinate system for a uni-directional composite ply

Despite the fact that composite materials are fundamentally heterogeneous materials, consisting of a reinforcing fibre and a supporting matrix, in analysis the material properties are often smeared over the volume of an Representative Volume Element (RVE) thus allowing for the material to be treated as homogeneous. For the initial linear elastic behaviour of the material (e.g. before the onset of damage) the material is assumed to be *ideally elastic*, so it completely recovers its form when applied forces are removed. Assuming only infinitesimal deformations occur, the generalised HOOKE's law is valid

$$\begin{aligned} \boldsymbol{\sigma} &= \boldsymbol{C} : \boldsymbol{\varepsilon} + \boldsymbol{\sigma^0} \\ \sigma_{ij} &= C_{ijkl}\varepsilon_{kl} + \sigma^0_{ij}. \end{aligned} \tag{1.1}$$

In Eqn 1.1 $\boldsymbol{C}$ denotes the forth order tensor of elastic material parameters called elasticity tensor or historically also referred to as stiffness tensor and $\boldsymbol{\sigma^0}$ are the initial stresses. Within this thesis it is assumed that the reference (initial) configuration is stress free and the initial stresses are neglected ($\boldsymbol{\sigma^0} = 0$). For the general case $\boldsymbol{C}$ consists of 21 independent material constants. This case is called *general anisotropy.* The material considered here exhibits certain symmetry and the number of independent stiffness parameters can be reduced. The following two cases of material symmetry can be applied.

An *orthotropic* body has material properties that are different in three mutually perpendicular directions at a point in the body and, further, has three mutually perpendicular planes of material property symmetry. The orthotropic elastic material response is governed by nine independent elastic properties. UD plies are often treated as orthotropic because they exhibit three planes of material symmetry, the 1-2 plane, the 1-3 plane and the 2-3 plane (see Fig 1.2). As a result Eqn 1.1 reads

$$\begin{pmatrix} \sigma_{11} \\ \sigma_{22} \\ \sigma_{33} \\ \sigma_{12} \\ \sigma_{23} \\ \sigma_{13} \end{pmatrix} = \begin{pmatrix} C_{11} & C_{12} & C_{13} & 0 & 0 & 0 \\ C_{12} & C_{22} & C_{23} & 0 & 0 & 0 \\ C_{13} & C_{23} & C_{33} & 0 & 0 & 0 \\ 0 & 0 & 0 & C_{44} & 0 & 0 \\ 0 & 0 & 0 & 0 & C_{55} & 0 \\ 0 & 0 & 0 & 0 & 0 & C_{66} \end{pmatrix} \begin{pmatrix} \varepsilon_{11} \\ \varepsilon_{22} \\ \varepsilon_{33} \\ 2\varepsilon_{12} \\ 2\varepsilon_{23} \\ 2\varepsilon_{13} \end{pmatrix}. \tag{1.2}$$

Following the assumption that the stress strain relations are invertible, the compliance tensor is obtained from the stiffness tensor

$$\boldsymbol{S} = \boldsymbol{C^{-1}} \tag{1.3}$$

and Eqn 1.2 can be rewritten

$$\boldsymbol{\varepsilon} = \boldsymbol{S} : \boldsymbol{\sigma} \tag{1.4}$$

allowing $\boldsymbol{S}$ to be expressed in terms of engineering constants. Eqn 1.4 reads in engineering notation

$$\begin{pmatrix} \varepsilon_{11} \\ \varepsilon_{22} \\ \varepsilon_{33} \\ 2\varepsilon_{12} \\ 2\varepsilon_{23} \\ 2\varepsilon_{13} \end{pmatrix} = \begin{pmatrix} \frac{1}{E_1} & -\frac{\nu_{12}}{E_1} & -\frac{\nu_{13}}{E_1} & 0 & 0 & 0 \\ -\frac{\nu_{12}}{E_1} & \frac{1}{E_2} & -\frac{\nu_{23}}{E_2} & 0 & 0 & 0 \\ -\frac{\nu_{13}}{E_1} & -\frac{\nu_{23}}{E_2} & \frac{1}{E_3} & 0 & 0 & 0 \\ 0 & 0 & 0 & \frac{1}{G_{12}} & 0 & 0 \\ 0 & 0 & 0 & 0 & \frac{1}{G_{23}} & 0 \\ 0 & 0 & 0 & 0 & 0 & \frac{1}{G_{13}} \end{pmatrix} \begin{pmatrix} \sigma_{11} \\ \sigma_{22} \\ \sigma_{33} \\ \sigma_{12} \\ \sigma_{23} \\ \sigma_{13} \end{pmatrix}. \tag{1.5}$$

From Eqn 1.5 it becomes clear that the 9 elastic constants for orthotropic material behaviour are E_1, E_2, E_3, G_{12}, G_{23}, G_{13}, ν_{12}, ν_{23}, ν_{13}.

For some cases the UD-ply can be further simplified. Assuming that the material properties are identical in any direction transverse to the fibre direction (1-direction) leads to isotropic material behaviour in the 2-3 plane. This behaviour is called *transversally isotropic*. For symmetry about the 1-axis Eqn 1.2 reduces to

$$\begin{pmatrix} \sigma_{11} \\ \sigma_{22} \\ \sigma_{33} \\ \sigma_{12} \\ \sigma_{23} \\ \sigma_{13} \end{pmatrix} = \begin{pmatrix} C_{11} & C_{12} & C_{12} & 0 & 0 & 0 \\ C_{12} & C_{22} & C_{23} & 0 & 0 & 0 \\ C_{12} & C_{23} & C_{22} & 0 & 0 & 0 \\ 0 & 0 & 0 & C_{44} & 0 & 0 \\ 0 & 0 & 0 & 0 & \frac{1}{2}(C_{22} - C_{23}) & 0 \\ 0 & 0 & 0 & 0 & 0 & C_{44} \end{pmatrix} \begin{pmatrix} \varepsilon_{11} \\ \varepsilon_{22} \\ \varepsilon_{33} \\ 2\varepsilon_{12} \\ 2\varepsilon_{23} \\ 2\varepsilon_{13} \end{pmatrix} \tag{1.6}$$

leaving only 5 independent material constants E_1, E_2, G_{12}, ν_{12}, ν_{23}.

Within the thesis the material is generally assumed to behave as orthotropic. Only in some exceptions transverse isotropic behaviour is considered.

1.4 Numerical constitutive modelling framework for non-linear material behaviour

Within the framework of FE, the constitutive model has to establish the relationship between applied displacements and resulting nodal forces. Initially, the material behaviour is assumed to be linear elastic. The material's rate dependent material behaviour, however, results in non-linear material behaviour. Furthermore, as damage initiates and the material departs from the linear elastic response, additional non-linear material behaviour is introduced into the constitutive equations. In transient analysis, explicit FE has already proven to be a powerful tool. The non-linear problem is solved incrementally with the calculation increment (time step) being defined by the material properties and the spatial dicretisation. For each time step, an increment of stress is predicted for a given increment of strain. The assessment of the current state of stress (at time t) is usually performed by an incremental stress predictor or trial stress

$$\boldsymbol{\sigma}_t^{tr} = \boldsymbol{\sigma}_{t-\Delta t} + \boldsymbol{C} : \boldsymbol{\Delta\varepsilon} \tag{1.7}$$

where $\boldsymbol{C}$ is the elasticity tensor of the previous calculation increment. The assessment of the current state of the material is based entirely on the trial stress $\boldsymbol{\sigma}^{tr}$. For convenience, the index t is not used within the thesis as the measure of stress is always related to the current time step unless stated otherwise.

As already mentioned above, composite materials are heterogenous materials. The constitutive model therefore depends on the scale on which modelling is performed. In general, three main scales are commonly identified for the composites used here. First, the microscale, where fibre, matrix and the interface between them are considered separately. Second, the mesoscale where the lamina is considered as a homogeneous material but the interface between laminas is still considered separate. Third, the macroscale, where several laminas of different orientation including the interfaces are considered as one homogeneous material.

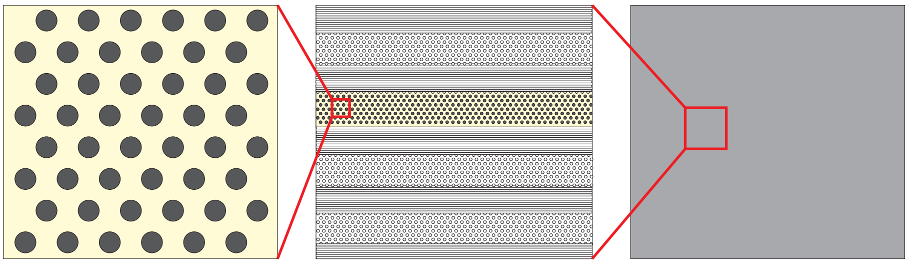

Figure 1.3: The three scales as identified in UD composites

In this study, modelling is performed on the mesoscale. In other words, the material is homogenised by smearing the behaviour of fibres and matrix over the RVE. The application of homogenisation requires a strict definition of the size of a RVE for which the constitutive model is valid. Within this thesis, the RVE represents a single unidirectionally reinforced lamina. In the framework of FE, each finite element represents a single RVE. Consequently, the spatial discretisation of the FE model should be chosen such that the maximum permitted size of the RVE is not exceeded (e.g. representing only one lamina). The definitions of damage initiation and propagation are mainly formulated in terms of stress. This restricts the minimal size of the finite element as the strength properties, which have to be provided as input, are usually measured values which represent an average over a certain volume (e.g. a homogenised measure of stress). The actual stresses at failure on the microscopic level are expected to be very different depending which constituent is present in the respective volume. Using a spatial discretisation which is too fine will therefore result in an unrealistic strength prediction and should be avoided.

1.5 Layout of the thesis

The objectives of the study involve several different aspects of composite materials. Therefore, no separate literature review chapter is included but the relevant literature is presented at the beginning of each chapter.

In the second chapter of the thesis an introduction to available composite failure theories is given. Suitable theories are selected, discussed and if necessary extended. The focus is on failure theories for general three dimensional stress states. Special attention was given to the prediction of failure mode dependent fracture planes. This feature of the proposed constitutive model is a key aspect for a physically sound prediction of composite material behaviour. The third chapter deals with damage evolution algorithms. Well known composite damage models are introduced and discussed. Based on the failure theories which were selected in Chapter 2, a novel composite damage model is proposed. The knowledge of the orientation of certain fracture planes is incorporated into the damage evolution algorithms to enable realistic material degradation due to damage growth. Chapter 4 presents experimental techniques to investigate the influence of strain rate on the intrinsic material properties. An extensive literature survey presents, summarises and discusses published strain rate dependent data of various composite materials. Optical measurement systems are introduced to the experiments to improve the accuracy of data analysis and to study the failure mechanisms. Finally, the rate dependent behaviour of selected composites is investigated experimentally. Here, the focus is on compressive behaviour as the published data indicates a lack of understanding for the material behaviour under such loading. Constitutive model verification data is presented in Chapter 5. An existing experimental setup for three point bending is verified and subsequently improved to increase accuracy of the obtained data. Simply supported beam bending experiments are performed at different loading rates and different span thus enabling the study of different composite failure modes and the subsequent damage evolution. These experiments are then modelled in Chapter 6 to verify the proposed constitutive model. Conclusions and suggestions for further research are given in Chapter 7 and 8.

Chapter 2

Prediction of the onset of damage in composite materials

This chapter begins by giving a brief historical overview of theories for the strength prediction of composite materials. The focus of this part is on novel physically based failure theories for general three dimensional states of stress. Selected theories are discussed in more detail. Building on these already existing failure theories, a three dimensional model for the prediction of the onset of damage evolution is proposed. Thereby, the model relies on the definition of fracture planes for each considered failure mode. Furthermore, the constitutive equations are extended to incorporate the strain rate dependency of the material.

2.1 Introduction

2.1.1 Yield criteria vs failure mode based criteria

The first composite failure theories were based on failure theories for isotropic materials. The well known yield criteria for ductile materials (eg. von Mises and Hill) were modified and applied. The term *yield criterion* is still used for composites even though the correct terminology should be *fracture condition*. Both, yield criteria and composite fracture conditions, are mathematically formulated in a similar way, but the underlying physical phenomena which they try to describe are fundamentally different.

The basic idea of yield criteria is the definition of the elastic limit of composites by a single failure envelope, usually in the mathematical form of tensor polynomial. One of the most acknowledged composite yield criteria is the Hoffman criterion for brittle materials [9]. Hoffman defined a single failure envelope based on stress invariants in orthotropic stress space using the Hill yield criterion. The proposed linear scalar yield criterion in principal stress space reads

$$C_1(\sigma_y-\sigma_z)^2+C_2(\sigma_z-\sigma_x)^2+C_3(\sigma_x-\sigma_y)^2+C_4\sigma_x+C_5\sigma_y+C_6\sigma_z+C_7\tau_{yz}^2+C_8\tau_{zx}^2+C_9\tau_{xz}^2=1. \tag{2.1}$$

In Eqn 2.1 $C_1...C_9$ are nine material parameters, uniquely determined from nine basic strength properties. Tsai [10] further developed the orthotropic yield criteria by introducing stress interaction terms. The failure envelope is thereby defined by two strength tensors $\boldsymbol{F}_i$ and $\boldsymbol{F}_{ij}$. In tensor notation the Tsai Wu criterion reads

$$\boldsymbol{F}_i\boldsymbol{\sigma}_i+\boldsymbol{F}_{ij}\boldsymbol{\sigma}_{ij}=1. \tag{2.2}$$

Tensor polynomial based yield criteria, like the Tsai Wu criterion, are widely used in composite design. The mathematical elegance of a single closed failure envelope and relatively small number of required material properties makes these criteria very interesting for designers. The big disadvantage of composite yield criteria is the missing physical basis of the formulations. The proposed interactions are often questionable [11] and the different failure modes, which are very typical for composites, are not reflected in a single failure envelope. Yield criteria usually only predict the onset of failure but give no information about the present failure mode. This information, however, is crucial for damage modelling.

Prediction of composite failure modes required new failure criteria to be developed on a sound physical basis. The failure mechanisms are entirely different for the different failure modes which are observed in composites. A single closed failure surface will therefore fail to represent all these different mechanisms. As a consequence, separate failure criteria for each failure mode are required. Work on such physically based failure theories started as early as 1973 with the Hashin Rotem criterion [12]. An extended theory has later been proposed by Hashin in 1980 [13]. This gave the foundation for physically based failure criteria. These criteria are sometimes referred to as phenomenological criteria or failure mode based criteria. The new approach defines separate failure envelopes or failure surfaces in stress space for each failure mode. This enables the failure mechanisms and underlying physics to be correctly reflected by the criteria. Hashin, for instance, proposed a set of two criteria for plane stress states to distinguish tensile and compressive fibre failure [13]

$$\begin{aligned} \left(\frac{\sigma_{11}}{X_t}\right)^2 + \left(\frac{\sigma_{12}}{S_{12}}\right)^2 &= 1 \qquad \text{for} \quad \sigma_{11} \geq 0 \\ \frac{\sigma_{11}}{X_c} &= 1 \qquad \text{for} \quad \sigma_{11} < 0 \end{aligned} \tag{2.3}$$

with $X_{t/c}$ being the tensile/compressive strength in fibre direction and S_{12} being the in-plane shear strength.

Physically based failure criteria can take various forms. The simplest form is the maximum stress criterion. Maximum stress criteria do not consider interaction of stresses to cause failure. A single stress term is compared with a strength value. A maximum stress criterion is widely used for the prediction of tensile fibre failure. The Hashin-Rotem criterion for fibre failure reads simply

$$\frac{\sigma_{11}}{X_t} = 1 \qquad \text{for} \quad \sigma_{11} > 0 \tag{2.4}$$

and can be extended by a second maximum stress criterion thus including the influence of shear stress

$$\left|\frac{\sigma_{12}}{S_{12}}\right| = 1. \tag{2.5}$$

More commonly, an interaction of several stress terms can be considered by the use of additive terms. Assuming a linear interaction, the above mentioned maximum stress citeria can be combined in the following form

$$\frac{\sigma_{11}}{X_t} + \left|\frac{\sigma_{12}}{S_{12}}\right| = 1. \tag{2.6}$$

This very simple form of interaction is hardly used, because experimental results indicate that it underpredicts the onset of failure under mixed loading conditions. The next higher order of interaction are quadratic additive criteria like the Hashin criterion for fibre rupture

$$\left(\frac{\sigma_{11}}{X_t}\right)^2 + \left(\frac{\sigma_{12}}{S_{12}}\right)^2 = 1. \tag{2.7}$$

This formulation is very common and used in many failure mode based criteria. It should be noted that there is no physical meaning behind the order of interaction. The chosen order is only a mathematical consideration in order to fit experimental data best. Higher order interaction terms are therefore not used because the experimental scatter of combined loading experiments is usually high and does not justify the significant higher computational effort of higher order interaction terms [14]. A comparison of the failure enveloped as defined by the above example failure criteria is presented in Fig 2.1.

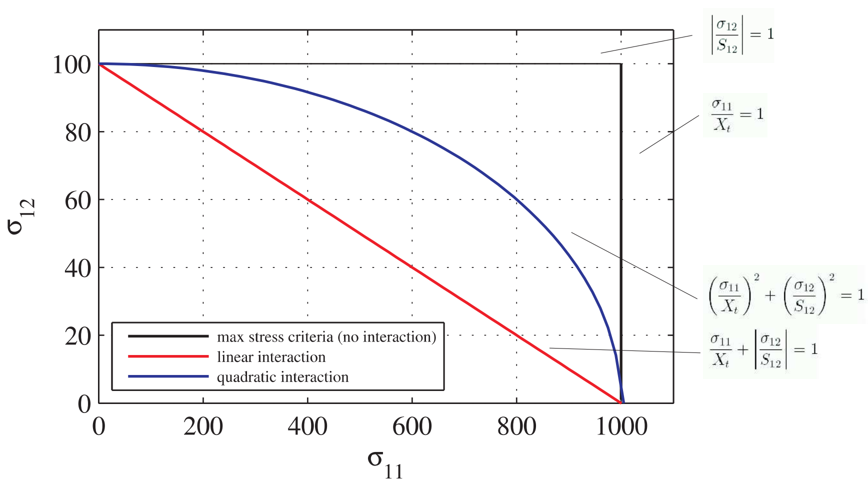

Figure 2.1: Influence of the order of interaction on the predicted failure locus

Which stress interactions are physically reasonable remains still unclear. At times, very intensive discussions have taken place about which interactions are valid [15, 16]. Biaxial test results which support the development of failure criteria are still rare and the experimental scatter significant.

Up to now various formulations for both, tensor polynomial criteria and failure mode based criteria have been proposed. A first attempt to compare and subsequently rank these criteria has been undertaken in the *World Wide Failure Exercise (WWFE)*. The round robin was initiated by Hinton and Soden in 1998 [17]. In part A, a number of test cases for certain laminate configurations and a set of material properties were given. Leading researchers in the field were invited to apply their failure theories to the selected test cases. After the strength predictions were published, a comparison with experimental results was performed in part B. Finally, in part C, additional theories were introduced and a final ranking of the theories was given. The results of the exercise were summed up in part B of the exercise in 2002 [18] and part C in 2004 [19]. Out of the 19 competing failure theories 5 were selected [20] to be most suited for designing composite structures even though no theory could accurately predict all test cases. The leading theories were proposed by Puck [21], Tsai [125], Cuntze [22], Zinoviev [126] and Bogetti [127]. All selected theories, with the exception of Tsai's tensor polynomial, are physically based. The theories of Tsai and Bogetti could not be completely assessed since they gave very different results compared to the other theories in regions where there are no experimental results available. The general conclusion of the WWFE was that physically based failure theories give qualitatively better results. Even though the Tsai Wu tensor polynomial was able to match experimental results very well, it is unable to predict the failure mode and some concern was expressed regarding the predictions in the compressive stress domain. The maximum stress/strain based theories of Zinoviev and Bogetti gave reasonable results, but the predicted failure envelopes seem to be unconservative for many stress regimes.

For this study, the focus is on physically based failure criteria. In the following, available failure criteria for the various composite failure modes are introduced in more detail.

2.1.2 Failure models for the prediction of Inter Fibre Failure

The failure behaviour of the matrix has been the focus of research for many years. Experimental observations lead to the conclusion that Inter Fibre Failure (IFF) is of brittle nature. Failure and subsequent fracture seems to happen instantaneously with no apparent inelastic deformation [21]. IFF is caused by two main failure mechanisms. The failure occurs due to cohesive fracture of the matrix and adhesive fracture of the fibre-matrix interface [22]. The fibre reinforcement and the brittle failure make a Mohr failure criterion based approach an appropriate choice.

Mohr postulated [23] that failure is caused only by the stresses which act on the fracture plane. The idea was initially applied to the prediction of IFF modes by Hashin [13]. The proposed criteria for IFF and a plane state of stress read

$$\begin{aligned} \left(\frac{\sigma_{22}}{Y_t}\right)^2 + \left(\frac{\sigma_{12}}{S_{12}}\right)^2 &= 1 \qquad \text{for} \quad \sigma_{22} \geq 0 \\ \left(\frac{\sigma_{22}}{2S_t}\right)^2 + \left(\left(\frac{Y_c}{2S_t}\right) - 1\right)\frac{\sigma_{22}}{Y_c} + \left(\frac{\sigma_{12}}{S_{12}}\right)^2 &= 1 \qquad \text{for} \quad \sigma_{22} < 0 \end{aligned} \tag{2.8}$$

where S_t is an out of plane shear strength (S_{23} or S_{13}). Basing his argument on Mohr's suggestion to only consider the fracture plane stresses for the initiation of failure Hashin proposed a three dimensional failure criterion. However, he did not pursue the idea because of excessive computational effort involved in finding the plane with a critical orientation which results in IFF. Subsequently, various criteria, basing on the Hashin model, have been proposed [11, 22, 1]. The underlying physical meaning, however, remained the same.

Puck took the basic idea of the Hashin criteria for IFF and extended it [11]. Following the idea of a Mohr Coulomb type of failure, a fracture plane is identified. IFF is assumed to occur on a plane parallel to the reinforcing fibres. This plane is inclined by an angle θ which is measured from the 3-axis (see Fig.2.2). There are three tractions acting on the fracture plane, the normal traction σ_n and the two shear tractions τ_{n1} and τ_{nt}. Only those three components of stress will contribute to failure. The failure criteria are therefore written in terms of fracture plane stresses. In it's simplest form, the Puck matrix failure criterion

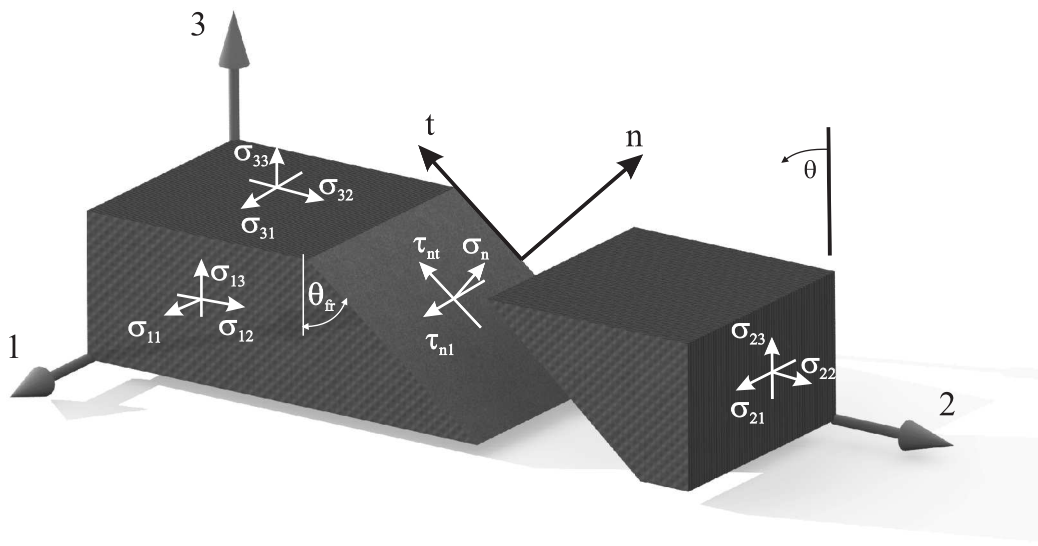

Figure 2.2: Definition of the fracture plane for IFF in the Puck model

reads

$$
\begin{aligned}
\left(\frac{\sigma_n}{R_n^{(+)}}\right)^2 + \left(\frac{\tau_{n1}}{R_{n1} - p_{n1}\sigma_n}\right)^2 + \left(\frac{\tau_{nt}}{S_{nt} - p_{nt}\sigma_n}\right)^2 &\geq 1 \qquad \text{for} \quad \sigma_n \geq 0 \\
\left(\frac{\tau_{n1}}{R_{n1} - p_{n1}\sigma_n}\right)^2 + \left(\frac{\tau_{nt}}{S_{nt} - p_{nt}\sigma_n}\right)^2 &\geq 1 \qquad \text{for} \quad \sigma_n < 0.
\end{aligned}
\tag{2.9}
$$

The slope parameters p_{n1} and p_{nt} represent internal friction influence (under compressive normal stress on the fracture plane, the apparent shear strength is increased). R_{n1} and R_{nt} characterise the resistance of the fracture plane against shear failure while $R_n^{(+)}$ is the resistance against tensile failure on the fracture plane.

The failure criteria in Eqn 2.9 define a failure surface in fracture plane stress space, called the *master failure surface*. The assessment of failure requires therefore finding a critical orientation θ. The plane defined by this critical angle θ_{fr} will become the plane of failure, called *fracture plane*. The angle θ_{fr} is called *fracture plane angle*. The fracture plane tractions are obtained by rotation of the stress tensor about the 1 axis

$$
\boldsymbol{\sigma}^{fr} = \boldsymbol{R}_1(\theta_{fr}) \cdot \boldsymbol{\sigma} \cdot \boldsymbol{R}_1^T(\theta_{fr}) \tag{2.10}
$$

with $\boldsymbol{R}_1(\theta_{fr})$ being the rotation matrix for an rotation about the 1-axis by the angle θ_{fr}.

The rotation can also be written as

$$\begin{pmatrix} \sigma_1 \\ \sigma_n \\ \sigma_t \\ \tau_{n1} \\ \tau_{nt} \\ \tau_{1t} \end{pmatrix} = \begin{pmatrix} 1 & 0 & 0 & 0 & 0 & 0 \\ 0 & c^2 & s^2 & 2cs & 0 & 0 \\ 0 & s^2 & c^2 & -2cs & 0 & 0 \\ 0 & 0 & 0 & c & 0 & s \\ 0 & -sc & sc & 0 & c^2-s^2 & 0 \\ 0 & 0 & 0 & -s & 0 & c \end{pmatrix} \begin{pmatrix} \sigma_{11} \\ \sigma_{22} \\ \sigma_{33} \\ \sigma_{12} \\ \sigma_{23} \\ \sigma_{13} \end{pmatrix} \tag{2.11}$$

with

$$\begin{aligned} s &= \sin(\theta_{fr}) \\ c &= \cos(\theta_{fr}) \end{aligned} \tag{2.12}$$

The fracture plane tractions are finally given by

$$\begin{aligned} \sigma_n &= \sigma_{22}\cos^2(\theta_{fr}) + \sigma_{33}\sin^2(\theta_{fr}) + 2\sigma_{23}\sin(\theta_{fr})\cos(\theta_{fr}) \\ \tau_{n1} &= \sigma_{12}\cos(\theta_{fr}) + \sigma_{13}\sin(\theta_{fr}) \\ \tau_{nt} &= -\sigma_{22}\cos(\theta_{fr})\sin(\theta_{fr}) + \sigma_{33}\cos(\theta_{fr})\sin(\theta_{fr}) + \sigma_{23}\left(\cos^2(\theta_{fr}) - \sin^2(\theta_{fr})\right). \end{aligned} \tag{2.13}$$

From Eqn 2.13 it becomes clear that all stresses, except σ_{11} contribute to the fracture plane tractions and therefore to IFF. The computational effort for finding the critical angle can be cumbersome. The concept of the fracture plane was already proposed by Hashin in 1980 but not pursued due to the lack of computing power. For a plane state of stress, analytical solutions have already been found [24], but no efficient angle search approach for three dimensional stress states has been proposed yet.

The main criticism of the Puck failure theory has been the comparatively large number of required parameters (eg. p_{n1} and p_{nt}). It is sometimes claimed that those parameters are of empirical nature and require extensive experimental material characterisation programs [25]. Puck gave some recommendations and pragmatic approximations for his model in [24]. Additionally, an intensive material characterisation program for various materials has been published in [3]. Experimental techniques to determine the parameters for the Puck model are proposed and the theory is verified for CFRP and GFRP.

Davila and Camanho [1] extended the Puck theory by suggesting ply thickness dependent strength parameters. Fracture mechanics based analysis was employed to derive the influence of the ply thickness on the strength. In particular, thin and thick embedded plies were investigated. The idea was further developed by Pinho et al. [26] for three-dimensional stress states.

In parallel with Puck, Cuntze and Freund [22] developed the failure mode concept. The fundamental assumptions for both theories are identical, but Cuntze defines his failure criteria in terms of stress invariants and avoids therefore a search for the critical fracture plane orientation. Cuntze composes the failure surface by a set of three different failure criteria. Each failure criterion characterises a certain failure mechanism and incorporates only one strength parameter. The first IFF mode is a tensile failure transverse to the fibre which is characterised by the transverse tensile strength Y_t. The second IFF mode is a shear failure which is characterised by the in-plane shear strength S_{12}. This failure results in a matrix crack which is oriented at $\theta_{fr} = 0°$ (see Fig 2.2). The third IFF mode is characterised by Y_c and results in a fracture plane which is inclined by $\theta_{fr} \neq 0°$. The failure criteria read

$$\begin{aligned}
&\text{IFF1:} \quad F_{\perp}^{\sigma} = \frac{I_2 + \sqrt{I_4}}{2Y_t} = 1 \\
&\text{IFF2:} \quad F_{\perp\parallel} = \frac{I_3^{2/3}}{S_{12}^3} + b_{\perp\parallel}\frac{I_2 I_3 - I_5}{S_{12}^3} = 1 \\
&\text{IFF3:} \quad F_{\perp}^{\tau} = (b_{\perp}^{\tau} - 1)\frac{I_2}{Y_c} + \frac{b_{\perp}^{\tau} - 1 I_4 + b_{\perp\parallel}^{\tau} I_3}{Y_c^2} = 1.
\end{aligned} \tag{2.14}$$

In Eqn 2.14 the parameters b characterise the slope of the failure envelopes and I denotes the following five stress invariants which have been chosen to best describe the multi-axial behaviour of the material [22]

$$\begin{aligned}
I_1 &= \sigma_{11} \\
I_2 &= \sigma_{22} + \sigma_{33} \\
I_3 &= \sigma_{12}^2 + \sigma_{13}^2 \\
I_4 &= (\sigma_{22} - \sigma_{33})^2 + 4\sigma_{23}^2 \\
I_5 &= (\sigma_{22} - \sigma_{33})(\sigma_{13}^2 - \sigma_{12}^2) - 4\sigma_{12}\sigma_{23}\sigma_{13}.
\end{aligned} \tag{2.15}$$

Furthermore, Cuntze defines mixed failure domains where certain failure modes interact. In the case of IFF two such mixed failure domains exist. First, between IFF1 and IFF2 and second, between IFF2 and IFF3. Cuntze proposed a power law to characterise the interaction in these zones in order to obtain the final failure locus. Therefore, resultant reserve factors are calculated from the failure criteria in Eqn 2.14 and the respective interaction is given by

$$\begin{aligned} \left(\frac{1}{f_{res}^{total}}\right)^m &= \left(\frac{1}{f_{res}^{IFF1}}\right)^m + \left(\frac{1}{f_{res}^{IFF2}}\right)^m \\ \left(\frac{1}{f_{res}^{total}}\right)^m &= \left(\frac{1}{f_{res}^{IFF2}}\right)^m + \left(\frac{1}{f_{res}^{IFF3}}\right)^m . \end{aligned} \tag{2.16}$$

The reserve factor f_{res}^{total} is the total reserve factor including the failure mode interaction and m a fitting coefficient. An example of a failure envelope as predicted by the Cuntze model is presented in Fig 2.3.

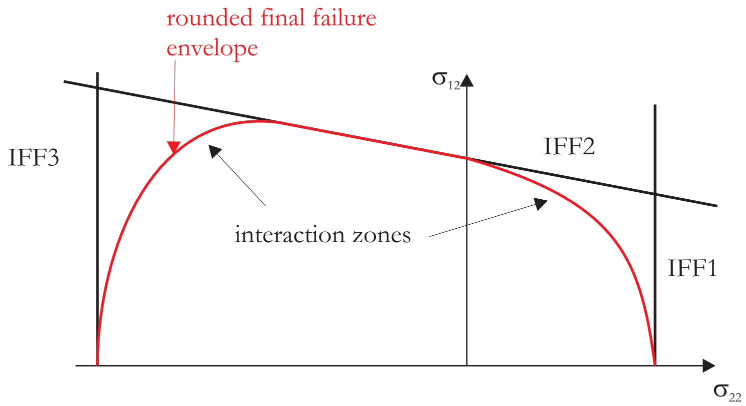

Figure 2.3: Example for a IFF failure envelope for the Cuntze model (schematic)

An important feature of the Cuntze model is the consideration of a probabilistic distribution of the strength properties. This enables incorporation of the significant scatter usually observed in composite testing into the calculation of reserve factors which are commonly used in structural design. Furthermore, Cuntze considers inelastic (e.g. plastic) deformation of the matrix material by introducing a Yield condition.

Both theories, Puck and Cuntze, give very similar failure predictions. The advantage of the Cuntze theory is that the fracture plane orientation is not necessary to predict failure.

However, Cuntze introduces additional non-physical parameters which makes a calibration more difficult.

Before criteria for fibre failure modes are discussed, a final remark on the nature of IFF is made. IFF is assumed to be a brittle failure. While this is a reasonable assumption at the meso-scale and macro-scale as used here, analysis on the micro-scale (fibres and matrix are modelled explicitly) shows different results. Recent efforts in micro mechanical modelling of IFF have clearly demonstrated local inelastic deformation of the matrix material in the failure plane [27]. Incorporating these effects might prove important especially for compressive failure.

2.1.3 Failure models for the prediction of fibre rupture

Fibre rupture is a tensile failure mode of the reinforcing fibres. Single filaments cannot carry the applied load and finally tear. The failure by fibre rupture is usually catastrophic. Due to the high stiffness of the fibres, the stresses cannot be redistributed by the surrounding matrix when the fibres fail. As a consequence the whole ply fails. The prediction of tensile strength in fibre direction is quite accurately achieved by a maximum stress criterion. The situation is completely different when it comes to combined loading like superimposed transverse and/or shear stress. The prediction of fibre failure under combined loading has led to intense debates in the past (see [16, 15]). In the following, an overview over existing theories is given.

The majority of researchers assume that in the tensile loading regime the maximum stress criterion

$$\frac{\sigma_{11}}{X_t} = 1 \qquad \text{for} \quad \sigma_{11} \geq 0 \tag{2.17}$$

predicts the fibre failure sufficiently accurate. This is definitely true for the case of uniaxial stress σ_{11} in the fibre direction, but what happens when other components of stress act in the same ply? Answering this question proves to be a difficult task, since there is only limited data available.

Puck and Schuermann [21] suggested an interaction between stress in fibre direction σ_{11} and stress transverse to the fibres σ_{22}. The proposed interaction is caused by the very different stiffness of fibre and matrix. This can result in a stress magnification when σ_{22} is present.

Hashin [13] proposed an interaction of normal stress σ_{11} in fibre direction and the two shear stresses σ_{12} and σ_{13} which are acting across the fibres. No experimental data was available to clarify the interaction, for which reason Hashin choose the following quadratic formulation

$$\left(\frac{\sigma_{11}}{X_t}\right)^2 + \left(\frac{\sigma_{12}}{S_{12}}\right)^2 + \left(\frac{\sigma_{13}}{S_{13}}\right)^2 = 1. \tag{2.18}$$

In Eqn 2.18, S_{12} and S_{13} are the strength of the fibres towards shear failure which Hashin assumed to be identical for both shear stresses.

Verification of the stress interaction towards fibre rupture proves difficult. A few data points have been published within the World Wide Failure Exercise (WWFE). In [2] stress combinations of σ_{11} and σ_{12} at failure are given. Unfortunately, the observed failure mode was not reported. The data points were all obtained at stresses σ_{11} close to the tensile strength in fibre direction X_t and show that superimposed shear stress lowers the tensile strength. However, the number of data points is too low to conclude on a relationship between shear stress and tensile fibre failure.

In general, the lack of experimental evidence prevented the formulation of a sound failure theory for the influence of stress terms other than σ_{11} on tensile fibre failure. Little experimental evidence indicates that in-plane shear stress lowers the tensile strength of the fibre.

2.1.4 Failure models for the prediction of compressive fibre failure

The strength prediction for compressive failure of CFRP has attracted significant attention in the research community for the last 30 years. This is caused by the fact that the measured compressive strength of UD reinforced composites can be as low as 60% of the tensile strength and can put a structure in a very high risk of failure at low stress levels. Compressive fibre failure occurs by various different failure modes and is governed by the matrix material which supports the fibres under axial compressive load. To date, the mechanisms of compressive fibre failure are still under discussion and new failure theories continue to emerge. A comprehensive review of the state of research has been published by Fleck [28] in 1997. According to Fleck the following compressive fibre failure modes can be observed in long fibre reinforced composites:

- *Elastic microbuckling*
- *Plastic microbuckling (fibre kinking)*
- *Fibre crushing*
- *Splitting*
- *Buckle delamination*
- *Shear band formation*

Historically, failure due to *Elastic microbuckling* was investigated first. The first theory describing the governing mechanisms has been proposed by Rosen [29]. Rosen postulated that compressive fibre failure occurs due to elastic instability. A microbuckling analysis was performed for two buckling modes. The extension mode where adjacent fibres buckle out of phase and a shear mode when all fibres buckle with the same wavelength and in the same phase. Rosen established a connection between buckle mode and fibre volume fraction. For UD composites with a fibre volume fraction of 30% or higher, as commonly found in many applications, the material would fail in the shear mode at a compressive stress

$$\sigma_c = \frac{G}{(1 - v_f)}. \tag{2.19}$$

In Eqn 2.19 G denotes the shear modulus of the matrix and v_f the fibre volume fraction of the composite. Comparison with experimentally measured strength values showed the predicted compressive strength was far too high. This indicates that most polymeric composites fail due to a different failure mechanism.

The theory was extended by Argon [30] who included an initial fibre misalignment ϕ^0 and a perfect plastic behaviour of the matrix. This results in *Plastic microbuckling* often referred to as *Fibre kinking.* The matrix deforms inelastically and fails to support the fibres which start to rotate. As the rotation increases the fibres finally break forming a kink band. The critical failure stress is given by

$$\sigma_c = \frac{Y_c}{\phi^0}, \tag{2.20}$$

where in this case Y_c denotes the yield stress of the matrix. The theory was later extended by Budiansky [31], now considering elastic and plastic shear deformation of the matrix

$$\sigma_c = \frac{Y_c}{\gamma_c + \phi^0}. \tag{2.21}$$

In Eqn 2.21 γ_c denotes the shear strain at yield. Experimental studies support Argon's theory and Yurgatis [32] measured the initial fibre misalignment in a carbon/PEEK composite as $\phi^0 = 3°$. Additionally, Martinez et.al. [33] investigated the influence of fibre misalignment on the mechanical properties of the composite. A clear relation between composite strength and fibre misalignment was identified.

Compressive failure by *Fibre crushing* occurs in composites where the fibre crushing strength is lower then the yield strength of the matrix. Modern carbon fibre/epoxy composites do not show this behaviour under normal conditions. One exception is composite applications at low temperatures (e.g. $-40°$).

The failure due to *Buckle delamination* is important for damage tolerant structures. Due to manufacturing problems or low velocity impact, small delaminations can be generated. Under axial subsequent compressive load the delamination grows and the composite fails due to buckling of the adjacent fibre layers.

The failure modes of *Splitting* and *Shear-Band formation* are mainly related to ceramic matrix composites or composites with very low fibre volume fractions. These failure modes are not relevant to the composites considered here.

In this study, the focus is on compressive failure due to fibre kinking. The phenomenon is widely reported in the literature [34, 35]. Special emphasis is given to the extended kinking theory initially proposed by Davila and Camanho [1] and later extended by Pinho et al. [26]. The theory assumes an initial fibre misalignment as shown for a plane state of stress in Fig.2.4.

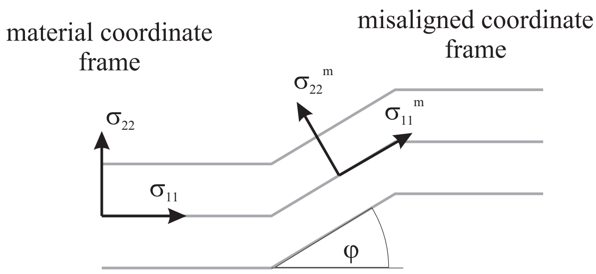

Figure 2.4: Fibre misalignment in 2D (after [1])

Failure due to fibre kinking is assumed to occur when the surrounding matrix fails to support the fibres in the misaligned region. The onset of fibre kinking can be predicted by assessing the stress state in a coordinate system rotated in the fibre misalignment frame. This allows the application of an IFF failure criterion for the prediction of the onset of fibre kinking. Essential for this approach is the knowledge of the initial fibre misalignment which can be obtained from microscopy. To avoid the difficult and time consuming measurement of the initial fibre misalignment, a pragmatic suggestion for the estimation of ϕ^0 is given in [1]. A simple uniaxial compression test is performed and the stress at failure measured. The macroscopic stress state in this experiment is very simple ($\sigma_{11} = -X_c$, $\sigma_{22} = \sigma_{33} = \sigma_{12} = \sigma_{23} = \sigma_{13} = 0$). In the case of uniaxial compression and assuming plane stress, the stress state in the misaligned coordinate frame is given by

$$
\begin{aligned}
\sigma_{11}^m &= \sigma_{11}\cos^2\phi \\
\sigma_{22}^m &= \sigma_{11}\sin^2\phi \\
\sigma_{12}^m &= -\sigma_{11}\sin\phi\cos\phi.
\end{aligned}
\tag{2.22}
$$

Only the transverse stress σ_{22}^m and the in-plane shear stress σ_{12}^m contribute to IFF in the misaligned frame. At failure these stresses become

$$
\begin{aligned}
\sigma_{22}^m &= -X_c\sin^2\phi^c \\
\sigma_{12}^m &= X_c\sin\phi^c\cos\phi^c.
\end{aligned}
\tag{2.23}
$$

The total fibre misalignment at failure ϕ^c is composed of the initial fibre misalignment ϕ^0, depending on the material and manufacturing route, and an additional misalignment ϕ^e caused by elastic deformation as load is applied

$$\phi^c = \phi^0 + \phi^e. \tag{2.24}$$

The misalignment angle ϕ^c is expected to be small. Hence the failure is going to be dominated by σ_{12}^m rather then σ_{22}^m and the fracture angle θ_{fr} is equal $0°$. This simplifies the Puck IFF criterion (Eqn 2.9) to

$$\frac{\sigma_{12}^m}{S_{12} - p_{n1}\sigma_{22}^m} = 1. \tag{2.25}$$

The stresses at failure are known (Eqn 2.23) and Eqn 2.25 reads

$$S_{12} = X_c\left(\sin\phi^c\cos\phi^c - p_{n1}\sin^2\phi^c\right). \tag{2.26}$$

Eqn 2.26 can then be solved for ϕ^c [1]. The elastic misalignment ϕ^e is given by

$$\phi^e = \frac{\sigma_{12}^m}{G_{12}} = \frac{X_c}{G_{12}} \tag{2.27}$$

using the small angle approximation. The initial fibre misalignment can finally be obtained from Eqn 2.24. This enables the prediction of fibre kinking for plane stress situations.

The model has been extended to three dimensions by Pinho et al. [4, 36]. The problem is significantly more complex in three dimensions as the kink band is not restricted to a single kink plane. Pinho defines three angles, the kink band angle ψ , the misalignment angle ϕ and the orientation of the matrix fracture plane θ to express the orientation of the kink band. Furthermore, the model incorporates non-linear shear behaviour of the matrix. The three dimensional extension of the kinking model has a great potential because an interaction of all stresses is considered towards the initiation of fibre kinking. This is a crucial aspect in the modelling of impact where complex stress states are very common.

2.1.5 Failure models for the prediction of onset of delamination

A failure mode which is widely observed in laminated composites is delamination. Failure occurs due to interlaminar shear stresses and through-thickness stresses, resulting in the separation of single laminae over significant areas. Delamination usually starts from stress concentrations which can be found at free edges, material defects or other local failure modes. In general, delamination initiation does not coincide with structural failure of the laminate. However, the initiated delamination may grow in an unstable manner and finally result in an interaction of in-plane failure modes which can cause an catastrophic final failure. Especially for compressive loading, delaminations can significantly reduce the strength of a laminate.

Delamination initiation criteria base mainly on two approaches, stress based criteria and fracture mechanics based criteria. In the following, some of the proposed criteria for both approaches are introduced. A review of delamination initiation criteria for both, stress based and fracture mechanics based models, can be found in [37].

An early approach for failure prediction using stress based failure criteria was proposed by Whitney et al. [38]. A study of notched laminates showed that a stress based failure criterion if using a localised maximum stress close to a stress concentration will result in a laminate strength which is too low. Therefore, a dimension parameter was introduced which describes the distance from a stress concentration over which the material must be critically stressed in order to initiate failure. The idea was applied to delamination failure criteria by Brewer [39], who formulated his failure criterion by the use of average stresses. Similar to Whitney, Brewer introduced a parameter x_{avg} which is used to average localised stresses as follows

$$\overline{\sigma}_{ij} = \frac{1}{x_{avg}} \int_0^{x_{avg}} \sigma_{ij}\, \mathrm{d}x. \tag{2.28}$$

In Eqn 2.28 x is the distance from the free edge and x_{avg} an experimentally obtained averaging dimension. The averaged stresses are then used in the following interaction criterion

$$\left(\frac{\overline{\sigma}_{13}}{S_{13}}\right)^2 + \left(\frac{\overline{\sigma}_{23}}{S_{23}}\right)^2 + \left(\frac{\overline{\sigma}^t_{33}}{Z_t t}\right)^2 + \left(\frac{\overline{\sigma}^c_{33}}{Z_c}\right)^2 = 1 \tag{2.29}$$

The Brewer criterion considers a contribution of compressive stress normal to the delamination plane to the onset of delamination. This seemed unrealistic. It is widely assumed that delamination does not initiate under normal compression in the delamination plane [40]. However, studies by Hou and Petrinic [41] showed that even under normal compressive stress, delamination can develop when the interlaminar shear stresses are high enough. The Brewer delamination criterion was therefore refined resulting in a formulation where compressive normal stress impedes delamination. The failure criteria read

$$\begin{aligned} \left(\frac{\sigma_{33}}{Z_t}\right)^2 + \left(\frac{\sigma_{13}+\sigma_{23}}{S_d}\right)^2 &= 1 \qquad \text{for} \quad \sigma_{33} \geq 0 \\ \left(\frac{\sigma_{13}+\sigma_{23}}{S_d}\right)^2 - \left(\frac{8\sigma_{33}}{S_d}\right)^2 &= 1 \qquad \text{for} \quad -\sqrt{\frac{(\sigma_{13}^2+\sigma_{23}^2)}{8}} \leq \sigma_{33} < 0 \end{aligned} \tag{2.30}$$

with Z_t being the trough thickness tensile strength and S_d being an out of plane shear strength. The Brewer delamination criterion in its various forms is widely used for prediction of the onset of delamination.

Another stress based failure criterion has been proposed by Puck [11]. Assuming that delamination is just a matrix crack with certain orientation, Puck proposed the application of his IFF criterion. Delamination will initiate, if the fracture plane angle $\theta_{fr} = 90°$. A more detailed discussion of this approach will be given later in this chapter.

An alternative way of formulating delamination criteria is based on fracture mechanics.

It is assumed that the material contains defects even before the onset of failure. The onset of delamination is therefore treated as a propagation of cracks which are already in the material. Strain energy release rates are calculated and failure is assumed to propagate if the strain energy release rate G reaches a critical energy release rate G_c. A simple example for this approach has been proposed by O'Brien [42]. He derived a simplified energy release rate G (energy per unit of delaminated area)

$$G = \frac{t\varepsilon_{11}^2}{2}\left(E_1^0 - E_1^{dam}\right) \tag{2.31}$$

and compared with a critical energy release rate G_c. In Eqn 2.31 E_1^0 refers to the original longitudinal laminate Young's modulus and E_1^{dam} refers to the longitudinal Young's modulus of the remaining sublaminates after delamination. The variable t denotes the thickness of the laminate. Today, the increasing use of FE solvers allows for more complex models and more accurate calculation of the energy release rates. In general, it was found that fracture mechanics gives more accurate results when a initial defect of known size is present [43]. However, at a structural level this is rarely the case. Therefore, in most applications stress based failure criteria are used to determine the onset of delamination and fracture mechanics based formulations find their application in the damage propagation laws.

The introduction gave a brief overview over composite failure modes and available failure theories for composite strength prediction. The general trend towards more accurate physical based failure theories was shown and recent failure theories introduced. The following part of the chapter will discuss and extend selected failure models for each composite failure mode. The focus is therefore on physically based theories for general three dimensional stress states.

2.2 Framework for the prediction of damage initiation

Impact events usually result in complex three dimensional stress states. Especially in the region of impact, high local out of plane stresses can be observed. As a consequence, many failure theories are often inadequate due to the common assumption of plane stress. Within this study the focus lies, therefore, on three dimensional theories for the prediction of the onset of material behaviour which is not linear elastic anymore.

The term *Failure criteria* usually indicates initiation of failure (or better fracture) in the composite. In the thesis, failure criteria are used to predict the departure from the linear elastic path by the evolution of damage within the material. It would therefore be more adequate to call the criteria *Damage initiation criteria*. However, the term failure criteria is widely accepted within the composite community and remains therefore unchanged within the thesis.

Research has shown that physically based failure criteria enable a more accurate prediction of the onset of damage evolution. The criteria allow for the prediction of strength *and* the associated damage mechanism. This is crucial for impact modelling as the prediction of damage evolution requires a clear understanding of the underlying physical phenomena. The chosen physically based failure criteria strictly incorporate only the stress terms which influence a given failure mode. Therefore, critical planes, on which damage is initiated, are identified within the UD ply. The initiation/propagation of damage is then assessed by failure criteria which incorporate the three tractions which are acting on that critical plane.

In the context of non-linear numerical analysis, involving an incremental predictor-corrector method, a measure of admissibility of elastically predicted stress state is introduced as the material exposure e. The material exposure indicates the onset of damage if the following condition is satisfied

$$e \geq 1. \tag{2.32}$$

All failure criteria used within the thesis are written so that e is related linearly to the stress. Therefore, only failure criteria which are homogenous in the stress terms (all stress terms of the same order) can be used. This has the advantage that a reserve factor f^{res} can be calculated directly from the material exposure by

$$f^{res} = \frac{1}{e}. \tag{2.33}$$

The reserve factor is a measure of how much additional stress in proportion the material can take before damage initiates. The importance of the reserve factor for the modelling of damage evolution will be shown later in the thesis. A separate material exposure is calculated for each failure mode. The following composite failure modes are considered in the model

- e_1 *fibre rupture*
- e_2 *fibre kinking*
- e_3 *IFF*
- e_4 *delamination.*

In the remaining part of the chapter, suitable failure criteria for each failure mode will be chosen and discussed. Finally, strain rate dependent material behaviour is introduced into the model for the prediction of the onset of damage.

2.3 Prediction of tensile fibre failure

2.3.1 Failure criteria for fibre rupture

It was already pointed out in the introduction that stress interaction leading up to fibre rupture is still subject to discussion. It is commonly assumed that only the normal stress in fibre direction σ_{11} causes fibre rupture. The simple maximum stress criterion which is commonly used [11] reads

$$\frac{\sigma_{11}}{X_t} = 1 \qquad \text{for} \quad \sigma_{11} \geq 0. \tag{2.34}$$

There is some data available [2] which indicates an interaction of σ_{11} and σ_{12}. The exact mechanisms are not fully understood yet, but it is assumed here that for a 3D state of stress a quadratic interaction of σ_{11}, σ_{12} and σ_{13} towards fibre rupture exists. The following failure criterion proposed by Hashin [13] is used

$$\left(\frac{\sigma_{11}}{X_t}\right)^2 + \left(\frac{\sigma_{12}}{S_{12}^f}\right)^2 + \left(\frac{\sigma_{13}}{S_{13}^f}\right)^2 = 1 \qquad \text{for} \quad \sigma_{11} \geq 0. \tag{2.35}$$

The strength X_t is obtained from simple uniaxial tension tests. The strength properties S_{12}^f and S_{13}^f mark a fibre failure due to pure shear loading. As the UD-ply is assumed to be transversally isotropic, there is no obvious reason to distinguish between S_{12}^f and S_{13}^f. Both strength properties characterise the same failure mode (see Fig 2.6(b) and 2.6(d). Therefore, the following simplification is used here

$$S_{12}^f = S_{13}^f = S_f. \tag{2.36}$$

Eqn 2.35 allows the calculation of the material exposure e_1 for fibre rupture by

$$e_1 = \begin{cases} \sqrt{\left(\frac{\sigma_{11}}{X_t}\right)^2 + \left(\frac{\sigma_{12}}{S_f}\right)^2 + \left(\frac{\sigma_{13}}{S_f}\right)^2} & \text{for} \quad \sigma_{11} \geq 0 \\ 0 & \text{otherwise} \end{cases} \tag{2.37}$$

A illustration of the failure surfaces as defined by both criteria is displayed in Fig 2.5. Note that the failure surface of the interaction criterion is a surface of revolution about the σ_{11} axis but only one half is plotted in Fig 2.5.

2.3.2 Determination of shear strength S_f

The shear strength S_f is the resistance of the material against fracture across the fibres due to pure shear stress σ_{12} or σ_{13} (see Fig 2.6). It is not common to use this strength property, because it is very difficult to measure. If a composite specimen is loaded in pure shear σ_{12} or σ_{13} the fracture will occur along the fibres as shown in Fig 2.6(a) and 2.6(c). This, however, is an IFF and not fibre rupture. The fibres themselves are not damaged and can still carry tensile load. It appears that the strength for IFF is always lower for which reason the pure shear failure of the fibres itself is difficult to observe experimentally. One possible experiment would be a punch test with thin panels to prevent rotation of the

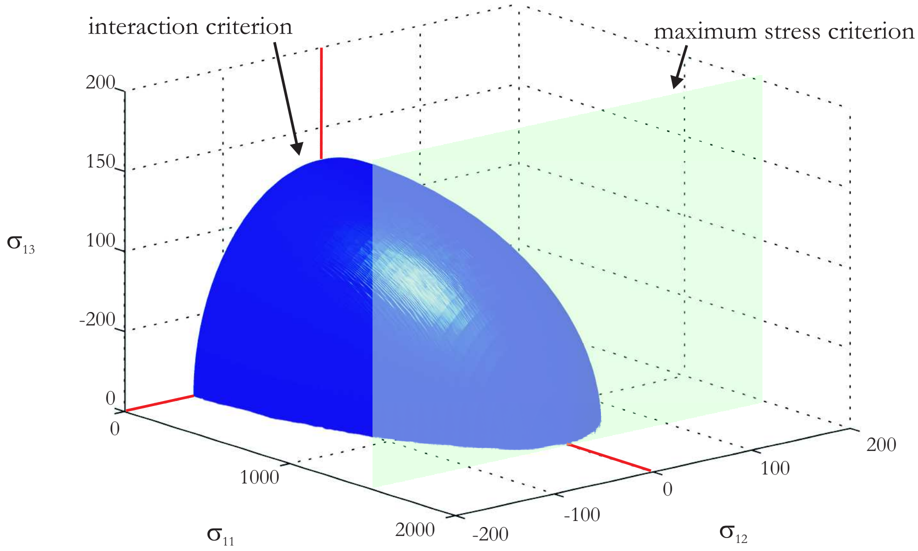

Figure 2.5: Failure envelope for fibre rupture in tension

fibres thus generating a pure shear failure. In this study S_f is estimated from experimental data presented in [7]. In the following section the chosen failure criterion is verified by some experimental results taken from the literature. The same data is then used to estimate S_f.

2.3.3 Verification of the failure model for fibre failure

The lack of experimental evidence related to multi-axial loading makes a verification of the predicted failure surface very difficult. A set of experimentally observed in-plane stress combinations which result in failure was published as input parameters for the WWFE in [7, 2]. The data points were obtained by testing tube specimens made from carbon fibre/epoxy (T300/BSL914C) under combined axial tension and torsion. All the specimens consist of the same material. Unfortunately, only the stress at failure, but not the present failure mode was reported in [2]. This makes a further comparison very difficult, since it is not clear whether every data point represents a fibre failure. A comparison of the strength prediction of both, interaction and maximum stress criterion, with the experimental data is presented in Fig 2.7. Please note that all predictions base on the input properties presented in Table 2.3.

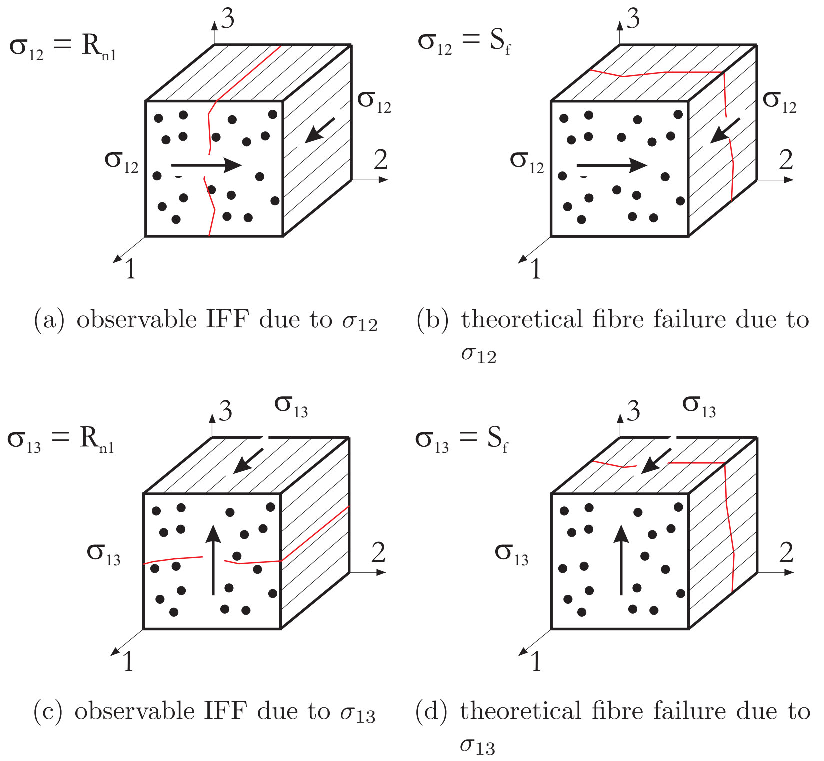

(a) observable IFF due to σ_{12}

(b) theoretical fibre failure due to σ_{12}

(c) observable IFF due to σ_{13}

(d) theoretical fibre failure due to σ_{13}

Figure 2.6: Theoretically possible and experimentally observed failure modes due to shear stress across the fibre

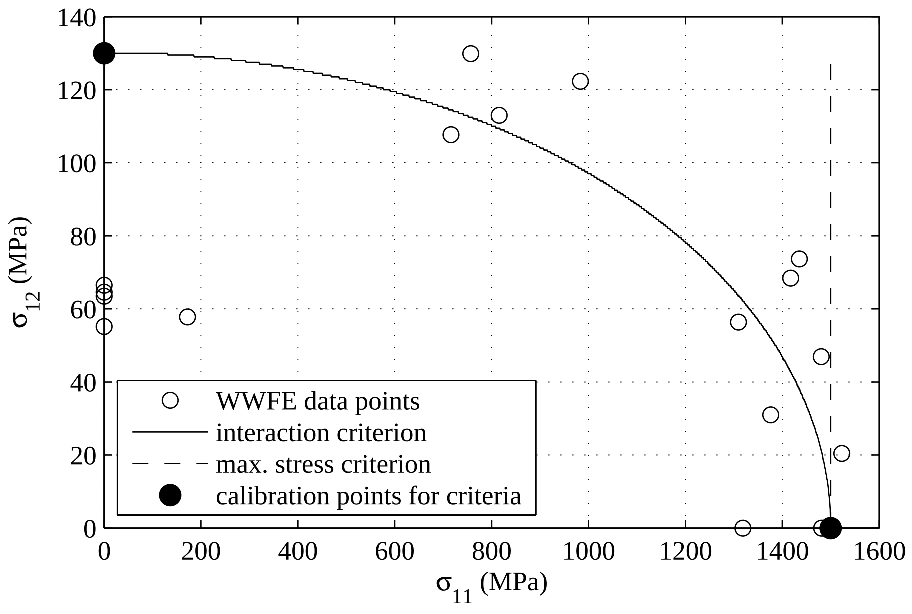

Figure 2.7: Comparison of predicted failure envelope $\sigma_{11}-\sigma_{12}$ with data points for T300/BSL914C from biaxial tests of tube specimens from the WWFE [2]

The data as presented in Fig 2.7 does not seem to show a plausible trend for the interaction of normal stress and shear stress. The data points beyond $\sigma_{11} = 600\,\mathrm{MPa}$ seem to support an interaction of normal and shear stress. However, the data points at $\sigma_{11} = 0\,\mathrm{MPa}$ show failure at much lower shear stresses and would not support a quadratic interaction as proposed by Hashin. This might be a result of having observed different failure mechanisms. According to the explanation given in Fig 2.6 it is plausible that the observed failure mode at $\sigma_{11} = 0\,\mathrm{MPa}$ is actually a shear failure of the matrix and not fibre rupture (e.g. the crack grows along the fibres but does not cut them). Therefore, the obtained stresses at failure might not be representative for fibre rupture and are excluded from the verification. For the data points beyond $\sigma_{11} = 600\,\mathrm{MPa}$ Hashin's interaction criterion (see Eqn 2.37 gives a good prediction. When fitted to the experimental data, the interaction criterion suggests that values of twice the matrix shear strength R_{n1} seems to be a reasonable choice for S_f.

The few available experimental data points indicate a good agreement between the interaction failure criterion and experimental data, but there is virtually no out-of-plane data available. Future experimental programs should address the stress interactions towards fibre rupture in order to built more confidence in current theories for strength prediction. The experimental focus should be shifted towards multi-axial stress states in order to verify existing failure theories.

2.4 Prediction of the onset of IFF

The Puck model has been chosen for the prediction of IFF within this thesis. The following sections will introduce the failure model in more detail starting with suggestions for the model parameters. Afterwards, different formulations of the failure criterion are introduced and discussed, before a novel numerical angle search algorithm for finding the inclination of the fracture plane is developed.

2.4.1 Definition of the parameters for the Puck failure criteria

The key idea of the Puck failure model is the assumption of a Mohr-Coulomb type of failure. Failure is assumed to be caused by the normal and shear tractions acting on a fracture plane. This plane is defined by the critical orientation θ_{fr} which maximises the material exposure for IFF (see Section 2.1.2). The fracture plane is therefore not necessarily aligned with the material coordinate system. Traditional failure criteria rely on classical strength properties which are derived from standard uniaxial or pure shear experiments. In some cases, however, these experiments result in a failure caused by a combination of stresses on the fracture plane and cannot be used to define the failure criteria. Therefore, Puck distinguishes strength properties (e.g. Y_t, Y_c, S_{12} and S_{23}) and fracture plane resistances ($R_n^{(+)}$, R_{n1} and R_{nt}). In general, the resistance of the fracture plane is the resistance of that plane against its fracture due to a single component of the stress traction vector acting on it (e.g. σ_n or τ_{n1} or τ_{nt}) [11]. Consequently, the IFF criteria define a master failure surface in terms of fracture plane tractions (e.g. σ_n, τ_{n1} and τ_{nt}) and fracture plane resistances $R_n^{(+)}$, R_{n1} and R_{nt} (see Eqn 2.9).

Failure due to pure tension (σ_{22} is acting as a single stress) and in-plane shear (σ_{12} is acting as a single stress) occur on fracture planes which are aligned with the material coordinate system (e.g. $\theta_{fr} = 0°$ or $\theta_{fr} = 90°$). The resistance terms for these failure modes are identical to the classical strength properties and can be derived from uniaxial experiments or shear experiments, hence

$$\begin{aligned} R_n^{(+)} &= Y_t \\ R_{n1} &= S_{12}. \end{aligned} \tag{2.38}$$

The transverse shear resistance R_{nt}, however, cannot be derived experimentally. The reason is, that uniaxial reinforced CFRP when subjected to a pure transverse shear loading (σ_{23} is the only acting stress) fail under an angle $\theta_{fr} \approx 45°$. In order to assume $R_{nt} = S_{23}$ the failure must happen in the same plane where σ_{23} is acting as a single stress (eg. $\theta = 0°$ or $\theta = 90°$). The inclined fracture plane indicates a failure due to a pure normal stress σ_n

on the fracture plane (see stress state 1 in Tab 2.2). What could be measured as strength S_{23} is therefore not suitable as parameter to define the master failure surface [11]. Because $R_{nt} \neq S_{23}$, the resistance R_{nt} has to be derived indirectly from a uniaxial compression test.

Experimental evidence showed, that CFRP under a pure transverse compressive loading ($-\sigma_{22}$) fails under a fracture angle of $\theta^0_{fr} \approx 50°$ [3]. Knowing the transverse compressive stress at failure enables calculation of the stress state at failure on the fracture plane thus giving one point on the master fracture surface. It is then possible to calculate what the resistance R_{nt} should be [11]. The procedure is demonstrated for the failure criterion as given in Eqn 2.9. This formulation incorporates a linear increase of the apparent shear resistance with increasing compressive stress σ_n on the fracture plane.

The Mohr circle for a uniaxial compression test transverse to the fibres is illustrated in Fig 2.8. The linear slope parameter p_{nt} is given by

$$p_{nt} = -\tan\alpha = -\frac{1}{\tan 2\theta^0_{fr}}. \tag{2.39}$$

Failure occurred due to a combination of σ_n and τ_{nt} (the point is indicated by the letter A in Fig 2.8). Having measured the transverse compressive strength Y_c and the inclination of the fracture plane θ^0_{fr} enables to calculate the fracture plane tractions at failure. In the case of uniaxial compression in the 2-direction failure occurres due to a single term in Eqn 2.9

$$\frac{\tau_{nt}}{R_{nt} - p_{nt}\sigma_n} = 1. \tag{2.40}$$

Hence, the missing shear resistance (see point B in Fig 2.8) is given by

$$R_{nt} = \frac{Y_c}{2\tan\theta^0_{fr}}. \tag{2.41}$$

In the absence of experimental data the following estimate of the missing slope parameter p_{n1} is given in [11]

$$p_{n1} = p_{nt}\frac{R_{n1}}{R_{nt}}. \tag{2.42}$$

A single negative normal stress σ_n does not cause failure. Therefore, no compressive normal resistance $R_n^{(-)}$ is required. The assumption of a Mohr-Coulomb type of failure results in

$$R_n^{(-)} = \infty \tag{2.43}$$

and consequently the master failure surface is therefore open in the $-\sigma_n$ direction as it will be shown later.

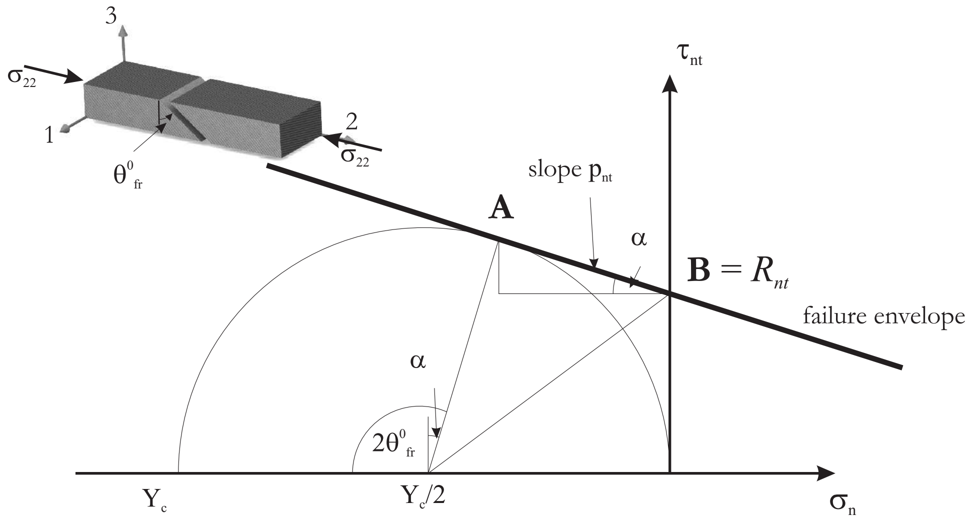

Figure 2.8: The determination of R_{nt} from the Mohr circle for uniaxial compression

2.4.2 Formulations of the Puck failure model

Various different formulations of the Puck model have been proposed. All of these formulations have in common that the UD ply is treated as transverse isotropic and a set of two criteria defines a single *master failure surface* on the fracture plane. The variations of the Puck failure criteria allow for slightly different shapes of the master failure surface and different amounts of flexibility to adapt to experimental data. An overview of formulations can be found in [3]. The main difference between the various formulation is the way the Mohr Coulomb behaviour is represented. Here linear criteria are compared with parabolic criteria. The terms linear and parabolic refer to the influence of the normal compressive stress on the shear resistance of the material. In the linear criteria, the shear resistance rises linearly while in the parabolic criteria the relation is parabolic.

The linear criteria have already been introduced in the introduction (see Eqn 2.9). For reference the criterion is given again below

$$\begin{aligned} \left(\frac{\sigma_n}{Y_t}\right)^2 + \left(\frac{\tau_{nt}}{R_{nt} - p_{nt}\sigma_n}\right)^2 + \left(\frac{\tau_{n1}}{R_{n1} - p_{n1}\sigma_n}\right)^2 &\geq 1 \qquad \text{for} \quad \sigma_n \geq 0 \\ \left(\frac{\tau_{nt}}{R_{nt} - p_{nt}\sigma_n}\right)^2 + \left(\frac{\tau_{n1}}{R_{n1} - p_{n1}\sigma_n}\right)^2 &\geq 1 \qquad \text{otherwise.} \end{aligned} \tag{2.44}$$

The formulation gives a clear mechanical representation of the Mohr Coulomb behaviour because the parameters p_{nt} and p_{n1} can be interpreted as internal friction parameters and directly relate to the slope when the fracture surface cuts the τ_{n1} or τ_{nt} axis. The frictional terms are equal in both criteria. This results in a smooth transition of the failure surface between the tensile and compressive failure modes.

An advantage of the linear criteria is the flexibility which is necessary to adapt the model to experimental data. The slope of the master failure is different for τ_{n1} and τ_{nt}. Furthermore, only slight changes would allow different friction parameters p_{n1} and p_{nt} for the tensile and compressive regimes. A disadvantage of the model is it's inhomogeneity of the failure criterion in terms of the order of the stress terms. The evaluation of Eqn 2.44 does not allow the direct calculation of a reserve factor. For this reason, a more complex set of parabolic criteria is used within the thesis.

The parabolic failure criteria read

$$e_3 = \begin{cases} \sqrt{(1-p_t)^2 \left(\frac{\sigma_n}{Y_t}\right)^2 + \left(\frac{\tau_{nt}}{R_{nt}}\right)^2 + \left(\frac{\tau_{n1}}{R_{n1}}\right)^2} + p_t \frac{\sigma_n}{Y_t} & \geq 1 \qquad \text{for} \quad \sigma_n \geq 0 \\ \sqrt{(p_c)^2 \left(\frac{\sigma_n}{Y_c}\right)^2 + \left(\frac{\tau_{nt}}{R_{nt}}\right)^2 + \left(\frac{\tau_{n1}}{R_{n1}}\right)^2} + p_c \frac{\sigma_n}{Y_c} & \geq 1 \qquad \text{otherwise} \end{cases} \tag{2.45}$$

The master failure surface is defined by 4 free parameters $(Y_t, Y_c, R_{n1}, \theta^0_{fr})$. The missing parameters are determined similarly to the approach as presented above in Section 2.4.1.

By adapting the Mohr circle to Y_c and the fracture angle for uniaxial transverse compressive failure θ^0_{fr} the resitance R_{nt} is given by

$$R_{nt} = Y_c \cos^2 \theta^0_{fr}. \tag{2.46}$$

and the parabolic parameter p_t is defined by

$$p_t = \frac{Y_t}{2Y_c}(\tan^4 \theta^0_{fr} - 1). \tag{2.47}$$

The parabolic parameter p_c is not mathematically restricted, but in order to avoid a kink of the failure surface, the slope of both, tensile fracture surface and compressive fracture surface, should match where they touch. This is achieved by

$$p_c = p_t \frac{Y_c}{Y_t}. \tag{2.48}$$

The parabolic failure criteria do not allow for a mapping of experimental data as easily as the linear criteria, but all stress terms in the criteria are of the same order which allows for a calculation of the reserve factor.

In order to visualise the different criteria an example material is selected from [3]. The input properties used are given in Table 2.1. An example master failure surface (for the

Table 2.1: Typical properties for carbon fibre reinforced epoxy composite T300/LY556, HT976 [3]

tensile strength 2-direction	Y_t	59.1 MPa
compressive strength 2-direction	Y_c	231.2 MPa
in-plane shear strength	R_{n1}	98.4 MPa
fracture angle for uniaxial compression	θ^0_{fr}	51°

linear criteria only) and a comparison of the shape of the failure envelopes for the linear and the parabolic criteria is displayed in Fig 2.9.

In order to select a set of criteria, the predicted failure envelopes are compared with experimental data available from literature. Unfortunately, only limited experimental evidence is available. For an initial assessment, however, some combined loading experiments for a plane stress state have been presented in [3]. Both formulations are compared with the experimental data from [3] (see Fig 2.10). The data has been obtained from combined tension/compression-torsion experiments of filament wound tubes. The investigated material is T300/LY556,HT976. Both models use the same input parameters. In order to

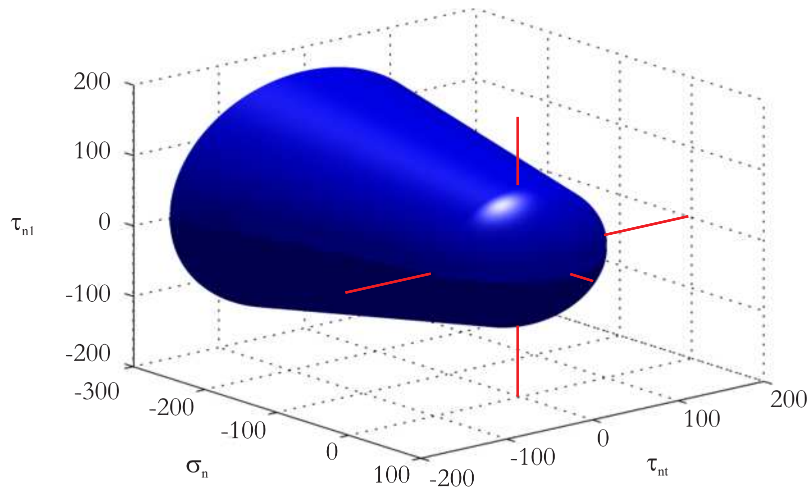

(a) the master failure surface in $\sigma_n, \tau_{n1}, \tau_{nt}$ space (linear criteria)

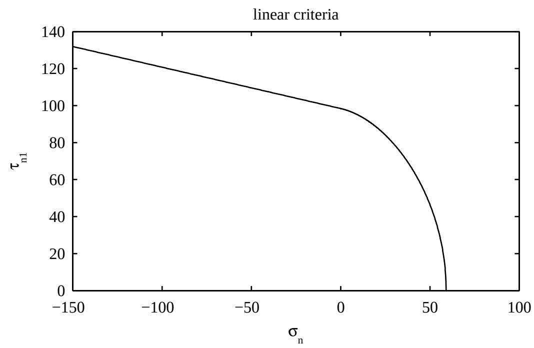

(b) failure envelope $\sigma_n - \tau_{n1}$ for the linear criteria

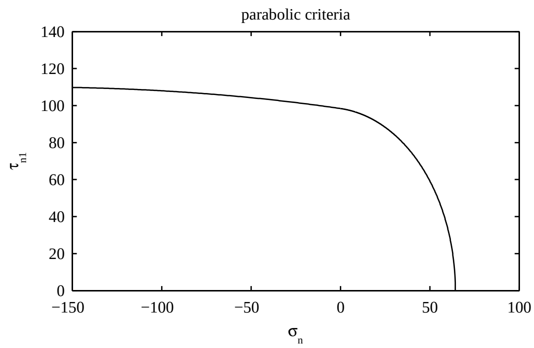

(c) failure envelope $\sigma_n - \tau_{n1}$ for the parabolic criteria

Figure 2.9: Visualisation of the Puck failure criteria for IFF

compare experimental data and predictions, the master failure surface has been transformed from the fracture plane coordinate system into the material coordinate system. More examples of Puck failure surfaces in material coordinates will be presented later in this Section.

The direct comparison (see Fig 2.10) shows that both sets of criteria yield very similar results. The parabolic criteria predict slightly higher shear strength in regions with higher compressive σ_{22} stress than the linear criteria, but the variations between both set of criteria lies well within the experimental scatter. Furthermore, it is demonstrated that the simplifications made for deriving the model parameters give a very good agreement with the experimental data. Within this work the parabolic criteria are preferred to the linear criteria simply because the criteria are homogeneous which allows for a reserve factor to

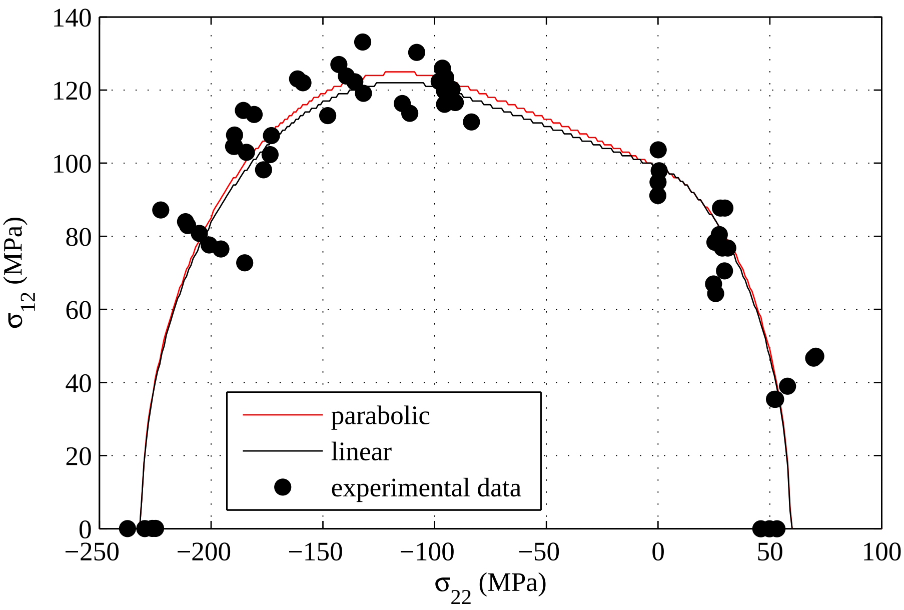

Figure 2.10: Comparison of the Puck model predictions with experimental data from [3] (input parameters from Tab 2.1)

be calculated. This will become important in the damage evolution algorithms which are presented in the next chapter.

2.4.3 The fracture angle search

Initially, the Puck IFF model was not well received in the research community. The reason was the large number of unknown parameters and the computationally expensive search of the fracture plane orientation. The suggestions Puck made for determining the required parameters (see above) resulted in a wider application of the theory. The computationally expensive search for the angle of the fracture plane, however, still remains a limiting factor. The application of the model in explicit Finite Element Analysis requires a reliable, accurate, yet numerically efficient fracture plane orientation search algorithm. For plane stress states, analytical formulations are already available [24]. The fracture angle for three dimensional states of stress, however, cannot be expressed in a closed form. Therefore, a numerical search procedure needs to be employed. So far, no efficient algorithms for finding the fracture plane angle for three dimensional states of stress have been proposed in open literature. This Section introduces a computationally efficient fracture angle search algorithm for the 3D Puck failure theory for IFF.

It is clear from Eqn 2.45 and 2.13 that the material exposure e_3 for IFF is a function of all components of stress (except σ_{11}) and the fracture angle θ_{fr}

$$e_3 = e_3\left(\sigma_{22}, \sigma_{33}, \sigma_{12}, \sigma_{23}, \sigma_{13}, \theta_{fr}\right) \tag{2.49}$$

Hence, failure can only be assessed if the fracture angle is known. Ability to calculate θ_{fr} requires further understanding of the relationship between the material exposure e_3 and the orientation of the fracture plane θ. The material exposure e_3 can be presented graphically for a fixed stress states while allowing for θ to vary. Due to symmetry the range of θ can be limited to $-90° \leq \theta \leq 90°$ [11]. In Fig 2.11 $e_3(\theta)$ is plotted for the example stress states presented in Tab 2.2.

Table 2.2: Stress states which cause IFF (calculated with properties from Table 2.1)

stress state	σ_{11}	σ_{22}	σ_{33}	σ_{12}	σ_{23}	σ_{13}	σ_n	τ_{n1}	τ_{nt}	θ_{fr}
1 (pure shear)	0.0	0.0	0.0	0.0	59.1	0.0	59.1	0.0	0.0	45°
2 (pure shear)	0.0	0.0	0.0	98.4	0.0	0.0	0.0	98.4	0.0	0°
3 (uniaxial compression)	0.0	-231.2	0.0	0.0	0.0	0.0	-92.0	0.0	-113.2	51°
4 (arbitrary 3d)	0.0	-10.0	40.0	21.0	24.0	43.3	49.7	47.8	0.75	67°

From Fig 2.11 it becomes clear that the fracture plane orientation is given by the angle θ for which the function reaches the global maximum. This orientation denotes the critical stress action plane. Hence, the fracture angle is given by

$$e_3(\theta_{fr}) = \max e(\sigma_{22}, \sigma_{33}, \sigma_{12}, \sigma_{23}, \sigma_{13}, \theta) \tag{2.50}$$

Stress state 1 in Fig 2.11 would therefore cause fracture in a plane inclined by $\theta_{fr} = 45°$ as observed experimentally. According to [11] $e_3(\theta)$ only has one global maximum in the interval $-90° \leq \theta \leq 90°$. However, it can be shown that for special cases the function $e_3(\theta)$ has two global extremes (as illustrated in Fig 2.11 for stress state 3). The function $e_3(\theta)$

is then symmetric and two theoretical fracture angles (same magnitude, but alternating sign) are possible.

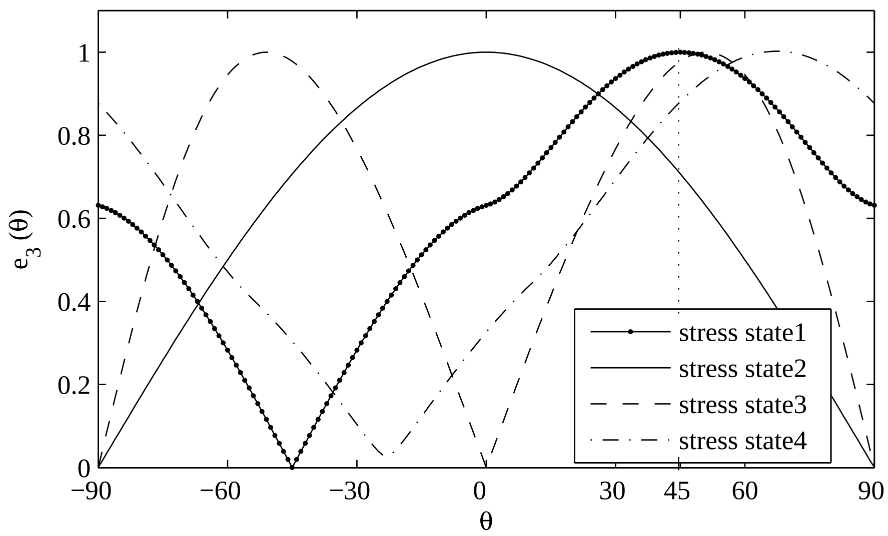

Figure 2.11: Typical examples of $e(\theta)$ plotted for the stress states in Table 2.2

The calculation of the fracture angle therefore turns into a search for the global maximum of the function $e_3(\theta)$ within the interval $-90° \leq \theta \leq 90°$. The lack of analytical solutions requires numerical solutions to be applied. The fracture angle θ_{fr} can be obtained by calculating $e_3(\theta)$ at a certain number of angles θ in the domain $-90° \leq \theta \leq 90°$. The accuracy of θ_{fr} then depends upon the number of angles θ for which $e_3(\theta)$ has been evaluated. This stepwise scan of $e_3(\theta)$ is a computationally very expensive procedure since for every evaluated point of $e_3(\theta)$ the stress tensor needs to be rotated by θ.

An efficient and accurate numerical algorithm for evaluation of the global maximum of e is therefore developed here. Numerical bisection methods for bracketing the extremes of one dimensional functions have been studied and the Golden Section Search [44] has been adapted to the problem of finding the fracture plane angle. In the remainder of this section the developed numerical algorithms are introduced which enable a robust approach to determination of the fracture angle.

2.4.3.1 Golden Section Search

Alternatively to a stepwise scan of $e(\theta)$, numerical bisection methods, like the Golden Section Search, for bracketing the extremum of scalar functions can be employed [44]. The Golden Section Search is a function maximisation/minimisation technique. The technique only applies to functions where a single extremum is known to exist within the search range. The extremum is found by successively narrowing the search range by evaluating the function at triples of points. The distances of these points form Golden Ratios which gives the technique its name.

The function $e(\theta)$ is evaluated at θ_1, θ_2 and θ_3 (see Fig 2.12). The angle is chosen by means of

$$\frac{b}{a} = \varphi \tag{2.51}$$

with φ being the golden ratio

$$\varphi = \frac{1+\sqrt{5}}{2}. \tag{2.52}$$

An additional point θ_4 is evaluated. The point is chosen as follows

$$\frac{b}{a} = \frac{a}{c} \tag{2.53}$$

thus guaranteeing that θ_4 is symmetric to θ_3 in the original search range. The decision how to narrow the search range in the next calculation step is taken by comparing $e(\theta_3)$ and $e(\theta_4)$. In case $e(\theta_4) \geq e(\theta_3)$(indicated as $e_b(\theta_4)$ in Fig 2.12) the new search range is limited by θ_3 and θ_2, otherwise (indicated as $e_a(\theta_4)$ in Fig 2.12) the search continues between θ_1 and θ_4. The choice of φ as ratio guarantees that the extremum is bracketed in the larger section which leads to an optimal method of function mimimisation/maximisation [44]. The iterative maximum search is performed until the distance between the outer points of the bracket is tolerably small. The decision what is tolerably small should be linked to the expected accuracy for θ_{fr}. Since the accurate value for θ_{fr} is definitely somewhere between the outer bounds $e(\theta_1)$ and $e(\theta_2)$, the distance

$$k = \theta_2 - \theta_1 \tag{2.54}$$

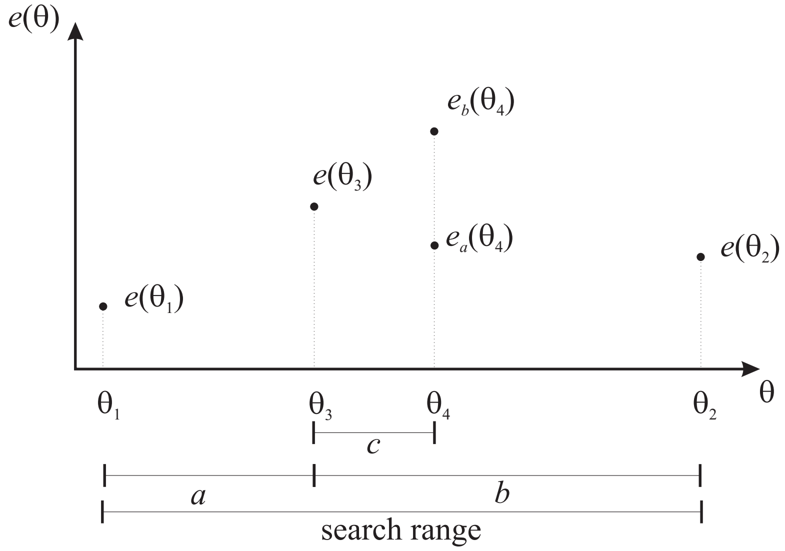

Figure 2.12: Golden section search algorithm schematic

is compared with the exit criterion k_{exit}. The iteration is stopped when the condition

$$k \geq k_{exit} \tag{2.55}$$

is satisfied. Thereby k_{exit} denotes the largest guaranteed error of the obtained fracture angle θ_{fr}. An example for the Golden Section search is illustrated in Fig 2.13.

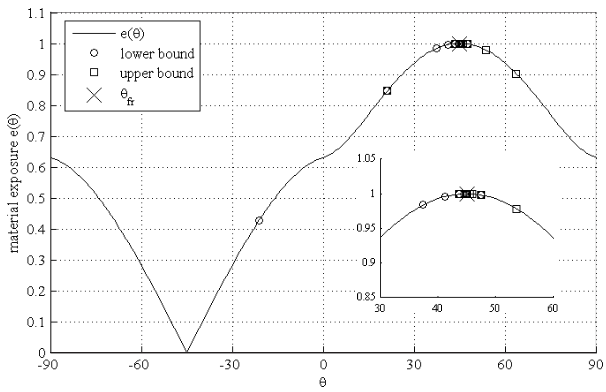

Figure 2.13: Fracture angle search by Golden Section search

2.4.3.2 Extended Golden Section Search

Fig 2.13 shows that the Golden Section search algorithm quickly brackets the maximum, but needs a quite large number of iterations to find an accurate value for $\max e(\theta)$. The efficiency of the method can be enhanced by replacing the Golden Section search algorithm with a curve fitting technique once the maximum has been bracketed sufficiently accurately. The shape of $e(\theta)$ suggests that a parabolic fit close to the maximum will allow for a reasonably accurate estimation of the maximum. The upper and lower bounds of the last Golden Section Search iteration and an arbitrary point between them are chosen to define this parabola. These three points $P_1(\theta_1, e_1(\theta_1)$, $P_2(\theta_2, e_2(\theta_2)$ and $P_3(\theta_3, e_3(\theta_3)$ fully define the parabola $p(\theta)$ by

$$p(\theta) = e(\theta_1)\frac{(\theta-\theta_2)(\theta-\theta_3)}{(\theta_1-\theta_2)(\theta_1-\theta_3)} + e(\theta_2)\frac{(\theta-\theta_1)(\theta-\theta_3)}{(\theta_2-\theta_1)(\theta_2-\theta_3)} + e(\theta_3)\frac{(\theta-\theta_1)(\theta-\theta_2)}{(\theta_3-\theta_1)(\theta_3-\theta_2)} \quad (2.56)$$

As the maximum of $p(\theta)$ is normally sufficiently close to the sought maximum of $e(\theta)$ the following approximation for θ_{fr} is adopted

$$\theta_{fr} \approx \theta_2 - \frac{1}{2}\frac{(\theta_2-\theta_1)^2(e(\theta_2)-e(\theta_3)) - (\theta_2-\theta_3)^2(e(\theta_2)-e(\theta_1))}{(\theta_2-\theta_1)(e(\theta_2)-e(\theta_3)) - (\theta_2-\theta_3)(e(\theta_2)-e(\theta_1))}. \quad (2.57)$$

Thus, the unnecessary iterations close to the maximum of $e(\theta)$ are avoided without compromising the accuracy of the algorithm. An example for the extended Golden Section Search is illustrated in Fig 2.14. The algorithm of the extended Golden Section Search is visualised in Fig 2.15.

2.4.3.3 Numerical efficiency

The application of the Puck IFF model in an explicit FE environment requires a fast fracture angle search algorithm to find the fracture plane. Within the fracture angle search, the transformation of the stress state from material coordinates on the fracture plane is the most computationally expensive step. The algorithm which evaluates the smallest number of values (and consequently has the lowest number of iterations) of $e_3(\theta)$ for a

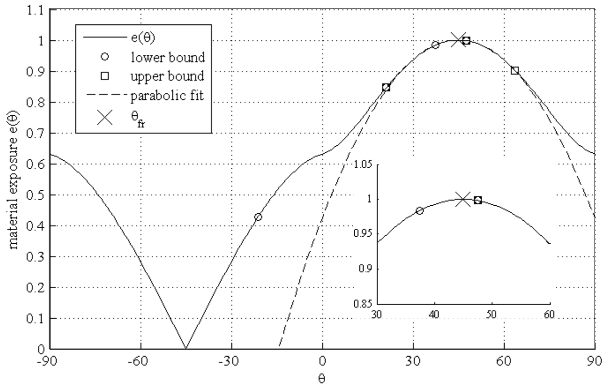

Figure 2.14: Extended Golden Section Search: bracketing the final maximum by inverse parabolic interpolation

given accuracy, will give the most numerically efficient solution. In the following, the three approaches, stepwise scan of $e_3(\theta)$, Golden Section Search and extended Golden Section Search are judged for their numerical efficiency. The assessment of the numerical efficiency presented is performed using stress state 1 in Tab 2.2. The required number of evaluated points depends on the respective stress state, but similar results have been achieved for other stress states. The stepwise scan is performed using a decreasing scanning step Δ allowing for an assessment of the relation between scan step and fracture angle accuracy. The Golden Section search and the extended Golden Section search were performed for decreasing values of the exit criterion k_{exit} which results in a increasing number of evaluated points and a decreasing error for θ_{fr}. The quoted error was calculated using the fracture angle obtained from a stepwise scan with a scanning step of $\Delta = 0.01$. The comparison of the results is presented in Fig 2.16.

Fig 2.16 demonstrates the advantages of the extended Golden Section Search. Reliable fracture angles are already calculated from as few as 6 evaluated points. The Golden Section search needs 13 points for a similar accuracy. The stepwise scan fails to predict the fracture angle with similar accuracy for a scanning step $\Delta > 1$, which results in 180 and more necessary evaluated points. It should be noted that the extended Golden Section Search requires at least 4 evaluated points and the Golden Section Search requires at least 2 data points. For this reason no error is quoted below these values.

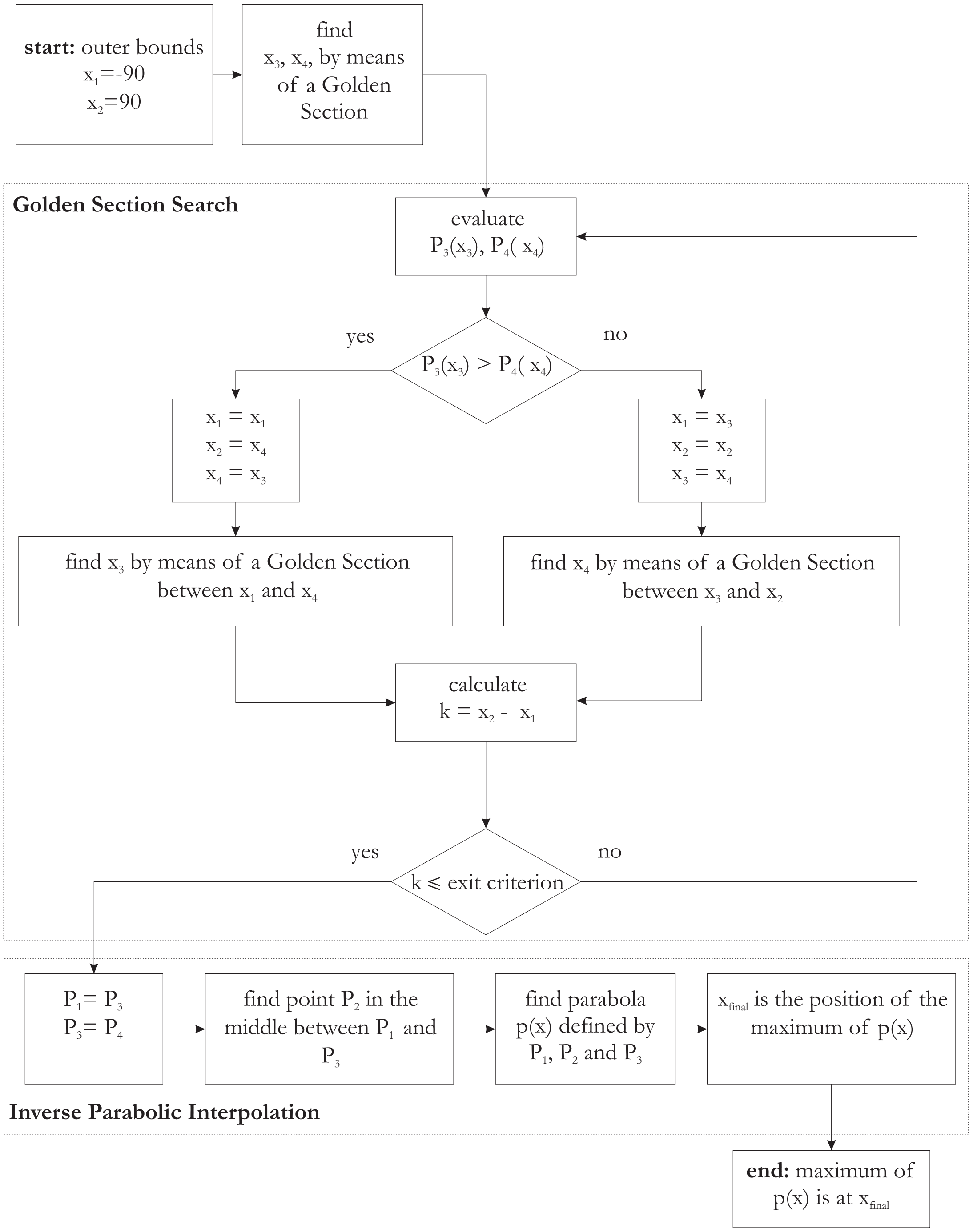

Figure 2.15: The fracture angle search algorithm, maximisation of function $e_3(\theta)$

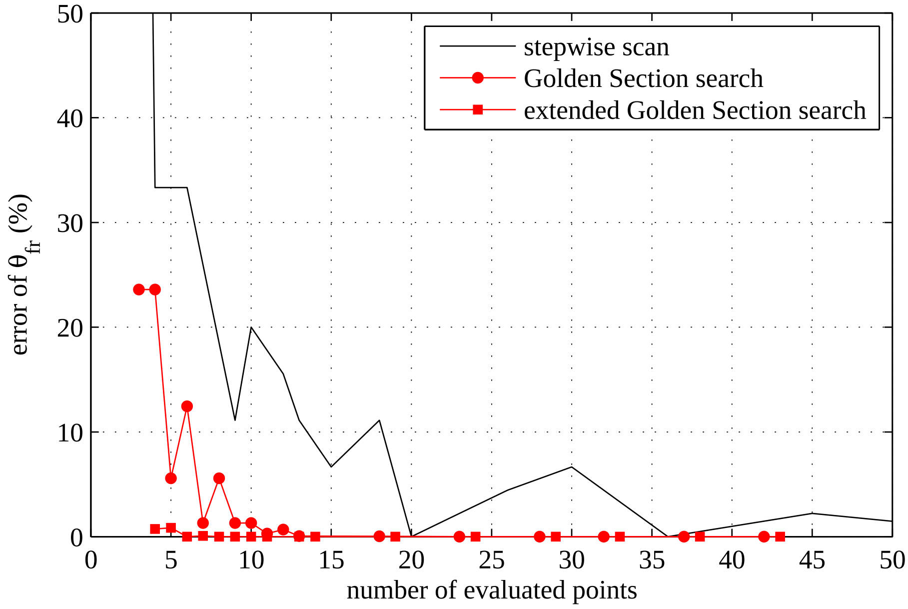

Figure 2.16: Assessment of numerical efficiency and accuracy of the fracture angle search algorithms

2.4.4 Visualisation and discussion of the failure criteria

As explained before, the master failure surface is defined in the fracture plane coordinate system. The proposed fracture angle search algorithm allows for the master failure surface in $\sigma_n - \tau_{n1} - \tau_{nt}$ stress space to be projected into material coordinates (σ_{22}, σ_{33}, σ_{12}, σ_{23}, σ_{13}). A graphical representation of the failure surface in 5 dimensional stress space is very difficult. For this reason, the interaction of three stress terms at a time is visualised in Fig 2.17. The surfaces have been calculated using the model parameters as given in Tab 2.1 and the parabolic failure criteria.

The graphical representation of the failure surface in material coordinates shows some interesting aspects of the Puck IFF model. All surfaces which include both normal stresses σ_{22} and σ_{33} are open in the direction of compressive σ_{22} and σ_{33} (see Fig 2.17(a), 2.17(b) and 2.17(c)). This, in fact, is a consequence of the Mohr-Coulomb type of failure. High levels of normal compressive stress is assumed to impede failure. With both normal compressive stresses increasing the shear resistance of the material rises which is reflected by the opening failure surface.

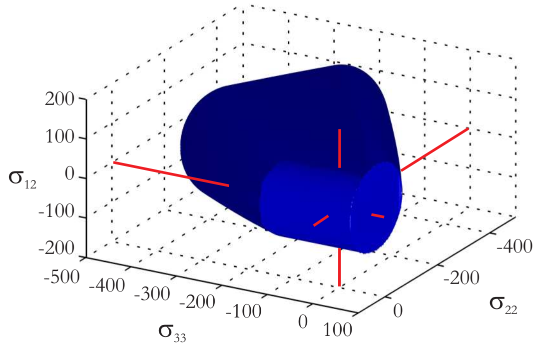

(a) failure surface in $\sigma_{22} - \sigma_{33} - \sigma_{12}$ space

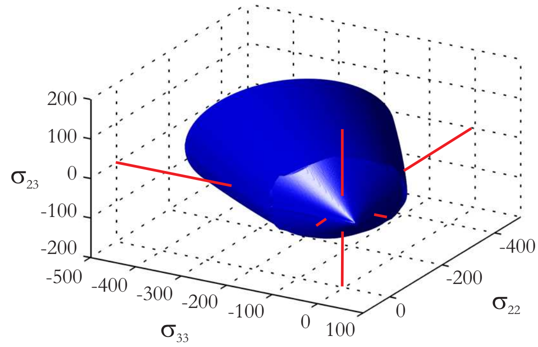

(b) failure surface in $\sigma_{22} - \sigma_{33} - \sigma_{23}$ space

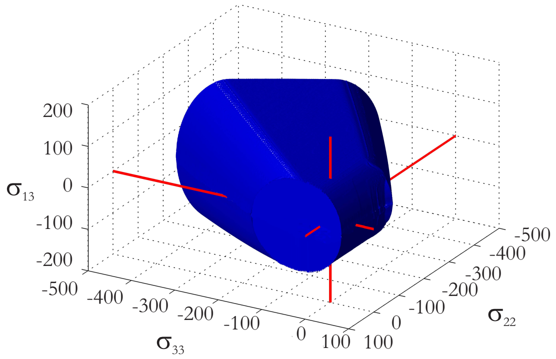

(c) failure surface in $\sigma_{22} - \sigma_{33} - \sigma_{13}$ space

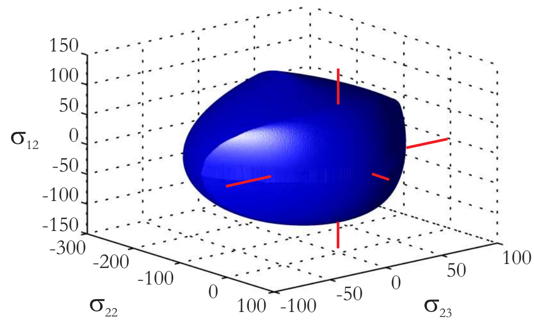

(d) failure surface in $\sigma_{22} - \sigma_{12} - \sigma_{23}$ space

Figure 2.17: Failure surfaces as defined by the Puck IFF failure model in material coordinates

In Fig 2.17(a) the failure surface appears to be cut at a certain level of tensile σ_{33} while for tensile σ_{22} the surface is rounded of. The stress level at the cut corresponds to the tensile strength in transverse direction Y_t. The reason for the cut is that there is no interaction between tensile σ_{33} and σ_{12} towards tensile failure. When σ_{33} reaches the tensile strength Y_t a matrix crack with the orientation 90° appears. This lead to Pucks assumption that the IFF failure criteria could be used as a delamination criterion [11]. This aspect of the model is discussed in more detail later in this chapter. In the σ_{22} direction, a clear interaction of σ_{22} and σ_{12} is visible. The shear resistance shrinks with increasing positive stress σ_{22}. The similar shape of the failure surfaces in Fig 2.17(a) and Fig 2.17(c) is a consequence of the assumption of transversally isotropic material behaviour in the Puck model.

The failure surface as shown in Fig 2.17(d) shows the interaction of one normal stress (σ_{22}) and two shear stresses (σ_{12} and σ_{23}). The failure surface forms a closed body which initially might appear a bit surprisingly. According to the Mohr-Coulomb failure the shear resistance should increase with increasing normal stress as shown for the master failure surface in fracture plane coordinates. The closed failure surface is a consequence of the fracture plane which rotates with increasing compressive stress σ_{22}. This results in what appears as a reduced shear resistance in material coordinates. The bearable shear stress on the fracture plane, however is increasing with rising levels of compressive normal stress. In order to clarify this aspect two 'slices' are cut out of the failure surface. Thus the failure envelopes σ_{22}-σ_{12} and σ_{22}-σ_{23} are obtained. In Fig 2.18 these envelopes are displayed together with the predicted fracture plane angle θ_{fr}.

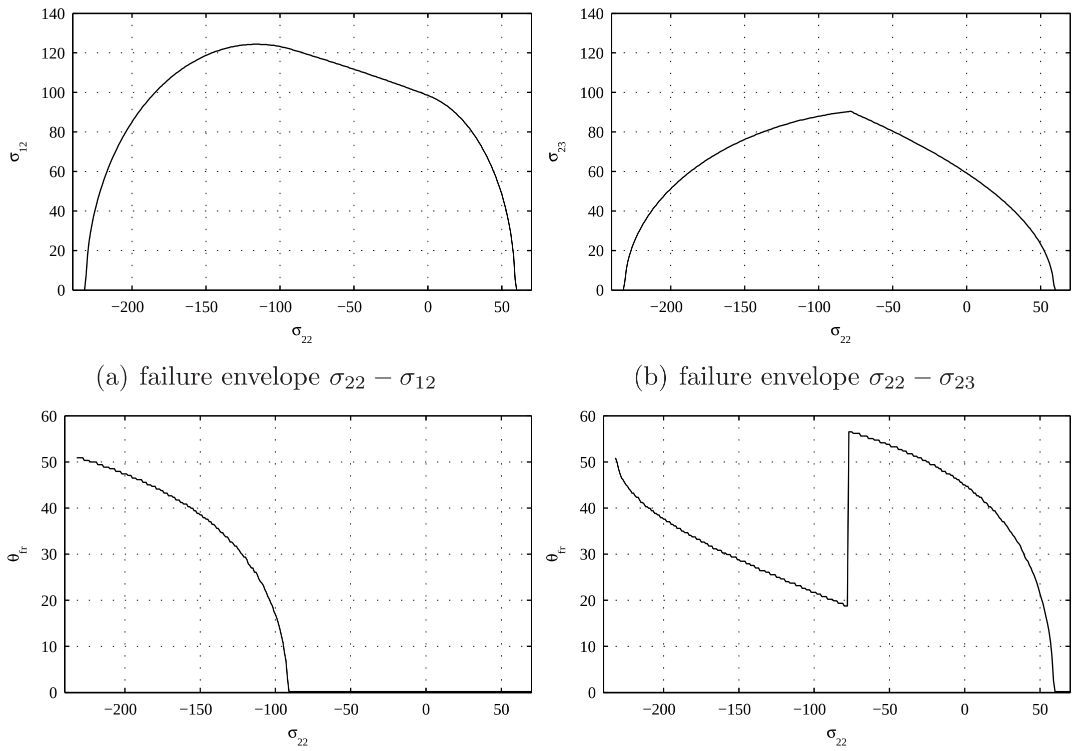

(a) failure envelope $\sigma_{22} - \sigma_{12}$

(b) failure envelope $\sigma_{22} - \sigma_{23}$

(c) fracture angle θ_{fr} for $\sigma_{22} - \sigma_{12}$

(d) fracture angle θ_{fr} for $\sigma_{22} - \sigma_{23}$

Figure 2.18: Failure envelopes in material coordinates and predicted orientation θ_{fr} of the fracture plane

Fig 2.18(a) and Fig 2.18(c) demonstrates the relation between shear resistance in material coordinates and fracture plane orientation. As the compressive stress σ_{22} increases the shear resistance rises. At some point the fracture plane starts to rotate which results in lower shear stress at failure in material coordinates. For this reason, composite materials fail at a certain fracture angle when subjected to uniaxial transverse compression. The failure envelope and the fracture angles have been confirmed experimentally in [3].

Fig 2.18(b) and Fig 2.18(d) shows another aspect of the model. Initially, both shear resistance and fracture angle increase. At some point the failure envelope shows a kink. At this point the fracture angle jumps to a lower value. The reason is that the normal stress on the fracture plane, σ_n switches from tension to compression at this stress state. Without knowledge of the fracture angle it is not possible to judge whether the matrix material fails due to tensile or compressive load. Furthermore, this explains why the fracture plane resistance $R_{nt} \neq S_{23}$. If it was possible to experimentally determine S_{23} this would correspond to the point on the failure envelope where $\sigma_{22} = 0$. R_{nt}, however, marks the shear stress at failure on the master failure surface when $\sigma_n = 0$. In Fig 2.18(b) this corresponds to the kink in the failure envelope.

The algorithm for finding the fracture plane orientation has been published in Composite Science and Technology [45].

2.5 Prediction of fibre kinking

The onset of fibre kinking is assumed to be defined by an IFF of the surrounding matrix material. The model for the prediction of kinking as used here, has initially been proposed by Davila and Camanho [1] for plane states of stress and later been extended to 3D by Pinho [4]. In the following, the model is introduced and extended.

2.5.1 The failure model for fibre kinking

The basic idea Davila and Camanho proposed in [1] is that compressive fibre failure is triggered by a failure of the matrix which is surrounding the fibres. As a consequence, the matrix cannot support the reinforcing fibres and the fibres start to rotate which results in the formation of a kink band. The failure of the matrix, in both, tension and compression can be predicted using the Puck IFF failure model as described in Section 2.4. Research has shown that compressive fibre failure is triggered by misaligned fibres [32, 33]. The key aspect for the prediction of fibre kinking is therefore to identify the fibre misalignment and to assess failure according to the stresses which act in this misalignment frame. Pinho et al. [4] proposed a set of three angles ψ_k, ϕ and θ_k which define the plane of failure in three-dimensions. The following section introduces the various planes involved in fibre kinking and shows how these planes can be obtained. Pinho's definition of the planes and respective coordinate systems involved in fibre kinking is given in Fig 2.19.

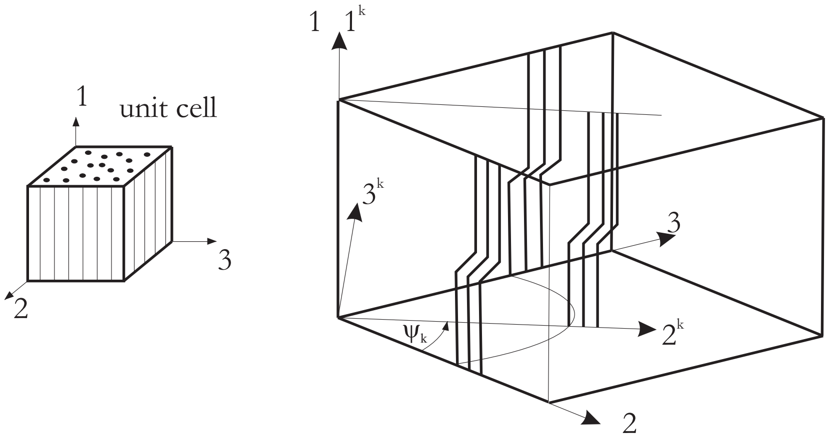

(a) unit cell and definition of kink plane

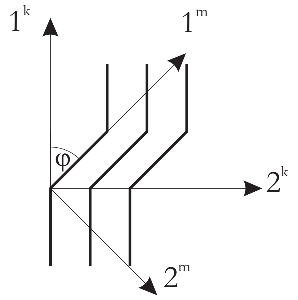

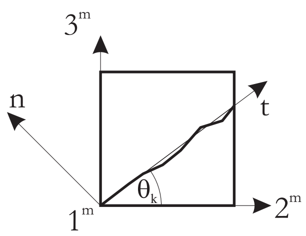

(b) definition of misalignment frame (c) definition of fracture plane for kinking

Figure 2.19: Definition of the various planes involved in fibre kinking (after [4])

Pinho proposed three coordinate systems. The first coordinate system defines the orientation of the kink plane (Fig 2.19(a)). Kinking can occur in any plane parallel to the 1-direction which denotes the fibre orientation in the unit cell. This coordinate system is denoted with the superscript k ($1^k = 1, 2^k, 3^k$) and the orientation is defined by the angle ψ_k also called the kink plane angle.

Kinking is promoted by misaligned fibres within the unit cell. This is taken into account by assuming a fibre misalignment ϕ (Fig 2.19(b)). The corresponding coordinate system is denoted by m $(1^m, 2^m, 3^m = 3^k)$ and is obtained by rotation from k by the misalignment angle ϕ about the 3^k axis.

The plane in which matrix failure will occur is finally given by the fracture plane angle θ_k which has already been introduced for IFF in the previous section (Fig 2.19(c)). The fracture plane coordinate system $(1^m, n, t)$ is obtained by rotation about the 1^m axis.

The angles ϕ and ψ_k are to some extend governed by the micro-structure of the composite and could be measured. The angle θ_k is similar to the orientation of the fracture plane for IFF as described earlier. How to obtain these angles will be described later in this chapter.

The following rotations of the stress tensor are required to obtain the tractions on the plane where IFF will initiate the kinking. The first rotation is from the material coordinate system $(1, 2, 3)$ into the kink plane coordinate system $(1^k, 2^k, 3^k)$ by

$$\boldsymbol{\sigma^k} = \boldsymbol{R_1}(\boldsymbol{\psi_k})\boldsymbol{\sigma}\boldsymbol{R_1^T}(\boldsymbol{\psi_k}). \tag{2.58}$$

Subsequently, the stress tensor is rotated into the misalignment coordinate system by

$$\boldsymbol{\sigma^m} = \boldsymbol{R_{3^k}}(\boldsymbol{\phi})\boldsymbol{\sigma^k}\boldsymbol{R_{3^k}^T}(\boldsymbol{\phi}). \tag{2.59}$$

Similar to Eqn 2.13, the tractions on the matrix fracture plane are finally given by

$$\begin{aligned}
\sigma_n &= \sigma_{22}^m \cos^2\theta_k + \sigma_{33}^m \sin^2\theta_k + 2\sigma_{23}^m \cos\theta_k \sin\theta_k \\
\tau_{nt} &= -\sigma_{22}^m \sin\theta_k \cos\theta_k + \sigma_{33}^m \sin\theta_k \cos\theta_k + \sigma_{23}^m(\cos^2\theta_k - \sin^2\theta_k) \\
\tau_{n1} &= \sigma_{13}^m \sin\theta_k + \sigma_{12}^m \cos\theta_k.
\end{aligned} \tag{2.60}$$

The stress rotations above allow to obtain the tractions on the matrix fracture plane. Initiation of kinking can now be assessed with the Puck IFF failure criteria (Eqn 2.45).

2.5.2 Determination of the orientation of the kink plane

Fibre kinking will happen due to an IFF in an arbitrary plane parallel to the locally misaligned fibres. This plane is defined by the three angles ψ_k, ϕ and θ_k.

The fracture plane angle θ_k is already defined in Section 2.4. Similar to IFF, θ_k defines the plane parallel to the locally misaligned fibres which maximises $e(\theta)$. The predicted IFF in that plane will then trigger the subsequent fibre kinking. The angle θ_k is obtained by the fracture angle search algorithm as described in Section 2.4.

The local fibre misalignment is given by the angle ϕ. The angle ϕ is composed from an initial fibre misalignment ϕ^0, which is a material property mainly defined by the manufacturing process, and the misalignment ϕ_e resulting from the elastic deformation [4]

$$\phi = \phi^0 + \phi_e^f + \phi_e^s. \tag{2.61}$$

In Eqn 2.61 ϕ_e^f denotes the misalignment due to elastic deformation contributed from the loading in fibre direction and ϕ_e^s due to the elastic shear deformation. If poisson effects are neglected,

$$\tan \phi_e^f = \frac{\sigma_{11}}{E_{11}} \tan \phi^0 \tag{2.62}$$

gives a good approximation for ϕ_e^f. The high stiffness of the fibre, however, will result in only very small deformation for which reason ϕ_e^f is neglected here. The elastic shear deformation will contribute significantly to the misalignment as loading rises. The rising amount of shear deformation will result in additional rotation of the already misaligned fibres. The angle ϕ_e^s is given by

$$\phi_e^s = \frac{|\sigma_{12}^k|}{G_{12}^k} \tag{2.63}$$

using small angle approximations. The shear stress σ_{12}^k is calculated by rotating the stress tensor $\boldsymbol{\sigma}$ from material coordinates in the kink plane. The absolute value of σ_{12}^k is taken because the angle ϕ is defined positive in order to obtain the highest fibre misalignment which is important for the assessment of failure. The shear stiffness G_{12}^k is the in-plane shear stiffness of the kink plane. It can be obtained by rotating the stiffness tensor of an orthotropic material by

$$G_{12}^k = G_{12}\cos^2\psi_k + G_{13}\sin^2\psi_k, \tag{2.64}$$

The failure theory as used here assumes the UD ply to behave in a transverse isotropic manner, hence

$$G_{12}^k = G_{12}. \tag{2.65}$$

As mentioned above, the initial fibre misalignment is a material property. Depending on the preform (crimped, non-crimped, woven) the misalignment can vary from almost perfectly straight fibres (non-crimped) to highly misaligned fibres (weaves). Additionally, the manufacturing process (e.g. resin transfer moulding, prepreg) in conjunction with the fibre volume content can influence the initial fibre misalignment ϕ^0. In general, it is assumed that the fibre misalignment follows a statistical distribution. Since for most materials ϕ^0 is not known, a pragmatic estimation is necessary. In [1] it is suggested to derive ϕ^0 from uniaxial compression in the fibre direction. Assuming a plane stress state at failure, the misalignment angle for pure compression ϕ^c can be obtained by inserting the stress at failure in the IFF criterion (in this case the linear criterion, see Eqn 2.44)

$$\frac{X_c\sin\phi^c\cos\phi^c}{R_{n1} + p_{n1}X_c\sin^2\phi^c} = 1. \tag{2.66}$$

In [1] Eqn 2.66 has been solved for ϕ^c which yields

$$\phi^c = \arctan\left(\frac{1 - \sqrt{1 - 4\left(\frac{R_{n1}}{X_c} + p_{n1}\right)\left(\frac{R_{n1}}{X_c}\right)}}{2\left(\frac{R_{n1}}{X_c} + p_{n1}\right)}\right). \tag{2.67}$$

The angle ϕ^c is composed of the initial fibre misalignment ϕ^0 and the misalignment due to elastic shear deformation at failure $\phi_e^s|_{X_c}$

$$\phi^0 = \phi^c - \phi_e^s|_{X_c}. \tag{2.68}$$

The misalignment due to elastic shear deformation at failure $\phi_e^s|_{X_c}$ is given by

$$\phi_e^s|_{X_c} = \frac{\sigma_{12}^m}{G_{12}}, \tag{2.69}$$

assuming linear elastic material. Under plane stress conditions using small angle approximation Eqn 2.69 can be rewritten as

$$\phi_e^s|_{X_c} = \frac{-\phi^c\sigma_{11} + \phi^c\sigma_{22} + (1-\phi^c)\sigma_{12}}{G_{12}}. \tag{2.70}$$

Considering uniaxial compression $\sigma_{22} = \sigma_{12} = 0$ and $\sigma_{11} = X_c$ gives

$$\phi_e^s|_{X_c} = \phi^c \frac{X_c}{G_{12}}. \tag{2.71}$$

The kink plane angle ψ_k is a parameter which depends on the orientation of the fibre misalignment in the UD ply. The evaluation of ψ_k has been addressed already in [4]. It was suggested to obtain ψ_k from a pragmatic estimation by the use of the direction of maximum principle stress given by

$$\tan 2\psi_k = \frac{2\sigma_{23}}{\sigma_{22} - \sigma_{33}}. \tag{2.72}$$

This gives an estimate for a plane stress state with only stresses σ_{22}, σ_{33} and σ_{23} non zero, but does not include the contribution of the shear stresses σ_{12} and σ_{13}. Furthermore, Eqn 2.72 will result in numerical errors if $\sigma_{22} = \sigma_{33} = 0$ and $\sigma_{22} = \sigma_{33}$ and is therefore not suitable for application in a three-dimensional failure model.

The shortcomings of the pragmatic estimation of ψ_k given in [4] required the development of a new strategy for obtaining this angle. The baseline for the new strategy is the assumption that fibre misalignment is oriented randomly in all directions within the unit cell. Kinking will then initiate in the orientation which is critical for a given stress state. This will give the most conservative prediction of failure in the absence of knowledge about the micro-structure of the composite.

The determination of this critical orientation can be performed similarly to the search of the fracture angle θ_k for IFF. This requires calculating the material exposure e_2 for fibre kinking, which is now a function of the stress state $\boldsymbol{\sigma}$, the kink plane angle ψ, the misalignment angle ϕ and the fracture plane orientation θ

$$e_2 = e_2(\boldsymbol{\sigma}, \psi, \phi, \theta). \tag{2.73}$$

The exposure e is calculated from the failure criteria which are used for IFF (see Eqn 2.45). For a given stress state $\boldsymbol{\sigma}$ the current fibre misalignment ϕ can be calculated. Finding the critical orientation of the fracture plane therefore requires a search for the critical angles ψ_k and θ_k. These angles are obtained from

$$e_2(\boldsymbol{\sigma}, \psi_k, \phi, \theta_k) = \max e_2(\boldsymbol{\sigma}, \psi, \phi, \theta) \tag{2.74}$$

and failure due to kinking will occur when

$$e(\boldsymbol{\sigma}, \psi_k, \phi, \theta_k) = 1. \tag{2.75}$$

In order to cover all possible orientations of ϕ the search for the maximum of e has to be performed over the full range between $0° \leq \psi \leq 360°$ (see Fig 2.20).

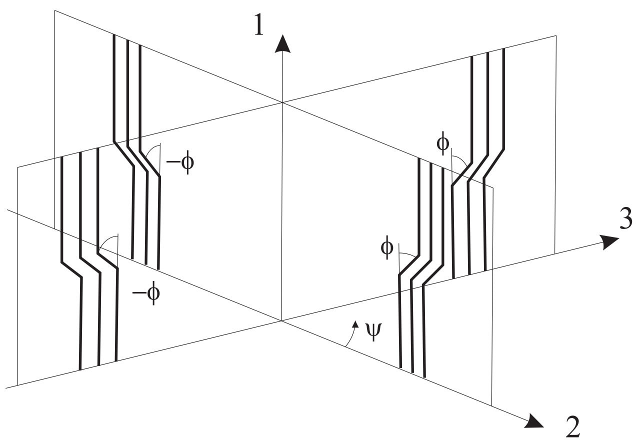

Figure 2.20: Possible orientations of the fibre misalignment in 3D

An example which illustrates the necessity of a search over the whole range is shown in Fig 2.21(a). The material exposure e_2 is plotted as a function of ψ for identical shear stresses σ_{12} and σ_{13} with alternating sign. It becomes clear that e_2 must be evaluated over the whole range of ψ in order to find the highest material exposure e_2 and therefore the critical orientation of the misalignment which causes failure.

In Fig 2.21(b) it is demonstrated why the pragmatic approximation for ψ (see Eqn 2.72) is not valid for a general three-dimensional stress state. Evaluating e_2 over certain range of ψ values shows two general cases. In case of σ_{22}, σ_{33}, σ_{23} being the only nonzero stresses, the material exposure $e_2(\psi)$ does not change significantly with ψ. This shows that the stresses σ_{22}, σ_{33} and σ_{23} do not significantly affect the orientation of the kink plane. The exposure $e_2(\psi)$ is therefore almost constant for varying ψ. Eqn 2.72 could be used for this special case. The situation changes if shear stresses σ_{12} and σ_{13} are acting in the RVE. Depending on the orientation of the fibre misalignment the shear stress can reduce the fibre misalignment ϕ thus preventing kinking, or increase ϕ which results in fibre kinking at a lower stress level. The influence of σ_{12} and σ_{13} is neglected in Eqn 2.72 which would result in a wrong prediction of ψ_k. The curves presented in Fig 2.21 have been calculated using the properties listed in Table 2.3.

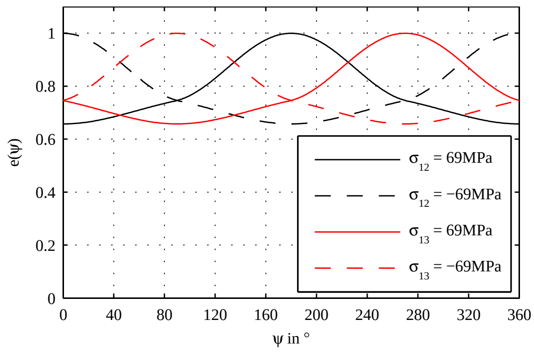

(a) influence of sign of shear stress on $e_2(\psi)$

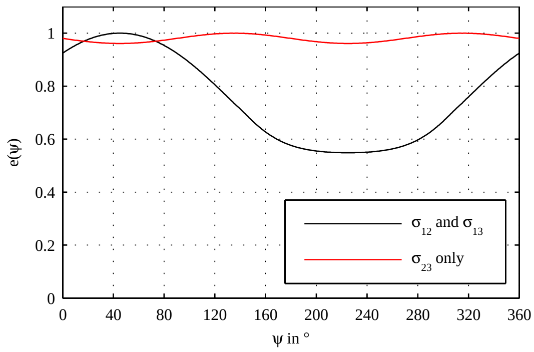

(b) e for two different loading states($\sigma_{11} = -200$MPa, σ_{12}=σ_{13}=47.7MPa) and ($\sigma_{11} = -200$MPa, σ_{23}=27.0MPa)

Figure 2.21: Influence of stress state on e_2

Finding the critical values for ψ_k and θ_k is achieved by searching for the maximum of $e(\boldsymbol{\sigma}, \psi, \phi, \theta)$ for a fixed stress state $\boldsymbol{\sigma}$ and consequently a known misalignment angle ϕ. Therefore, a similar approach to the one used for finding the fracture plane angle θ_{fr} for IFF can be applied. The Golden Section search algorithm is used to search for both angles.

The material exposure e is evaluated for certain values of ψ. The angles ψ are chosen by means of golden ratios thus allowing to bracket the maximum of $e(\boldsymbol{\sigma}, \psi, \phi, \theta)$. For each ψ the respective value θ_k is found by the use of the fracture angle search algorithm as proposed earlier in this chapter. The shape of the scalar function $e(\psi, \theta)$ suggests that a the region near the maximum can be approximated by a parabola. Therefore, inverse parabolic interpolation can be used to find the maximum of $e(\psi, \theta)$ and keep the number of evaluated angles ψ as low as possible.

Evaluating e for fibre kinking is computationally very expensive. Therefore, the search algorithm is only applied when the shear stresses σ_{12} and σ_{13} are significantly nonzero (significantly nozero is defined by the machine precision of the used computer). As concluded earlier, the other stress terms do not promote a particular orientation of the kink band and it can be assumed $\psi_k = 0°$. The value for θ_k, however, is still found by maximising e. A flowchart of the kink band angle calculation is presented in Fig 2.22.

It should be noted that the algorithm as presented in Fig 2.22 could be further streamlined. The chosen approach relies on a 1D optimisation which is nested in another 1D

Table 2.3: CFRP properties (T300/BSL914C) from the WWFE [7]

Young's modulus 1 direction	E_{11}	138 GPa
Young's modulus 2 direction	E_{22}	11 GPa
Young's modulus 3 direction	E_{33}	11 GPa
in plane shear modulus	G_{12}	5.5 GPa
out of plane shear modulus	G_{23}	5.58 GPa *
out of plane shear modulus	G_{13}	5.5 GPa
Poisson's ratios	ν_{12} ν_{13}	0.28
Poisson's ratio	ν_{23}	0.06*
tensile strength 1-direction	X_t	1500 MPa
compressive strength 1-direction	X_c	900 MPa
tensile strength 2-direction	Y_t	27 MPa
compressive strength 2-direction	Y_c	200 MPa
in-plane shear strength	R_{n1}	80 MPa
fracture angle for uniaxial compression	θ^0_{fr}	53° (only assumed)
shear strength of the fibre	S_f	130 MPa (only assumed)

* estimated based on the Chamis theory
using the University of Twente micromechanics modeller

optimisation. It is well known that a 2D optimisation (e.g. find the maximum/minimum of a surface rather than a curve) would find the respective function extreme of $e(\psi, \theta)$ more efficiently. This will be part of future work and was not pursued within this thesis. Primary aim of the study was more the investigation of the fundamental relation of the angles and the material exposure for kinking.

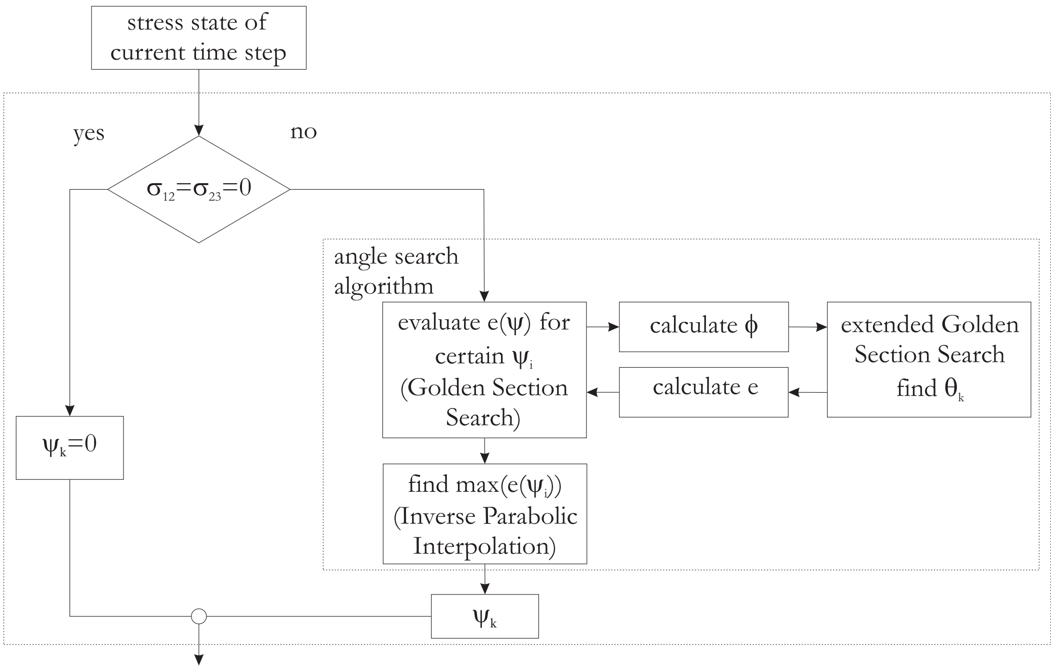

Figure 2.22: Flow chart of the calculation of ψ_k and θ_k

2.5.3 Visualisation and verification of the failure model for compressive fibre failure

Due to the enormous computational effort to find the critical angles ψ_k and θ_k it has so far been prohibitive to study the interaction of the different stress terms which lead to fibre kinking. According to the theory chosen here, all six components of the stress tensor contribute to fibre kinking. In conjunction with the proposed angle search algorithm it was possible to study the various stress interactions leading to fibre kinking. Especially the two shear stresses σ_{12} and σ_{13} seem to have a significant influence on the compressive strength as demonstrated in Fig 2.21. Therefore, the failure surface in σ_{11}-σ_{12}-σ_{13} stress space has been computed and is displayed in Fig 2.23(a).

From Fig 2.23(a) it becomes obvious that the shear resistance towards fibre kinking decreases almost linearly with increasing compressive stress σ_{11}. This becomes even clearer if a cross section of the failure surface is plotted. Similar to IFF, the failure surface can be reduced to a failure envelope. Here, the failure envelope σ_{11}-σ_{12} is chosen (see Fig 2.23(b)).

Two distinct sections of the failure surface become evident from Fig 2.23(b). For a small compressive stress σ_{11} the shear resistance rises with increasing compressive stress in fibre direction. In this part of the envelope failure is predicted due to a tensile stress σ_n on the fracture plane. As the compressive stress rises, the stress σ_n becomes negative. This is visible by the kink in the envelope. The change of the sign of the normal traction on the fracture plane causes a jump of the fracture angle θ_k. The angle search algorithm does not seem to predict this sudden change very accurately. For even higher compressive stress σ_{11} the shear resistance lowers almost linearly until there is almost no shear resistance left close to X_c.

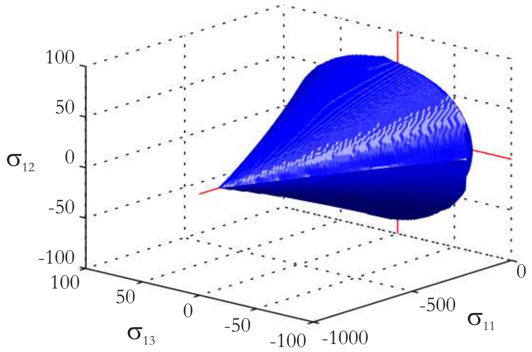

(a) the failure surface σ_{11}-σ_{12}-σ_{13}

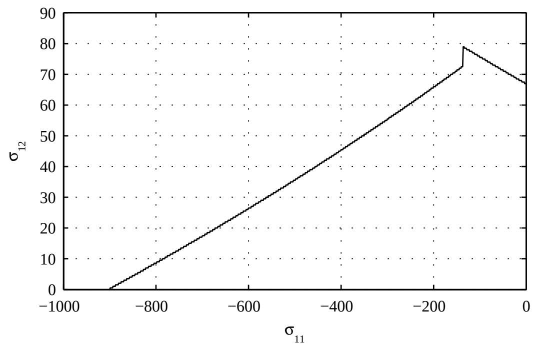

(b) the failure envelope σ_{11}-σ_{12}

Figure 2.23: The interaction of σ_{11} and the shear stresses σ_{12} and σ_{13} towards fibre kinking

There is limited available verification data for the interaction of stress components for compressive fibre failure is only limited. Jelf and Fleck [5] published experimental results of combined compression/torsion experiments on pultruded unidirectional reinforced CFRP tube specimens. The results indicate a linear decrease of the shear strength with increasing compressive stress in fibre direction. The reported failure mode was plastic micro-buckling which resulted in fibre kinking. For a pure shear load the failure mode switched to splitting parallel to the fibres. For the purpose of verification the strength of the UD composite has been predicted using the proposed kinking model and is compared with the experimental results in [5]. The relevant material properties were taken from [5] and where necessary complemented by properties from the WWFE [7]. The values are displayed in Tab 2.4 and the comparison of experiment and model prediction is shown in Fig 2.24.

Table 2.4: CFRP properties for the prediction of compressive fibre failure from [5] and [7]

in plane shear modulus	G_{12}	5.12 GPa
compressive strength 1-direction	X_c	1302 MPa
tensile strength 2-direction	Y_t	27 MPa
compressive strength 2-direction	Y_c	200 MPa
in-plane shear strength	R_{n1}	77 MPa

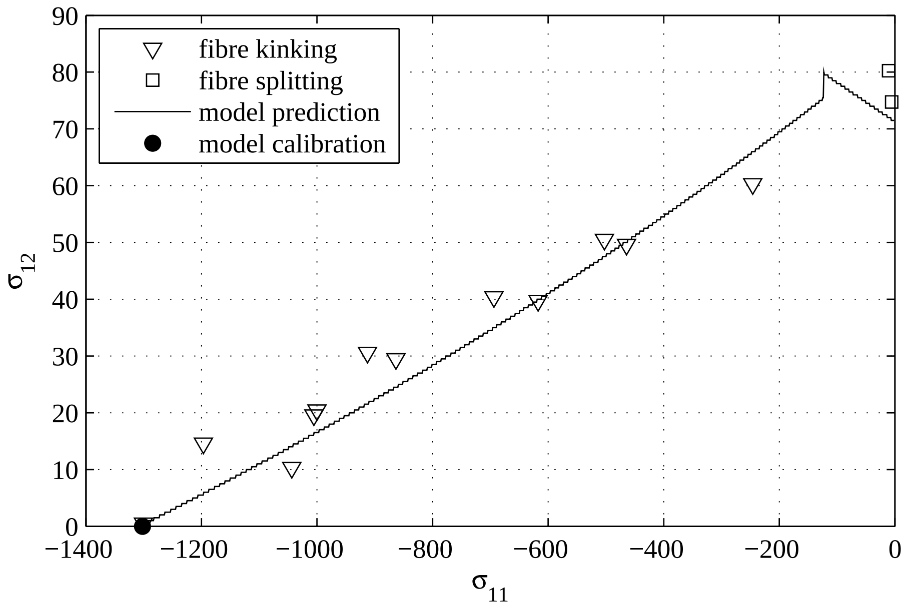

Figure 2.24: Comparison of experimentally observed compressive failure modes (from [5]) and model prediction

The model prediction is in a very good agreement with the experimental data. Interestingly, the region where Jelf and Fleck identified fibre splitting coincides with the part where the kinking model predicts failure due to tensile normal stress on the fracture plane. This shows the potential of the failure model to represent compressive failure due to splitting. A full verification, however, would require more experimental data.

2.6 Prediction of delamination

Failure due to delamination occurs on the interface between adjacent plies. Different strategies for the prediction of delamination have been proposed in the past (see Section 2.1.5). Within the thesis, the focus will be on stress-based failure criteria for the prediction of delamination initiation. A fracture mechanics based approach would be more accurate, but requires knowledge of the existence and size and location of initial defects which is usually not available or difficult to include into FE models. Stress-based criteria, on the other hand, suffer notoriously from mesh dependency. Usually, this is addressed by stress averaging procedures in regions close to stress concentrations. The scale on which modelling is performed here (ply level) already incorporates a certain stress averaging due to the size of the finite elements. Therefore, no additional stress averaging procedures are used. The correct application of stress based delamination criteria, however, requires a well designed FE mesh.

In the following, two stress based delamination criteria are investigated in more detail. First, the application of the Puck IFF model to delamination prediction is investigated and second, the delamination criterion based on Brewers criterion with the extensions made by Hou. The predictions of both approaches are compared and discussed.

2.6.1 Prediction of delamination initiation by the Puck IFF model

The Puck IFF model predicts matrix failure transverse to the fibre direction. The transverse isotropic nature of the UD lamina allows for an application to delamination. Delamination is treated as a matrix crack with a fracture angle of $\theta_{fp} = 90°$. The Puck model, in conjunction with the fracture angle search algorithm, should therefore be able predict delamination initiation. In order to show the model prediction, failure envelopes are computed using the material properties provided in Tab 2.3. Delamination is assumed to be caused by the through-thickness normal stress σ_{33} and the two out of plane shear stresses σ_{23} and σ_{13}. Below, the failure envelope σ_{33}-σ_{13} and the failure envelope σ_{33}-σ_{23} are presented together with the predicted angle of the fracture plane θ_{fr}. The failure envelopes are displayed in Fig 2.25.

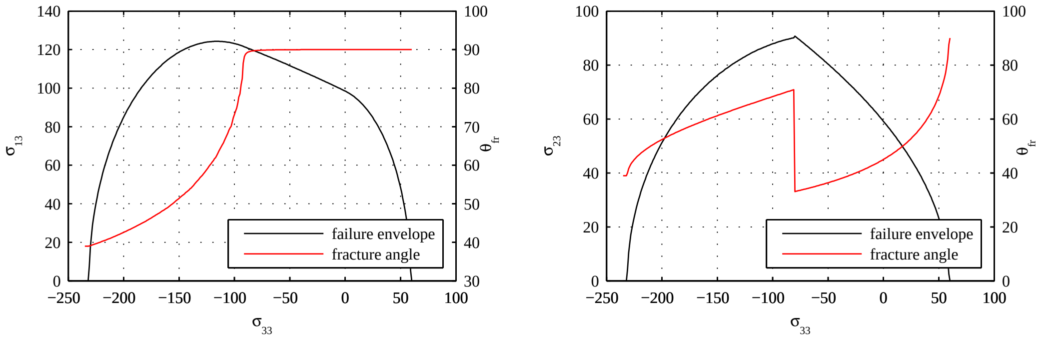

(a) the failure envelope σ_{33}-σ_{13} ($\sigma_{23} = 0$) (b) the failure envelope σ_{33}-σ_{23} ($\sigma_{13} = 0$)

Figure 2.25: Failure envelopes for delamination and predicted fracture angle θ_{fr}

Fig 2.25(a) demonstrates that for a $\sigma_{33} - \sigma_{13}$ stress state the fracture angle is predicted as 90° if the through thickness stress σ_{33} is tensile. Interestingly, delamination is predicted even under small compressive stress σ_{33}. This indicates that delamination can occur even if compressive stress is acting on the delamination plane if the shear stress is high enough and has already been reported from experiments [41]. This feature had to be added as an extension of the Brewer criterion by Hou and Petrinic, while the Puck criterion seems to automatically take this into account.

The model prediction is very different for the stress combinations σ_{33} and σ_{23} (see Fig 2.25(b)). The model does not seem to predict a fracture angle $\theta_{fr} = 90°$ except for a through the thickness stress equal to the transverse strength Y_t. According to this prediction, out of plane shear stress σ_{23} would not contribute to delamination failure, but rather force the matrix crack to diverge from the interface in the lamina. While this would be characteristic for a stack of UD plies it is not suitable to predict delamination of neighbouring plies with different fibre orientation. It is exactly these interfaces, however, which are usually prone to delamination.

Plotting the projected failure surface in σ_{33}-σ_{23}-σ_{13} stress space (see Fig 2.26) underlines the above mode observation. Even a small amount of σ_{23} stress leads to the prediction of $\theta_{fr} \neq 90°$ and therefore IFF rather than delamination. The range of stress states which actually would result in a prediction of delamination is very limited (see marked area in Fig 2.26). The prediction could be interpreted, that it is more likely to delaminate along the fibres than delaminating transverse to them.

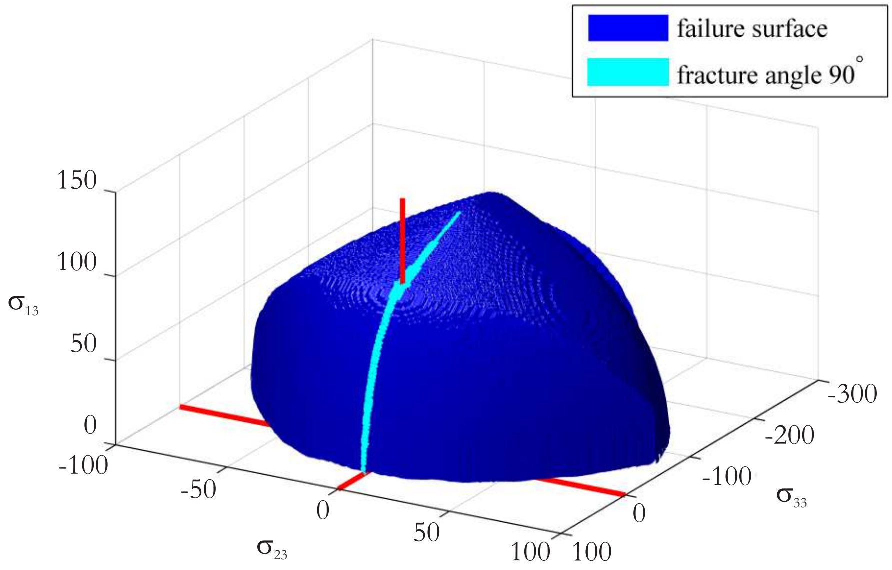

Figure 2.26: The Puck failure surface for σ_{33}, σ_{23}, σ_{13} (the marked region contains stress states which would cause delamination)

It should be noted, that the Puck IFF predictions are valid only within a UD lamina. The delamination usually occurs in the interface of two adjacent layers. According to [11] a delamination analysis would require a comparison between the delamination prediction of neighbouring laminas. Delamination should be expected where both plies predict a matrix crack with $\theta_{fr} = 90°$. The interface between plies shows often strength properties weaker than the transverse strength of the lamina. In [11] a knockdown factor of 0.8 for all strength properties for $\theta_{fr} = 90°$ is proposed. This seems simple to implement, but will result in numerical problems for the fracture angle search. The switch of material properties for certain fracture plane orientations could result in very small local extremes of $e(\theta)$ which would make a numerical fracture angle search very difficult to be performed accurately.

2.6.2 Prediction of delamination initiation by Brewer based failure criteria

Delamination occurs between composite layers and is therefore a failure mode of the interface rather then the material itself. Delaminations are caused due to normal stress, shear stress or a combination of both in the delamination plane. Delamination is mainly generated under tensile normal stress conditions, but it can occur under normal compressive stress if the shear stresses are high enough. Thereby, the danger of delamination reduces with increasing normal compressive stress. The Brewer delamination criterion, including Hou's extension [41], reads

$$\begin{aligned} \left(\frac{\sigma_{33}}{Z_t}\right)^2 + \left(\frac{\sigma_{13}+\sigma_{23}}{S_d}\right)^2 &= 1 \qquad \text{for} \quad 0 \le \sigma_{33} \\ \left(\frac{\sigma_{13}+\sigma_{23}}{S_d}\right)^2 - 8\left(\frac{\sigma_{33}}{S_d}\right)^2 &= 1 \qquad \text{for} \quad -\sqrt{\frac{\sigma_{23}^2+\sigma_{13}^2}{8}} < \sigma_{33} < 0. \end{aligned} \tag{2.76}$$

The resistance S_d to shear stresses σ_{23} and σ_{13} are chosen to be identical, since the interface layer can be seen as a resin rich layer which does not show any dependance upon fibre reinforcement. It should be noted that this is a simplification. Studies have already demonstrated that the delamination propagation highly depends on the ply orientation of the neighbouring plies [46]. It could therefore be expected that the initiation is influenced by the orientations of the neighbouring plies too. In this case, the strength properties will depend on this and are probably not identical. Eqn 2.76 allows for the calculation of the material exposure e_4 by

$$e_4 = \begin{cases} \sqrt{\left(\frac{\sigma_{33}}{Z_t}\right)^2 + \left(\frac{\sigma_{13}+\sigma_{23}}{S_d}\right)^2} & \text{for} \quad 0 \le \sigma_{33} \\ \sqrt{\left(\frac{\sigma_{13}+\sigma_{23}}{S_d}\right)^2 - 8\left(\frac{\sigma_{33}}{S_d}\right)^2} & \text{for} \quad -\sqrt{\frac{\sigma_{23}^2+\sigma_{13}^2}{8}} < \sigma_{33} < 0. \\ 0 & \text{otherwise} \end{cases} \tag{2.77}$$

The failure surface, defined by the set of failure criteria in Eqn 2.76, is illustrated in Fig 2.27.

For positive interlaminar normal stress σ_{33} the failure surface is very similar to the

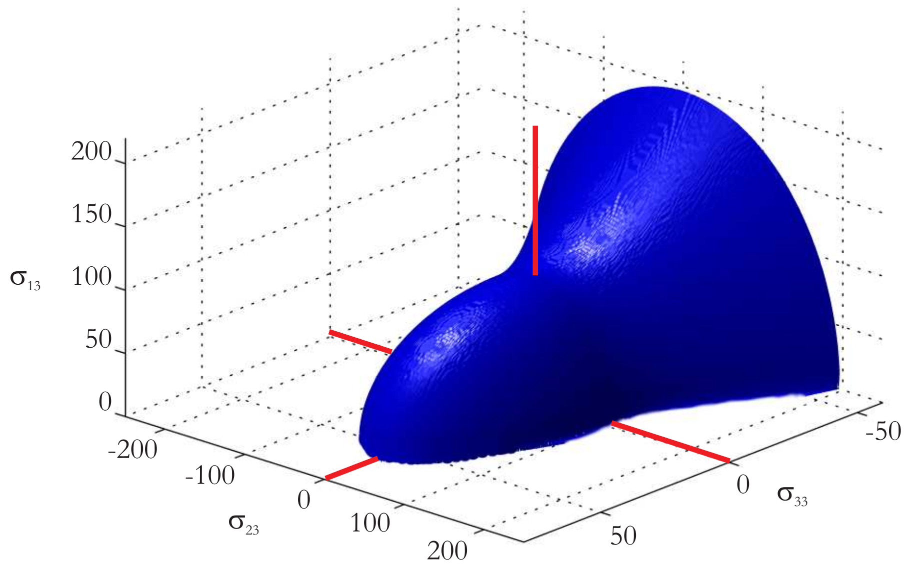

Figure 2.27: The Brewer failure surface for delamination initiation

failure surface for fibre failure as defined by Hashin. Furthermore, Fig 2.27 clearly shows the influence of the compressive stress σ_{33} on the shear strength of the interface. With increasing compression of the interface the strength rapidly grows, thus impeding delamination.

2.6.3 Comparison and verification of the criteria

In order to compare the predictions of both models, the criteria have been implemented into LS-DYNA [75]. A simple 3 point beam bending test has been modelled and compared with results from a quasi static experiment. The beam consisted of a $[[0/90]_3]_s$ carbon epoxy laminate. The 3 mm thick laminate was tested using a span of 40mm thus triggering delamination in the beam midplane. Since no directly measured material properties were available, the elastic constants of the UD layer were derived theoretically using the software U20MM (a micromechanics utility developed within the Composites Group of the University of Twente [47]). The UD properties were calculated from the properties of the constituents using Composite Cylinder Assemblage (CCA). This set of theoretical properties has been further refined in a manual inverse modelling approach. Each ply of the laminate has been modelled with one element through the thickness and the indenter is given identical velocity as in the experiment. The force deflection response was compared with the experimental results and finally matched by changing the longitudinal and transverse modulus. In order to compare both theories, the stress state in the region of delamination initiation was extracted and used to obtain the relevant strength properties. The delamination prediction of the Brewer and the Puck criterion are compared in Fig 2.28.

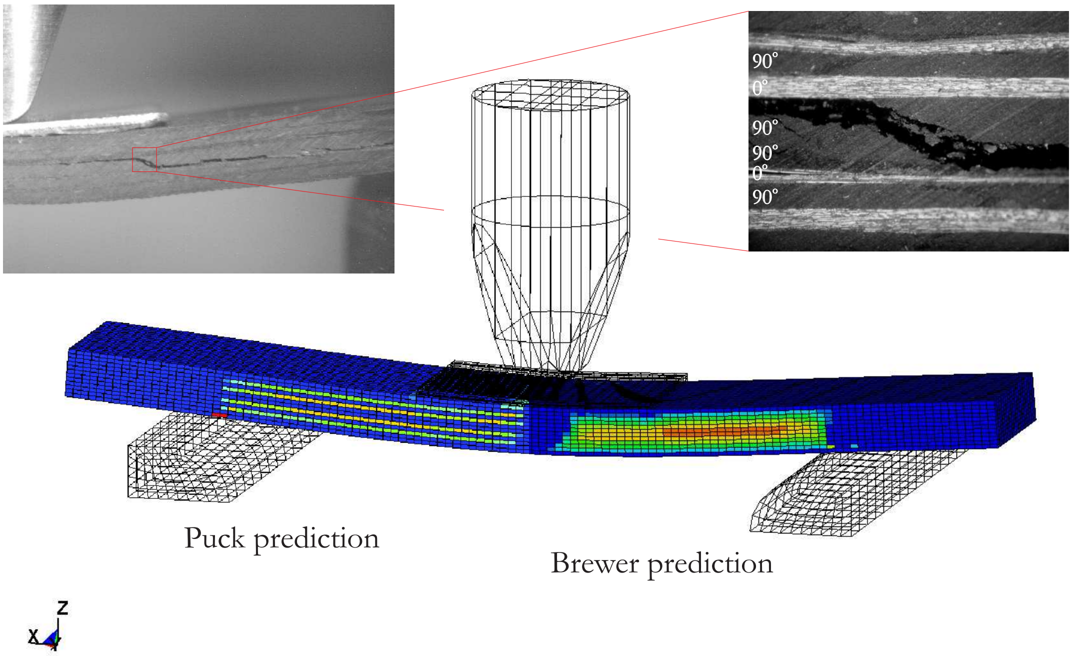

Figure 2.28: Comparison of delamination initiation prediction for the Puck criterion and the Brewer criterion

The region of delamination initiation was correctly predicted by the Brewer criterion. The limitations of the Puck criterion are confirmed by the comparison with the experimental results. The Puck model can only predict delamination initiation for plies which fibres are aligned with the beam axis (x-axis in Fig 2.28). If, as stated by Puck, delamination would occur only when two adjacent plies predict the onset, no delamination would have been predicted in this example. Both delamination models have been implemented based on continuum mechanics thus not being able to predict the exact interface in which delamination will initiated. This is a shortcoming compared to interface models. However, the interface could be modelled explicitly with thin solid elements or cohesive elements which would then allow for a prediction of the delaminating interface.

The given example demonstrated the advantages of the Brewer delamination criterion compared to the Puck criterion. The Brewer criterion was able to correctly predict the region where delamination initiated. Especially, the extension made by Hou and Petrinic [41] increased the accuracy significantly as it allows to predict delamination under normal compressive stresses. Therefore, the Brewer criterion is chosen here for the prediction of the onset of delamination.

2.7 Rate dependency

The experimental evidence in Chapter 4 demonstrates, strain rate dependent material behaviour is very pronounced in composite materials. Therefore, the application of the proposed failure model to impact related problems requires strain rate effects on the material properties to be considered. The following section introduces how strain rate dependent material behaviour can be introduced into the constitutive equations. Composite materials are well known for their rate dependent material behaviour caused by the the viscoelastic behaviour of the matrix material. Predicting the rate dependent material properties is a strong focus of current composite research related to impact problems. Several models have already been proposed to derive the change of properties directly from the behaviour of the epoxy resin in which the reinforcing fibres are embedded. This is the focus of a parallel study at the University of Oxford [48]. Alternatively, curve fitting techniques can be used to make the mechanical properties a function of strain rate. This requires experimental measurement of the change of the bulk mechanical properties at different loading rates. A more detailed discussion of the experimental procedures as well as currently available data can be found in Chapter 4.

Within this study, a simple curve fitting approach is used. Both, strength and stiffness properties, are defined as functions of strain rate $\dot{\boldsymbol{\varepsilon}}$. The influence of the strain rate on the material properties is represented by a factor f which is a function of strain rate $\dot{\boldsymbol{\varepsilon}}$.

For convenience, the following equations are written using Voigt notation. The following function was found to fit experimental data well

$$f_i(\dot{\varepsilon}_i) = 1 + \sqrt{K\dot{\varepsilon}_i} \text{ for } i = 1, 2, 3, 4, 5, 6 \tag{2.78}$$

where K is a fitting parameter which is identical for all i. As already explained above, each failure mode happens in a different plane. It is therefore important to calculate the strain rate dependent factors according to the strain rate in the relevant coordinate system. For this reason it is necessary to define a different set of factors f for the stiffness properties and each respective failure mode. The following notation for these factors is used in the thesis

- $f_i^s(\dot{\varepsilon}_i)$ *elastic properties*
- $f_i^1(\dot{\varepsilon}_i)$ *fibre rupture*
- $f_i^2(\dot{\varepsilon}_i^f)$ *fibre kinking*
- $f_i^3(\dot{\varepsilon}_i^m)$ *IFF*
- $f_i^4(\dot{\varepsilon}_i)$ *delamination*

where $\dot{\boldsymbol{\varepsilon}}^{\boldsymbol{f}}$ and $\dot{\boldsymbol{\varepsilon}}^{\boldsymbol{m}}$ correspond to the strain rate tensor rotated in the respective fracture plane for fibre kinking and IFF. In the following, it is introduced how the strain rate factors are applied to the material properties.

Rate dependent elastic properties

The focus of this study lies on CFRP. The stiffness of carbon fibres in longitudinal direction is assumed to be rate insensitive. The other Young's and shear moduli show rate dependent behaviour as the matrix material significantly contributes to the response in these directions. Hence

$$
\begin{aligned}
E_{11} =& E^0_{11} \\
E_{22} =& E^0_{22} f^s_2 \\
E_{33} =& E^0_{33} f^s_3 \\
G_{12} =& G^0_{12} f^s_4 \\
G_{23} =& G^0_{23} f^s_5 \\
G_{13} =& G^0_{13} f^s_6
\end{aligned}
\tag{2.79}
$$

The strain rate dependent stiffness behaviour of CFRP is well known to be dominated by the viscoelastic behaviour of the matrix material. The above equation only represents the change of the stiffness with strain rate, but does not include the time dependent material response as a consequence of viscoelasticity. Viscoelastic material behaviour can be described by a spring damper system. Commonly used models are the Kelvin-Voigt (spring and damper in parallel), the Maxwell model (series of spring and damper) and the Zener model (Kelvin-Voigt with spring in series or Maxwell with spring in parallel). The viscoelastic effects are reflected in the constitutive model by a damper which controls the rate dependent stiffness response. In order to enable a numerical efficient implementation, a simple single parameter model has been chosen here. The strain rate used to calculate the current elastic properties (see Eqn 2.79) is incorporated as follows

$$\dot{\boldsymbol{\varepsilon}} = d_{rate}\dot{\boldsymbol{\varepsilon}}_{t-\Delta t} + (1 - d_{rate})\dot{\boldsymbol{\varepsilon}}_t \tag{2.80}$$

where d_{rate} is a damping constant, $\dot{\boldsymbol{\varepsilon}}_{t-\Delta t}$ is the strain rate from the previous time step and $\dot{\boldsymbol{\varepsilon}}_t$ is the strain rate from the current time step.

Rate dependent strength properties for fibre rupture

Fibre rupture is assumed to be rate insensitive, hence

$$f^1_i = 1 \text{ for } i = 1, 2, 3, 4, 5, 6. \tag{2.81}$$

Rate dependent strength properties for fibre kinking

Fibre kinking occurs on a plane which is not aligned with the material coordinate system. Consequently, the strength properties, or better fracture plane resistances, are defined on this plane. The orientation of the initiation plane is given by the angles ψ_k, ϕ and θ_k. The strain rate tensor needs therefore be rotated into the respective plane by

$$\dot{\boldsymbol{\varepsilon}}^m = \boldsymbol{R}(\psi_k, \phi, \theta_k) \cdot \dot{\boldsymbol{\varepsilon}} \cdot \boldsymbol{R}^T(\psi_k, \phi, \theta_k). \tag{2.82}$$

The rotation matrix $\boldsymbol{R}(\psi_k, \phi, \theta_k)$ is found by Euler's rotation theorem

$$\boldsymbol{R}(\psi_k, \phi, \theta_k) = \boldsymbol{R}_1(\psi_k)\boldsymbol{R}_{3^k}(\phi)\boldsymbol{R}_{1^m}(\theta_k) \tag{2.83}$$

As kinking is initiated by a matrix failure, all involved strength parameters are assumed to be rate dependent. Consequently, the respective strain rate dependent strength parameters are then obtained as follows

$$\begin{aligned} Y_t &= Y_t^0 f_2^2(\dot{\varepsilon}_2^f) \\ Y_c &= Y_c^0 f_2^2(\dot{\varepsilon}_2^f) \\ R_{n1} &= R_{n1}^0 f_4^2(\dot{\varepsilon}_4^f) \\ R_{nt} &= R_{nt}^0 f_5^2(\dot{\varepsilon}_5^f) \end{aligned} \tag{2.84}$$

Rate dependent strength properties for IFF

For IFF, this plane is defined by the fracture plane inclination angle θ_{fr}. Consequently, the strain rate tensor $\dot{\boldsymbol{\varepsilon}}$ is rotated by

$$\dot{\boldsymbol{\varepsilon}}^m = \boldsymbol{R}_1(\theta_{fr}) \cdot \dot{\boldsymbol{\varepsilon}} \cdot \boldsymbol{R}_1^T(\theta_{fr}). \tag{2.85}$$

Similar to the rate dependency of the resistance against kinking, the IFF strength parameters are the obtained as follows

$$\begin{aligned} Y_t &= Y_t^0 f_2^3(\dot{\varepsilon}_2^m) \\ Y_c &= Y_c^0 f_2^3(\dot{\varepsilon}_2^m) \\ R_{n1} &= R_{n1}^0 f_4^3(\dot{\varepsilon}_4^m) \\ R_{nt} &= R_{nt}^0 f_5^3(\dot{\varepsilon}_5^m) \end{aligned} \tag{2.86}$$

As it will be discussed in Chapter 4, the inclination parameters p_t and p_c are assumed to be rate insensitive here.

Rate dependent strength properties for delamination

The available data for rate dependency of delamination initiation suggest that this failure mode is rate insensitive (see Chapter 4 and [50, 51, 52]). This is surprising as delamination is basically a failure of the matrix in the interface between plies, which is clearly rate dependent. In the absence of experimental evidence, however, no strain rate dependency is assumed here. Hence,

$$f_i^5 = 1 \text{ for } i = 1, 2, 3, 4, 5, 6. \tag{2.87}$$

The function (Eqn 2.78) needs to be fitted to experimental data. Therefore, the curve fit parameters for the stiffness K_1 and the strength properties K_2 need to be determined. As the rate dependent model is only applied to strength parameters related to the matrix, only one curve fit parameter K_2 is needed. As an example, the curve fit to neat RTM6 epoxy resin data from [49] is illustrated in Fig 2.29. The stiffness data as presented in Fig 2.29(a) represents an apparent modulus which is the secant modulus between the origin and 1% strain [49]. A more detailed discussion of strain rate dependent material properties is presented in Chapter 4.

2.8 Summary

This chapter introduced failure theories for unidirectional reinforced composites for fibre rupture, fibre kinking, IFF and delamination. Three dimensional physically based failure theories were selected for the prediction of the onset of damage. Special emphasis was given to the prediction of orientations of potential fracture planes for each failure mode. Therefore, novel fracture plane prediction algorithms have been developed and verified. The algorithms enable the numerically efficient prediction of planes of critical orientation for a given stress state within the framework of explicit FE. The onset of damage evolution

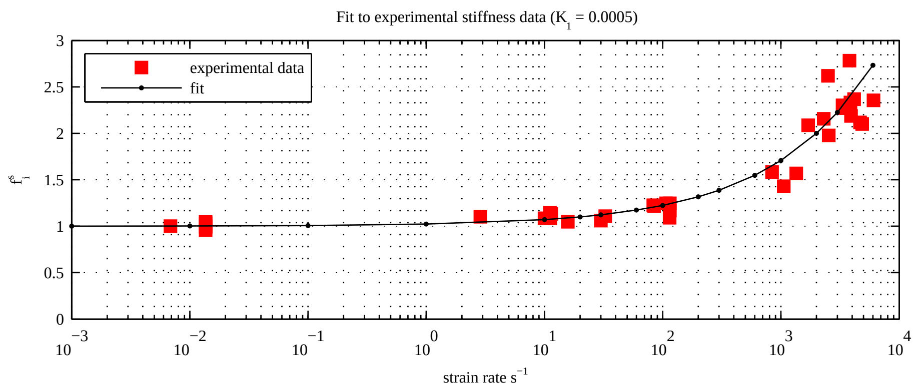

(a) fit of experimental stiffness data

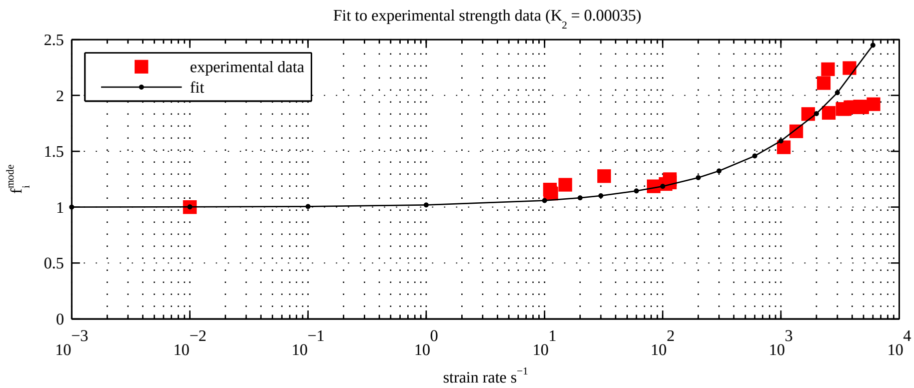

(b) fit of experimental strength data

Figure 2.29: Curve fitting of experimental rate dependent material properties

is then assessed by means of fracture plane tractions on respective fracture planes.

Another key aspect of the proposed model is the calculation of the material exposure e. All selected failure criteria are homogeneous in the stress terms (e.g. all stress terms are in the same order) which enables the efficient calculation of reserve factors. Consequently, e can be used as a measure of admissibility of elastically predicted stress states and enables it to be used as a dissipation potential for the prediction of damage evolution. This, together with the calculated reserve factor and the predicted fracture plane orientation, will be used in the following chapter to predict damage evolution and enable a physically based material degradation.

The application to impact related problems requires consideration of strain rate effects on the mechanical properties of the material. The knowledge of the fracture plane orientations enabled the use of the local strain rate acting on the respective fracture plane to obtain the rate dependent properties. This allows for a more accurate modelling of rate effects. Rate dependent material properties are obtained from a simple curve fitting approach in the model. The apparent elastic constants and certain strength properties are consequently a function of strain rate. The function which is describing the rate dependency is of empirical nature and fitted to experimental data.

The proposed model for damage initiation uses an original approach for strength prediction. Available failure theories have been carefully selected to enable the consequent use of fracture plane tractions within three dimensional failure criteria. This was only possible due to the novel fracture plane orientation algorithms which have been developed in this study. The framework, as given here, will be used in the following chapter to built a model for damage evolution basing on the predicted fracture planes and the material exposure.

Chapter 3

Prediction of damage evolution in composite materials

This chapter proposes a model for damage evolution in composite materials for general three dimensional stress states in unidirectional reinforced CFRP. In the first part, damage modelling strategies available in literature are presented in order to introduce the constitutive modelling framework based on Continuum Damage Mechanics (CDM). A constitutive model is proposed, based on CDM and the physically based failure criteria as introduced in the previous chapter. Key aspects of the proposed model for damage evolution is the prediction of damage growth on fracture planes based on physically sound dissipation potentials. Furthermore, an approach for the reduction of mesh dependent energy dissipation is proposed.

3.1 Introduction

The modelling of damage evolution of composite material has been focus of research for several decades. The heterogenous nature of composites results in a complex failure behaviour. UD composites fail due to several failure modes some of which occur at relative low load levels long before the maximal load is reached. The subsequent damage evolution within the composite results in complex stress redistributions which affect the global behaviour of the whole laminate. Predicting the impact response of composite materials requires therefore the correct representation of all relevant failure modes and the subsequent damage evolution. A realistic and physical sound model for the damage evolution is therefore needed for an accurate prediction of the material behaviour from the onset of damage until final failure.

Damage, as a mathematical concept, is only valid within the model for which it was defined [53]. One has to distinguish between damage entities and damage modes. According to Talreja [53] damage entities are individual identifiable changes in the microstructural constitution of a solid. Examples for damage entities in composites are matrix micro cracks, voids in the matrix, single broken filaments or debonded areas between matrix and fibres. A damage mode corresponds to a set of damage entities which evolve in a similar fashion. These are the macroscopical observable phenomena like IFF, fibre rupture or delamination. The damage in the RVE is subsequently represented by a set of damage modes. From the definition of the damage entities it becomes obvious that the length scale of the chosen model plays an important role in the definition of damage [54]. In the context of CDM, the chosen damage entities and corresponding damage modes must be chosen according to the size of the RVE.

Two main strategies are used to represent damage in composite materials, micro mechanical modelling and Continuum Damage Mechanics (CDM). Micro mechanical models focus on explicit modelling of damage entities using fracture mechanics, while Continuum Damage Mechanics (CDM) use a homogenised approach where the local effect of damage is smeared out over the RVE. The focus of this work lies in macroscopic modelling of composites as a continuum for which reason the micro mechanical modelling is not considered. The literature review, as presented here, does not aim at a full record of all proposed models, but only to introduce the main approaches and to give an overview about the available concepts of CDM models.

3.1.1 The general concept of CDM

In general, CDM aims to represent the effect of changes at the micro-scale, like the formation of cracks, on the macro-scale [55]. The focus is on the identification of damage entities and the impact of these on the material properties. CDM originate from the work of Kachanov [56] where the concept of representing damage by an internal damage variable in a continuum model was introduced to failure modelling of creep rupture. The approach was further developed by Rabotnov [57] who introduces the parameter $(1-\omega)$ as a measure of damage due to void growth and coalescence. The parameter ω is defined as change of cross section area as a consequence of void growth. The scalar damage variable introduced by Kachanov and Rabotnov cannot take into account directional dependence of the damage entity. A damage tensor was therefore later proposed by Murakami and Ohno [58]. The relation between damage tensor and elastic constants was finally established by Lemaitre and Chaboche [59].

To represent damage in a smeared manner over a RVE, two measures of stress are introduced, applied macroscopic stress $\boldsymbol{\sigma}$ and effective stress $\hat{\boldsymbol{\sigma}}$. The applied macroscopic stress represents an averaged stress over damaged and undamaged regions within the RVE and is the relevant stress measure from a macroscopic point of view. Effective stress is the stress acting on the cross-section which is effectively resisting the applied load [4]. Applied and effective stress are defined as follows

$$\begin{aligned} \hat{\boldsymbol{\sigma}} &= \boldsymbol{C}^0\boldsymbol{\varepsilon} \\ \boldsymbol{\sigma} &= \boldsymbol{C}(\boldsymbol{\omega})\boldsymbol{\varepsilon}, \end{aligned} \tag{3.1}$$

$\boldsymbol{C}^0$ refers to the undamaged stiffness tensor and $\boldsymbol{C}(\boldsymbol{\omega})$ denotes the damaged stiffness tensor. Based on the approach of strain equivalence, the relation between applied stress and effective stress can be expressed as follows

$$\boldsymbol{\sigma} = \boldsymbol{M}(\boldsymbol{\omega})\hat{\boldsymbol{\sigma}}, \tag{3.2}$$

where $\boldsymbol{M}(\boldsymbol{\omega})$ is a transformation tensor as a function of the damage state $\boldsymbol{\omega}$. Introducing the stress-strain relationship (Eqn 3.1) into Eqn 3.2 yields

$$\boldsymbol{\sigma} = \boldsymbol{M}(\boldsymbol{\omega})\boldsymbol{C}^0\boldsymbol{\varepsilon} = \boldsymbol{C}(\boldsymbol{\omega})\boldsymbol{\varepsilon}. \tag{3.3}$$

The CDM model has to establish the relation between damage and the elastic coefficients. Therefore, internal damage variables are introduced which often are functions of strain or strain rate. This general approach for the representation of damage has found application in many CDM models. However, various approaches to establishing the relation of damage and change in elastic properties have been proposed. In the following, some of the currently available CDM models are introduced in more detail.

3.1.2 CDM models for composite materials

Most CDM models rely on very similar representation of damage by introducing a set of internal damage variables or a damage tensor which is applied to the stiffness tensor as described above. A fundamental difference between the various CDM models is the definition of damage evolution. The approaches range from very simplistic linear damage evolution laws to damage evolution equations derived from thermodynamical potentials or experimentally measured functions. One of the simplest models, the Chang-Chang model [60], is already implemented into the commercial FE solver LS-DYNA. The elastic properties are diminished within 100 time steps as soon as damage initiation is predicted. The damage variables are therefore not a function of load or deformation. This approach is very unrealistic and numerically very unstable. Furthermore, the damage evolution suffers from intense mesh dependency.

A more rigorous approach to damage evolution is the use of thermodynamical potentials. Prominent models for this approach were proposed by Ladeveze and Le Dantec [61] and Matzenmiller et al. [62]. Internal variables which characterise damage are introduced into the strain energy function

$$U = f(\boldsymbol{\sigma}, \boldsymbol{\omega}). \tag{3.4}$$

Eqn 3.4 allows for the calculation of energy release rates per unit volume $\boldsymbol{Y}$ by

$$Y_i = \frac{\partial U}{\partial \omega_i}. \tag{3.5}$$

$\boldsymbol{Y}$ characterises energy release or dissipation due to increasing damage. The concept is borrowed from fracture mechanics where energy release rates per unit area govern crack development. Basing on the energy release rates $\boldsymbol{Y}$ (often referred to as conjugated forces or thermodynamical forces) damage evolution laws can be defined. Usually, one thermodynamical force is associated (conjugated) with one internal damage variable.

The Ladeveze model [61] proposed simple damage evolution laws where damage $\boldsymbol{\omega}$ is defined as a function of $\boldsymbol{Y}$

$$\omega_i = \frac{Y_i - Y_0}{Y_c}. \tag{3.6}$$

The reader should note that Ladeveze originally used the damage variable $\boldsymbol{d}$. This has been modified here to $\boldsymbol{\omega}$ for consistency. In Eqn 3.6 the quantities Y_0 and Y_c are threshold values which control the onset of damage evolution for the respective damage mechanism (e.g. IFF, fibre rupture). Y_i is the maximum value over the loading history thus ensuring irreversibility

$$Y_i(t) = \max(\sqrt{Y_i(\tau)}) \text{ with } \tau \geq t. \tag{3.7}$$

The Ladeveze model is well established in the composite community and implemented in the commercial FE solver PAMCRASH . A good example for the application of the model to fabrics has been proposed by Johnson et al. [63] and later extended by Greve and Pickett [64].

The model proposed by Matzenmiller [62] relies on damage evolution laws which are driven by a scalar growth functions ϕ_i and the vector functions $\boldsymbol{q}_i$ which govern the interaction of different damage mechanisms. The rate of damage evolution is given by

$$\dot{\boldsymbol{\omega}} = \sum_i \phi_i \boldsymbol{q}_i. \tag{3.8}$$

The growth function depends on the stress state, the damage state and the strain rate and is obtained from strain based failure criteria (Matzenmiller calls them loading surfaces and derives them from stress based failure criteria). The prediction of damage growth thereby relies on obtaining the strain gradient when the strain path crosses the loading surface. The coupling function $\boldsymbol{q}$ only provides information about the coupling of different damage mechanisms. The Matzenmiller model considers only plane stress states and three different damage modes. Recently, Curiel Sosa et al. [65] extended the Matzenmiller model to three dimensional stress states. Williams and Vaziri [66] implemented a simplified version of the Matzenmiller model into LS-DYNA and found significant improvements compared to the Chang Chang damage model available in LS-DYNA.

Even though not explicitly stated, Maimi et al. [67, 68] recently proposed a CDM model for plane stress basing on some of the features as proposed by Matzenmiller. Physical based failure criteria are used to define a set loading functions ϕ_i in stress space (ϕ_i is equivalent to the exposure e_i as described in the previous chapter). The gradient $\dot{\phi}_i$ is used to evaluate the onset and evolution of damage. Elastic domain threshold variables r_i are introduced into the failure criteria to represent the shrinking elastic domain for increasing damage. In case of predicted damage evolution the rate of elastic domain contraction $\dot{r}_i$ is obtained from from the loading function $\dot{\phi}$. The damage variables are then defined as a function of g_i and the energy dissipation due to crack growth. Damage evolution is thus driven by the rate at which the failure surface is exceeded. The model takes into account the orientation of the fracture plane for compressive IFF. The fracture plane orientation, however, is not calculated explicitly, but set to a constant angle. The model uses a smeared formulation. The energy dissipated to generate a crack of a certain area is smeared over the volume of the element, thus avoiding mesh dependent energy dissipation.

Hufenbach et al. [69] proposed a damage model based on experimentally obtained damage evolution laws. Therefore, damage evolution has been monitored insitu by acoustic emission. The experimentally obtained evolution laws were then embedded within a CDM framework similar to Matzenmiller.

Most CDM models are limited to plane states of stress. A three dimensional CDM model was recently proposed by Pinho et al. [4]. The model relies on the well known approach where the fracture energy necessary to entirely break the RVE is used as a driving parameter for damage evolution [70]. The rate of damage growth per increment of deformation is calculated such that the dissipated energy corresponds to experimentally obtained fracture energies. Hence, the energy release rates are fit to experimental data rather than calculated from thermodynamical potentials. The chosen damage evolution laws are linear. Important features of the model are the consideration of inclined fracture planes and a advanced model for fibre kinking. Furthermore, the damage evolution equation take into account the size of the finite element for energy dissipation thus reducing mesh dependent energy release which is characteristic for many CDM models.

3.1.3 Modelling of delamination propagation

The concept of CDM is well established for intralaminar failure modes. Delamination, however, is a failure mode which happens on the interface of adjacent plies. As a consequence, a large macro crack is formed thus separating the plies. The formation of the macro crack resulted in both, damage mechanics and fracture mechanics, to be used in the prediction of delamination propagation. A recent review by Elder et.al. [71] compares both approaches for delamination propagation under low velocity impact. In the following, a brief introduction of both methods is given.

Damage mechanics are mainly used for simulations where the interface is modelled as a resin rich zone between the plies. The proposed models rely on the principles of CDM as outlined above. A prominent model is the meso-modelling approach taken by Allix and Ladeveze [72]. Delamination is assumed to occur within a resin rich layer between adjacent plies. Crack growth is represented by three internal damage variables, one for normal through thickness stress and two for the respective out of plane shear stresses. Crack opening is simulated by damaging the respective components of the stress tensor thus ensuring correct energy release. CDM based delamination models are already implemented in commercially available FE solvers like LS-DYNA.

The formation of large macro cracks make fracture mechanics an appropriate choice for the modelling of delamination. Recently, cohesive zone models have been proposed and implemented into FE solvers. The interface is modelled as a system of springs which connect the nodes of adjacent plies. Bilinear damage laws are introduced to relate the force (or stress, if regularised) between the nodes to opening displacement δ. The springs are removed when a critical opening displacement is reached. In order to represent the correct release of energy due to crack propagation the critical opening displacement is often chosen such that the released energy corresponds to the fracture energy of the material. Mixed mode situations are taken into account by the popular power law

$$\left(\frac{G_I}{G_{IC}}\right)^{\alpha I} + \left(\frac{G_{II}}{G_{IIC}}\right)^{\alpha II} + \left(\frac{G_{III}}{G_{IIIC}}\right)^{\alpha III} = 1 \tag{3.9}$$

where G_I is the Mode I fracture energy, G_{IC} is the Mode I fracture toughness and αI is constant which allows to fit experimental data. Cohesive zones can be modelled using cohesive elements [40, 73], by connecting adjacent plies with beam elements [74] or using tied contact algorithms based on the penalty formulation [75].

3.2 Damage model framework

The damage generated due to impact loading is represented using the framework of Continuum Damage Mechanics. The proposed model considers three dimensional stress states and uses physically based failure criteria (see Chapter 2) as dissipation potentials. The damage evolution equations as proposed here are valid for damage propagation within a single RVE.

Unlike in most other CDM models, energy dissipation is not enforced by a damage evolution function. The propagation of damage is entirely driven by the rate at which certain failure surfaces are exceeded. The failure criteria which were introduced in the previous chapter are used as energy dissipation potentials. The respective damage variables and consequent stress reduction, however, is obtained implicitly rather than by direct differentiation of the damage potential. The material exposure e is used as a measure of excess strain energy in the RVE. Damage is represented by contracting failure surfaces thus shrinking the domain where the material remains elastic. The material degradation is determined by means of stress return algorithms on respective fracture planes. This ensures a physically based material degradation. Furthermore, an element size dependent parameter is introduced into the constitutive equations to reduce the mesh dependent energy dissipation which is typical for many CDM models.

The constitutive model considers four different damage modes which correspond to the failure modes as defined in Chapter 2.

Damage mode 1 contains damage caused by tensile fibre rupture. This damage mode usually results in catastrophic failure. The very high stiffness of the fibres result in a significant amount of strain energy stored in the fibres at the onset of damage. The subsequent fibre rupture causes significant damage in the material. Initially single filaments break and trigger rupture in neighbouring filaments. In that process failure of the fibre-matrix bond is often observed and results in local fibre pullout. The damage progresses rapidly until all fibres in the RVE are broken.

Damage mode 2, fibre kinking, is initiated by IFF around the fibres under compression in fibre direction. The matrix fails to support the fibres and deforms inelastically. Subsequently, the fibres rotate locally and break thus forming a kink band.

Damage mode 3, IFF, represents matrix cracks. The matrix is assumed to behave in a brittle manner. The number of micro cracks within the RVE is dependent on the size of the RVE. Within this model, only a single matrix crack is considered.

Damage mode 4 denotes the debonding of adjacent layers by delamination. This damage mode is treated separately from IFF since the interface between composite UD layers often exhibit properties different from the UD layer itself.

The damage model is developed for an application within an explicit FE environment. For the purpose of demonstration, the model is implemented into LS-DYNA.

3.3 Damage evolution

The damage evolution is driven by the rate at which certain failure surfaces are exceeded. A damage growth function g_i is defined for each damage mode. The rate of damage growth $\dot{g}_i$ is evaluated using the material exposure e_i as defined in Chapter 2. In the framework of explicit FE the increment of damage growth per time step Δg_i is given by

$$\Delta g_i = \begin{cases} 0 & \text{if } e_i \leq 1 \\ e_i - 1 & \text{if } e_i > 1 \end{cases} \tag{3.10}$$

All chosen failure criteria are homogeneous in stress and allow for the calculation of reserve factors. As a consequence, Δg_i can be interpreted as a measure of excess strain energy in the material. It should be noted that above expression is only valid for homogeneous failure criteria. For other failure criteria the relation between $\boldsymbol{\sigma}$ and e_i is not linear and cannot be used directly to calculate the rate of damage growth. The damage growth function $\boldsymbol{g}$ is incrementally updated by

$$\boldsymbol{g}_t = \boldsymbol{g}_{t-\Delta t} + \Delta \boldsymbol{g}. \tag{3.11}$$

From Eqn 3.10 and Eqn 3.11 it becomes obvious that damage evolution can only be positive. This is a sufficient condition to fulfill the second law of thermodynamics.

Each damage mode is represented by a single scalar damage threshold variable r_i. The variable r_i is not an actual damage variable in the classical sense. It is an internal variable which controls the domain in which the material behaves elastically and can be compared to the damage threshold as used in the models as proposed by Matzenmiller [62], Hufenbach [69] and Maimi [67]. The threshold variable r_i is used to reduce the strength of the RVE thus resulting in contracting failure surfaces (e.g. the elastic region of the material shrinks as damage increases). The elastic domain threshold variable is given by

$$r_i = g_i f^e. \tag{3.12}$$

In Eqn 3.12 f^e is a coefficient which controls the energy release of the RVE and depends on the material and the size of the RVE. How to derive this parameter and an example of the resulting damage evolution will be discussed later in this chapter.

In the current implementation a single variable r_i is used for each damage mode thus resulting in proportional contraction of the failure surface. For future work directional threshold values are conceivable. The direction of the loading vector with respect to the failure surface, for instance, could be used to shrink the elastic domain to represent experimental data better. The contracting failure surface is represented by the introduction of damaged strength parameters. In the following, the damaged strength parameters are presented.

Damage mode 1 is driven by the tensile stress in fibre direction and the shear stresses acting across the fibres. The strength properties associated with this damage mode are X_t and S_f. Hence

$$\begin{aligned} X_t =& (1 - r_1) X_t^0 \\ S_f =& (1 - r_1) S_f^0. \end{aligned} \tag{3.13}$$

Damage mode 3 (IFF) is driven by the three stresses acting on what will become the fracture plane. Therefore, the internal variable r_3 has to be applied to fracture plane resistances rather then the strength properties

$$\begin{aligned} Y_t =& (1 - r_3) Y_t^0 \\ R_{n1} =& (1 - r_3) R_{n1}^0 \\ R_{nt} =& (1 - r_3) R_{nt}^0. \end{aligned} \tag{3.14}$$

The damage mode 4 (delamination) is driven by the stresses which act on the interface between neighbouring plies. The internal variable r_4 is therefore applied to the strength properties which represent the resistance of this interface towards fracture

$$\begin{aligned} Z_t =& (1 - r_4) Z_t^0 \\ S_d =& (1 - r_4) S_d^0. \end{aligned} \tag{3.15}$$

For damage modes 1, 2 and 4 the damage initiation criteria can also be used as an energy dissipation potential. The mechanisms associated with these damage modes are represented by the stresses in the respective failure criteria. For damage mode 2 (fibre kinking) this is not the case. As already explained in Chapter 2, fibre kinking is initiated by failure of the surrounding matrix. After the onset of kinking is predicted, however, the misaligned fibres start to rotate and damage localises in a kink band. As a consequence of the rotation, the fibres eventually break. The whole kinking process happens in a plane different to the one predicted by the initiation criterion. The damage evolution has therefore to be assessed on the actual plane where the kinking happens. In the following, the kink propagation coordinate system is introduced and a simple kink propagation criterion proposed.

The orientation of the kink plane has already been defined by the angle ψ. Experimental observations have shown that the kink band does not propagate perpendicular to the fibres, but inclined by the kink band inclination angle β (see Fig 3.1). For the representation of damage due to fibre kinking, the kink propagation coordinate system $(1^p, 2^p)$, aligned with the kink band angle β, is introduced. It is this plane where the actual kinking occurs.

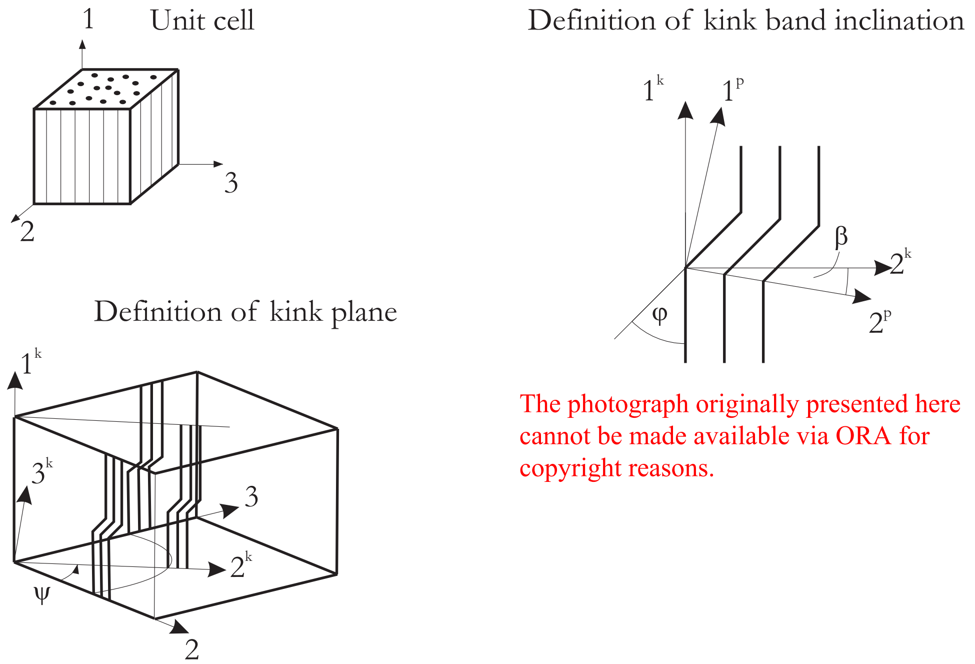

Figure 3.1: Definition of the kink band inclination β (photograph from [6])

While the initiation criterion can be used to find the kink plane orientation, the magnitude of β cannot be predicted. Few attempts have been made for the prediction of β , but currently no sound theories are established which allow for a reliable prediction [76]. Experimental observations in [77] reported kink band inclination angles β ranging from $20°$ to $30°$ while in [34] kink band inclinations of $12°$ to $16°$ have been reported. Within this work a fixed kink band inclination angle of $\beta = 20°$ is used. This corresponds to the theoretical predictions presented in [78].

From Fig 3.1 it becomes obvious that the kinking process in the propagation plane can conveniently be reduced to a 2D problem assuming that the kink band does not change orientation within the RVE (which is reasonable for small RVE's). Therefore, only the stresses σ_{11}^p, σ_{22}^p and σ_{12}^p are assumed to contribute to damage in this plane. When fibre kinking is initiated by failure of the surrounding matrix, the damage propagation is dominated by the rotation of the fibres together with a shear failure of the surrounding matrix. As the damage process happens in a different plane than the damage initiation, the initiation criteria cannot be used as an energy dissipation potential. For this reason a kink band propagation criterion is introduced. The in-plane shear stress in the kink propagation frame seems to drive the damage propagation. Therefore, a simple maximum shear stress criterion is chosen here to assess whether the kink band propagates. The following criterion is used

$$e_2^p = \frac{|\sigma_{12}^p|}{S_{kink}}. \tag{3.16}$$

The parameter S_{kink} can be interpreted as shear resistance against kinking in that plane and is determined when kinking initiation is predicted ($e_2 = 1.0$) as

$$S_{kink}^0 = |\sigma_{12}^p| \,. \tag{3.17}$$

It should be noted that the above introduced kink propagation criterion is only a very simplistic dissipation potential. Future developments should rely on more realistic potential where all stresses, which contribute to this damage mode, are represented

The increment of damage growth Δg_2 for fibre kinking is given by

$$\Delta g_2 = \begin{cases} 0 & \text{if } e_2^p \leq 1 \\ e_2^p - 1 & \text{if } e_2^p > 1 \end{cases} \tag{3.18}$$

The variable r_2 is applied to the resistance against kink propagation

$$S_{kink} = (1 - r_2) S^0_{kink}. \tag{3.19}$$

3.4 Stress return algorithm

Loading the material beyond the elastic limit results in inadmissable stress states. As a consequence, the material degrades (e.g. lower stiffness and reduced strength) which is represented by increasing damage. The model predicts the onset and evolution of damage using the material exposure e_i which is driving the respective internal threshold variables r_i thus resulting in shrinking failure surfaces due to increasing damage. The current inadmissable stress state in the RVE needs therefore to be returned to the damaged (shrunk) failure surface to represent material degradation. The concept is similar to the 'radial return' method of plasticity [83]. The chosen return algorithm within this model, however, relies entirely on reserve factors calculated from the failure criteria. In the following, the return algorithms for tensile and compressive damage modes are introduced. Tensile and compressive damage modes are distinguished according to the stress acting normal on the predicted fracture plane.

The stress return is performed for each damage mode separately. Therefore, four temporary stress tensors $\boldsymbol{\sigma}^{(i)}$ are calculated. These four stress tensors are then combined to form the macroscopic stress tensor $\boldsymbol{\sigma}$ for the RVE as it will be explained later in the chapter.

3.4.1 Stress return algorithm for tensile failure modes

Tensile failure modes result in cracks which are opening. As a consequence all tractions which are acting on the fracture plane (e.g. one normal traction, two shear tractions) need to be diminished as no force can be transmitted anymore. The stress state outside of the failure surface is inadmissable and needs to be returned to the now contracted failure surface. In general, two strategies for stress return are available. First, returning the stress state to the closest point on the updated failure surface or secondly, to return along a vector which points to the origin in the fracture plane traction space in which the respective failure surface is defined. Both approaches are visualised in Fig 3.2. Here, the return to the origin is chosen. This has the advantage of a numerical very efficient non-iterative single step stress return by the use of the reserve factor.

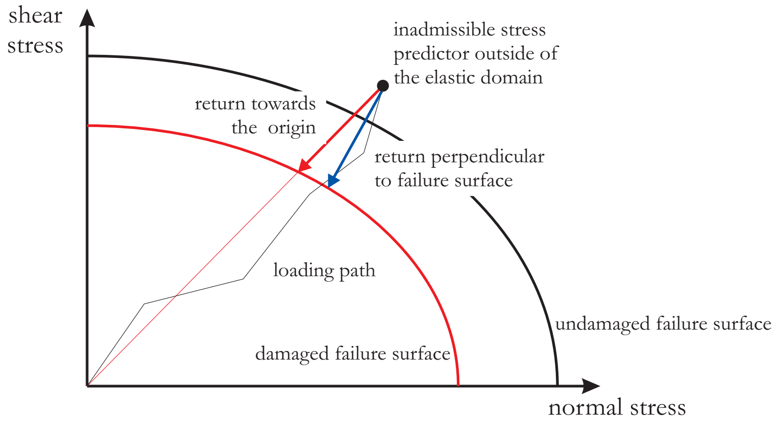

Figure 3.2: Stress return to the origin for the tensile failure modes (schematic)

The return to the origin can be performed by scaling the stress vector. The reserve factor obtained from the failure criteria can be used as scale factor. The respective reserve factors and the subsequent stress return are summarised in Tab 3.1.

Table 3.1: Stress return for the tensile failure modes

damage mode	f_i^{res}	stress return
1 fibre rupture	$f_1^{res} = \frac{1}{e_1}$	$\sigma_{11}^{(1)} = f_1^{res}\sigma_{11}^{tr}$ $\sigma_{12}^{(1)} = f_1^{res}\sigma_{12}^{tr}$ $\sigma_{13}^{(1)} = f_1^{res}\sigma_{13}^{tr}$
3 IFF	$f_3^{res} = \frac{1}{e_3}$	$\sigma_n = f_3^{res}\sigma_n$ $\tau_{n1} = f_3^{res}\tau_{n1}$ $\tau_{nt} = f_3^{res}\tau_{nt}$
4 delamination	$f_4^{res} = \frac{1}{e_4}$	$\sigma_{33}^{(4)} = f_4^{res}\sigma_{33}^{tr}$ $\sigma_{23}^{(4)} = f_4^{res}\sigma_{23}^{tr}$ $\sigma_{13}^{(4)} = f_4^{res}\sigma_{13}^{tr}$

The stress return for damage mode 3 is performed on the fracture plane. The returned stress in material coordinates $\boldsymbol{\sigma}^{(3)}$ is obtained by rotating the returned stress on the fracture plane $\boldsymbol{\sigma^{fr}}$ back into the material coordinate system

$$\boldsymbol{\sigma}^{(3)} = \boldsymbol{R}_1^T(\theta_{fr}) \cdot \boldsymbol{\sigma^{fr}} \cdot \boldsymbol{R}_1(\theta_{fr}). \tag{3.20}$$

3.4.2 Stress return algorithm for compressive failure modes

Not all stress terms used in the definition of the failure surface contribute to damage propagation in the compressive regime. Usually, the normal compressive stress impedes damage evolution. Therefore, a different approach is needed for each damage mode which takes into account the respective damage mechanism. In the following, the return algorithms for each of the compressive damage modes are presented.

The fibre kinking damage mode is assumed to be driven only by the shear stress acting in the kink band σ_{12}^p. The calculation of the reserve factor for the maximum shear stress criterion employed for the kink band propagation is simply given by

$$f_2^{res} = \frac{1}{e_2^p}. \tag{3.21}$$

During the development of the kink band the fibres do not only rotate but tend to break as well. Therefore, the reserve factor is not only applied to the shear stress σ_{12}^p, but also to the normal stress σ_{11}^p. The stress return is performed as follows

$$\begin{aligned} \sigma_{11}^p &= f_2^{res} \sigma_{11}^p \\ \sigma_{12}^p &= f_2^{res} \sigma_{12}^p. \end{aligned} \tag{3.22}$$

The stress in material coordinates for kinking is then obtained by rotating back $\boldsymbol{\sigma}^p$ into the material coordinate system

$$\boldsymbol{\sigma}^{(2)} = \boldsymbol{R}^T(\psi_k, \beta) \cdot \boldsymbol{\sigma^p} \cdot \boldsymbol{R}(\psi_k, \beta) \tag{3.23}$$

where $\boldsymbol{R}(\psi_k, \beta)$ is obtained by

$$\boldsymbol{R}(\beta, \psi_k) = \boldsymbol{R}_1(\psi_k) \cdot \boldsymbol{R}_{3^k}(\beta). \tag{3.24}$$

On the fracture plane for IFF the shear stresses τ_{n1} and τ_{nt} cause failure while the normal stress σ_n impedes failure. This needs to be taken into account for the stress return. While the material fails in a shear mode, compressive stress can still be transmitted. Therefore, only the shear stresses are reduced. Similar to the tensile failure modes, a reserve factor is calculated to return the fracture plane stresses. The failure criterion for compressive matrix failure can be rewritten

$$1 = \sqrt{\left(p_c \frac{\sigma_n}{Y_c}\right)^2 + \left(\frac{f_3^{res}\tau_{nt}}{R_{nt}}\right)^2 + \left(\frac{f_3^{res}\tau_{n1}}{R_{n1}}\right)^2} + p_c \frac{\sigma_n}{Y_c} \tag{3.25}$$

and solved for f_3^{res}

$$f_3^{res} = \sqrt{\frac{1 - 2p_c \frac{\sigma_n}{Y_c}}{\left(\frac{\tau_{n1}}{R_{n1}}\right)^2 + \left(\frac{\tau_{nt}}{R_{nt}}\right)^2}}. \tag{3.26}$$

The shear stresses on the fracture plane are subsequently returned to the updated failure surface as follows

$$\begin{aligned} \sigma_n &= \sigma_n \\ \tau_{n1} &= f_3^{res}\tau_{n1} \\ \tau_{nt} &= f_3^{res}\tau_{nt}. \end{aligned} \tag{3.27}$$

The returned stress for damage due to IFF in material coordinates $\boldsymbol{\sigma}^{(3)}$ is consequently obtained from Eqn 3.20.

Similar to compressive IFF, delamination is impeded under compressive normal stress on the delamination plane. Only the shear stresses are damaged. The reserve factor for delamination is obtained from

$$1 = \left(\frac{f_4^{res}\sigma_{13} + f_4^{res}\sigma_{23}}{S_d}\right)^2 - 8\left(\frac{\sigma_{33}}{S_d}\right)^2 \tag{3.28}$$

as

$$f_4^{res} = \sqrt{\frac{S_d + 8\sigma_{33}^2}{\sigma_{23}^2 + \sigma_{13}^2}}. \tag{3.29}$$

Subsequently the stress is returned as follows

$$\begin{aligned}\sigma_{33}^{(4)} &= \sigma_{33}^{tr} \\ \sigma_{23}^{(4)} &= f_4^{res} \sigma_{23}^{tr} \\ \sigma_{13}^{(4)} &= f_4^{res} \sigma_{13}^{tr}.\end{aligned} \tag{3.30}$$

A schematic illustration of the algorithm is provided in Fig 3.3.

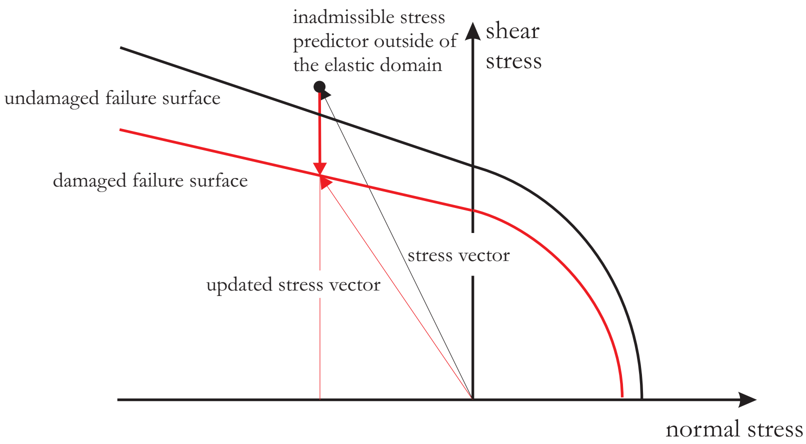

Figure 3.3: Stress return for the compressive IFF and compressive delamination damage mode (schematic)

3.4.3 Damage mode interaction and definition of the damaged stress tensor

A separate stress tensor $\boldsymbol{\sigma}^{(i)}$ is calculated and stored temporarily for each damage mode. In order to obtain the response of the damaged RVE as a whole, the macroscopic stress tensor $\boldsymbol{\sigma}$, including damage from all damage modes, needs to be determined. It should be noted that damage mode 4 (delamination) is excluded here. Delamination is not a damage mode of the bulk material, but of the interface. The delamination model is therefore implemented separately as it will be explained later in this chapter. The following procedure is used to determine the macroscopic stress of the RVE.

In case of only one active damage mode $\boldsymbol{\sigma}$ is simply given by

$$\begin{aligned}\text{fibre rupture: } \boldsymbol{\sigma} &= \boldsymbol{\sigma}^{(1)}\\ \text{fibre kinking: } \boldsymbol{\sigma} &= \boldsymbol{\sigma}^{(2)}\\ \text{IFF: } \boldsymbol{\sigma} &= \boldsymbol{\sigma}^{(3)}.\end{aligned} \tag{3.31}$$

Two other interactions are possible. The first interaction is between matrix damage and fibre rupture. Fibre rupture as a catastrophic failure mode will govern the damage process. Therefore, all stresses affected by fibre failure will be obtained from $\boldsymbol{\sigma}^{(1)}$. The remaining stress terms will be obtained from $\boldsymbol{\sigma}^{(3)}$. The updated stress tensor $\boldsymbol{\sigma}$ is given by

$$\begin{aligned}\sigma_{11} &= \sigma_{11}^{(1)}\\ \sigma_{22} &= \sigma_{22}^{(3)}\\ \sigma_{33} &= \sigma_{33}^{(3)}\\ \sigma_{12} &= \sigma_{12}^{(1)}\\ \sigma_{23} &= \sigma_{23}^{(3)}\\ \sigma_{13} &= \sigma_{13}^{(1)}.\end{aligned} \tag{3.32}$$

The second possible interaction is between IFF damage and damage due to fibre kinking. Both damage modes are initiated by a matrix failure. The damage created by fibre kinking, however, includes damage of the fibre itself. For this reason, the fibre kinking damage mode is seen as dominant when occurring together with IFF damage, hence

$$\boldsymbol{\sigma} = \boldsymbol{\sigma}^{(2)}. \tag{3.33}$$

This fully defines the macroscopic stress tensor $\boldsymbol{\sigma}$ of the RVE, including all damage modes.

3.5 The damaged stiffness tensor

The set of threshold variables r_i and the returned stress $\boldsymbol{\sigma}$ fully define the current state of damage. The prediction of damage evolution by the use of the material exposure e_i, however, requires the current state of damage to be incorporated into the stiffness tensor $\boldsymbol{C}$. This ensures that the stress predictor $\boldsymbol{\sigma}^{tr}$ and subsequently the respective material exposure e_i reflect a realistic amount of strain energy stored in the element in the next increment of loading. Furthermore, the correct calculation of stress in case of unloading requires the damage to be represented in the constitutive law. Therefore, the damage tensor $\boldsymbol{\omega}$ is introduced here.

Within the framework of CDM the effective stress $\hat{\boldsymbol{\sigma}}$ (stress acting on the undamaged cross section of the RVE) is related to the applied macroscopic stress $\boldsymbol{\sigma}$ (using Voigt-Kelvin notation) by

$$\boldsymbol{\sigma} = \boldsymbol{M}\hat{\boldsymbol{\sigma}} \tag{3.34}$$

where $\boldsymbol{M}$ is the stiffness damage tensor

$$\boldsymbol{M} = \mathrm{diag}\left[\begin{array}{cccccc} (1-\omega_1) & (1-\omega_2) & (1-\omega_3) & (1-\omega_4) & (1-\omega_5) & (1-\omega_6) \end{array}\right]. \tag{3.35}$$

Eqn 3.34 can be rewritten

$$\boldsymbol{\sigma} = \boldsymbol{M}\boldsymbol{C}^0\boldsymbol{\varepsilon} = \boldsymbol{C}(\boldsymbol{\omega})\boldsymbol{\varepsilon} \tag{3.36}$$

and yields the damaged stiffness tensor $\boldsymbol{C}(\boldsymbol{\omega})$

$$\boldsymbol{C}(\boldsymbol{\omega}) = \begin{pmatrix} (1-\omega_1)C_{11} & (1-\omega_1)C_{12} & (1-\omega_1)C_{13} & 0 & 0 & 0 \\ (1-\omega_2)C_{12} & (1-\omega_2)C_{22} & (1-\omega_2)C_{23} & 0 & 0 & 0 \\ (1-\omega_3)C_{13} & (1-\omega_3)C_{23} & (1-\omega_3)C_{33} & 0 & 0 & 0 \\ 0 & 0 & 0 & (1-\omega_4)C_{44} & 0 & 0 \\ 0 & 0 & 0 & 0 & (1-\omega_5)C_{55} & 0 \\ 0 & 0 & 0 & 0 & 0 & (1-\omega_6)C_{66} \end{pmatrix}. \tag{3.37}$$

The above damaged stiffness tensor might become unsymmetrical as damage evolves. The assumption of orthotropic material behaviour, however, remains unchanged as a loss of material symmetry due to damage evolution is not included in the model. The damage variables $\boldsymbol{\omega}$ characterise the influence of *all* damage modes on the stiffness of the RVE while the internal threshold variables r only represent damage for each *single* damage mode.

Most CDM models calculate the macroscopic (damaged) stress $\boldsymbol{\sigma}$ from the constitutive law and the current state of damage (Eqn 3.34 or Eqn 3.36). The model as proposed here relies on return algorithms to obtain $\boldsymbol{\sigma}$. This has the advantage that the stress state is well defined by the failure surfaces in three dimensions. Knowing the trial stress $\boldsymbol{\sigma}^{tr}$ and the macroscopic stress $\boldsymbol{\sigma}$ allows for calculation of the increment of damage for the current loading increment. The stress tensors $\boldsymbol{\sigma}^{tr}$ and $\boldsymbol{\sigma}$ are given by

$$\begin{aligned} \boldsymbol{\sigma}^{tr} &= \boldsymbol{M}_{t-\Delta t} \boldsymbol{C}^0 \boldsymbol{\varepsilon} \\ \boldsymbol{\sigma} &= \boldsymbol{M}_t \boldsymbol{C}^0 \boldsymbol{\varepsilon} \end{aligned} \tag{3.38}$$

which results in

$$\boldsymbol{M}_{t-\Delta t} \boldsymbol{\sigma}^{tr} = \boldsymbol{M}_t \boldsymbol{\sigma} \tag{3.39}$$

where $\boldsymbol{M}_{t-\Delta t}$ represents the state of damage of the previous time step and $\boldsymbol{M}_t$ represents the current state of damage. Eqn 3.39 allows to obtain the increment of stiffness damage from the ratio of stress predictor and applied stress by

$$\boldsymbol{M}_t = \frac{\boldsymbol{M}_{t-\Delta t} \boldsymbol{\sigma}}{\boldsymbol{\sigma}^{tr}} \tag{3.40}$$

with

$$\boldsymbol{M}_{t-\Delta t} = \mathrm{diag} \begin{bmatrix} (1-\omega_1) & (1-\omega_2) & (1-\omega_3) & (1-\omega_4) & (1-\omega_5) & (1-\omega_6) \end{bmatrix} \tag{3.41}$$

and

$$\begin{aligned} \boldsymbol{M}_t = \mathrm{diag}[1-(\omega_1+\Delta\omega_1) \quad & 1-(\omega_2+\Delta\omega_2) \quad 1-(\omega_3+\Delta\omega_3) \\ 1-(\omega_4+\Delta\omega_4) \quad & 1-(\omega_5+\Delta\omega_5) \quad 1-(\omega_6+\Delta\omega_6)] \end{aligned} \tag{3.42}$$

The increment of stiffness damage $d\omega_i$ is given by

$$\Delta\omega_i = \frac{(1-\omega_i)(\sigma_i^{tr} - \sigma_i)}{\sigma_i^{tr}} \tag{3.43}$$

In order to model the effects of cracks closing when the loading is reversed, the damage variables ω are distinguished in tension and compression

$$\begin{aligned}\Delta\omega_i =& \frac{(1-\omega_i)(\sigma_i^{tr}-\sigma_i)}{\sigma_i^{tr}} \text{ for } \sigma_i^{tr} \geq 0 \text{ and } i=1,2,3 \\ \Delta\omega_{ic} =& \frac{(1-\omega_i)(\sigma_i^{tr}-\sigma_i)}{\sigma_i^{tr}} \text{ for } \sigma_i^{tr} < 0 \text{ and } i=1,2,3\end{aligned} \tag{3.44}$$

The stiffness damage variables are then updated incrementally for every calculation step

$$\begin{aligned}\omega_i^t =& \omega_i^{t-\Delta t} + \Delta\omega_i \qquad \text{for } i=1,2,3,4,5,6 \\ \omega_{ic}^t =& \omega_i^{t-\Delta t} + \Delta\omega_{ic} \qquad \text{for } i=1,2,3.\end{aligned} \tag{3.45}$$

3.6 Passive damage

The four proposed damage modes are evaluated independently but might interact with each other depending on the current stress state. This is accounted for by the introduction of the concept of active and passive damage states [62]. The definition as given in [62] relates active and passive damage to the sign of the acting stress. A compressive fibre failure, for instance, results in the complete loss of tensile strength and stiffness. The proposed model operates on fracture planes of different orientation, so that the sign of stress cannot easily be used to distinguish in active and passive damage. Therefore a phenomenological approach is taken here.

The first coupling is the obvious case where a compressive fibre failure due to kinking results in a loss of tensile strength. Therefore, the following relation is proposed

$$r_1 = \max(r_1, r_2). \tag{3.46}$$

Compressive failure of the fibre is basically triggered by an IFF. Therefore, the following coupling is assumed to exist

$$r_3 = \max(r_2, r_3). \tag{3.47}$$

On the other hand, the failure due to matrix cracking does not necessarily result in fibre kinking. Therefore, no coupling is assumed here. The damage modes 1 to 3 are related to intralaminar failure mechanisms, while delamination is a interlaminar failure mechanism. No coupling is assumed between the intralaminar and interlaminar damage modes.

Similar to the coupling of the strength threshold variables, the stiffness damage variables are coupled. The loss of stiffness in compression results in loss of stiffness in tension, hence

$$\omega_i = \max(\omega_i, \omega_{ic}) \text{ for } i = 1, 2, 3. \tag{3.48}$$

The loss of tensile stiffness, however, does not contribute to the loss of stiffness under compression as cracks close and still transmit force. An example of the interaction of damage modes is illustrated in Fig 3.4. The stress-strain curve as presented in Fig 3.4 corresponds to a uniaxial tension-compression-tension loading in fibre direction.

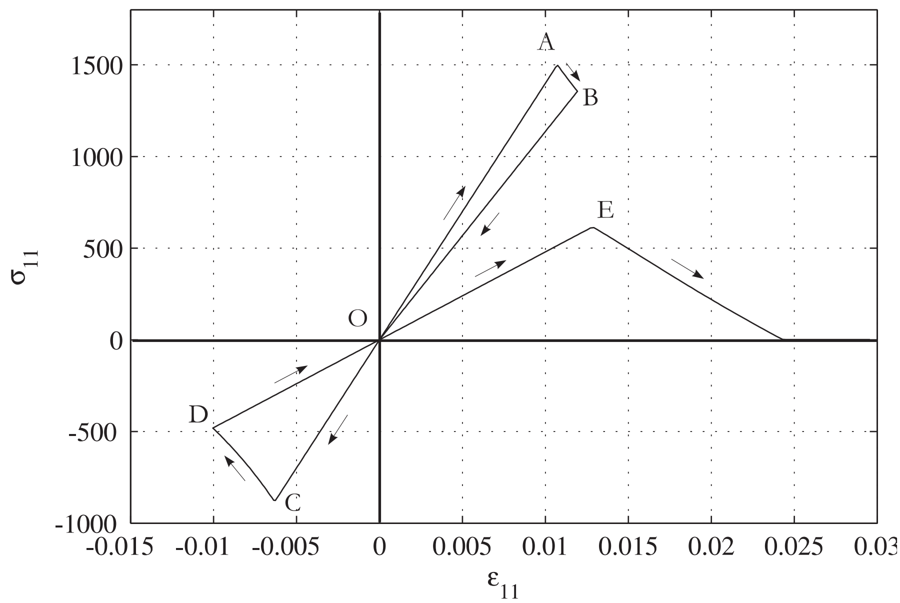

Figure 3.4: Example of passive damage for reverse loading cycle in fibre direction (loading followed path O-A-B-O-C-D-O-E)

3.7 Model calibration and mesh dependency

The calibration of composite damage models has been widely discussed in the composite research community. Ideally, the damage evolution should be directly measured from experiments. The brittle nature of most composites, however, makes this a difficult task. Novel insitu measurement techniques, like acoustic emission, already enable the monitoring of formation of micro cracks. In [69], damage evolution functions have been directly measured using this techniques.

Another popular method of calibrating damage models relies on experimentally obtained fracture energies. The idea is to design experiments which generate damage only due to a certain damage mode. Monitoring of the boundary conditions and the extend of either generated damaged volume or crack size allow for a calculation of the dissipated energy. Significant progress has already been made in this field. Experiments like end notched flexure, double cantilever beam [79] or mixed mode bending [80] tests for determination of mode I and mode II fracture energy are widely used and to some extend standardised. Recently, modified compact tension (CT) and compact compression (CC) specimens have been proposed in [8] to obtain the fracture energy for tensile fibre failure and fibre kinking. The problem with fracture energy based model calibration is that the measure of the total fracture energy itself does not give information about the evolution of damage. Additionally, many experimental procedures generate more than only one damage mode which makes an association of fracture energy and damage mechanism difficult.

The majority of above mentioned approaches are limited to quasi-static loading conditions. Energy dissipation measurements at elevated rates of strain are still in their infancy. Within this thesis, model calibration will rely on fracture energies. The reason is that there is already a broad basis of data available for all damage modes which are considered here.

A very recent approach for parameter identification is the use of numerical optimisation algorithms. This approach relies on numerical optimisation techniques to obtain best guesses for parameters for a given set of experimental results and a certain constitutive model. An inverse modelling approach for parameter determination is currently developed at the University of Oxford and has already been successfully applied to metals [81]. Although not used within this thesis, the approach seems to have a high potential for model parameter calibration and should be considered in the future.

The model calibration is affected by the inherent mesh sensitivity characteristic to CDM. The reason is that the localised damage process is smeared over the volume of the finite element. The released energy per unit area is therefore not constant but depends on the finite element volume. This problem is a well know shortcoming of CDM models and is addressed by introducing a measure of the element size into the formulation of the constitutive model [82]. In [4] and [68] a characteristic element length is introduced for each failure mode. That enables the correct geometric quantity to be associated to the energy release. The introduction of a characteristic element length provides an implicit way of estimating the area of the crack evolving through the element under consideration. A similar approach is taken here. The energy necessary to grow a crack through the RVE is smeared over the whole volume of the finite element. The total amount dissipated energy U of the whole element is given by

$$U = \Gamma \cdot A_{crack} \tag{3.49}$$

where Γ is the energy released per unit area and A_{crack} is the area of the generated crack. Γ is a material property often referred to as energy release rate. The difficulty lies in the definition of a reliable measure of the size of a potential crack within the finite element, especially for highly distorted elements. An approximation of the area of a crack in the element is given by

$$A_{crack} = \frac{V_{element}}{l^c} \tag{3.50}$$

with l^c being a characteristic element length parameter. In the following, the estimation of the characteristic element length l^c is presented in view of the proposed damage modes.

3.7.1 Calculation of the characteristic element length

The size of the element perpendicular to the crack plane is chosen as the characteristic element size parameter l^c. In the thesis l^c is calculated for hexahedral elements only. However, a similar approach can be adopted for different types of solid elements. While it is relatively easy to obtain l^c for an undistorted hexahedral element with the material axes aligned to the element edges, the situation becomes more difficult when the material is oriented arbitrarily in the element or the element is distorted itself. The approach taken here relies on the projection of the spatial diagonals of the hexahedral element on a vector $\boldsymbol{s}$ which is oriented normal to the plane where the crack is expected to appear. The position of the nodes of the hexahedral element with respect to the global coordinate system is given by the vector $\boldsymbol{n}$. The projection of $\boldsymbol{n}$ on $\boldsymbol{s}$ is given by

$$\boldsymbol{n}_i' = \mathrm{proj}_r \boldsymbol{n}_i = \frac{\boldsymbol{n}_i \cdot \boldsymbol{s}}{|\boldsymbol{s}|^2}. \tag{3.51}$$

The projected space diagonal p_{ij} of the element is obtained as follows

$$\boldsymbol{p}_{ij} = \boldsymbol{n}_i' - \boldsymbol{n}_j'. \tag{3.52}$$

The topology of the hexahedral element results in four space diagonal projections ($\boldsymbol{p}_{17}$, $\boldsymbol{p}_{28}$, $\boldsymbol{p}_{35}$, $\boldsymbol{p}_{46}$). The characteristic element length l^c is given by the longest of the four projections

$$l^c = \max\left(|\boldsymbol{p}_{17}|, |\boldsymbol{p}_{28}|, |\boldsymbol{p}_{35}|, |\boldsymbol{p}_{46}|\right) \tag{3.53}$$

An example of the projection is shown in Fig 3.5. In Fig 3.5 $\hat{\boldsymbol{e}}_1$, $\hat{\boldsymbol{e}}_2$ and $\hat{\boldsymbol{e}}_3$ are orthogonal basis vectors aligned with the material coordinate system. The definition of $\boldsymbol{s}_i$ depends on the damage mode and the resulting orientation of the fracture plane (see Chapter 2). In the following, the definition of the four vectors $\boldsymbol{s}_i$ is presented.

For damage mode 1 (fibre rupture), the fracture will occur transverse to the fibre direction, hence

$$\boldsymbol{s}_1 = \hat{\boldsymbol{e}}_1. \tag{3.54}$$

Damage mode 2 (fibre kinking) results in fracture which propagates in a plane which is transverse to the locally misaligned fibres. The vector $\boldsymbol{s}_2$ is therefore obtained by rotation of the orthogonal basis vector $\hat{\boldsymbol{e}}_1$ into the misalignment frame defined by the angles ψ and β (see Fig 3.6(a))

$$\boldsymbol{s}_2 = \boldsymbol{R}_3(\beta)\boldsymbol{R}_1(\psi)\hat{\boldsymbol{e}}_1. \tag{3.55}$$

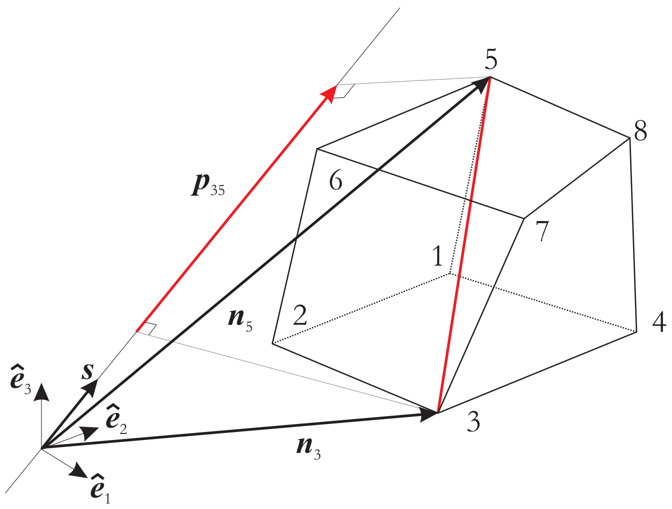

Figure 3.5: Projection $\boldsymbol{p}_{35}$ on the vector $\boldsymbol{s}$

The orientation of the IFF failure plane for damage mode 3 is defined by the angle θ_{fr}. The vector $\boldsymbol{s}_3$ is given by the following rotation (see Fig 3.6(b))

$$\boldsymbol{s}_3 = \boldsymbol{R}_1(\theta_{fr})\hat{\boldsymbol{e}}_2. \tag{3.56}$$

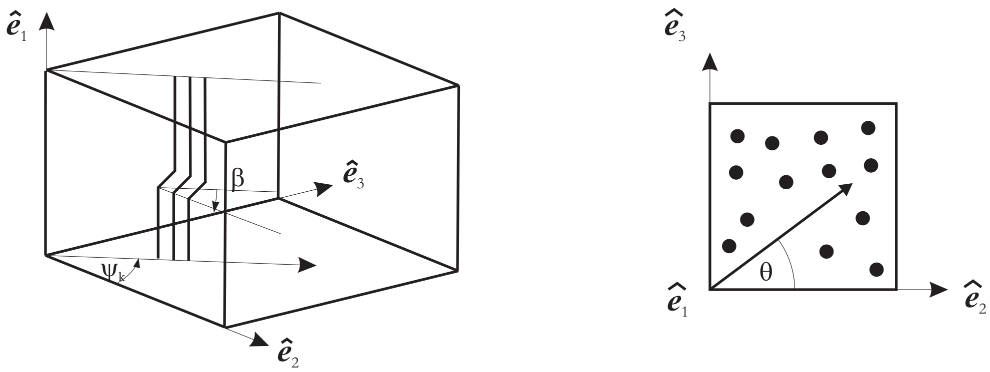

(a) damage mode2 (fibre kinking)

(b) damage mode3 (IFF)

Figure 3.6: Rotation of the orthogonal basis vectors into the fracture planes

The delamination plane is, similarly to fibre rupture plane, aligned with material coordinate system and simply given by

$$\boldsymbol{s}_4 = \hat{\boldsymbol{e}}_3. \tag{3.57}$$

Controlling mesh dependent energy dissipation within the damage model requires the introduction of the element volume V and the size of a potential crack A_{crack} into the damage evolution equations. The basic idea is to keep the total energy released per unit area constant for varying element sizes. The energy release is controlled by the energy release parameter f^e in the damage rule (Eqn 3.12). Constant energy release requires this parameter to become a function of element volume and crack area $\frac{V}{A_{crack}}$ which corresponds to the characteristic element length l^c . Two calibration procedures for the calculation of f^e are suggested. The first calibration procedure applies to damage mode 1 and 2. Both damage modes do not result in a clear fracture plane, but generate damage which is to some extend distributed over the whole RVE. The second calibration procedure applies to damage mode 3 and 4. Both damage mode result in clear fracture planes being formed.

3.7.2 Calibration of damage mode 1 and damage mode 2

Fibre rupture and fibre kinking do not result in a clear recognisable fracture plane. Fibre rupture causes fracture of the fibres and the surrounding matrix as well as fibre pullout. Fibre kinking, on the other hand, forms a kink band of a certain width. Within this kink band damage represents broken fibres and crushed matrix. Both damage entities are distributed over the width of the RVE thus forming a damaged volume. The fracture mechanisms are therefore not distinguished into mode I and mode II. A single, element size dependent release parameter f^e is calculated for each respective damage mode.

The energy release parameter ensures that the energy dissipated over the whole volume of the element corresponds to the fracture energy Γ necessary to drive a crack through the element. Damage evolution is driven by the material exposure e on fracture planes which are often not aligned with the material coordinate system. This makes an closed form analytical calculation of f^e very difficult. A numerical procedure for the determination of $f^e(l^c)$ is therefore employed. The proposed constitutive model is applied to a range of element sizes thus covering the relevant range of l^c. A bisection algorithm is employed to find the value of l^c which gives the correct energy dissipation for a given element size. The calibration is performed for the uniaxial case in both tension and compression. An example of the obtained curve for f^e is displayed in Fig 3.7. Please note that f^e is plotted over A_{crack}/V (equal to $1/l^c$) in Fig 3.7. This visualises better the relation between element geometry and energy dissipation.

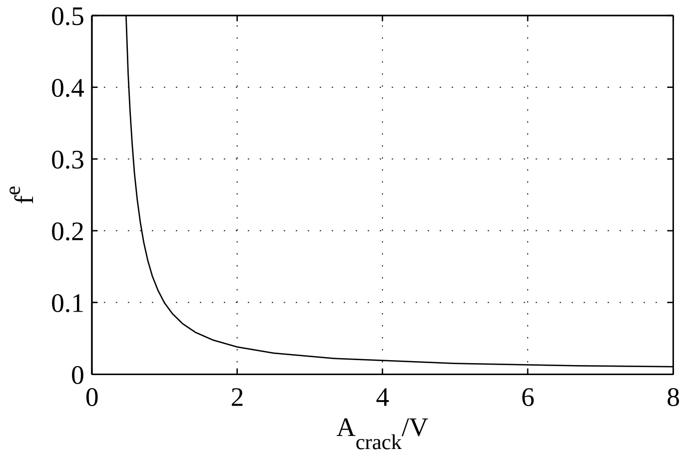

Figure 3.7: The influence of the element size on the damage parameter f^e for a constant energy release per area (for fibre failure and $\Gamma = 90kJ/m^2$)

From Fig 3.7 it becomes obvious that the relation between element size and energy release parameter f^e is non-linear. The value of f^e goes towards infinity for small values of A_{crack}/V (meaning large values for l^c). The reason is that with increasing element volume the elastic energy stored in the element becomes higher than the energy actually necessary to drive a crack through the element. This has already been reported in [4] and [68]. A correct energy dissipation is not possible anymore and the mesh needs to be refined.

In order to demonstrate the effect of a smeared formulation, a constant geometry meshed with three different mesh densities has been subjected to uniaxial tension in fibre direction. The force displacement curves obtained on the boundary are compared for a mesh dependent damage evolution and for the smeared approach. For a realistic simulation, the force displacement curve, and consequently the energy dissipated, should be mesh independent. The comparison is displayed in Fig 3.8.

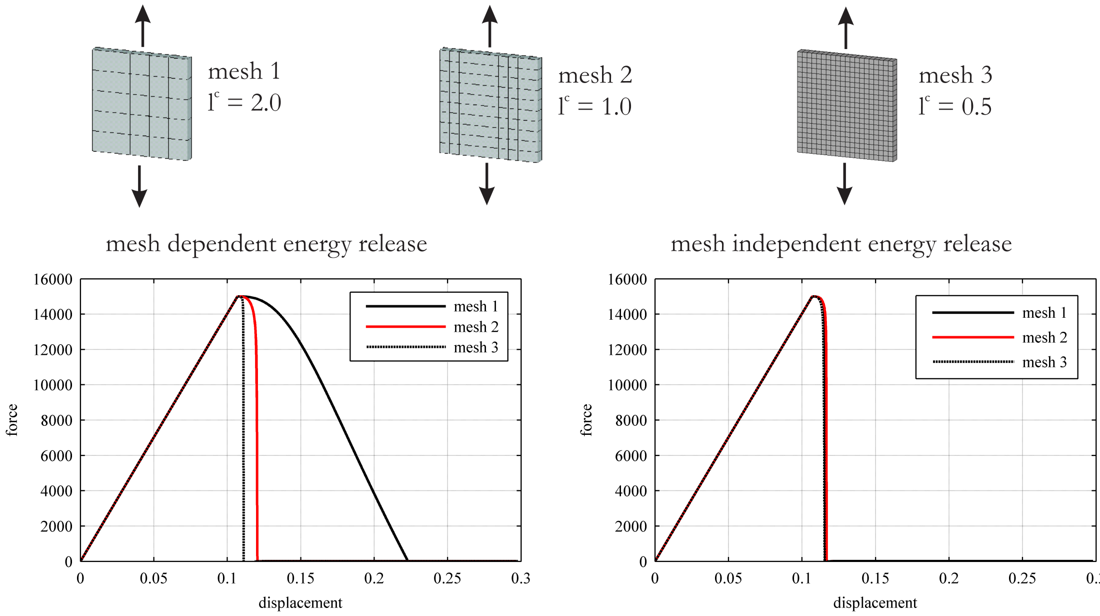

Figure 3.8: Comparison of mesh sensitive and smeared damage model for different mesh densities

3.7.3 Calibration of damage mode 3 and damage mode 4

Damage mode 3 and 4 result in the formation of a single crack. This only holds for small RVE's for damage mode 3. Larger RVE's can contain more than one matrix crack which is not considered here. For both damage modes the crack is a result of a normal stress and two shear stresses acting in the plane where the crack will form. Two energy dissipation mechanisms are distinguished, an opening mode (mode I) and a shear mode (mode II). This is very common in interface models and widely used for the modelling of delamination by the use of cohesive elements. In many situations, both mechanisms are present, which is referred to as mixed mode delamination.

The ratio of shear and normal load is usually defined in terms of opening displacements for mode I (δ_1) and for mode II (δ_2 and δ_3). The implementation in a solid element requires a definition in terms of strain. On the fracture plane the mode I component is ε_n while the shear components are ε_l and ε_t. The resulting shear deformation ε_s on the interface is then given by

$$\varepsilon_s = \sqrt{\varepsilon_l^2 + \varepsilon_t^2}. \tag{3.58}$$

Many interface model use

$$\eta = \frac{\varepsilon_s}{\varepsilon_n}. \tag{3.59}$$

to determine the ratio of mode I and mode II in a mixed mode situation. This results in a division by zero in case of pure shear and causes difficulties in a numerical implementation. An alternative ratio has been proposed in [73] which overcomes this

$$\eta = \arccos\left(\frac{\varepsilon_s}{\varepsilon_{total}}\right) \tag{3.60}$$

with

$$\varepsilon_{total} = \sqrt{\varepsilon_n^2 + \varepsilon_s^2} \tag{3.61}$$

The ratio is evaluated only once for each element at the onset of delamination and subsequently kept constant.

Once delamination is initiated the crack propagation is governed by the well known propagation criterion

$$\left(\frac{G_I}{G_{Ic}}\right)^{\alpha} + \left(\frac{G_{II}}{G_{IIc}}\right)^{\alpha} = 1. \tag{3.62}$$

In Eqn 3.62 G_{Ic} and G_{IIc} are the critical energy release rates for mode I and mode II respectively. The parameter α is used to fit experimental data and holds usually values between 1 and 2 for the materials as considered here. The energy release rates G_I and G_{II} are the mode I and mode II components in a mixed mode situation. From Eqn 3.62 the total energy release rate G_c due to both modes is given by

$$G_c = \left(\left(\frac{\cos^2\eta}{G_{Ic}}\right)^{\alpha} + \left(\frac{\sin^2\eta}{G_{IIc}}\right)^{\alpha}\right)^{-\frac{1}{\alpha}}. \tag{3.63}$$

The damage model as proposed here does not enforce the energy release rate by defining a final strain value ε_f, but by the energy release parameter f^e. In order to take mode I and mode II crack propagation into account, two energy release parameters are required. Correct energy release for pure mode I is enforced by f_n^e and for pure mode II by f_s^e. Eqn

3.63 can be replaced by

$$f_i^e = \left(\left(\frac{\cos^2\eta}{f_n^e}\right)^\alpha + \left(\frac{\sin^2\eta}{f_s^e}\right)^\alpha\right)^{-\frac{1}{\alpha}}. \tag{3.64}$$

The above equations only apply in case of a normal tensile stress on the fracture plane. For compressive stress normal to the fracture plane a pure mode I crack propagation is assumed. The energy release parameter f_i^e is simply given by

$$f_i^e = f_s^e. \tag{3.65}$$

The constitutive model does not require the strain tensor $\boldsymbol{\varepsilon}$ to be stored as a state variable. However, for the determination of the mixed mode ratio, an estimation of the strain is required. The model assumes linear behaviour in the elastic domain. Therefore, the strain can be calculated from the stress as follows

$$\begin{aligned}
\varepsilon_{11} =& \frac{\sigma_{11}}{E_{11}} - \frac{\nu_{21}\sigma_{22}}{E_{22}} - \frac{\nu_{31}\sigma_{33}}{E_{33}} \\
\varepsilon_{22} =& -\frac{\nu_{12}\sigma_{11}}{E_{11}} + \frac{\sigma_{22}}{E_{22}} - \frac{\nu_{32}\sigma_{33}}{E_{33}} \\
\varepsilon_{33} =& -\frac{\nu_{13}\sigma_{11}}{E_{11}} - \frac{\nu_{23}\sigma_{22}}{E_{22}} + \frac{\sigma_{33}}{E_{33}} \\
\varepsilon_{12} =& \frac{\sigma_{12}}{G_{12}} \\
\varepsilon_{23} =& \frac{\sigma_{23}}{G_{23}} \\
\varepsilon_{13} =& \frac{\sigma_{13}}{G_{13}}.
\end{aligned} \tag{3.66}$$

The strain on the fracture plane for damage mode 3 is given by

$$\boldsymbol{\varepsilon}^{fr} = \boldsymbol{R}(\theta_{fr}) \cdot \boldsymbol{\varepsilon} \cdot \boldsymbol{R}^T(\theta_{fr}) \tag{3.67}$$

with

$$\begin{aligned}
\varepsilon_n =& \varepsilon_{22}^{fr} \\
\varepsilon_l =& \varepsilon_{12}^{fr} \\
\varepsilon_t =& \varepsilon_{23}^{fr}.
\end{aligned} \tag{3.68}$$

The energy release parameters f_n^e and f_s^e are functions of the characteristic element length

l^c and obtained as described earlier. Single elements of different size are loaded either in uniaxial tension transverse to the fibres or in pure shear. A numerical bisection algorithm is then used to find the parameters $f_n^e(l^c)$ and $f_s^e(l^c)$ which result in correct energy dissipation for each considered element size.

The delamination plane is aligned with the material coordinate system. Therefore, the strain components on the fracture plane are simply given by

$$\begin{aligned} \varepsilon_n =& \varepsilon_{33} \\ \varepsilon_l =& \varepsilon_{13} \\ \varepsilon_t =& \varepsilon_{23}. \end{aligned} \tag{3.69}$$

A CDM approach has been chosen for the modelling of delamination. The interface in which delamination occurs is therefore modelled with very thin solid elements. For these elements the characteristic element length l^c remains constant. This allows to simplify the parameters f_n^e and f_s^e to be constant rather than a function of l^c.

3.8 Numerical implementation of the model and verification

This section explains the implementation of the proposed constitutive model in the explicit finite element solver LS-DYNA. The model is implemented into LS-DYNA as a user defined material model. Therefore the model has been divided into the intralaminar model and interlaminar model. The intralaminar model contains the the damage modes which characterise the failure mechanisms of the UD ply itself (fibre rupture, fibre kinking, IFF). The interlaminar model deals with failure mechanisms related to the interface between neighbouring plies (delamination). Both models have been implemented for the use with 8 noded hexahedral elements with a single integration point. It should be noted that only minimal effort would make the proposed approach work with other solid element types.

The energy release parameters f_i^e are read in as load curves. For future applications, it would be possible to implement the calibration algorithm as preprocessing routine thus avoiding the external calibration procedure. This would allow for the direct input of the respective energy release rates. Currently, the calibration is implemented within Matlab which then provides the required load curves.

Delamination happens on the interface between two adjacent plies. The failure mechanism is often attributed to a resin rich area between plies. The nature of the interface ideally requires a zero thickness element. Here, delamination is modelled by the use of very thin brick elements. Usually, this results in very small time steps for the explicit calculation which is not acceptable. Therefore, the stiffness which is reported from the material model routine to the time step calculation is modified thus excluding the interface elements from the time step calculation. This approach violates the stability condition of the explicit solution and should be used with caution.

The implementation of the constitutive model is visualised in Fig 3.9.

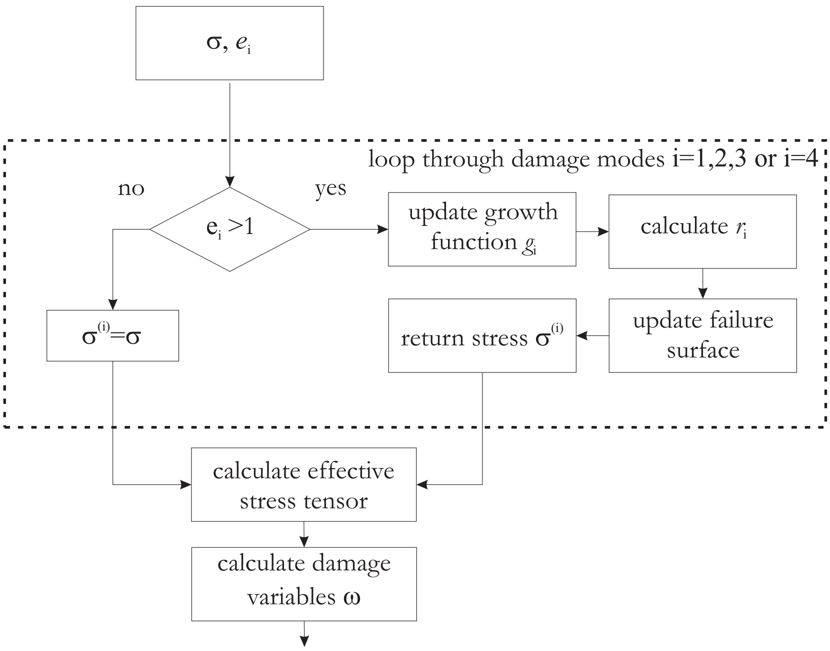

Figure 3.9: Flow chart of the damage model

3.8.1 Example1: uniaxial tension in fibre direction

A single element, free to contract laterally, has been pulled in the fibre direction. Fig 3.10 illustrates the history of damage evolution.

Initially, the element behaves as linear elastic. The material exposure e_1 rises linearly as the element is loaded. The linear relation between stress (and subsequently strain) and e_1 is a consequence of the chosen homogeneous failure criteria. For inhomogeneous criteria, the relation would be non-linear and reserve factors would be more difficult to obtain. At $e_1 = 1$ initiation of damage is predicted and the threshold value r_1 starts to rise (see Fig 3.10(b)). The stress return algorithm keeps the stress state on the shrinking failure surface thus ensuring $e_1 = 1$ while the material is damaging. As a consequence of rising damage the damage variable ω_1 starts to rise. From Fig 3.10(c) it becomes obvious that only ω_1 is rising. This is a shortcoming of the indirect calculation of the damage variables. In the case of uniaxial tension, the shear stresses σ_{12} and σ_{13} are zero and no increment of damage Δw_4 and Δw_6 is therefore predicted. The material would therefore retain the shear stiffness (but not strength) which is unrealistic. This aspect of the model will need further attention. The predicted stress-strain curve is illustrated in Fig 3.10(d). It should be noted that only σ_{11} is plotted because all other stresses are equal to zero.

As already pointed out earlier in the chapter, the proposed model does not explicitly enforce a certain function for the energy dissipation. In order to compare the evolution of damage with other CDM models, the damage variable is plotted as a function of strain $\omega_i\left(\varepsilon_i\right)$ in Fig 3.11 together with other commonly used enforced damage evolution laws. The following damage evolution laws have been used for the comparison and plotted in Fig 3.11 (please note that not all presented curves would result in the same amount of dissipated energy, purpose of the comparison is only to assess the general shape of the function)

- *Matzenmiller* $\omega_i = 1 - exp\left(-\frac{1}{me}\left(\frac{E_i^0\varepsilon_i}{X}\right)^m\right)$
- *linear damage evolution* $\omega_i = A\varepsilon_i$

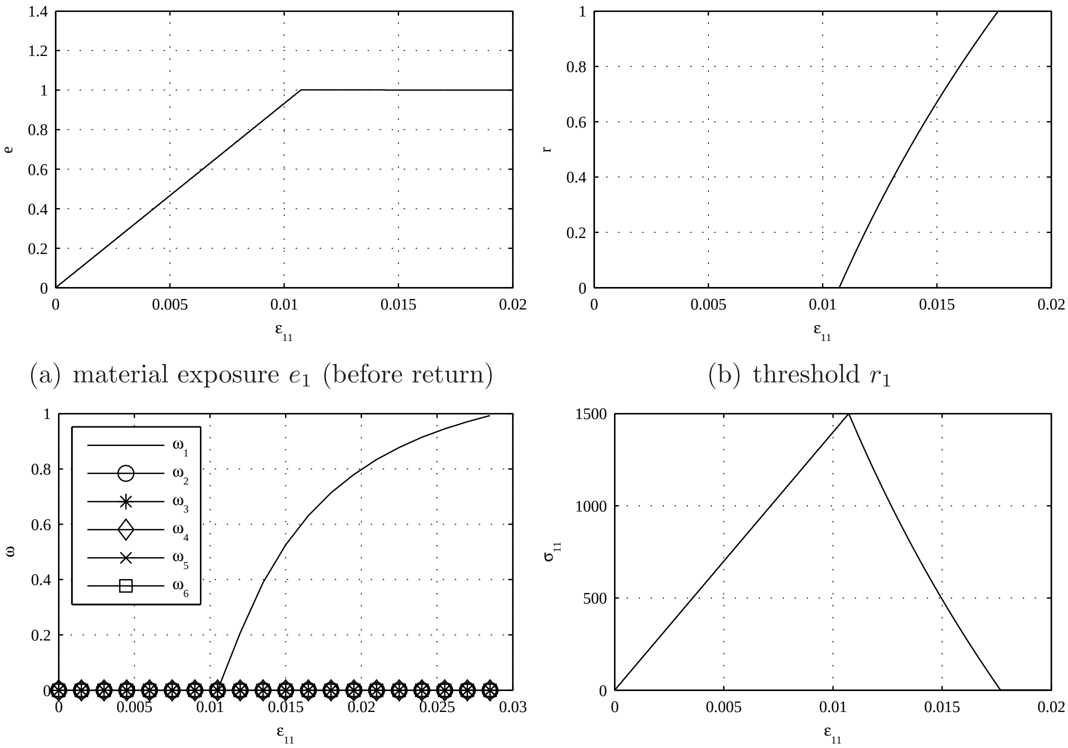

(a) material exposure e_1 (before return)

(b) threshold r_1

(c) damage variables ω

(d) predicted stress-strain curve

Figure 3.10: Model prediction for uniaxial tension in fibre direction

From Fig 3.11 it can be seen that the damage evolution as predicted by the proposed model is very similar to some widely used damage evolution functions (e.g. Matzenmiller). This is encouraging but does not allow conclusions concerning the validity. For a final assessment of the approach, experimentally obtained damage evolution data are needed.

3.8.2 Example2: modelling of a compressive matrix crack

For the purpose of demonstration, a single UD ply has been modelled with two mesh densities and subjected to transverse compression. The ply is then compressed transverse to the fibres (see Fig 3.12(a)). Failure initiation is triggered by some weaker elements in the middle of the modelled ply.

In Fig 3.12(b) the orientation of the fracture plane has been predicted by the algorithm as introduced in Chapter 2. It can be seen that two planes of preferred fracture orientation are predicted. This is caused by the fact that the material exposure is equal on both

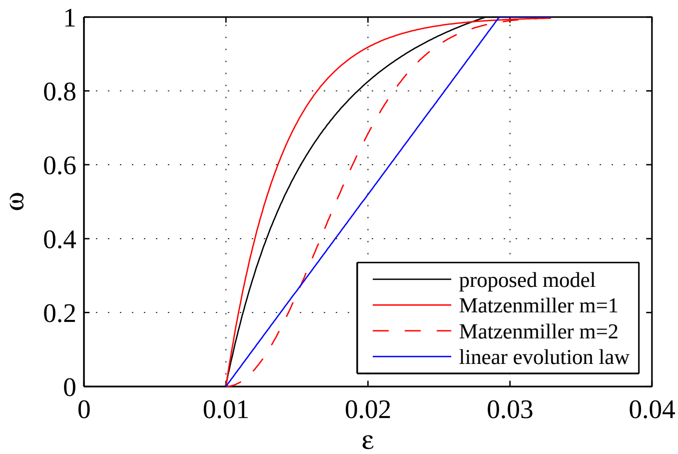

Figure 3.11: Comparison of commonly used damage evolution function

planes, 53° and −53°. In experiments, only one fracture plane is usually observed. This is caused by imperfections in the material which result in some preferred fracture orientation and is not modelled here. If the fracture angle is forced to be positive, only one fracture plane orientation will emerge (see Fig 3.12(c)). The algorithm and the subsequent damage evolution correctly predict the experimentally observed fracture plane inclination. The same geometry has been modelled using bigger elements (element volume is four times bigger). In Fig 3.12(d) it is demonstrated that a crack band of the same orientation is formed.

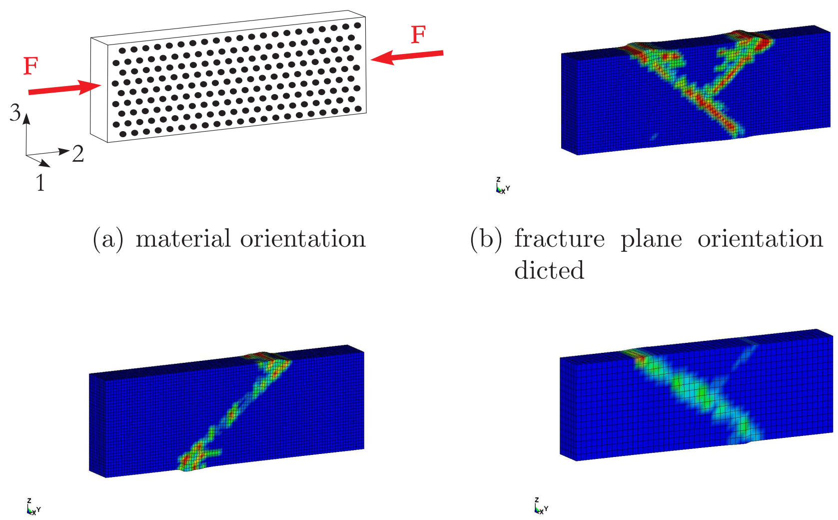

(a) material orientation

(b) fracture plane orientation as predicted

(c) fracture plane orientation fixed to 53°

(d) fracture plane orientation as predicted for the coarse mesh

Figure 3.12: Prediction of the fracture plane for uniaxial compression transverse to the fibres

3.8.3 Example3: modelling of kink band propagation

The kink band propagation is demonstrated similar to the transverse compression case as presented above. A single UD ply is modelled and subjected to uniaxial compression in fibre direction (see Fig 3.13(a)). Kink initiation is triggered by weaker elements on the edge of the modelled ply.

In Fig 3.13(b), Fig 3.13(c) and Fig 3.13(d) three different kink band angles ψ have been enforced while the propagation direction remained constant $\beta = 20°$. This example demonstrates the three dimensional nature of the proposed model. Once fibre kinking is predicted, the propagation continues in the plane as defined by ψ. The kink band inclination itself, however, β is not predicted by the model. Experimental results suggest [78] that β is not constant during the propagation. The model is not able to predict this. An attempt for predicting the inclination angle has been made in [4] where β developed as a consequence of stress degradation in the misalignment frame. It is not clear whether this corresponds to the physical process of kink propagation. More detailed micro-mechanical models are needed for the prediction of β. Within the modelling as proposed here the obtained level of accuracy is satisfying.

3.9 Summary

A model for damage evolution for general three dimensional states of stress has been introduced in this chapter. The emphasis was on novel physically based damage evolution laws which are driven by dissipation potentials on respective fracture planes. The dissipation potentials contain only stress terms which contribute to damage evolution and mainly base on the failure criteria as introduced in Chapter 2. The damage evolution and consequently energy dissipation is not driven by a subscribed function but is entirely given by the rate at which respective failure surfaces are exceeded. The material degradation due to damage growth is performed on the respective fracture planes thus enabling a physically based representation of the experimentally observed damage. Novel computational efficient

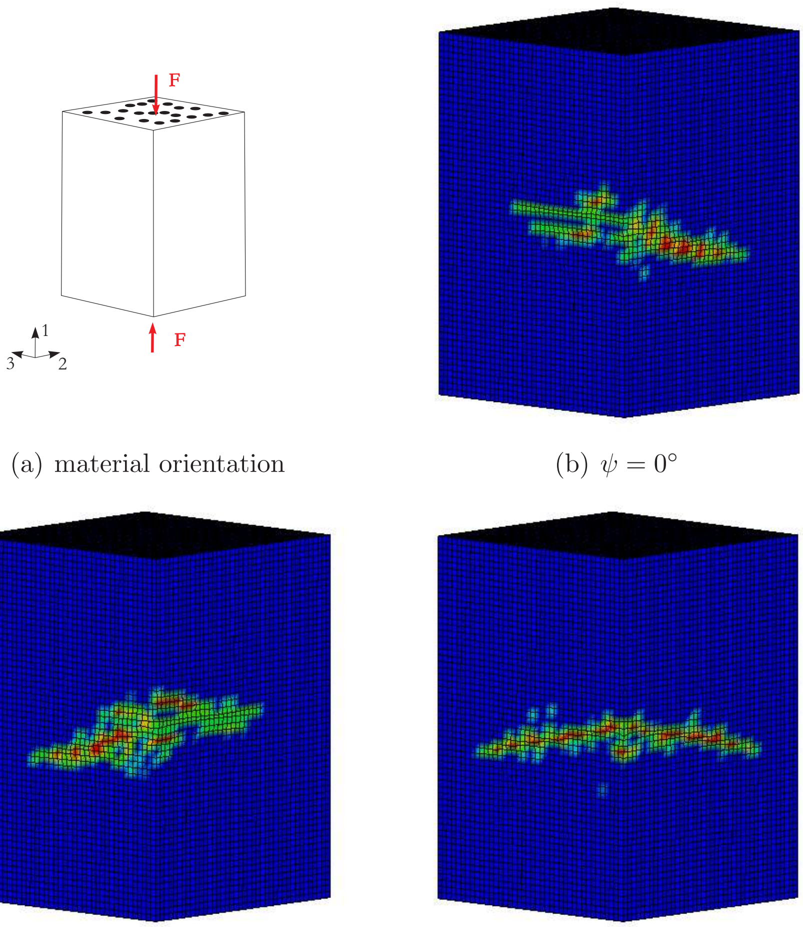

(a) material orientation (b) $\psi = 0°$

(c) $\psi = 90°$ (d) $\psi = 45°$

Figure 3.13: Prediction of a kink band for different kink band orientation

three dimensional single step stress return algorithms are employed to return inadmissable stress states back on the damaged failure surface. Furthermore, a calibration procedure is proposed which allows for less mesh sensitive energy dissipation. Therefore, a novel estimation of the cracked area within the RVE has been developed. The procedure relies on the projection of element space diagonals on respective fracture planes to give a damage mode dependent area estimation which helps to reduce mesh dependency of the energy dissipation in the framework of CDM.

The following chapter presents the experimental investigation of composite damage initiation. The focus is on the characterisation of rate dependent material behaviour, especially under compressive loading.

Chapter 4

Characterisation of strain rate dependent material behaviour

Strain rate dependent material behaviour is a well known phenomenon in composite materials. The mechanical properties of composites do not only change noticeably with the direction in which loading is applied, but also with the rate at which the loading is applied. The aim of this chapter is to introduce the experimental techniques for characterisation of strain rate dependent material properties and to investigate some of the phenomena which can be observed in the material behaviour as the loading rate increases.

In the past, many studies were dedicated to CFRP strain rate dependence. A literature review will introduce the experimental methodologies used to characterise rate dependency in composite materials and the results obtained in these studies. In the second part of the chapter, two laminates are experimentally investigated towards their rate dependent behaviour. The focus is thereby on the compressive behaviour in fibre direction and transverse to the fibres.

4.1 Introduction

The material response of composites is well known to be sensitive to the rate at which a displacement is applied. Intrinsic strain rate dependency has been widely studied for metals, but reliable data for fibre reinforced polymers is still rare and experimental scatter large. The major tendencies and a review of results have been published at several instances in [84, 85, 86]. In the following, the current state of research is introduced and discussed. In the first part of the introduction the available experimental approaches for determination of high strain rate material properties will be briefly introduced. The second part will then entirely focus on the obtained results.

4.1.1 Experimental methods for the determination of rate dependent material properties

Testing composite materials at high loading rates has a long history since this high performance engineering material finds it's application widely in the aerospace industry as well as in military applications. The largest part of available data, however, is derived from experiments at large scales such as impact experiments on composite structures. These experiments are usually performed with complex specimen geometries which involve complex stress states and do not easily allow for conclusions to be drawn about constitutive relations and intrinsic material properties. The assessment of rate dependency, however, relies on well controlled experiments such as uniaxial testing. The number of experiments performed on small specimen coupons subjected to uniaxial loading with varying strain rates is limited. In the following, experimental techniques commonly used to derive such data are briefly introduced. A more comprehensive review of available experimental techniques can be found in [87].

Hydraulic rigs

Hydraulic rigs are standard testing machines. A specimen is inserted between a rigid clamp and a crosshead which is moved by hydraulics thus generating either tensile or compressive load. Hydraulic testing rigs are commonly used for quasi-static and medium rate testing (up to $100s^{-1}$) where inertia effects and wave propagation are not important yet. The load is directly measured by calibrated load cells and deformation can be obtained by strain gauges or optical measurement systems such as lasers. The bulk of data in the medium rate domain is generated with hydraulic testing machines.

Drop towers

The drop weight impact test is a very flexible and inexpensive method of testing composites in compression at various rates of strain and can be widely found in research and industry. The principle of a drop weight testing apparatus is rather simple. A weight of known mass is dropped on a specimen from a certain height. The drop weight is usually instrumented with an accelerometer which allows the calculation of the force acting during impact, assuming the drop weight behaves as a rigid body. The setup is very sensitive to the contact conditions between the drop weight and specimen and suffers from noise due to ringing and vibration. In order to avoid load measurement based on accelerometers on the drop weight, some experimental setups rely on load cells mounted below the specimen, thus only measuring the transmitted force. This prevents signal filtering which often results in inaccurate results.

Split-Hopkinson bars

Split-Hopkinson bars (SHB) are commonly used for characterisation of high strain rate behaviour of materials. The technique relies on the measurement of elastic stress waves propagating in thin rods. The specimen is placed between two instrumented bars of known impedance. The bars are excited above their natural frequency (e.g. by a direct impact with a projectile) while monitoring elastic stress waves in the bars. The stress waves in the bars are transmitted into the specimen resulting in its deformation. One dimensional wave analysis can be used to calculate the specimen strain and force acting in the cross section. Split-Hopkinson bars can be used for tensile (Split-Hopkinson tension bar - SHTB), compressive (Split-Hopkinson pressure bar - SHPB) and torsional loading in strain rate regimes from $10^2 - 10^4 s^{-1}$. A more detailed description of the technique is given in Section 4.2. The disadvantage of SHB's is the relatively small specimen geometry (see Fig 4.2(a)). The specimen size is usually governed by the desired strain rate in the gauge section, inertia effects and achieving the mechanical equilibrium in the specimen during the experiment. For example, a relative short gauge section is required to achieve high strain rates and establish mechanical equilibrium quickly. For mechanical equilibrium to be established the stress wave needs to be reflected up to 4 times within the specimen [88]. This can be challenging as the usually low strain to failure (> 1%) results in a very short duration of the experiment (approx. 100 µs). Additionally, the specimen diameter is usually restricted by the diameter of the loading bars. This often results in questionable results as scale effects are very pronounced in composite materials which show quite large unit cells. Typical signals obtained from a SHB experiment are displayed in Fig 4.1. The data was taken from experiments performed for this thesis in Oxford.

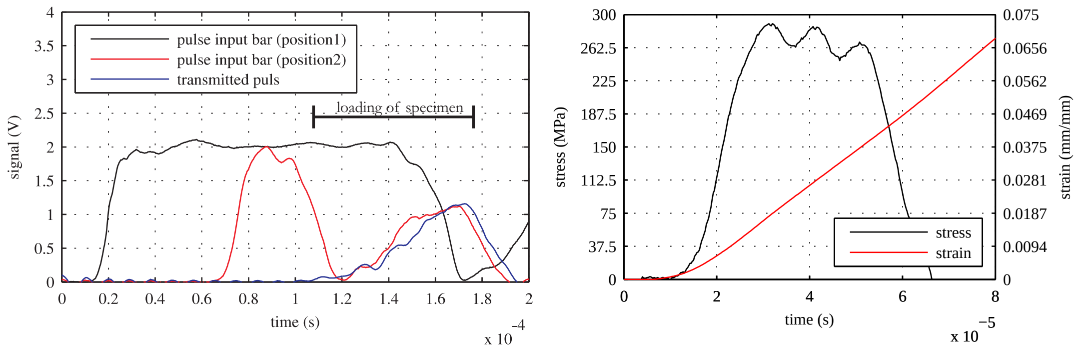

(a) signals obtained from SHB experiment (b) typical stress and strain history for SHB experiment

Figure 4.1: Specimen geometries commonly used for tensile testing in fibre direction

Pressurised rings

Daniel et.al. [89] proposed the expanding rig test as method of testing composites at high strain rates. A similar device is used by Almaliky and Parry [90] for high rate testing of polymers. Assembled in a special fixture, a specimen ring forms a reservoir which can be subjected with a shock wave. The shock wave is generated using an explosive charge and strain rates similar to SHPs can be achieved. Depending whether the liquid is pressurised inside or outside of the specimen ring, the material can be loaded in tension or compression (see Fig 4.2(b)). The strain is measured by means of strain gauges attached to the specimen and the load is calculated from the pressure in the liquid. The advantage of this method is the simple transmission of tensile load without issues of specimen clamping as often found in SHB's.

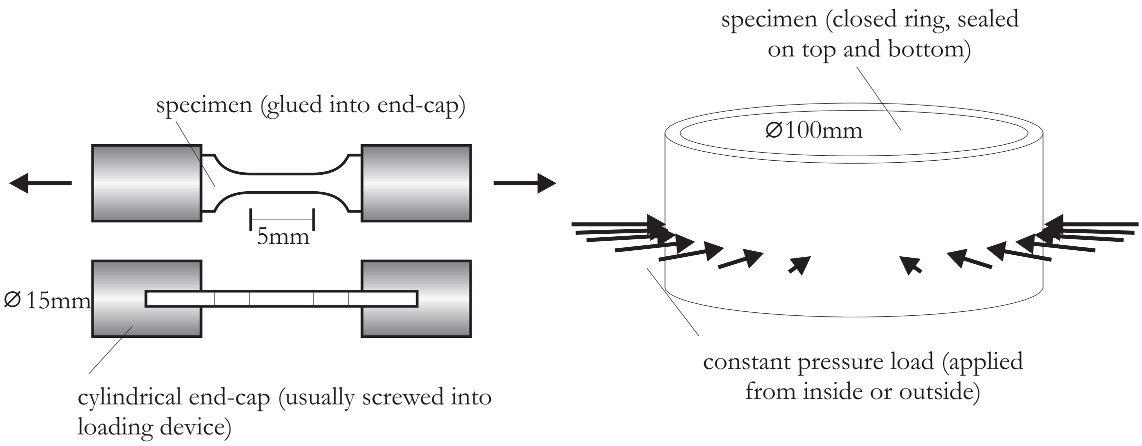

(a) uniaxial specimen for SHP (with typical dimensions)

(b) ring specimen (with typical dimensions)

Figure 4.2: Specimen geometries commonly used for tensile testing in fibre direction

In the following, rate dependent material data of neat epoxy resin and UD CFRP from literature is presented.

4.1.2 Influence of strain rate on the neat epoxy resin properties

Before available data for composite material is presented and discussed, results obtained from experiments with neat epoxy resin are investigated. The research community widely agrees that the strain rate dependent material behaviour in composite material is mainly caused by the viscous part of the viscoelastic behaviour of the matrix material. Few experimental data are available for epoxy resins and the relevant literature is mainly limited to compression experiments. The data presented here have been generated at the University of Oxford by Buckley et.al. [91] and by Gerlach et.al. [49]. Different epoxy resins have been tested at a range of different strain rates in compression and tension.

The difficulty with tensile experiments and epoxy resins is their brittle behaviour. The stress and strain at failure are usually very low, which results in difficulties to achieve mechanical equilibrium in the high strain rate experiments. This results in failure outside of the specimens gauge section. Additionally, the specimens show a high sensitivity to surface defects [49]. In order to obtain valid experimental data pulse shaping techniques and high quality surface finish such as polishing the specimens are required.

Buckley et.al. [91] investigated three different epoxy systems (CT200, PR500, Cycom 5250-4) at three different strain rates in compression and two different strain rates in tension. The yield stress was found to increase almost linearly with $\log \dot{\varepsilon}$. The assessment in the tensile loading regime proved to be more difficult. Only data at two strain rates was obtained. Many specimen showed failure outside of the gauge sections for the reasons as explained above. The yield stress showed only moderate rate dependency while the modulus rose by a factor of 4 from quasi-static to 2000 s^{-1}. The influence of temperature has been assessed in the experiments showing only modest rise of temperature in the specimen as loading is applied.

Gerlach et.al. [49] recently investigated RTM-6 epoxy covering a wider range of strain rates in tension and compression. Non linear behaviour of the resin was discovered in both tension and compression when plotted on a logarithmic scale. Modulus and yield stress initially rise linearly until about 100 s^{-1}. The slope of the rise increases quite dramatically at higher strain rates. Special care was taken to ensure mechanical equilibrium in the specimens and a good surface finish. The data showed only a small amount of scatter and failure was always observed in the gauge section.

The available data is normalised and compared in Fig 4.3 thus allowing to draw general conclusion of epoxy behaviour at different strain rates.

The yield stress data in compression is very consistent and indicates a moderate increase of approx. 40% from quasi static to 100 s^{-1}. At higher strain rates ($< 1000 s^{-1}$) the results show more scatter. Buckley et.al. reports a slightly lower increase of the properties than Gerlach et.al.. No modulus was reported from Buckley et.al. for compression. The Young's modulus reported from Gerlach et.al. showed a non-linear increase similar to the yield stress. The yield stress data provided in tension shows very different trends. Buckley et.al. reported problems with non valid failure modes, which might explain the significantly lower increase at higher strain rates. Gerlach et.al. covers more strain rates and shows a consistent non-linear increase of yield stress with rising strain rate. The reported increase of the Young's modulus is non-linear and similar in all presented data sets.

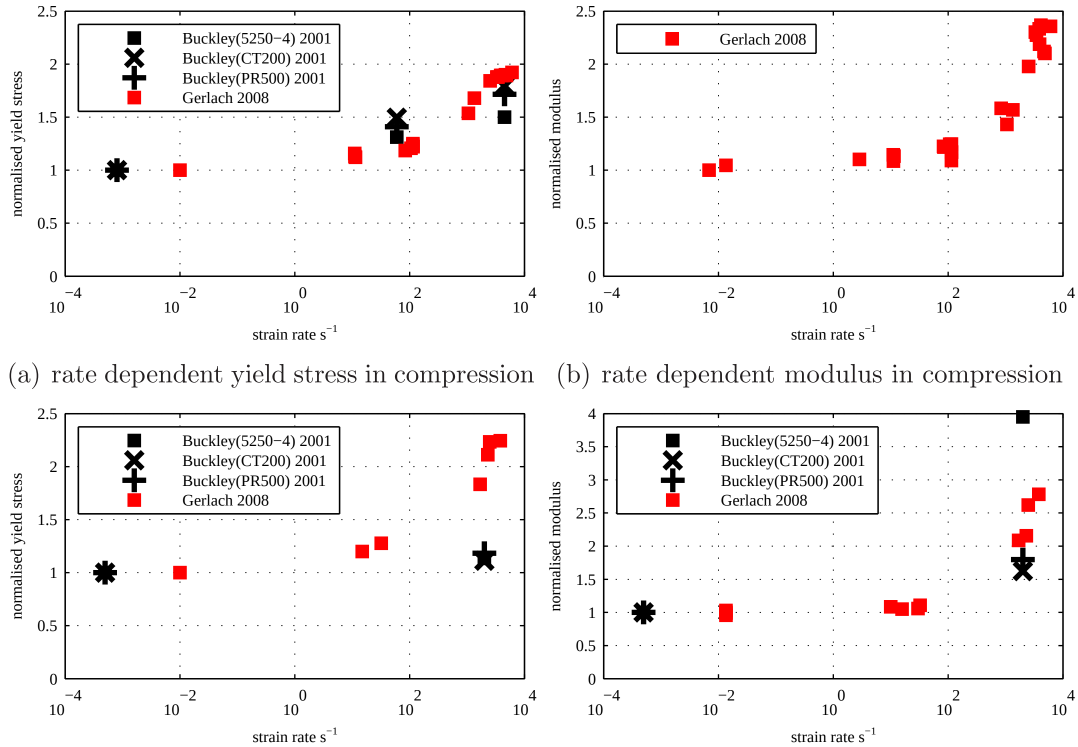

(a) rate dependent yield stress in compression (b) rate dependent modulus in compression

(c) rate dependent yield stress in tension (d) rate dependent modulus in tension

Figure 4.3: Rate dependent material properties of the neat epoxy resin in compression

Different epoxy resin will show different rate dependent behaviour. However, a certain similar pattern can be observed. Initially, the material properties do not seem to change dramatically. At a certain strain rate, which can be different for each epoxy resin, the moderate almost linear increase of properties switches to an exponential increase. All the epoxy resins, of which data are presented here, showed this behaviour.

4.1.3 Influence of strain rate on the tensile material properties in fibre direction

The behaviour of carbon fibre reinforced polymers under tensile load in fibre direction is widely regarded to be rate insensitive [94]. This makes sense as the influence of the matrix material, and subsequently the assumed cause of rate dependent material behaviour, is negligible in this material direction. Testing CFRP in fibre direction under tensile load poses difficulties. The main problems arise from introducing the high load into the specimen and reaching dynamic force equilibrium. Special load transmission approaches need to be employed to prevent pull out of the specimen and to break the actual fibres. This problem is very pronounced in standard dog-bone specimens (see Fig 4.2(a)). The axial load needs to be transferred from the clamping device into the fibres through the weak matrix which often results in pull out at low load levels. The alternative is testing of pressurised rings (see Fig 4.2(b)). Force transmission is not a problem for these experiments, however, the pressure load is usually generated by explosive charges in a liquid which make optical observation of the experiment more difficult.

First data was published by Daniel and Liber in 1976 [92]. UD CFRP coupons were tested at low and medium strain rates using a hydraulic machine. Daniel et.al. continued the investigation with a new testing approach which allows higher strain rates [93]. Composite rings were tested using pressurised liquid. Further studies were performed by Daniel et.al. in 1995 [89] with a similar experimental setup. Another set of data was published Harding et.al. who tested UD specimens in fibre direction [94, 95] using a SHTB.

The results showed no significant change of modulus or strength at medium strain rates. At higher strain rates the data shows more scatter, but the average suggests constant strength (see Fig 4.4(a)). The situation is slightly different for the modulus. At medium strain rate no increase was detected. At higher strain rates, the available data suggests a very mild rate sensitivity. Despite the scatter in the results a small increase is reported almost consistently. This is reasonable as the the Young's modulus of the resin increases rapidly at high strain rates. However, it is very difficult to give a set value of increase due to the scatter in the data.

4.1.4 Influence of strain rate on the compressive material properties in fibre direction

Unlike the tensile behaviour in fibre direction, the failure in compression is highly governed by the behaviour of the matrix and the interface between fibre and matrix. Therefore distinct rate dependency should be observable. The expected rate dependent behaviour resulted in more available data for this case. Relevant data has been found in [96, 89, 88,

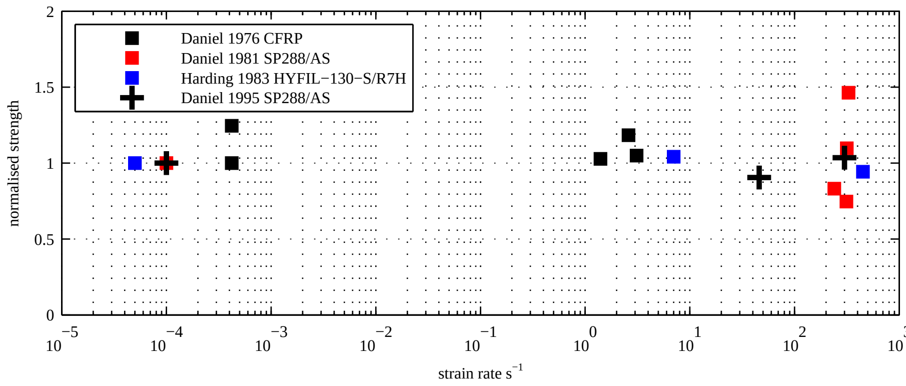

(a) rate dependent strength in tension

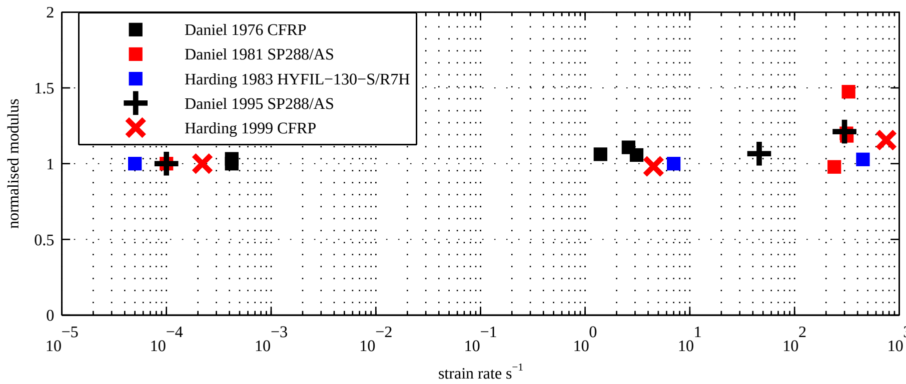

(b) rate dependent modulus in tension

Figure 4.4: Rate dependent material properties in fibre direction in tension

95, 97, 98, 99]. The published data suggests an increasing strength at strain rates above $1s^{-1}$ (see Fig 4.5). There is only very limited data available in the medium strain rate regime ($1s^{-1} - 100s^{-1}$). The few available data points suggest only a mild increase of strength. The scatter in the high strain rate data, however, is substantial. The increase in strength is between 10 to 80%.

The large scatter in the available strength data can have various reasons. An explanation of the scatter would be the present failure mode. As explained in Chapter 2, specimens fail due to various failure modes in compression. Many of the observed failure modes are not representative for the material, but an artefact of the specimen geometry. Assessment of the results requires therefore an accurate observation of the failure mode. As this poses no difficulty in quasi static tests (test can be interrupted) it is significantly more difficult in high rate experiments. The available data is normalised and plotted in Fig 4.5.

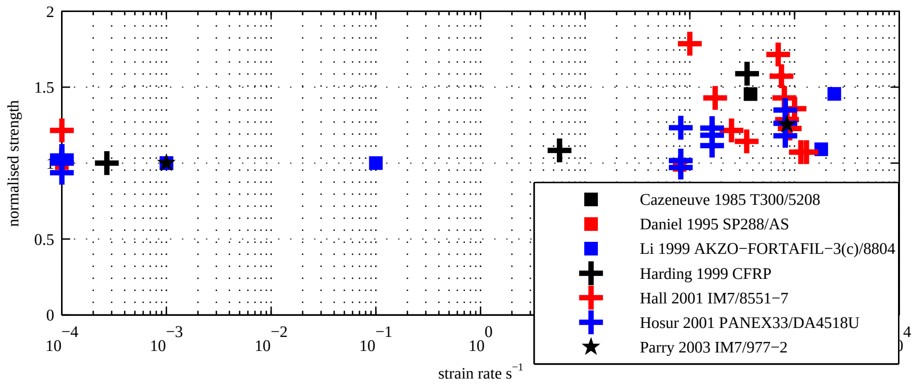

(a) rate dependent strength in compression

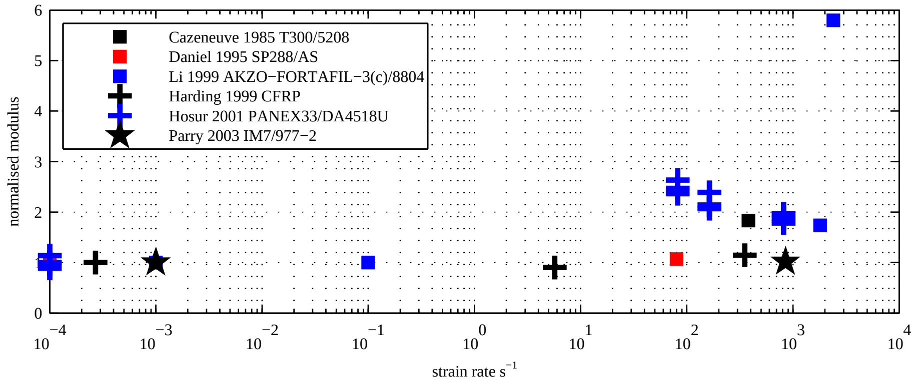

(b) rate dependent modulus in compression

Figure 4.5: Rate dependent material properties in fibre direction in compression

Hall and Guden [97] proposed inserting steel rings parallel to the specimen in SHPB's. This stops the deformation after a certain displacement of the bars. The specimens do not get crushed entirely and can be examined afterwards. Hall and Guden found fibre splitting and kinking failure modes in his experiments. Hosur et.al. [98] used a modified SHPB setup to stop loading at certain levels of deformation. By attaching an additional reaction mass, the compressive pulse supplied by the collision of striker bar and input bar is cut after a certain time. This allowed for investigation of the failure mode. Reported failure modes vary from delamination to splitting and crushing. Bing and Sun [100] reported the strength in off axis tests (off axis angle $5-65°$). Different strength was observed for varying failure modes. Depending on whether the specimens where coated on the contact surfaces, failure occurred by either matrix shear along the fibres or by microbuckling. Unfortunately, failure modes are only reported for strain rates below $1s^{-1}$.

All approaches described above suffer from the limitation that only certain states of damage can be frozen rather than monitoring the damage evolution. A consequent characterisation of the present failure modes and correlation with obtained strength values would require recording of such experiments with high speed cameras. The experiments should be designed such that the failure mode is reproducible and the failure initiation is well observed by high speed photography.

The data for the modulus are very coherent for strain rates up to approx. $100s^{-1}$. At strain rates beyond that the data are not conclusive. Some researchers suggest no rate dependency [89, 95, 99] while others found significant increase [96, 88, 98]. The discrepancies might be caused by the difficulties in obtaining the deformation in high strain rate experiments. Valid data are only obtained if the specimen is in equilibrium from an early stage of the experiment. The quite low strain to failure makes this a difficult task.

4.1.5 Influence of strain rate on the tensile material properties transverse to the fibres

The following section presents the published date for rate dependent behaviour transverse to the fibre direction. The amount of transverse tensile data is significantly higher compared to longitudinal tensile data. This is mainly caused by the reduced problems in force transmission in the specimen. Since the transverse tensile strength is very low compared to the fibre strength, specimen clamping is not an issue. However, establishing dynamic equilibrium is still a difficult task as specimens usually fail at small strain.

Experimental results for tensile loading transverse to the fibres has been reported in [92, 93, 89, 101, 95, 102, 103]. The obtained results are normalised and illustrated in Fig 4.6. For comparison, the data as obtained for the neat RTM6 resin is included in Fig 4.6.

The available data can be divided in two major groups. The first group found significant strain rate effects while the second group reported non or only mild rate dependent behaviour. The data in the first group was reported by Daniel et.al. in 1981 [93] and 1995 [89]. The data was obtained by testing composite rings with a pressurised liquid and seem

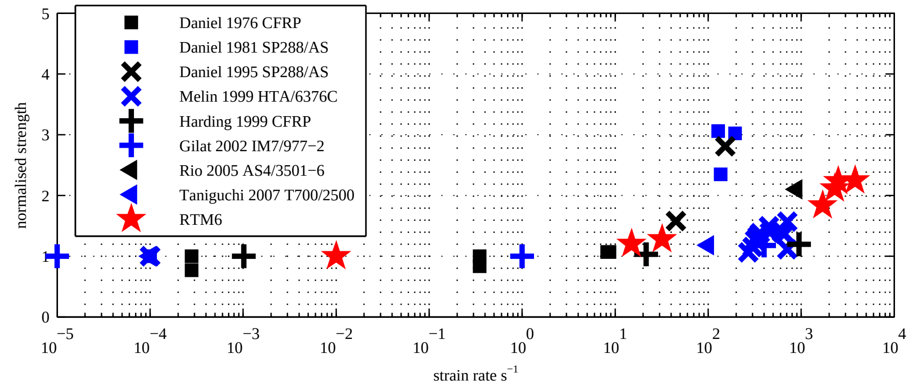

(a) rate dependent strength in tension

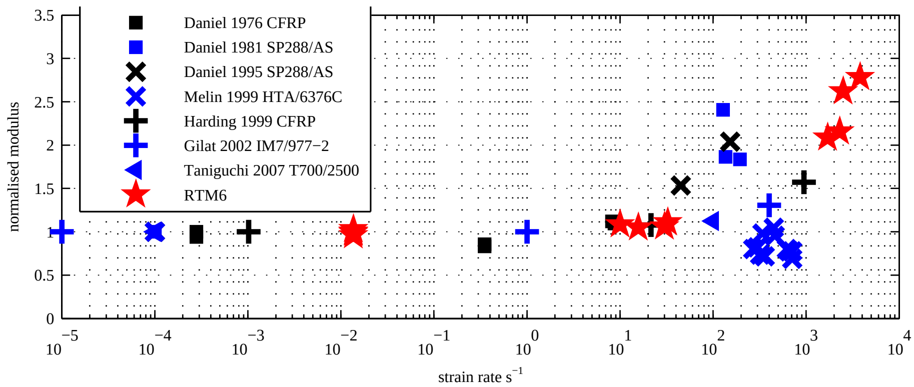

(b) rate dependent modulus in tension

Figure 4.6: Rate dependent material properties transverse to the fibre in tension

quite consistent. The other group consists of data published by various researchers who reported the results independently from each other (Melin and Asp [101], Harding [95], Gilat et.al. [102], Rio et.al. [104] and Taniguchi et.al. [103]. All results have been obtained by testing in a SHTB using flat specimens. The reported strength properties seem to be relatively consistent while great differences were reported for the modulus.

The obtained results seem to strongly depend on the testing method or specimen geometry. Especially the specimen size can introduce inertia effects into the results. Similar to neat epoxy resin, the composite in the transverse direction shows a very brittle response and low failure strains (e.g. strain at failure of less than 1 %). It is therefore quite difficult to establish mechanical equilibrium because the strength of the material is very low. Furthermore, the experimentally obtained strength will be very sensitive to the surface finish.

Daniel's experimental approach uses thin composite rings with an diameter of approx. 100 mm. Mechanical equilibrium should be established rather rapidly as the whole ring expands under evenly distributed pressure. Despite the quite large specimen size, this experimental approach should not be very sensitive to inertia effects as no significant mass is moved when the ring expands. The whole experimental setup is placed within a containment system as the pressure load is generated by an explosive charge. This makes a direct observation of the experiment very difficult and measurement consequently entirely relies on strain gauge readings.

The SHTB experiments are very sensitive to specimen geometry and specimen preparation. A smooth transmission of the stress wave into the specimen needs to be guaranteed in order to minimise wave reflections. In order to obtain mechanical equilibrium, the stress wave will have to travel 4 times back an fourth in the specimen [88]. This requires short specimens in order to ensure mechanical equilibrium in the specimen early on in the experiment. Not having established equilibrium will render invalid the stiffness measurement. Typical specimens show a parallel gauge section of less than 10 mm and specimen width of approx. 10 mm. The calculation of stress and strain requires a failure within the gauge section. Ideally, the experiment should be recorded using high speed photography to ensure a valid failure mode. As mentioned earlier, the brittle nature of the material makes the experimental results very sensitive to the surface finish as small surface imperfections and initial cracks result in much lower strength properties.

For comparison, the data for neat RTM6 resin [49] is added to the charts in Fig 4.6. The material behaviour in the transverse direction is greatly affected by matrix. It is therefore reasonable to expect similar behaviour as in neat epoxy resin. However, the interface between fibre and matrix might influence the properties too.

The comparison clearly demonstrates that the high strain rate data obtained from pressurised rings is much higher for both strength and modulus. The trends as obtained from data given by Daniel et.al. agrees well with the data obtained from RTM6. The exponential rise of properties, however, seems to happen at lower strain rates compared to

RTM6. This might be due to the properties of the epoxy resin used for the investigated composite.

The strength data obtained from the SHTB experiments varies significantly. The reported values are similar [104, 103] or lower [101, 95, 102] then the RTM6 data. The modulus values reported in [95, 102, 103] agree with the resin data. The reported rate insensitive modulus by Melin and Asp seems unreasonable and might be due to difficulties in establishing mechanical equilibrium.

The available data indicates that the transverse strength and modulus shows a similar behaviour as neat epoxy resin. However, further investigation should clarify whether the strength of the composite is slightly less rate sensitive due to the fibre matrix interface. In the absence of experimental data it seems reasonable to use assume a similar rate dependency as observed in neat RTM6.

4.1.6 Influence of strain rate on the compressive material properties transverse to the fibres

Data for UD reinforced CFRP loaded in transverse direction under compression has been published in several instances [96, 89, 95, 98, 99]. As the composite behaviour is mainly governed by the resin in the transverse direction, the literature data for neat RTM6 epoxy resin [49] is given as comparison. The comparison is displayed in Fig 4.7. Similar to the previous section, the reported data is normalised.

The reported strength properties agree very well with the neat resin data for lower strain rates. For higher strain rates, the experimental scatter is significantly higher. However, the mean value seems to follow a similar trend as the neat epoxy. The data presented by Harding [95] seems to be unreasonably high and is not supported by any other study. The reported data for the modulus agrees quite well with the neat epoxy resin data. A similar trend becomes apparent from Fig 4.7(b). The modulus reported by Parry and Al-Hazmi [99] seems to be unrealistically low.

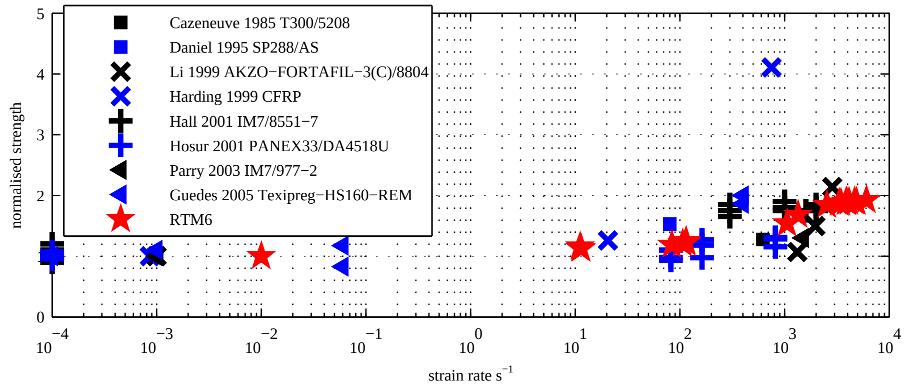

(a) rate dependent strength in compression

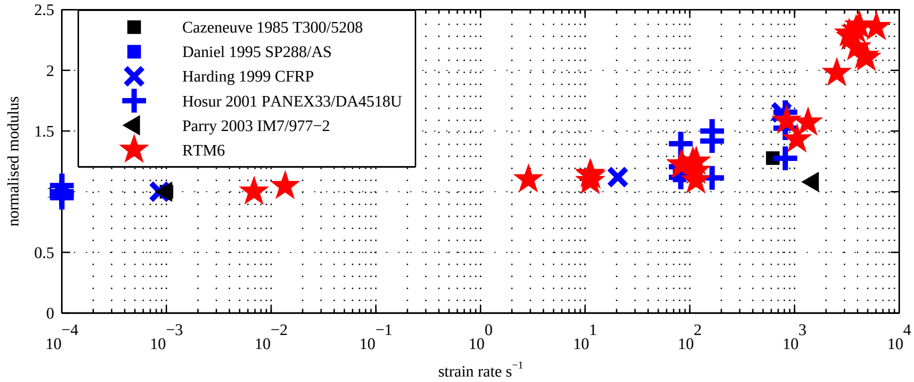

(b) rate dependent modulus in compression

Figure 4.7: Rate dependent material properties transverse to the fibre in compression

Failure in transverse compression is a shear failure mode of the matrix. In quasi-static experiments an inclined fracture plane is observed (see Chapter 2). It is quite obvious that this failure mode depends not only on the matrix but on the fibre matrix interface as well. The resistance against this matrix shear failure is governed by the fibre volume fraction and probably by the way the composite is manufactured (prepreg, RTM). The argument is supported by the large scatter of reported fracture plane inclinations in quasi-static experiments [3]. In high strain rate experiments, this might result in varying rate dependent behaviour because the crack cannot find the path of lowest resistance but is forced to grow in the direction of initial orientation. This requires a study of the observed fracture plane inclination. So far, the compressive failure mode at higher strain rates has only been described by Hosur et.al. [98]. Drawings of the observed shear failure are presented, but no measurement of the fracture angle and the scatter of observed angles is presented.

The data available in literature suggests that using neat resin data for the rate dependency transverse to the fibre under compression is a reasonable choice. The failure mode, however, needs to be characterised at varying loading rates, as no data is available in literature.

4.1.7 Influence of strain rate on the in-plane and out-of-plane shear properties

In general, the composite shear behaviour is distinguished into intralaminar shear and interlaminar shear. Intralaminar shear is related to the shear deformation of the UD-ply itself while interlaminar shear occurs in the through-thickness direction and is usually governed by the interface between adjacent plies.

Intralaminar shear

The in-plane shear behaviour of composites is highly non-linear and mainly matrix governed. In-plane shear tests can be performed by loading UD or cross ply specimens 45° to the fibre orientation. The change of material properties due to varying loading rates has been described in several occasions [92, 93, 89, 95, 102, 103]. All reported results show an increase of both, strength and modulus.

The scatter of reported strength values rises with strain rate. On average, the data suggests a linear increase with the exception of Taniguchi et.al [103] who reported a significant rise of strength at high strain rates. The reported values of the modulus are more consistent than the strength values. The modulus seems to increase linear with $\log \dot{\varepsilon}$. The amount of scatter in the reported results is much lower compared to the strength values. The data is displayed in Fig 4.8.

Interlaminar shear

Several attempts have been made to determine the interlaminar shear strength (ILSS) for laminated composites at impact rates of strain [50, 51, 52]. A major problem, even at quasi-static loading rates, is to design a test in which interlaminar failure occurs under a state of pure shear, i.e., where the shear stress on the interlaminar failure plane is relatively

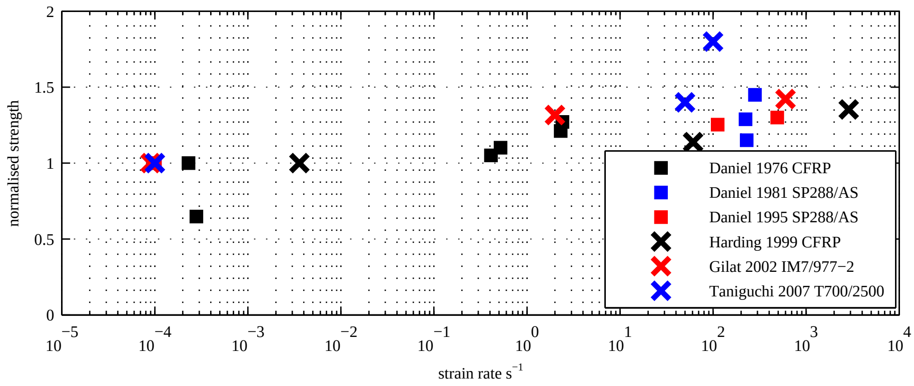

(a) rate dependent in-plane shear strength

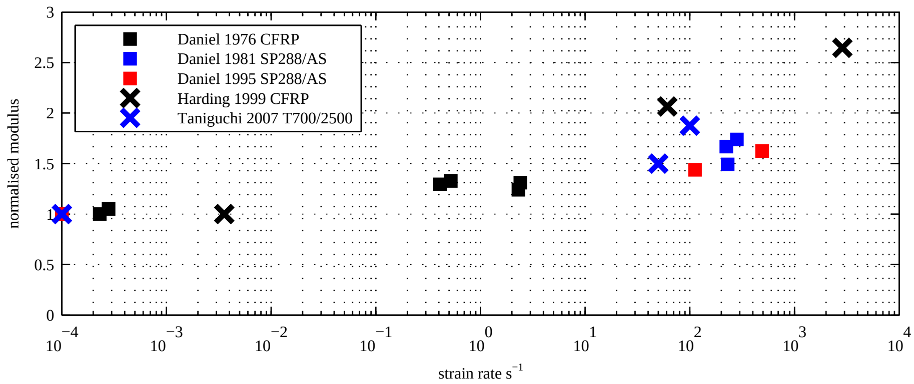

(b) rate dependent in-plane shear modulus

Figure 4.8: Rate dependent material properties in-plane shear

uniform and the normal (tensile) stress is relatively small. The requirement of mechanical equilibrium in the specimen at higher shear strain rates puts additional restrictions on the specimen design. This prevents the use of some of the more successful specimen geometries, such as the Iosipescu specimen [105], which have been developed for quasi-static loading only.

Bouette et.al. [50] and Yokoyama and Nakai [52] performed out-of-plane shear test with SHPB's and double notch specimens (see Fig 4.9(b)). Dong and Harding [51] performed similar experiments with a z-shape specimen (see Fig 4.9(a)). Both specimen geometries suffer from non constant shear stresses in the gauge length. FE analysis has been performed to optimise the geometry in favor of a better shear stress distribution within the gauge section.

The experiments with the DNS specimen reported no rate dependency for the strength

The figure originally presented here cannot be made available via ORA for copyright reasons.

The figure originally presented here cannot be made available via ORA for copyright reasons.

(a) Z specimen geometry used by Dong and Harding [51]

(b) DNS specimen geometry used by Bouette et.al. [50] and by Yokoyama and Nakai [52]

Figure 4.9: Specimen geometries for out-of-plane shear testing

properties. Dong and Harding found only a very small increase of strength (10%) at high strain rates. The data is illustrated in Fig 4.10. The shear modulus was only reported by Bouette et.al. who did not observe any rate dependency.

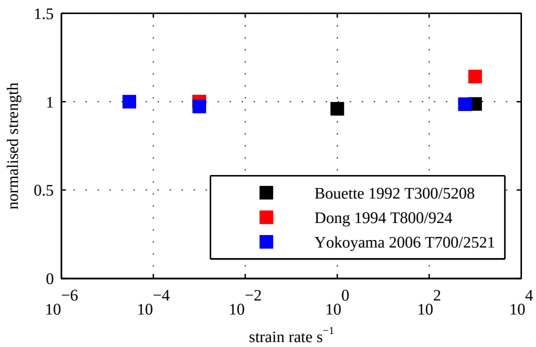

Figure 4.10: Rate dependent UD material properties for out-of-plane shear

Additionally to UD material Dong and Harding investigated a ±45° laminate using the same specimen geometry. A clear rate dependency was reported for the strength. The strength increased by 50% was reported from static to high rate loading.

Only very little data is currently available for the characterisation of the ILSS at varying rates of strain. The reported trends suggest no rate dependency for out-of-plane shear. This is somewhat surprising, as this failure mode mainly involves deformation of matrix. However, the shear strength is rather governed by the interface fibre-matrix than the strength of the resin. More experimental evidence is needed, including a study on the influence of fibre orientation on the out of plane properties. As Dong and Harding have demonstrated, the rate dependency seems to be highly influenced by the fibre orientation on the ply interface.

The previous part of the chapter gave an introduction into experimental technique for strain rate testing. Furthermore, available results in literature were summarised and discussed. In the following, the experimental procedures used in the thesis are introduced in more detail and the obtained experimental results are presented. The focus of the experimental program is on the compressive material behaviour with special emphasis on the characterisation of the observable failure modes.

4.2 Experimental technique for material characterisation at different loading rates

The very limited access to material within this work did not allow for the desired full material characterisation program. Therefore, the focus is on loading conditions for which no satisfactory published data is available. The rate dependency transverse to the fibre under compressive load is investigated for a UD laminate. Furthermore, a cross ply laminate is tested under compressive load.

Digital high speed photography enables the investigation of the observed failure modes and their changes due to varying loading rates. This section describes the applied experimental methods and measurement techniques.

Measurement of intrinsic material properties such as strength and stiffness at different loading rates requires three different loading devices. In order to compare the results between the loading rates, the specimen geometry, clamping and acquired data must be similar to ensure that the only difference between the obtained results is the rate at which loading is applied. The specimen design is thereby mainly governed by the high strain rate experiments where inertia effects must be minimised and mechanical equilibrium must be reached early in the experiment. The experimental setups, as used here, are introduced below.

4.2.1 Loading devices and measurement systems

For quasi-static loading a standard screw driven testing machine is used. The load is measured by calibrated load cells and displacement is measured by a high precision laser extensometer (by Fiedler Optoelektronik, resolution 0.1 µm). The laser extensometer monitors the position of white markers attached to the gauge section of the specimen thus allowing for an accurate strain measurement.

Medium rate experiments ($1s^{-1}$ to $100s^{-1}$) are performed on a hydraulic machine. The specimen is inserted between a fixed bar and a piston. The piston can be accelerated to a constant speed by hydraulic oil thus loading the specimen. A control unit allows adjustment of piston stroke length and time interval and consequently loading velocity and strain rate within the specimens gauge section. The loading rate is still sufficiently small for wave effects to be ignored. This enables load measurement by a strain gauge which is attached to a bar fixed to the hydraulic rig. The strain gauge signals are converted into a force by an experimentally obtained conversion factor. Deformation measurement is more complicated for medium rate experiments. In the past, LVDT sensors have been positioned parallel to the specimen to measure extension. This extension measurement, however, includes the compliance of the whole fixture and the specimen. Strain data obtained from LVDT's can therefore not be compared directly to quasi-static experiments where strain is obtained directly from within the gauge section. All experiments where recorded using a digital high speed camera. This enabled optical deformation measurement by image analysis. The applied techniques are described in Section 4.2.2.

The mechanical properties at strain rates beyond 10^2s^{-1} are measured with a Split-Hopkinson pressure bar (SHPB). The principle of applying rapid loading by stress waves in thin bars dates back to Hopkinson who performed the first experiment of that kind in 1914 [106]. The propagation of waves in bars was investigated by Davies in 1948 [107] .The first split Hopkinson bar has later been developed by Kolsky in 1949 [108]. The technique has been used widely for high strain rate experiments since the 70's [87] and became a standard measurement device. A general description of the technique can be found in

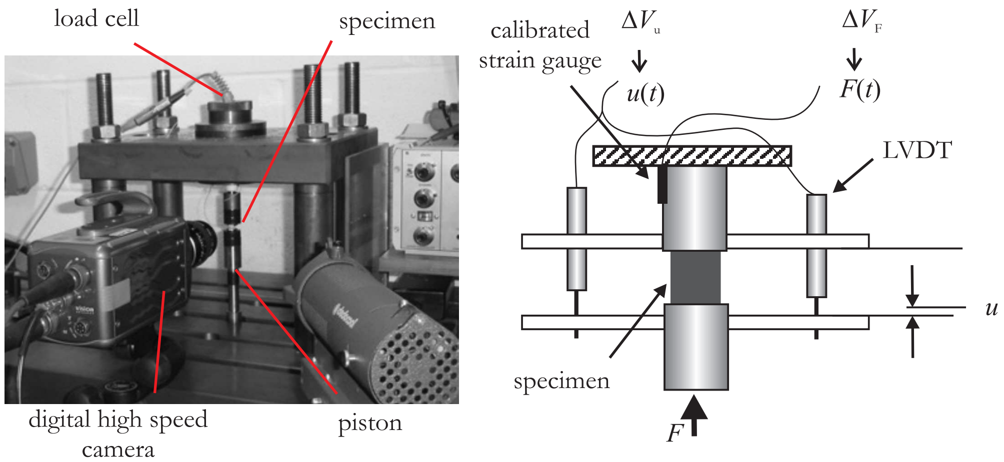

(a) experimental setup for medium strain rates (with high speed camera)

(b) experimental setup for medium strain rates (extension measured with LVDT's)

Figure 4.11: Experimental setup for medium strain rate testing

[109].

A projectile is accelerated by gas gun and collides with an instrumented bar of identical impedance, the input bar (or incident bar). The generated stress wave (α-wave) travels along the input bar and is measured by two sets of strain gauges. The specimen is mounted between the input bar and an output bar (or inertia bar) which is free to move. Due to the mismatch of impedance between input bar and specimen, part of the stress wave is reflected back (β-wave) into the input bar by the bar-specimen interface. Having attached two strain gauges to the input bar allows for the calculation of the reflected β stress wave even though it overlaps with the α-wave. Part of the α-wave is transmitted into the specimen which starts to deform. The output bar is also instrumented with a strain gauge thus enabling measurement of the force transmitted by the specimen.

All strain gauges are connected in Wheatstone bridge circuits and have been calibrated allowing for a conversion of the obtained signals into force history data. The device is designed such that only small strains occur in the loading bars and the bar material remains elastic. Knowing the elastic properties of the bar material and the bar geometry enables

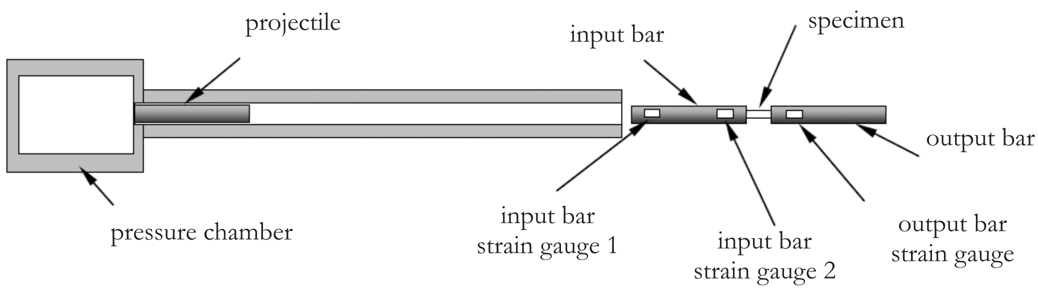

(a) Split-Hopkinson pressure bar schematic

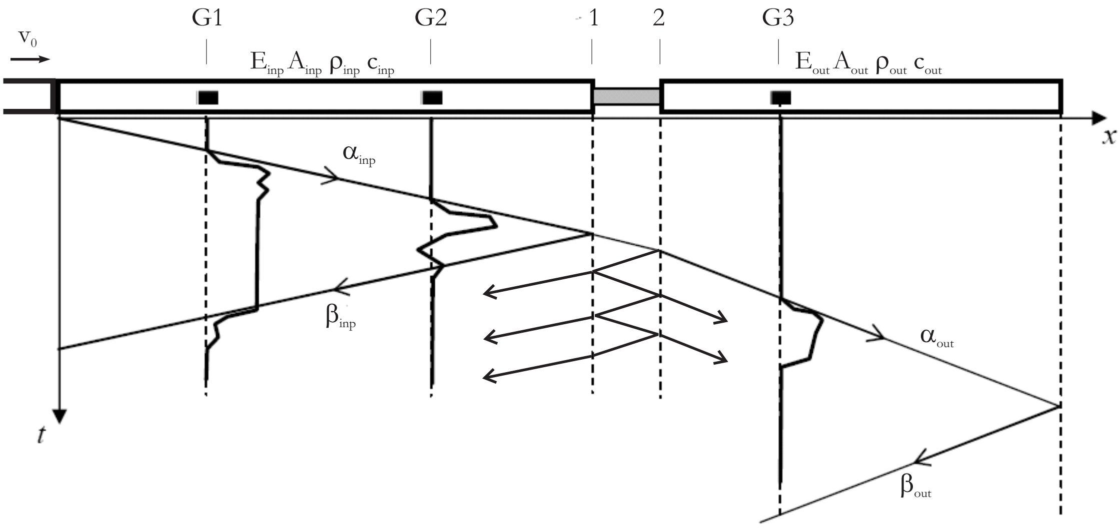

(b) Langrange chart of wave propagation in SHPB

Figure 4.12: Principle of SHPB's

to calculate the stress history data at the strain gauges.

$$
\begin{aligned}
\sigma(G1,t) =& \frac{F(G1,t)}{A_{inp}} \\
\sigma(G2,t) =& \frac{F(G2,t)}{A_{inp}} \\
\sigma(G3,t) =& \frac{F(G3,t)}{A_{out}}
\end{aligned}
\tag{4.1}
$$

The stress in the bars consists of α and β stress waves which are travelling in opposite directions at the materials wave speed c. One dimensional wave analysis can be employed to calculate the stress waves at any time and any position in the input and output bar from the strain gauge signals thus allowing calculation of $\alpha_{inp}(x,t)$, $\beta_{inp}(x,t)$, $\alpha_{out}(x,t)$ and $\beta_{out}(x,t)$. It should be noted that the use of one dimensional analysis makes the assumption of a constant stress over the cross section of the bar and neglects Poisson's effects. Despite these simplifications the one-dimensional wave analysis is valid for thin rods. The specimen fails before any wave reflections are present on the strain gauge readings of the output bar so that the magnitude of β_{out} is not needed for analysis.

The stress at the bar interfaces to the specimen (position 1 and 2 in Fig 4.12(b)) is then given by

$$\begin{aligned} \sigma(1,t) = \sigma_{inp} =& \alpha_{inp}(1,t) + \beta_{inp}(1,t) \\ \sigma(2,t) = \sigma_{out} =& \alpha_{out}(2,t) \end{aligned} \tag{4.2}$$

Analogously the particle velocity v is given by

$$\begin{aligned} v(1,t) = v_{inp} =& \frac{\alpha_{inp}(1,t) - \beta_{inp}(1,t)}{\rho_{inp} c_{inp}} \\ v(2,t) = v_{out} =& \frac{\alpha_{out}(1,t)}{\rho_{out} c_{out}} \end{aligned} \tag{4.3}$$

with ρ being the materials density. The material constants ρ and c are used to calculate the characteristic acoustic impedance

$$Z_0 = \rho c \tag{4.4}$$

which is an important parameter to characterise the wave propagation in different materials. Integrating v gives the displacement

$$\begin{aligned} u_{inp} &= \int v_{inp} dt \\ u_{out} &= \int v_{out} dt \end{aligned} \tag{4.5}$$

which then allows for calculation of the specimen extension

$$\Delta u = u_{inp} - u_{out}. \tag{4.6}$$

This is used to calculate the specimen strain assuming that all deformation is localised in the specimens gauge section.

When the stress at the two specimen-bar interfaces is the same, the specimen can be

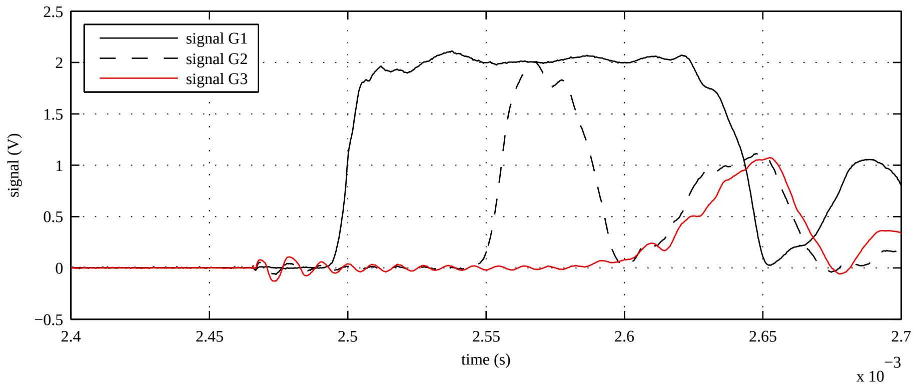

(a) strain gauge data

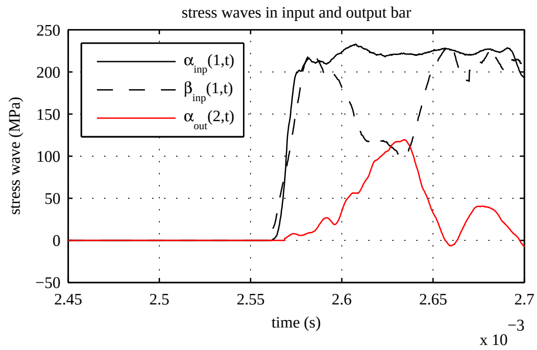

(b) stress waves in the bars

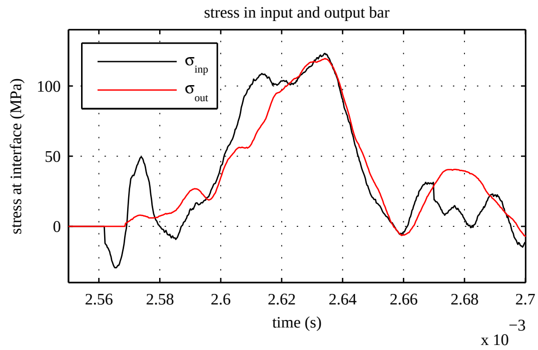

(c) stress at interface input bar-specimen and specimen-output bar

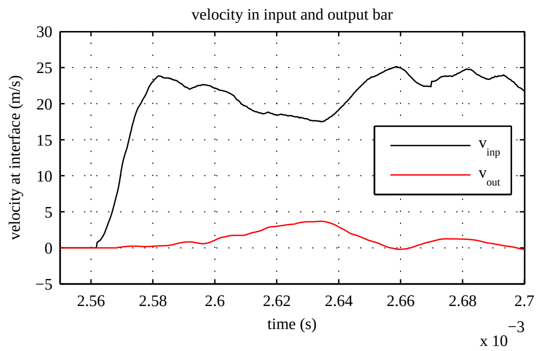

(d) velocity at the bar ends

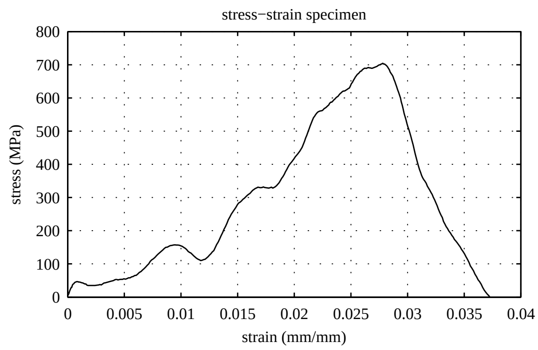

(e) stress-strain curve of the specimen

Figure 4.13: Wave analysis of SHPB

assumed to be in mechanical equilibrium, meaning that a constant force is acting in all cross sections of the specimen. This permits the assumption that the force acting on the end of the bars is equal to the force acting in the gauge section and enables calculation of the stress which is acting in the gauge section. The assessment of mechanical equilibrium is very important for brittle materials as the strain to failure is usually very low. A discussion of the issues related to establishment of mechanical equilibrium can be found in [88] and [110]. For composite materials it has found that usually 3 to 4 stress wave reflections are needed to establish mechanical equilibrium in the specimen. The time to establish equilibrium is therefore dependent on the length of the specimen as well as the material's wave speed.

All experiments are recorded by digital photography. Three different digital cameras were used. The quasi static experiments were recorded with high resolution standard digital cameras which record up to 1Hz at a resolution of 5 megapixel. The medium rate experiments were recorded with a digital Phantom IV high speed camera. This camera has a trade off between resolution and acquisition rate. The experiments were therefore recorded at a frame rate of 40000 frames per second at a resolution of approx. 500x120 pixels. A ultra high speed camera (Cordin 550) was used for the experiments performed on the SHPB. The camera is able to record a total of 64 frames with a resolution of 1 megapixel at frame rates up to 4 million frames per second. The following section describes how these digital images were used to enhance data analysis.

4.2.2 Deformation measurement by image analysis

The use of digital photography enables the application of novel, non contact, measurement techniques. Within this study Digital Speckle Photography (DSP) was used for image analysis.

DSP is a displacement measuring technique which relies on tracking of unique features on a series of images. The unique features can be either certain geometric shapes which occur only once on an image or random patterns such as speckle. The position of such template feature is tracked on every image by an FFT based cross correlation algorithm. If the timing of the images and the size of each pixel is known, the displacement of that feature can be obtained. When applied to speckle patterns, the region of interest on the image is usually divided in a regular mesh of patches. Each patch is tracked independently allowing for a full field displacement measurement. For a more detailed description of the method the reader is referred to [111, 87] and [112]. It should be noted that the technique is sometimes referred to as Particle Image Velocimetry (PIV). The principle of both techniques is very similar, only that PIV is used to track particles in a fluid or soil.

Within this thesis, two different software packages were used. First, a Matlab based in house developed package and secondly, the Matlab based software GeoPIV developed at the Cambridge University Engineering Department [111]. Both packages rely on FFT based cross correlation with subpixel accuracy and have been verified.

In this section DSP is applied to the measurement of specimen strain in the gauge section. In a later section, DSP will be applied to track the position of rigid objects during impact experiments.

4.2.2.1 DSP based strain measurement

The accurate measurement of strain is still a challenge in uniaxial experiments at elevated loading rates. Commonly used measurement techniques like laser extensometers, LVDT's or strain gauges are often not suitable due to the required data acquisition rates, because of reliability or due to inertia restrictions. The consequent use of standard digital photography, high speed photography and ultra high speed photography in the experimental setup enables the use of non contact DSP image analysis to measure strain (medium rate experiments) or to verify strain measurement (high rate experiments).

For the determination of rate dependent material properties it is crucial that the strain measurements in each experimental setup are comparable. This requires for the strain to include only the deformation of the gauge section and not the entire specimen fixture. The investigation of strain rate dependence requires material testing at different loading devices with different data acquisition systems. Deformation measurement by image analysis represents a convenient way of ensuring that strain is measured in the relevant part of the specimens, the gauge section in all experimental setups. As baseline strain measurement the high precision laser extensometer (resolution 0.1 µm) fitted to the quasi static experimental setup is used. This allows for strain measurement in the gauge section by monitoring the position of reflecting markers. A similar strain measurement can be obtained by DSP. A speckle pattern is applied to the specimen surface by the use of an airbrush device. Patches on both ends of the gauge section are then tracked on all recorded images. This results in a gauge section strain measurement similar to the laser extensometer. For verification purpose, a strain measurement obtained from the laser extensometer is compared with strain obtained by DSP from digital images taken at the same time. The comparison is shown in Fig 4.14(a) and confirms that the DSP technique can be used to obtain reliable measurement of strain.

In the past, strain was measured by LVDT's in medium strain rate experiments. This had the disadvantage that strain was not obtained in the gauge section only, but of the whole specimen fixture. Furthermore, the inertia of the LVDT's caused oscillations on the obtained signals. For this reason, the strain is measured by DSP only. This allows a comparable strain measurement between quasi static and medium rate experiments.

In the high rate experimental setup, strain is calculated from the displacement of the two ends of the loading bars between which the specimen is positioned. A comparable strain measurement would require a direct strain measurement in the gauge section. Unfortunately, ultra high speed cameras do not record enough images to entirely obtain strain by DSP analysis. However, the few available images enable the verification of the strain as obtained from the wave analysis and, if required, a correction of it. An example of a verified strain measurement from the wave analysis is shown in Fig 4.14(b).

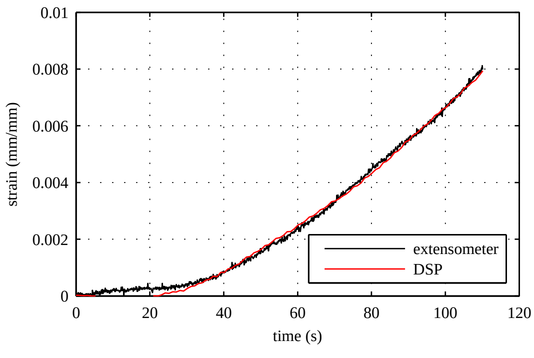

(a) verification of DSP in a quasi static experiment

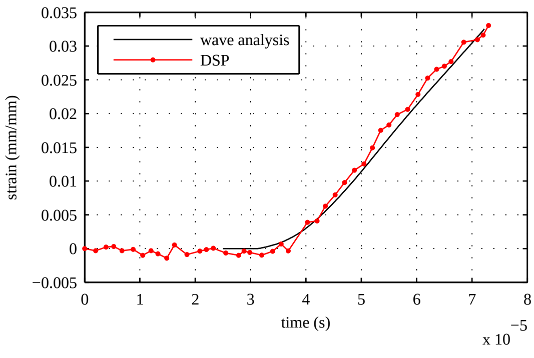

(b) verification of strain in a Hopkinson bar analysis

Figure 4.14: Strain measurement by DSP

4.2.2.2 Detection of bending in compression experiments

Depending on the specimen geometry, bending can be a serious problem in uniaxial compression tests. Especially thin and long specimen geometries are prone to bending and subsequent failure due to buckling. This instability failure mode is a consequence of the specimen geometry and does not allow for the determination of intrinsic material properties. Therefore, it is essential to assess if and how much bending is present in the compression experiments. The most common way of bending assessment is by the measurement of the surface strain on both gauge section surfaces by strain gauges. According to the ASTM standard D3410/D3410M-03 [113] percent bending B_y is given by

$$B_y = \frac{\varepsilon_{11} - \varepsilon_{22}}{\varepsilon_{11} + \varepsilon_{22}} \cdot 100. \tag{4.7}$$

For a valid experiment B_y should not exceed 10%. It should be noted that above equation often results in values in excess of 10% for very small strain (e.g. as loading is just initiated). This is an artefact of the division of small values and does not indicate bending of the specimen.

The small specimen geometries used here and the need of digital photography for the determination of the failure mode prevents the application of strain gauges in the gauge section. Instead, surface strain data is generated using DSP analysis as described above. This procedure requires that the specimen is filmed so that the through thickness side is visible. A speckle pattern is attached to the specimen surface and subsequently divided into a mesh of patches. The displacement of each patch is tracked which allows for the determination of the full field deformation which in turn allows the calculation of strain. It is important that a row of patches is defined close to both edges as this will give a strain measurement similar to strain gauge data. An example of a DSP analysis is illustrated in Fig 4.15.

The full field deformation allows for the calculation of strain along the edges and enables the assessment whether bending is present in the specimen. An illustration of results without and with bending is given in Fig 4.16.

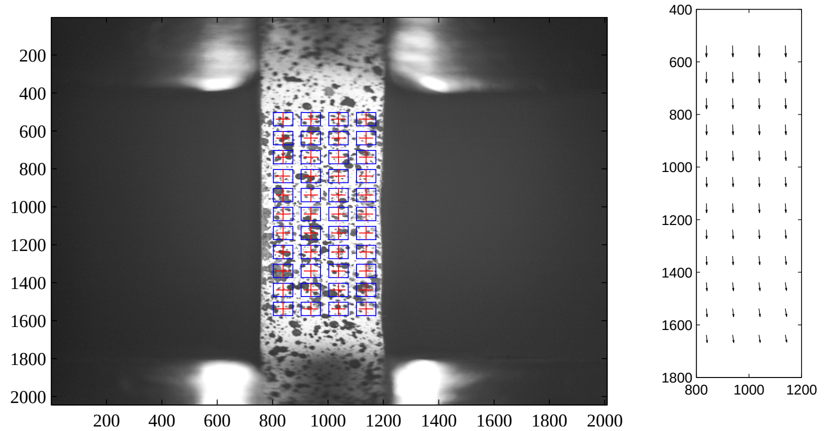

(a) Mesh for DSP analysis (b) Full field deformation results

Figure 4.15: Full field deformation measurement for bending assessment

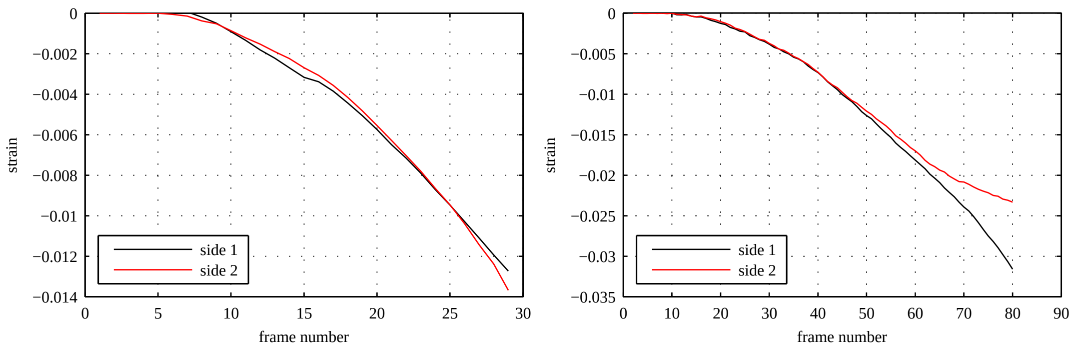

(a) no bending present (b) bending present

Figure 4.16: Strain on opposite specimen sides as obtained from DSP analysis

4.3 Determination of compressive bahaviour in transverse direction at different loading rates

The chosen failure theory for failure transverse to the fibres relies on the assessment of tractions acting on the fracture plane. Especially under compressive loading this fracture plane may not be aligned with the main material directions, but can be inclined. For uniaxial compression transverse to the fibre this has been demonstrated experimentally already at quasi static loading. However, the orientation of the fracture plane has not been investigated at higher loading rates. The aim of this study is to investigate whether the failure mechanism for transverse compression changes and which preferred inclination of the fracture plane can be found in experiments at higher strain rates. This will help to determine if and which parameters of the Puck failure model are strain rate dependent.

4.3.1 Experimental setup

A UD reinforced panel consisting of UTS carbon fibre embedded into RTM6 epoxy resin has been manufactured by resin transfer moulding. The laminate consists of 18 layers with the lay-up $[90/0/0/0/0/0/0/0/0]_s$. Specimens were waterjet cut from the panel. Subsequently, the flanks of the gauge section were further machined to allow for parallel flanks and to improve the surface finish. Finally, the 90° layers on the surface were removed within the gauge section. Special care was taken to ensure that no fibres of these layers remained on the specimen, as this would significantly affect the experimentally obtained results. The final gauge section thickness was approximately 2.5 mm. Each specimen is glued into steel endcaps which allows attaching the specimen to the various loading devices in use. The specimen geometry is given in Fig 4.17.

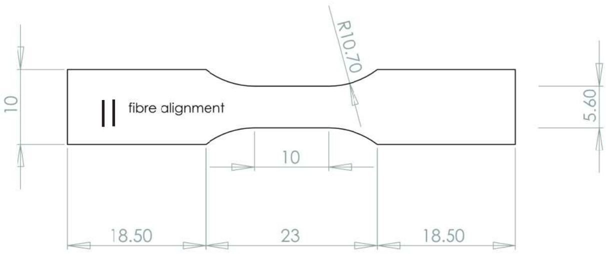

(a) specimen geometry

(b) specimen with and without endcaps

Figure 4.17: Specimen design for uniaxial compression in transverse direction

The specimens were screwed into bars which are attached to the respective loading device. For quasi-static and medium rate testing, the bars were guided by a solid steel frame to ensure alignment and the bars of the SHPB are aligned by ball bearings (see Fig 4.18). This minimises bending effects on the specimen during testing. All experiments were recorded using digital photography. This enabled the identification of the onset of failure, the initial failure mode and the observation of the inclination of the fracture plane.

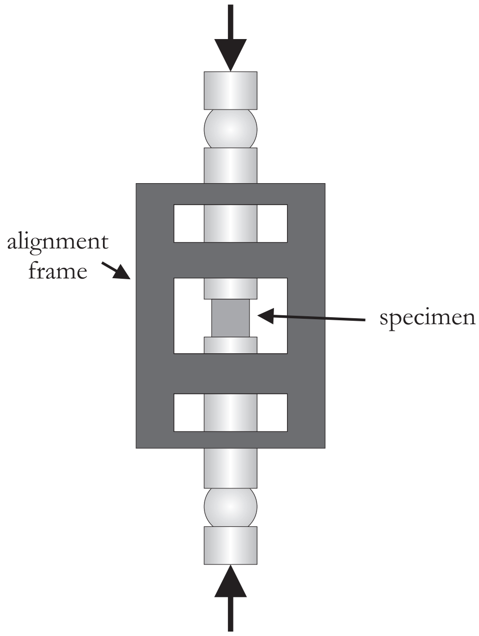

(a) alignment fixture for quasi-static and medium rate testing

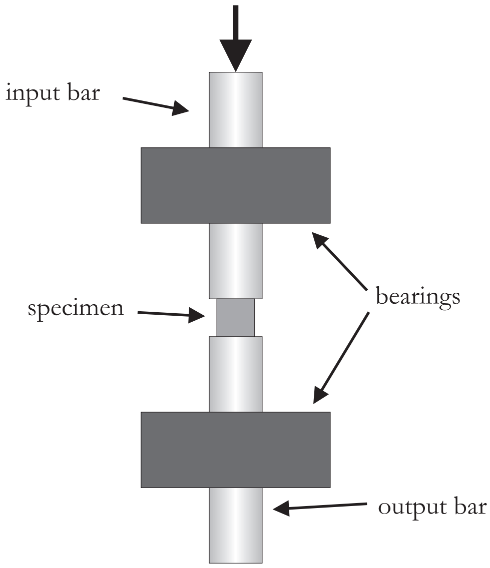

(b) alignment of SHPB

Figure 4.18: Alignment of the compressive experiments

4.3.2 Results

Before the results are presented, all experiments performed are investigated for bending (see Fig 4.19). From Fig 4.19(b) and Fig 4.19(c) it becomes obvious that most medium rate and quasi static experiments suffered from bending in higher strain regimes close to failure. It remains debatable whether the observed bending is an indication of the onset of a localised failure or whether buckling occurred. The experiments with the highest amount of bending at quasi-static and medium rate loading have been removed from the discussion. Unfortunately, this leaves only two valid experiments per strain rate regime. It should be noted the very high values of bending at low levels of strain are a consequence of the mathematical formulation of the bending assessment equation and do not reflect the actual bending of the specimen. The validity of the experiments is assessed by the percentage bending at higher strain values.

In Fig 4.20 the high strain rate data is investigated for mechanical equilibrium and for strain rate at failure. The stress in the input bar shows initially significant oscillations

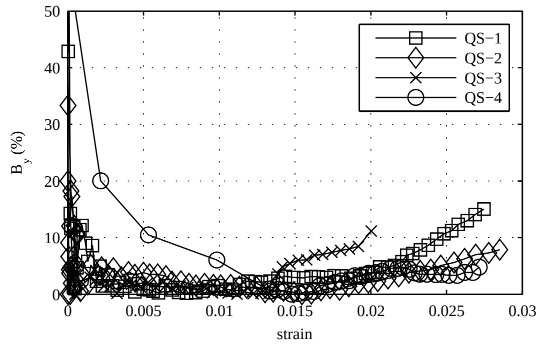

(a) Bending in the quasi static experiments

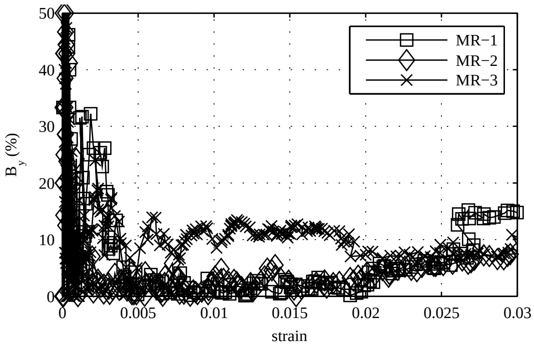

(b) Bending in the medium rate experiments

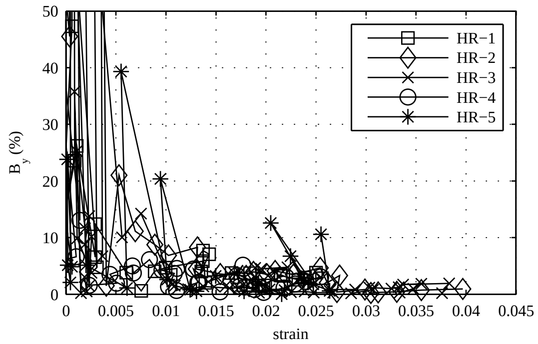

(c) Bending in the high rate experiments

Figure 4.19: Assessment of bending in the transverse compression experiments (please note that data has been cut at failure)

(see Fig 4.20(a). This is an artefact of the stress calculation from the superposition of α and β waves. As the stress levels for transverse loading are relatively low, small differences which can be easily caused by small measurement errors, can result in large errors for the input bar stress. This phenomenon becomes less significant as load rises but remains a problem in the data analysis. A comparison with the output bar stress, however, shows a similar trend. This indicates that similar forces are acting on both sides of the specimen and mechanical equilibrium has been achieved at the time of failure. However, the initial differences between input and output bar indicate that equilibrium is not achieved yet and for this reason no stiffness properties were extracted from the experiments. The data presented in Fig 4.20(b) show that the strain rate reached a constant level at the time of failure.

All experiments were filmed by digital high speed photography. This enabled the determination of the fracture plane inclination from the recorded images. The fracture plane angle θ_{fr} is obtained manually from digital images (see Fig 4.21). The mode of failure seem

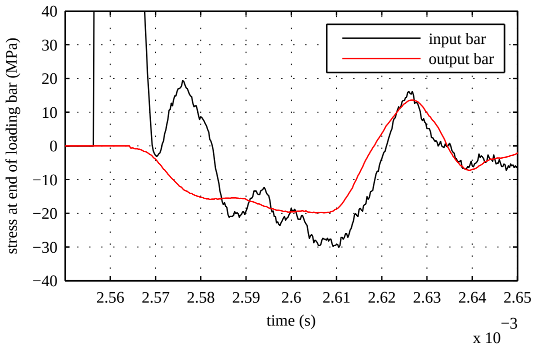

(a) Assessment of mechanical equilibrium in the high rate experiments

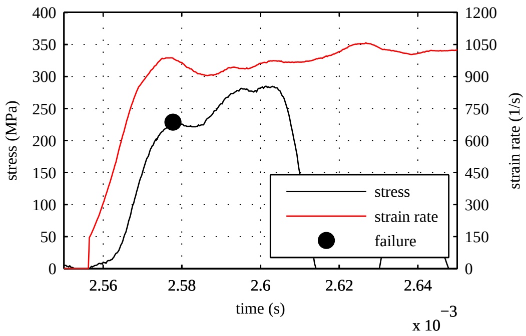

(b) Estimation of the strain rate at failure

Figure 4.20: Analysis of the high strain rate data

to be similar at all strain rates. Failure occurs on a inclined plane parallel to the fibres. The formation of the fracture plane, however, seems to change. The high rate specimens fail by forming a single fracture plane. The quasi static and medium rate specimens show various bifurcating cracks. It is still possible to identify a global fracture plane, but more than one fracture is observed. The reason is assumed to be related to the manufacturing of the material. The panels were produced using a moulding technique. The fibre orientation should therefore be less aligned than in prepreg materials for instance. This affects the plane of preferred failure in the quasi static and medium rate experiments, but does not seem to affect the high rate results. One explanation would be that the crack, once initiated, is driven on the same direction through the whole specimen. The loading is applied so rapidly that crack does not have 'time' to change direction. In general, the obtained fracture angles scatter around a value of approx 50°. This corresponds to quasi static data available in literature [3]. The measured fracture plane angles in the medium strain rate experiments seem to be a bit lower. This might be caused by the slightly higher amount of bending in the experiments and would need further experimental confirmation.

All results are summarised in Tab 4.1 and the obtained stress strain curves are displayed in Fig 4.22.

The stress strain curves have been cut at the point where failure was detected on the recorded images. From Fig 4.22 it can be seen that the material behaviour turns non-linear before first failure is detected. Especially the high rate response shows a pronounced non-

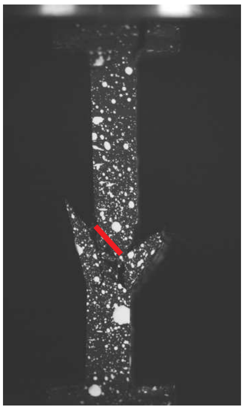

(a) Fracture plane as observed at quasi-static strain rate

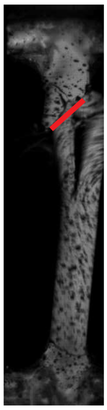

(b) Fracture plane as observed at medium strain rates

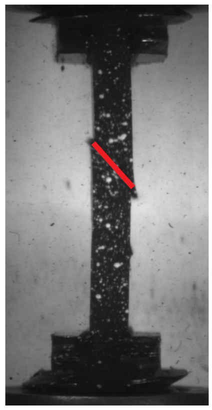

(c) Fracture plane as observed at high strain rates

Figure 4.21: Strain rate dependent material behaviour - summary

Table 4.1: Results for uniaxial compression in transverse direction

name	strength (MPa)	strain rate (s^{-1})	fracture plane angle (°)
QS-3	163	8.6e-5	57
QS-5	172	1.1e-4	58
QS-average	168	1.0e-4	
MR-2	186	4.8	48
MR-3	184	2.7	44
MR-average	185	3.7	
HR-1	243	837	50
HR-2	243	1003	47
HR-3	268	988	55
HR-4	229	986	-
HR-5	289	1035	49
HR-average	254	970	

linearity. It seems that the material after reaching a stress level of approx. 250 MPa starts to deform inelastically at an almost constant stress level. This indicates that the onset of failure does not coincide with the visible formation of the fracture plane. The strength in the high rate experiments is therefore not obtained from the images but is chosen at the point where the stress strain curves seems to leave the elastic path. The stress strain curves of the quasi static and medium rate experiments show non-linear behaviour which is less pronounced, but seems to initiate at relatively low strain values. It was not possible to determine a certain stress level at which inelastic deformation initiated. Therefore the strength was obtained using the failure as visible on the images.

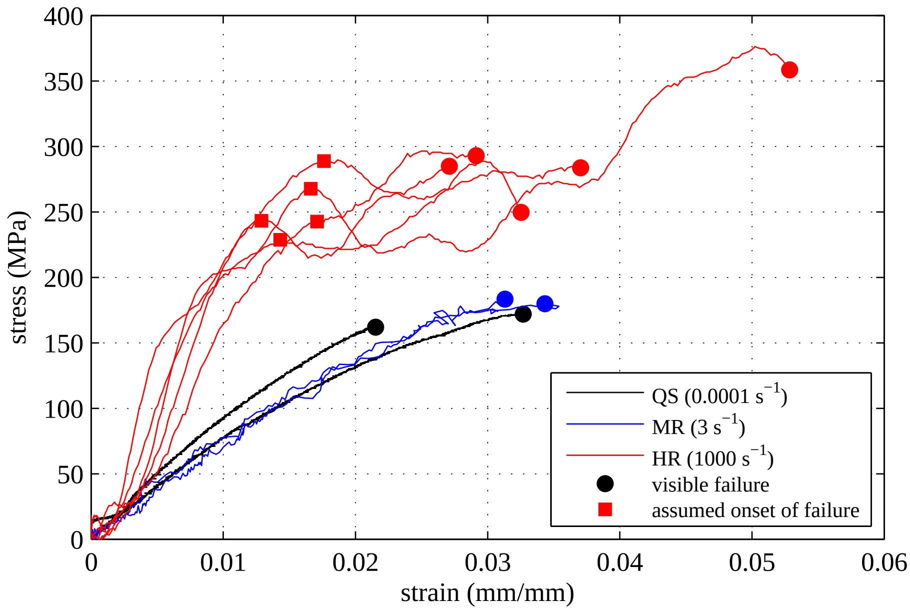

Figure 4.22: Stress strain curve for transverse compression of a UD UTS/RTM6 composite (please note: data has been cut at failure)

The obtained strength data of all experiments is plotted versus the strain rate on a logarithmic scale. This enables the visualisation of the rate dependance of the material. The materials strength seems to rise only very little from quasi static to medium strain rates while the increase from medium to high strain rate is significant (see Fig 4.23(a)). The materials stiffness has not been extracted from the results as it is not entirely clear up from when the specimens were in mechanical equilibrium during the experiment. Especially during the early stage of the loading, significant oscillations of the imput/output bar stress were observed (see Fig 4.20(a)). The comparison with available data from literature shows good agreement (see Fig 4.23(b)). Especially the data points obtained by neat RTM6 resin seem to correspond very well with the composite with RTM6 matrix. This reinforces the general assumption that rate dependent material behaviour in composite is mainly caused by the behaviour of the matrix material.

The study showed a clear strain rate dependence of strength. Rate dependent stiffness was observed but has not been evaluated due to the quality of the data. The rate dependency does not seem to evolve linear on a logarithmic scale, but shows a rather exponential

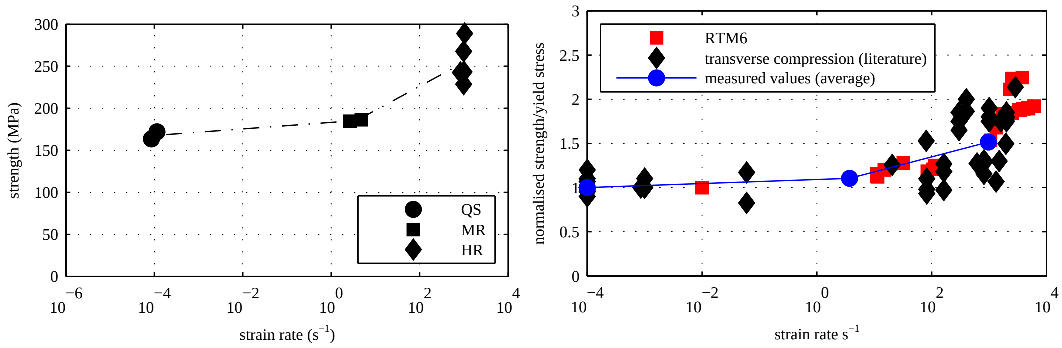

(a) strain rate dependency of the strength of UD UTS/RTM6

(b) comparison with data from literature

Figure 4.23: Strain rate dependent material behaviour - summary

behaviour similar to neat resin data (see Fig 4.3). The failure mechanism did not change with strain rate. An inclined fracture plane formed at all rates whereby fracture occurred less uniform at lower strain rates. The specimen failed by several fracture planes of similar orientation. Only in the high strain rate experiments a clear single fracture plane could be observed. The fracture plane inclination angle did not seem to change dramatically in the different strain rate regimes. An interesting phenomenon was observed at high strain rates. The stress strain curve reached a plateau relatively quickly. Afterwards, the specimen continued to deform without a significant increase of stress. This might indicate inelastic deformation of the matrix before an actual fracture plane can be observed. Further experiments with higher quality digital ultra high speed camera capability are needed to verify the onset of damage by a full field strain analysis. Additionally, a higher number of specimen should be tested to establish a statistical distribution of fracture angles at different strain rates.

The experimentally observed results allow additional conclusions about the rate dependency of the parameters of the Puck IFF model. A comparison of the rate dependent strength of RTM6 in tension and compression shows very similar behaviour up to strain rates of approx. $2000s^{-1}$ (see Fig 4.24). The inclination of the fracture plane for uniaxial compression does not seem to change with increasing loading rate. The two inclination parameters p_t and p_c of the Puck model are given by

$$p_t = \frac{Y_t}{2Y_c}(\tan^4 \theta^0_{fr} - 1) \tag{4.8}$$

and

$$p_c = p_t \frac{Y_c}{Y_t}. \tag{4.9}$$

Assuming a similar rate dependent behaviour of the composite as observed in the neat resin, the ratio Y_t and Y_c should be rate insensitive. Consequently, the inclination parameters p_t and p_c are assumed rate insensitive here too. The argumentation relies on the assumption that the composite strength properties change similarly to the resin's yield stress in tension and compression. Unfortunately, no consistent data set for a given composite in both tension and compression has been found in literature. This aspect will need to be addressed in future experimental characterisation programs.

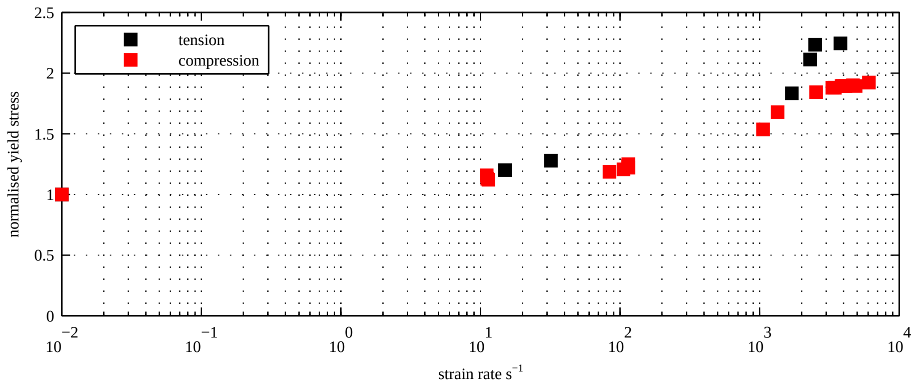

Figure 4.24: Comparison of the rate dependent yield stress in tension and compression for RTM6

4.4 Determination of the compressive behaviour in fibre direction at various rates of loading

The available data in literature does not allow sound conclusions to be drawn for compressive fibre failure at higher strain rates. As a possible reason different failure modes at high strain rates have been identified. Most data points were obtained without sufficient documentation of the specimen failure mode. The availability of ultra high speed digital photography equipment within this study enabled an accurate observation of the specimen failure mode. The key is to generate comparable failure modes at all different rates of strain.

The specimens were cut from a single panel which consists of 12 UD non crimped composite plies with the lay-up $[[0/90]_3]_s$. The respective UD plies were manufactured from T700 fibres which are embedded in MTM44 epoxy resin. The panel has been produced using a resin transfer moulding (RTM) process resulting in a total panel thickness of 3 mm. The RTM process was performed in non closed mould which resulted in a smooth surface and a rough surface. Beam specimens 30 mm long and 10 mm wide were cut with a water cooled diamond saw. All experiments were recorded using digital photography which allows assessment of the correct failure mode and judgement whether bending was present during the experiment. Two different specimen geometries were used. A simple unwaisted beam specimen was used in the high rate experiments, while the specimen was waisted in the medium rate and quasi-static experiments. This was necessary because the onset of failure was outside of the gauge section for not waisted specimens at quasi-static and medium rate loading. The recorded force is converted into stress by dividing through the cross section area thus allowing for a direct comparison of the results. It should be noted that this is a homogenised measure of stress as the specimen consists of a cross-ply laminate. The specimen design and dimensions are illustrated in Fig 4.25.

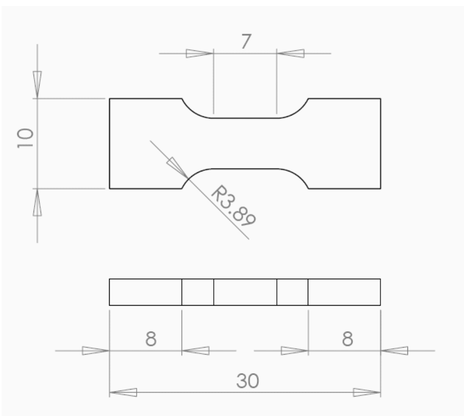

(a) specimen for quasi-static and medium rate experiments

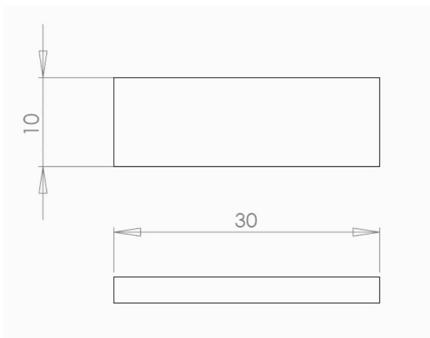

(b) specimen for high rate experiments

Figure 4.25: Specimen design for uniaxial compression in fibre direction

4.4.1 Development of specimen fixture

The specimen design is a key issue in compression testing of composite materials, especially in fibre direction. The strength of the reinforcing fibres is quite high, which can result in various other failure modes before the actual fibre compressive failure mode occurs. Another very important issue for specimen design is avoiding of bending during the experiment.

The challenge is therefore the development of a specimen clamping approach which allows for uniaxial compression without bending of the specimen. At the same time, failure must be observed within the gauge section. Failure near the specimen boundary, where loading is applied, usually occurs because of stress concentrations due to the specimen geometry or edge effects and does not permit conclusions of the intrinsic material strength. Furthermore, the clamping approach must be applicable to all three loading rigs in order to keep the boundary conditions constant. A set of different specimen geometries have been investigated towards their suitability for compressive testing.

The simplest specimen design would be a specimen with a quadratic cross-section that remains constant throughout the length of the specimen. For high strain rate experiments, this enables reliable determination of force and displacement at the end of the loading bars. Bending is usually not a problem with this geometry as the specimens are quite thick. However, generating a valid failure mode can be challenging. Failure is usually triggered close to the corners of the specimen as a consequence of a complex three dimensional stress state and subsequently propagates through the specimen. Even changing the length to thickness ratio did not change the observed failure initiation (see Fig 4.26(a) and 4.26(b)).

In order to move the failure in the gauge section, the specimens were waisted. This should result in higher uniaxial compressive stress in the gauge section compared to the shoulders. Initially, the specimen was waisted in the through thickness direction. The failure initiated in the shoulders and propagated as a delamination (Fig 4.26(c)). Subsequently, a trial specimen was waisted in the width direction(Fig 4.26(d)). This has the advantage, that fibres are actually reaching into the shoulders, therefore more effectively preventing a delamination failure. Unfortunately, the material strength in the gauge section was still too high and failure initiated at the edge. Non of the investigated specimen geometries is therefore suitable for the uniaxial compressive testing.

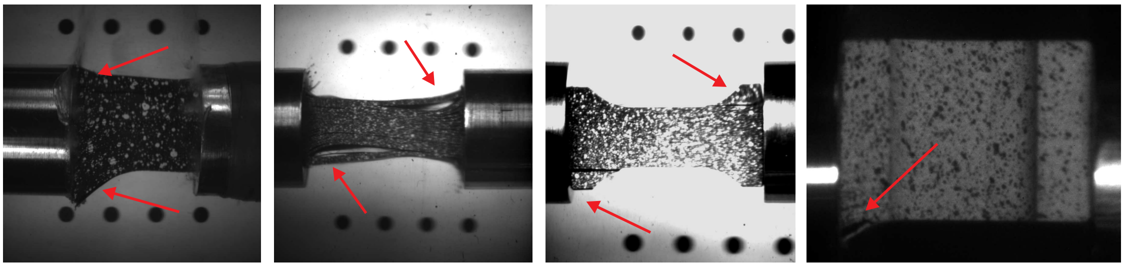

(a) strait specimen (thick) (b) strait specimen (thin) (c) specimen waisted in thickness direction (d) specimen waisted in width direction

Figure 4.26: Investigated specimen geometries and observed failure modes at high strain rates

As the generation of valid failure modes was not possible by adjusting the specimen geometry only, a new fixture needed to be developed. The idea was to utilise slotted end-caps which could be attached to each loading rig. This would constrain the specimen and prevent the onset of failure close to the edge. The geometry of the end-cup was chosen to minimise impedance jumps in the high rate experiments, thus allowing for the calculation of the displacement of the bars and the force applied to the specimen (see Fig 4.27(a)). A couple of trail experiments at high strain rate showed that failure initiates in the gauge section. However, as failure propagates, the specimen gets squeezed in the slot and bends the fixture. Therefore, a set of additional clamps have been attached to the fixture to prevent opening in the high strain rate experiments (see Fig 4.27(b)).

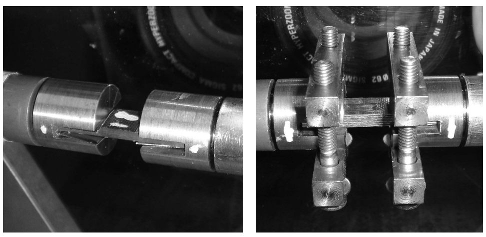

(a) without clamps (b) with clamps

Figure 4.27: Specimen fixture with slotted end caps

The slotted end-cups seem to be the most promising experimental setup and have therefore been chosen. Alignment of the specimens is achieved like for the transverse compression experiments (see Fig 4.18).

During the experimental program, it became obvious that at high strain rates, the specimen was first slightly pushed into the slot of the fixture, before it was loaded directly. The deformation measurement of the wave analysis is therefore not accurate as the initial strain is only due to some initial compliance of the fixture rather than compressing the specimen itself. Therefore, it was necessary to determine which amount of deformation as given by the wave analysis resulted in actual specimen deformation and in fixture compliance respectively. The initial setup of the Cordin550 ultra high speed camera only delivered images of low quality as most of the CCD's were misaligned (the camera setup was later improved for the transverse compression experiments). It was therefore not possible to measure strain entirely by image analysis. Two markers were attached to the specimen to obtain a rough estimate of the strain in the specimen (see Fig 4.28(b)). The position of the two markers was tracked individually on each frame. The obtained strain history data was then used to correct the wave analysis results. A comparison of stress-strain curves obtained from wave analysis and image analysis shows, that a simple shift of strain was sufficient to correct the wave data (see Fig 4.28(a)) for the fixture compliance. All high rate experiments have been corrected by the use of image analysis.

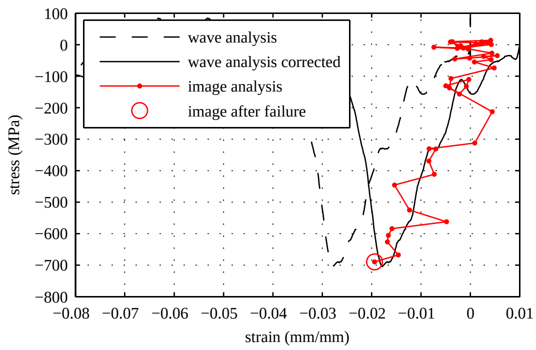

(a) correction of the wave analysis by image analysis

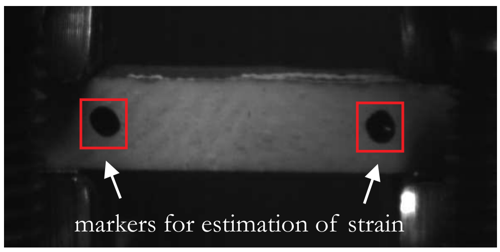

(b) specimen marking for strain estimation

Figure 4.28: Correction of the wave analysis deformation data

4.4.2 Experiments and results

The purpose of the experiments was the determination of the influence of strain rate on the mechanical properties of the material. While for quasi-static and medium rate experiments the strain rate can be considered as constant, the experiments at high strain rates suffer from varying strain rates. Usually, it takes some initial time for the whole system to overcome inertia and get into motion. Therefore, the strain rate will slowly rise in the beginning. Ideally, it should reach a plateau quickly and stay constant. However, the resistance of the material often results in drop of strain rate as the material starts to deform. This kind of behaviour was observed here. In Fig. 4.29(a) a typical strain rate response is shown together with the stress strain response. Initially, the strain rate quickly grows to about $600s^{-1}$ but then drops to approx. $400s^{-1}$ as the stress in the specimen is rising. After the onset of failure, the strain rate rises back again to the initial level of $600s^{-1}$. The strain rate at failure is determined as the actual strain rate acting at that time of failure.

As already discussed earlier, a crucial aspect of testing at high strain rates is to ensure that mechanical equilibrium has been established in the specimen before failure occurs. Only when the specimen is in equilibrium the force as obtained in the input bar and the output bar is representative for the force acting in the gauge section. All high strain rate experiments have been investigated regarding the establishment of mechanical equilibrium by comparing input bar stress and output bar stress. An example is shown in Fig. 4.29(b). The more complex clamping device for this experimental setup seemed to result in mechanical equilibrium being established late in the experiment. The slotted end caps and additional clamps cause more stress wave reflections on the strain gauge signals. Therefore, the obtained data is not used to evaluate the materials stiffness at high strain rates.

Bending in the specimens has been assessed according to the procedure as described earlier. Unfortunately, no speckle pattern was applied for the high strain rate experiments. At the time the specimens were tested, the camera image quality was not good enough for DSP. Experience with the transverse compression specimen and the relative low amount of

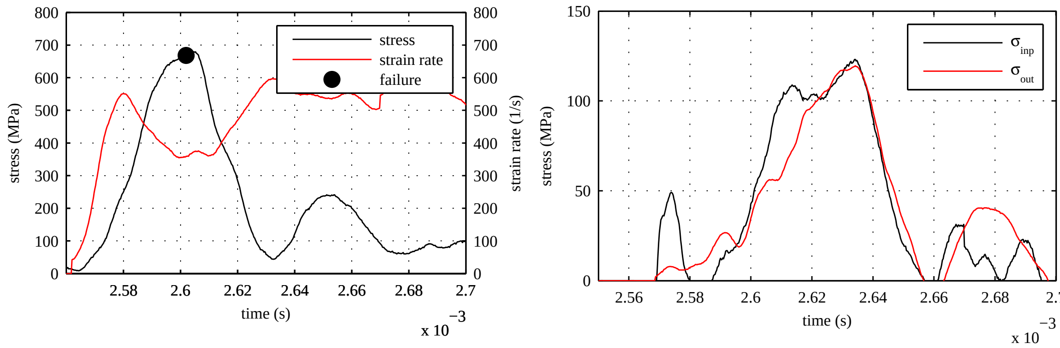

(a) strain rate at failure (b) equilibrium during high rate experiment

Figure 4.29: Assessment of high strain rate results

bending at quasi-static and medium rate give enough confidence to assume that bending was no issue in the experiments. An investigation of the ultra high speed footage did not show any signs of bending before failure.

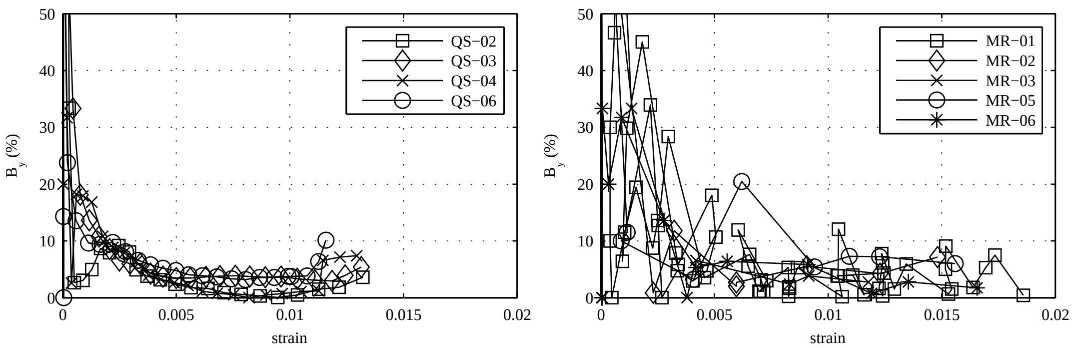

(a) Bending in the quasi static experiments (b) Bending in the medium rate experiments

Figure 4.30: Assessment of bending for compression in fibre direction experiments

The observed mode of failure did not change with rising loading rate. Failure initiation was observed within the gauge section in all experiments. The specimens failed by a compressive fibre failure in the 0° plies and shear matrix failure in the 90° plies. Subsequently, long delamination grew between the plies. Failure always happened instantaneously and was catastrophic (see Fig 4.31). The use of digital ultra high speed photography enabled to show the initiation and propagation in high strain rate experiments (see Fig 4.32).

The measured strain data is very noisy for the medium and high strain rate experiments. The stress strain response seems to be slightly non-linear (see Fig 4.33), which corresponds to observations made in [114]. The measured uniaxial strength increases with increasing

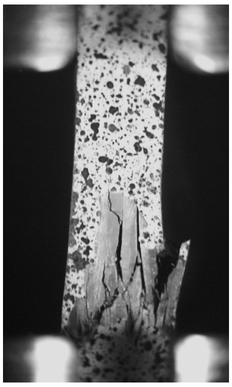

quasi-static failure

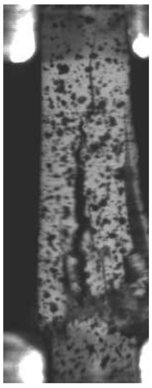

failure at medium strain rate

failure at high strain rate

Figure 4.31: Failure modes observed at different strain rates

Figure 4.32: Initiation and propagation of damage in a high strain rate experiment

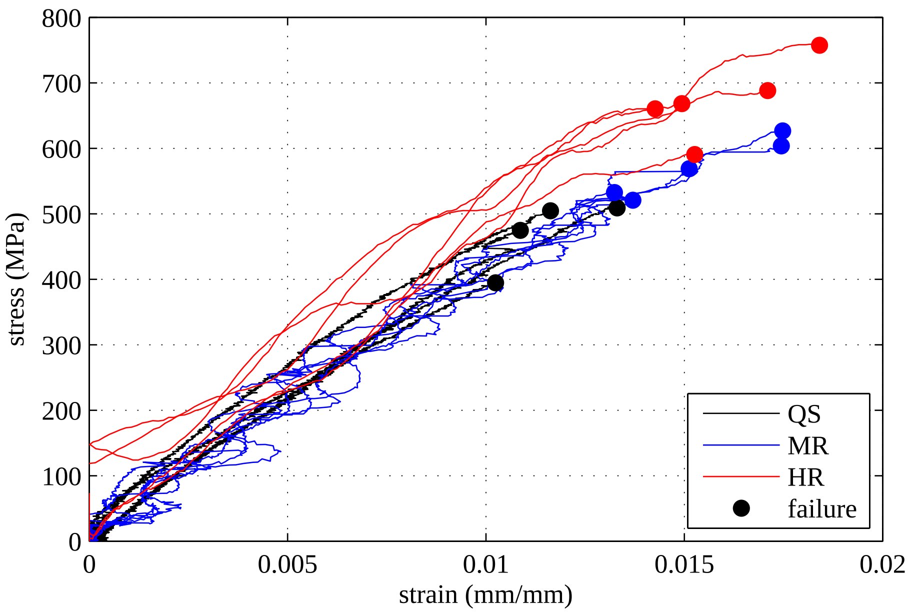

Figure 4.33: Stress strain curves for three strain rates

strain rate. Fig 4.34(a) suggests a linear relation between strength and strain rate when strain rate is plotted on a logarithmic scale. The scatter on the data is significant, however, the increase in strength is clearly visible. A comparison of the obtained properties with published data is displayed in Fig 4.34(b). The obtained strength properties seem to be in good agreement with the published data. Only in the region of medium strain rates, the measured results suggest a slightly higher rate dependency. The experimental results are documented in Tab 4.2.

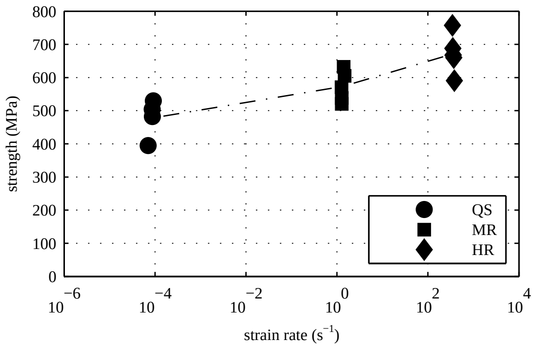

(a) strain rate dependency of the strength

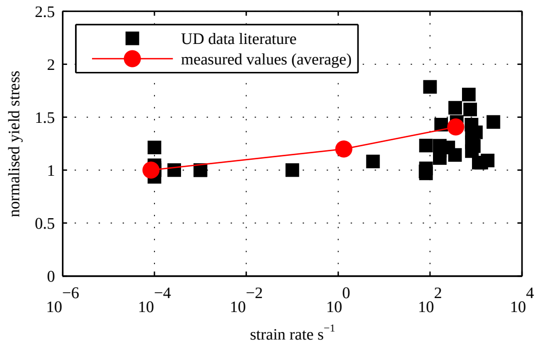

(b) comparison of the uniaxial compressive strength

Figure 4.34: Strain rate dependent material behaviour for uniaxial compression in fibre direction - summary

The experiments allowed to establish the trends of strain rate dependent material behaviour. The obtained data is in good agreement with data published for rate dependent material behaviour. A consistent failure mode was observed across all strain rates. Digital photography enables to establish the rate dependency of a certain failure mode, which was fibre kinking. The results suggest a linear increase of strength on a logarithmic strain rate scale. Future experimental programs should focus on unidirectionally reinforced laminates to allow for a direct measurement of the lamina properties. The experimental program should include more strain rates to generate more data in the medium strain rate regime. The specimen clamping needs to be refined to minimise stress wave reflection and to establish mechanical equilibrium faster thus allowing for an investigation of the materials stiffness.

Table 4.2: Results for uniaxial compression in fibre direction

name	strength (MPa)	strain rate (s^{-1})
QS-02	482.5	8.78e-005
QS-03	529.8	9.17e-005
QS-04	504.4	8.66e-005
QS-06	394.5	7.09e-005
average	477.8	8.42e-005
MR-01	632.2	1.40
MR-02	538.2	1.27
MR-03	520.8	1.28
MR-05	571.1	1.26
MR-06	604.8	1.47
average	573.4	1.33
HR-06	757.4	345.3
HR-08	688.0	351.7
HR-09	590.4	382.6
HR-10	668.2	359.2
HR-11	660.2	370.7
average	672.8	361.9

4.5 Summary

This chapter presented the literature review for strain rate dependent material behaviour of unidirectionally reinforced composites consisting of carbon fibres in a epoxy matrix. Commonly used experimental procedures to measure the strain rate dependency of such materials are introduced. The techniques which were used within this study are introduced and discussed in detail. Special focus was given to Split-Hopkinson Pressure Bars and optical full field deformation measurement techniques.

The compressive material behaviour transverse to the fibre of a UD reinforced material was investigated to establish the rate dependency of the Puck failure model for failure transverse to the reinforcement direction. Therefore, the orientation of the fracture plane is studied. The experiments suggest a constant fracture plane inclination at all applied loading rates.

A cross ply laminate was investigated under uniaxial compression. Special emphasis was given to the failure initiation. Digital photography was utilised to monitor the damage initiation at all strain rates. Different specimen geometries were investigated towards the failure initiation. A specimen clamping approach and specimen geometry was developed allowing for a comparable failure mode in the gauge section at all loading rates. The obtained data was compared to data from literature to establish the rate dependency of the compressive material properties in fibre direction.

In the next chapter, and improved method for beam bending is presented. Additionally, beam bending experiments at quasi-static and impact loading were performed to study the failure mechanisms under complex stress states.

Chapter 5

Improved experimental method for impact beam bending

Bending experiments are widely used in characterisation of composite materials. The experimental setups are usually straightforward with simple and well defined boundary conditions thus enabling the verification and validation of numerical constitutive models. The wide range of observable failure modes make beam bending a useful experiment for the generation of constitutive model verification data.

In this chapter, an already existing experimental setup is improved thus resulting in increased accuracy of the obtained results. Both, numerical and analytical methods are used to identify sources of mechanical vibrations which reduce the accuracy of the obtained force-deflection data. Consequently, the experimental setup is modified to deliver less noisy data. High speed photography is utilised for the verification of the data reduction procedures. Furthermore, the high speed footage enables the identification of the onset and evolution of damage during the experiment.

A number of composite beams are tested at different span and with different ply orientations, thus addressing all relevant composite failure modes. The experiments are performed both, quasi-statically and at impact loading to identify rate effects. The experimental results obtained here, will be used to verify the proposed constitutive model in a later chapter.

5.1 Introduction

Three-point-beam-bending is probably the most commonly used type of bending experiment. In the case of composite materials, different failure modes can be investigated by changing only a few experimental parameters. For example, increasing/decreasing the span to beam height ratio results in a switch to/from a fibre failure mode to an inter-laminar failure mode.

Bending experiments are already a standard testing procedure and widely in use in material characterisation when the load is applied at quasi static rates [115]. At higher loading rates the experimental setups are more complex and different methodologies have been proposed. For example, impact bending experiments with drop weight testing devices are widely used [116] despite their limitations. In these experiments an impactor of known weight is instrumented with an accelerometer and dropped from a defined height. The velocity of the impactor prior to impact against the targeted specimen must be measured despite the theoretical ability to relate it to the drop height. During the impact, the deceleration of the drop weight is measured using accelerometers which enable calculation of the force-time and displacement-time histories. The drop weight testing has already been standardised [117] despite the fact that the obtained force history data is usually polluted by numerous stress wave reflections. These reflections result from the complex geometry and boundary conditions of the commonly used bulky drop weights. The noise may be of a similar order of magnitude as the response generated from the interaction with the specimen itself. Consequently, extensive data filtering operations are required to estimate the force transmitted in the actual specimen [118]. An alternative force measurement approach incorporates measurement on the non moving boundaries of the specimen. This method relies on complicated design of a specimen support to minimise wave reflections [119, 120]. Additional measurement techniques, such as those relying upon high speed photography or upon miniature strain gauges fitted directly onto specimens are necessary if measurement of deformation during loading in drop weight experiments is required.

An alternative approach to dynamic three-point-beam-bending extends from the well established Split-Hopkinson-Bar technique commonly used in uniaxial tensile and compressive testing at high rates of strain [87] (see Fig 5.1(a)). A bending apparatus utilising long thin rods has been proposed by Hallet [121]. The Split-Hopkinson pressure bar (SHPB) technique (see Chapter 4) has been modified to monitor longitudinal stress waves in a long impactor rod resulting from impact loads applied at the rod's end (see Fig 5.1(b)). The waves are measured some distance away from the bar ends and so one-dimensional analysis of the measured stress waves may be used in the calculation of force-time and displacement-time histories of the bar end in contact with the target specimen. This makes additional displacement measurement systems redundant. The use of long thin rods should yield considerably more accurate measurements than drop weight towers.

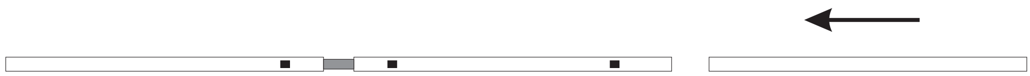

(a) SHPB for uniaxial compression testing

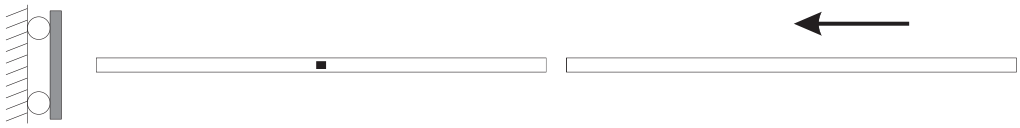

(b) modified SHPB setup for bending experiments

Figure 5.1: Hopkinson bar based devices for dynamic testing of materials (dark spots on the bars denote positions of strain gauges on the bars' surface)

5.2 Improved dynamic bending test

In the following, the experimental technique for impact bending is introduced. An existing experimental setup is improved for more accurate measurement of deformation and force.

5.2.1 Original experimental apparatus

The apparatus previously used for dynamic three-point-beam-impact-bending testing is similar to the device as described in [121]. A thin rod (the projectile) is accelerated by compressed air in order to make it collide with an instrumented rod (the impactor) of exactly the same material and geometric properties. In theory, the kinetic energy is entirely transferred from the projectile to the impactor bar which flies unstressed towards the targeted specimen. When the impactor bar collides with the specimen, the history of longitudinal stress in the impactor bar generated during the interaction with the specimen is recorded by a set of strain gauges mounted on the surface of the impactor, approximately mid length of the bar. The geometry of the impactor bar allows for the application of one-dimensional wave analysis to calculate the force-time and velocity-time histories in any chosen cross section [122] (as already described in Chapter 4). Therefore, stress waves in the impactor bar are monitored by the attached strain gauge. Initially, all recorded stress waves originate from the interaction of impactor and specimen (α waves). The overall duration of the bending experiment, however, results in stress wave reflections (β waves) to be present on the strain gauge readings after a certain time (exactly the time the first wave needs to travel from strain gauge to the free end and back). The α and β waves can be separated knowing the geometry and impedance of the impactor material. The reflected β waves were initially recorded as α waves when traveling down the impactor. Having a certain time of undisturbed α waves and knowing that these α waves will be reflected as β waves of same magnitude but different sign allows for separation of α and β waves at the position of the strain gauge. This enables monitoring of the α waves which carry the information of the actual impact over the whole duration of the experiment. This methodology, however, relies on a stress free impactor bar prior to impact.

A sketch of the original experimental setup used as the inspiration for this study is given in Fig 5.2. In this setup both bars had an identical impedance, however, the impactor bar is slightly shorter than the projectile and shaped as a blunt symmetric chisel in order to apply a line load across the width of the beam specimen or a hemispherical tip for plate impact experiments.

In order to test of the original setup before any modifications, a number of simple steel beams were impacted with an initial velocity of approx. 7 m/s. The signals recorded on the impactor bar showed an intense ringing before the impactor bar collides with the specimen. This indicates trapped strain energy from the collision of projectile and impactor bar

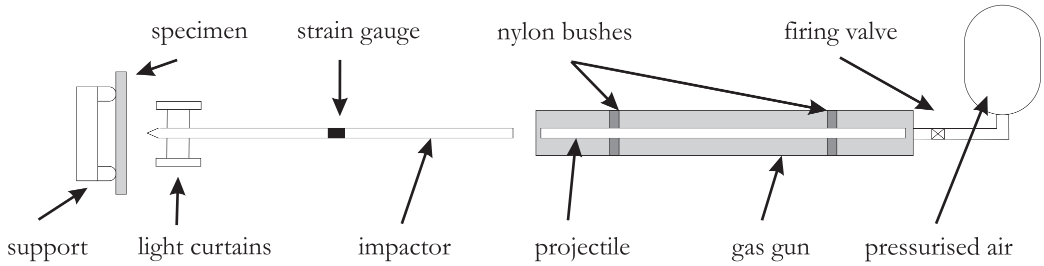

Figure 5.2: The original impact bending apparatus (schematic)

which does not dissipate sufficiently rapidly and remains significant during the interaction between the impactor and the beam specimen (see Fig 5.3). The ringing does not carry any information about the interaction of impactor and specimen and is considered as noise here.

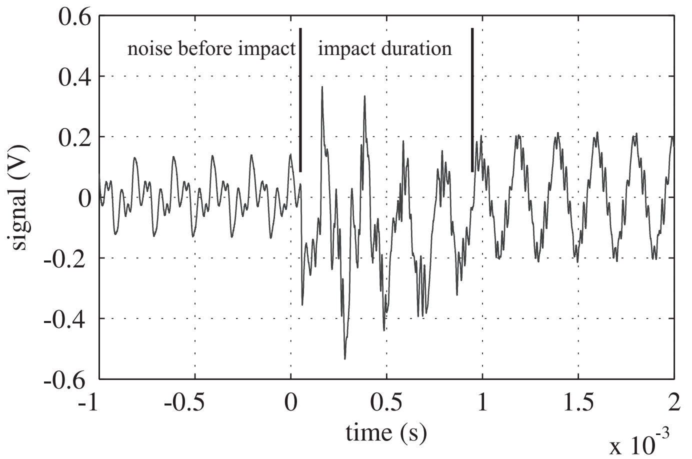

Figure 5.3: Strain gauge signal as measured for the original experimental setup (impact impactor bar and specimen occurs at time 0)

In order to help improve the understanding of the system, all experiments were recorded using a PHANTOM digital high speed camera. Images with a resolution of 800x256 pixels were obtained at a frame rate of 15000 frames/s. The displacement of the impactor tip was monitored by means of image analysis using the tools as described in Chapter 4. The impactor tip displacement from image analysis can be directly compared with the results of the wave analysis and enables a verification of the analysis procedure. The results of the comparison are displayed in Fig 5.4.

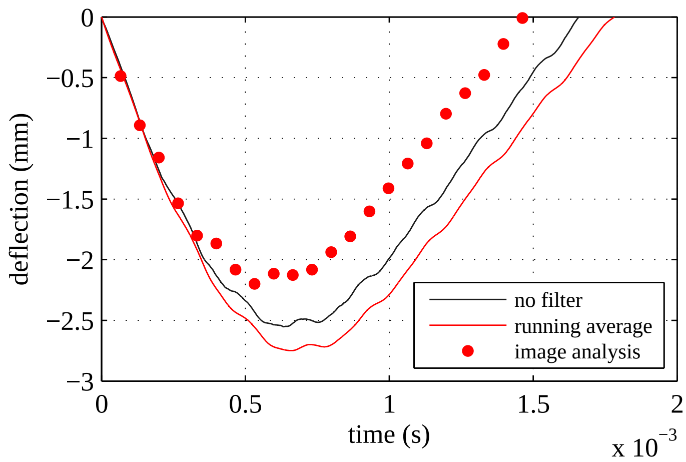

Figure 5.4: Comparison of deflection history as obtained from the wave analysis and the image analysis

From Fig 5.4 it becomes clear that the deflection calculation by wave analysis can yield a significant error. Initially, both wave analysis and image analysis, correspond very well. However, as the specimen continues to bend, the wave analysis over predicts the deformation. Both deflection and force history are calculated from the alpha and beta waves travelling in the impactor bar and so it can be assumed that the calculated force data is inaccurate too.

The one dimensional wave analysis can only be applied assuming that the impactor bar is stress free before it contacts with the target specimen. This allows for the correct separation of α and β waves from the strain gauge reading. The trapped strain energy in the impactor bar prior to impact will result in inaccurate calculation of the wave propagation in the rod and subsequently reduced accuracy of the calculated force and displacement histories. It has been suggested in [121] that a simple low pass filter, such as a running average, could be used to reduce the noise on the strain gauge data. This would appear reasonable as it has been demonstrated analytically in [116] that the high frequency vibrations in the loading bar could not be transmitted into the specimen. However, the experimental investigation supported by high-speed-photography showed a greater error in deflections calculated using filtering (see Fig 5.4). Even though the high frequent oscillations are not transmitted into the specimen, they still contribute to the calculation of the displacement of the impactor itself and subsequently the predicted force and deflection histories.

The conclusion of this investigation is that the current experimental procedure is not accurate enough to provide useful data for constitutive model verification. In order to improve the experimental procedure for impact bending a numerical verification of the one dimensional wave analysis is undertaken. In addition, identification of the sources of the trapped strain energy in the strain gauge signal recordings and investigation of potential improvements have been undertaken.

5.2.2 Numerical verification of the data analysis method

The propagation of elastic stress waves in thin rods is well understood and widely used. The relatively long duration of the impact results in a significant amount of wave reflections being present on the strain gauge readings. Therefore, it has been investigated whether data analysis based upon the simplifications of a 1D analysis can accurately predict the reflections and allows for correct calculation of contact force and impactor tip displacement over the whole impact duration. A virtual test has been performed numerically to model the ideal situation of no stress waves being present prior to impact on the specimen. The experimental setup has been modelled in the explicit FE solver LS-DYNA using 8 noded hexahedral elements with a single integration point. The impactor is modelled in full length while the specimen support is simplified as a rigid body. A linear elastic constitutive model (MAT01) has been chosen to model both the impactor and the beam specimen. The material properties are displayed in Tab 5.1. The contact between impactor bar, beam and fixture was established using a simple surface to surface contact based upon the penalty method. The impactor bar was given an initial velocity of 10 m/s to enable impact between impactor bar and beam. A section of the FE-model is displayed in Fig 5.5.

Table 5.1: Material properties used for the LS-DYNA analysis

	impactor	beam	bushes
material	titanium	steel	polymer
density ($\frac{g}{cm^3}$)	4.93	7.85	1.00
Young's modulus (GPa)	115	210	10
Poisson's ratio	0.36	0.285	0.36

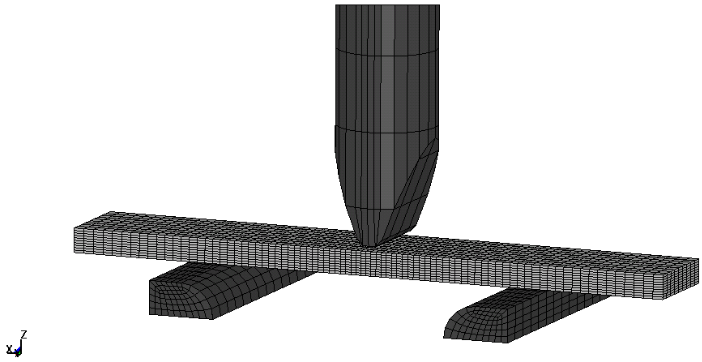

Figure 5.5: Numerical model of the experimental setup

The axial force of the impactor bar has been extracted from the position on the impactor bar where the strain gauge is attached in the real experiment. This force history has been used as virtual input data for the wave analysis. The contact force and the impactor tip displacement have been calculated and are compared with the prediction of the FE model. The comparison is presented in Fig 5.6.

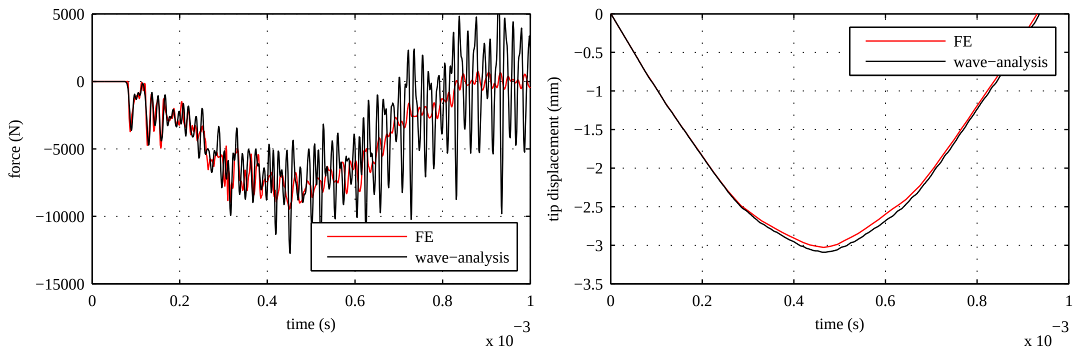

(a) contact force (b) specimen deflection

Figure 5.6: Comparison of the results obtained from wave analysis and virtual test

The obtained deflection history is almost identical (2% difference in the maximum deflection). The comparison of the contact force, acting on the impactor tip, however, reveals that the accuracy of the wave analysis decreases with time. The force history data from the wave analysis shows a high frequency vibration with increasing amplitude over time. This is probably caused by a small error calculated with each wave reflection resulting from the simplification within one-dimensional theory. The general trend in the force history, however, seems to be correct. It is therefore suggested to apply a low pass filter to the force history data.

The virtual test has demonstrated that the one dimensional wave analysis is capable of accurately predicting impact force and beam deflection histories, given no stress waves present in the impactor bar before impact on the specimen. In the following section, the source of the trapped strain energy is identified and possible improvements of the experimental setup are suggested.

5.2.3 Investigation of the strain gauge signals

The pre impact oscillations on the strain gauge signals are the result of a mechanical vibration initiated by the initial collision of projectile and impactor. The oscillations on the signal are a consequence of stress waves which are trapped in the impactor bar after impactor and projectile separate. Improving the quality of the strain gauge signal requires a detailed investigation of the interaction between the projectile and impactor bar. This initial collision can be recorded by the strain gauge (see data in Fig 5.8). In an ideal situation, the impact of the projectile should generate a steeply rising stress wave to a constant magnitude in the impactor. The initiated compressive wave travels through the impactor at the materials wave speed and gets reflected as a tensile wave of identical magnitude at the free end. The back travelling tensile wave cancels the compressive wave as they meet. The projectile and impactor have the same impedance and so they travel together with an velocity

$$v = \frac{v_0}{2}, \tag{5.1}$$

after the collision. In Eqn 5.1 v_0 is the impact velocity of the projectile. Only once the reflected tensile wave reaches the interface between impactor and projectile do both separate. The impactor bar continues travelling at v_0 while the projectile stops because all of the momentum has been transferred to the impactor bar. The wave propagation in both bars is illustrated for an ideal situation in Fig 5.7(a).

In the recorded signal the initiated stress wave rises in two steps. The first sharp rise is the originated compressive stress wave when projectile and impactor bar collide. This pulse is followed by a smaller less steep rise. The second rise seems to be caused by an additional reflection in the projectile which is transmitted into the impactor as both bars are still in contact (see Fig 5.7(b)). The time shift between the two steps enables calculation of the location in the projectile where the reflection occurs. The analysis shows that the first of the two nylon bushes is attached to the projectile in that region. The impedance mismatch at the bushes causes parts of the compressive wave to be reflected. This reflection is visible as an additional compressive pulse on the strain gauge readings. An analytical and numerical analysis of the experimental setup has been performed to demonstrate the effect.

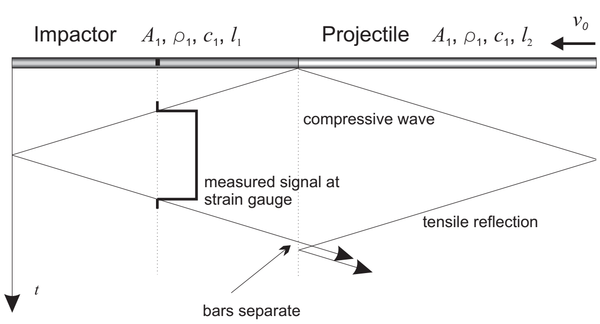

(a) projectile with no bushes

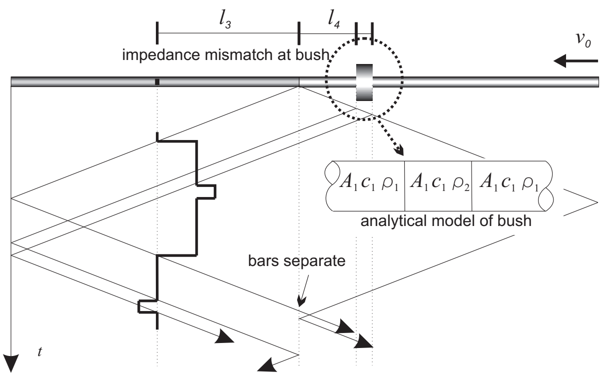

(b) projectile with bushes

Figure 5.7: Lagrange diagrams of the collision projectile-impactor bar (schematic)

For this simple case the wave propagation can be calculated analytically. The addition of bushes is modelled as a change in density resulting in a change of impedance. The density for this section of the bar is obtained by concentrating the mass of the bush in the actual bar. The cross section and the wave speed are assumed to be constant (see Fig 5.7(b)). This simplification implies a perfect bond between bush and projectile which is not the case in the experimental setup. Furthermore, only the first bush is modelled, which is sufficient to demonstrate the source of the trapped waves.

The impact of projectile and impactor with a velocity v_0 initiates a compressive stress wave of the magnitude

$$\alpha_1 = \frac{1}{2}\rho_1 c_1 v_0 \tag{5.2}$$

When the stress wave α_1 hits the bush in the projectile, the change in impedance causes a compressive stress wave of the magnitude

$$\beta_1 = \frac{\rho_2 - \rho_1}{\rho_2 + \rho_1}\alpha_1 \tag{5.3}$$

to be reflected, while a compressive wave α_2 of magnitude

$$\alpha_2 = \frac{2\rho_2}{\rho_2 + \rho_1}\alpha_1 \tag{5.4}$$

continues to travel down the projectile. At the other end of the bush the wave α_2 hits another impedance mismatch (density decreases) which results in a tensile reflection

$$\beta_2 = \frac{\rho_1 - \rho_2}{\rho_1 + \rho_2}\alpha_2 \tag{5.5}$$

Knowing the dimensions of projectile and impactor and the position of the bush as well as the wave speed in the material, the stress history at the position of the strain gauge on the impactor bar can be calculated. The analytical stress history is compared with the example obtained from an experiment (see Fig 5.8).

The analytical wave propagation predicts the main artifacts of the collision between projectile and impactor. The reflection of the bush arrives at the strain gauge at a similar time to the second step in the experimentally obtained data. The slope and magnitude, however, could not be predicted correctly. This is assumed to be a result of the simplifications of the analytical model. Additionally, the analytical model shows how the additional compressive wave gets trapped in the impactor bar, after projectile and impactor separate. This is the source of the ringing which influences the accuracy of the experimental data reduction.

A numerical study was conducted to model the scenario more realistically and to demonstrate how the signals can be improved. The numerical analysis was performed using the

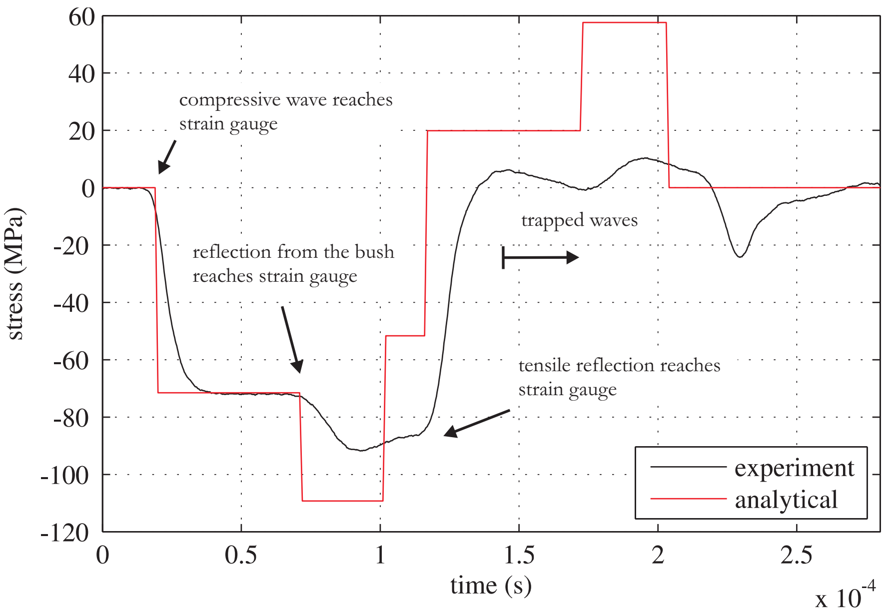

Figure 5.8: Comparison of stress waves generated by the collision of projectile and impactor bar

explicit FE solver LS-DYNA using the model described earlier in this chapter. A detailed simulation including both bushes and a simulation without bushes has been performed. In the detailed simulation the bushes are modelled explicitly fixed to the projectile. For comparison, the stress in the cross section, where the strain gauge is attached, is extracted. The comparison of experiment and numerical results is displayed in Fig 5.9.

The detailed simulation with both bushes supports the analytical results and clearly demonstrated the influence of the bushes on the quality of the signal. The difference between experiment and numerical simulation might be explained by the definition of the contact between bush and projectile. The simulation assumed a perfect bond, while the bushes can slightly move in the actual experimental setup. The simulation with no bushes results in a square pulse with only little strain energy being trapped in the impactor after the bars separate. The remaining vibrations are assumed to be mainly caused by the non ideal stress wave reflections at the wedge shaped impactor tip. Compared to the effect of the polymer bushes, this is of minor importance. In summary, modifying the experimental setup can significantly reduce the amount of trapped strain energy and subsequently improve the accuracy of the data reduction.

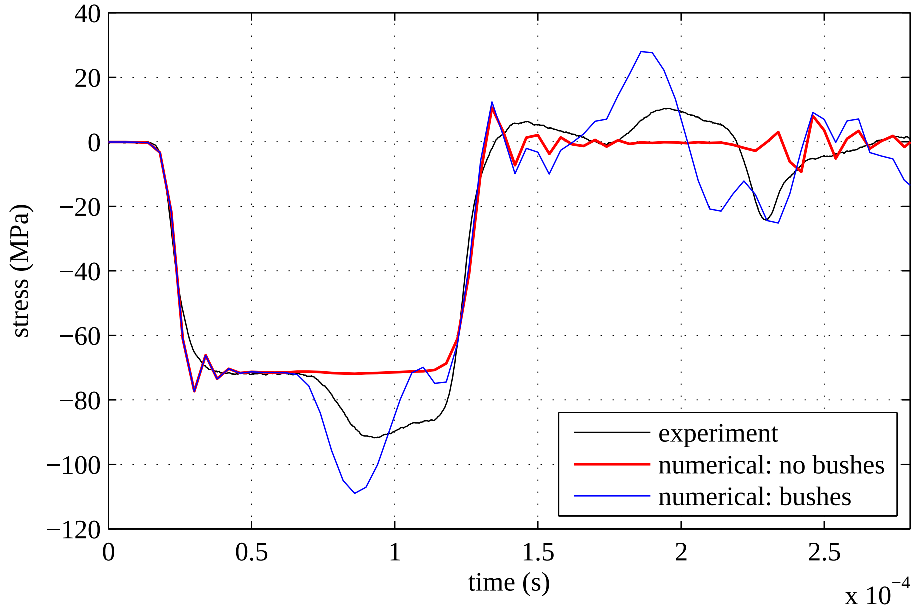

Figure 5.9: Stress wave during the collision of projectile and impactor bar: comparison of experiment and numerical simulation

5.2.4 Improved experimental setup and verification

Having demonstrated the main source of the trapped stress waves and shown that this is the reason for the inaccurate deflection prediction, the experimental setup was modified. The projectile now runs on nylon inserts which are attached to gun barrel rather than the projectile itself. As a result, no additional mass is attached to the projectile so that no impedance jumps occur along the bar. A comparison of the recorded signals obtained with the original and improved experimental setup is shown in Fig 5.10(a). The modified experimental setup results in a square pulse when projectile and impactor bar collide. Subsequently, fewer stress waves are trapped in the impactor as it flies towards the target specimen. The few remaining stress waves are a result of the non-uniform reflection of the wedge shaped impactor bar tip. The high frequent oscillations which appear when projectile and impactor collide are artifacts of wave dispersion and widely reported in Hopkinson bar experiments [109]. The oscillations usually decay before the impactor bar hits the beam specimen.

For the purpose of verification of the improved experimental setup, the experiments with steel beams are repeated. Again, the impactor bar movement is tracked using high speed photography. The accuracy has improved significantly as shown in Fig 5.10(b), compared to Fig 5.4. Finally, in Fig 5.10(c) the signal as obtained from the actual impact of bar and specimen is shown. The noise just before impact is significantly reduced in the improved setup.

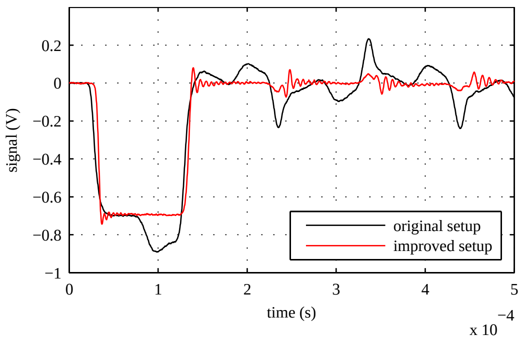

(a) improved strain gauge signal

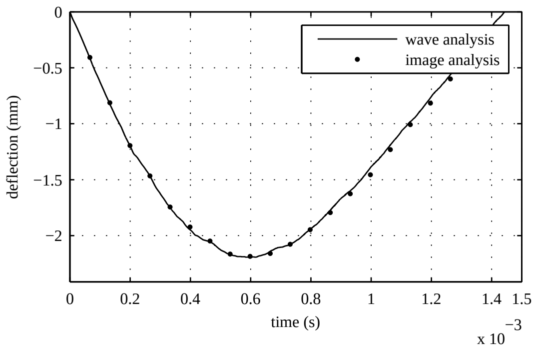

(b) improved deflection prediction

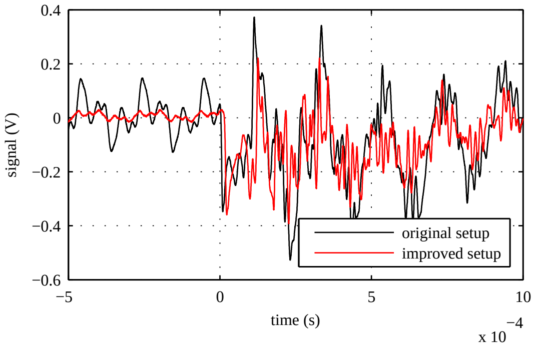

(c) comparison of the recorded impact signal

Figure 5.10: Verification of the improved experimental setup for impact bending

The experience of dynamic bending tests has shown that there is always some variation in the results because it is difficult to keep the testing conditions identical. In order to assess the reliability of the analysis, five steel specimens have been impacted with the original and the modified setup respectively. The difference between the deflection calculated by the use of the wave analysis and the deflection as obtained from the image analysis has been used as an assessment criterion for the accuracy. In order to eliminate effects of varying impact velocities, the difference has been normalised with respect to the maximum deflection as seen by the image analysis. The comparison is displayed in Fig 5.11.

The improvement of result accuracy is visible from Fig 5.11. The original experimental

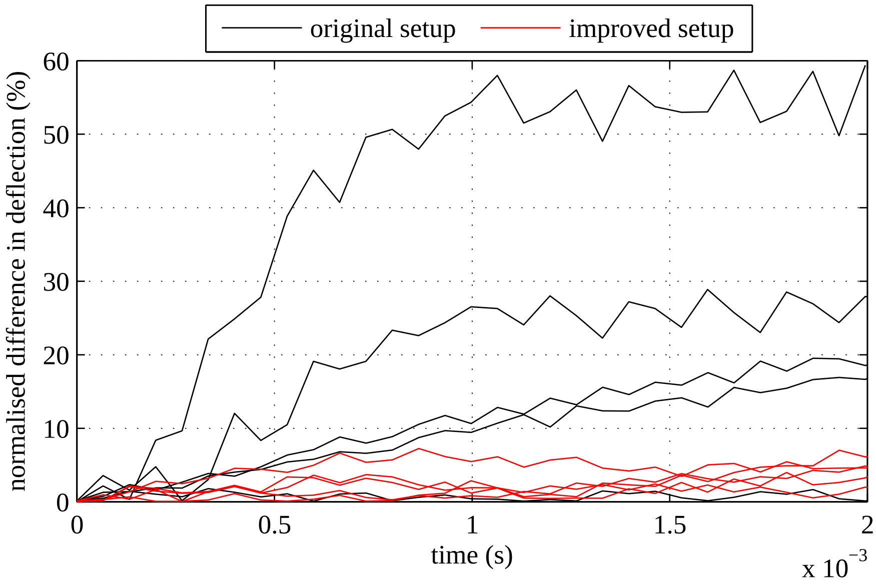

Figure 5.11: Repeatability of analysis accuracy for both experimental setups

setup yielded an unreliable estimation of beam deflection. In some cases the error could rise up to 60%. The modifications allow for a more accurate calculation of deflection and less scatter in the results. According to the tests performed her, the deflection is calculated with a measurement error well below 10%.

Additionally to the signal improvements as described above, the use of optical measurement techniques enabled a better measurement of the impact velocity v_0. The data reduction is very sensitive to an accurate measurement of the impact velocity. The currently used light curtains do not give a very accurate measurement of the impact velocity and should therefore be replaced with laser based light curtains in the future.

It should be noted that the proposed methodology is not limited to beam bending but can be readily applied to plate bending experiments. The following section describes the bending setup being used to investigate the performance of composite beams in both, quasi-static and impact loading.

5.3 Three point bending experiments

In the previous chapter the uniaxial material response due to changing loading rate was studied. While this enables determination of intrinsic rate dependent material properties, it does not allow a verification of failure initiation due to multi-axial stress states. Furthermore, failure in uniaxial experiments occurs suddenly and catastrophically. This usually prevents a study of damage propagation. In order to verify the three dimensional failure model presented in Chapter 2, and to study the subsequent damage evolution, CFRP beams have been subjected to three point beam bending quasi-statically and under impact loading. The beam experiments have been designed to address a wide range of failure modes, from tensile/compressive fibre failure to IFF and delamination. The purpose of the experimental bending program is not the determination of intrinsic material properties but to measure boundary conditions for a subsequent constitutive model verification.

5.3.1 Specimen preparation and experimental setup

The specimens were cut from a single panel which consisted of 12 UD non crimped composite plies with the lay-up $[[0/90]_3]_s$ forming a 3 mm thick laminate. The respective UD plies were manufactured from T700 fibres embedded in MTM44 epoxy resin. The panel was produced using a resin transfer moulding (RTM) process in a non closed mould which resulted in one smooth surface and one rough surface. All specimens were loaded on the smooth surface. The specimens were cut with a water cooled diamond saw to a length of 80 mm and a width of 9 mm. The diamond blade guaranteed a good surface finish. The experimental setup for quasi-static and impact loading is illustrated in Fig 5.12.

Generating all the desired failure modes required two different specimen configurations. The highest axial stress in the beam is found in the surface layers where the axial strain reaches a maximum while the beam is bending. Specimens have been cut such that the fibres are oriented along the beam axis in the surface layers. These specimens are referred to as 0°-specimens. Additionally, specimens with fibres oriented transverse to the beam

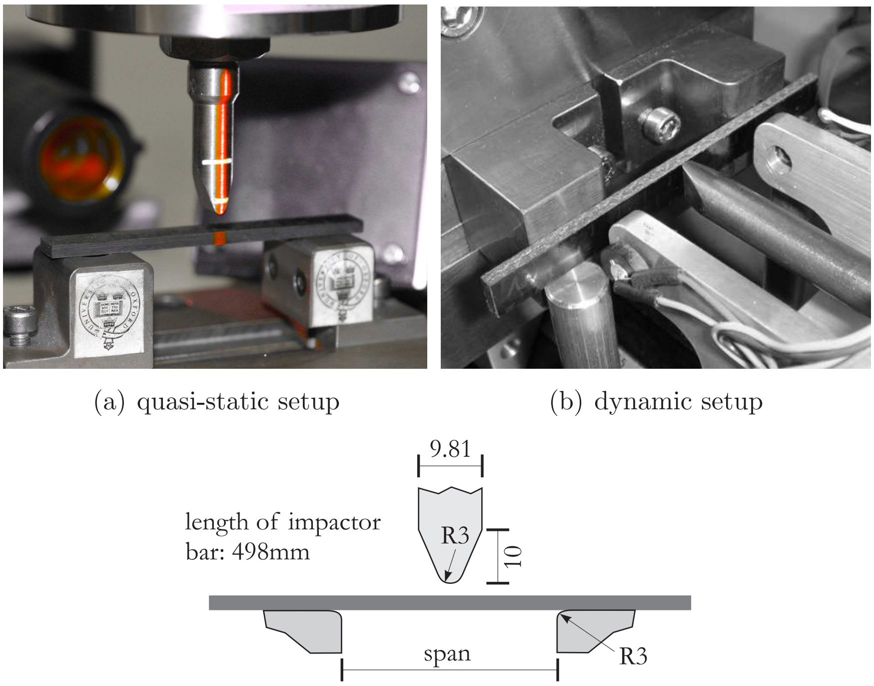

(a) quasi-static setup (b) dynamic setup

(c) rig dimensions

Figure 5.12: The experimental setup for three point bending

axis, the 90°-specimens, were also cut from the panel. This enabled fibre dominated failure modes as well as matrix dominated failure modes to be observed.

Both laminate configurations were subjected to quasi-static and impact bending. Each configuration was loaded at spans of 50 mm and 30 mm thus enabling failure modes of the outside surface layers and interlaminar failure modes around the centre plies due to high out of plane shear. This, together with the two laminate configurations enabled the study the influence of ply orientation on the delamination behaviour. All beams were loaded quasi-statically at a fixed loading velocity of 0.45 mm/min. The impact tests at a span of 30 mm were performed using impact velocities between 4.5 and 5.5 m/s. The impact at 50 mm span was performed with velocities ranging from 6.5 to 7.5 m/s. The impact velocities were chosen slightly above the threshold velocities which mark the onset of damage.

The surface of the beams loaded at a span of 50 mm was covered by a 0.5 mm thick steel shim, the protector, in the loaded region. The protector reduces contact stresses in the surface layers of the specimen thus avoiding premature compressive failure modes due to high contact stresses (see Fig 5.13). The force and deflection at failure initiation almost doubled when the protector was used.

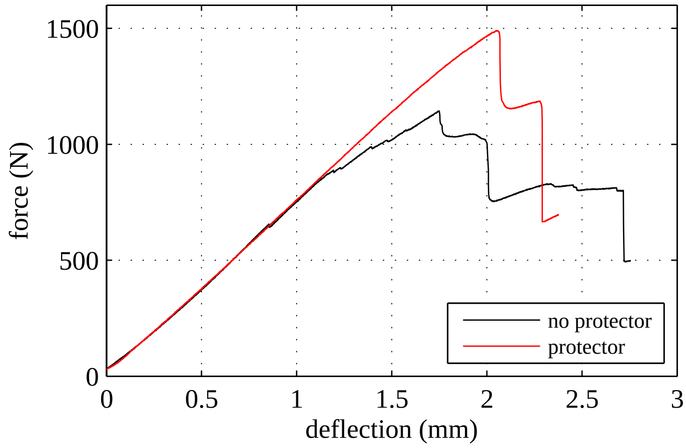

Figure 5.13: Influence of the protector on the failure initiation of the beam specimens

In the impact tests, the protector results in unfavorable strain gauge signals. The metal shim creates an additional impedance jump which results in stress wave reflections that do not represent the actual impact force on the specimen. Therefore, the force history data (not the strain gauge data) has been filtered using a low pass filter such as an running average. A comparison of force history data obtained with and without a protector sheet is displayed in Fig 5.14.

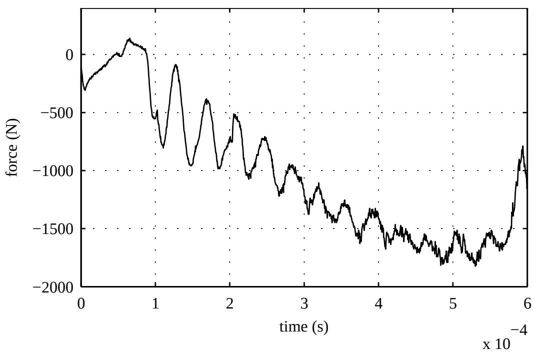

(a) no protector

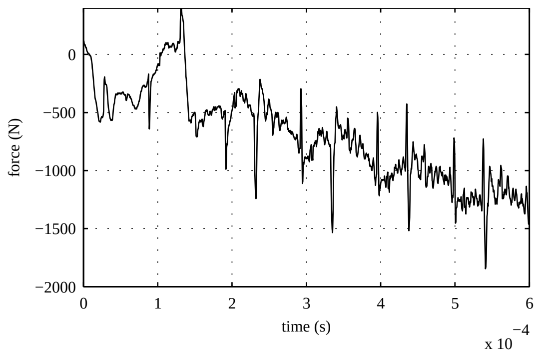

(b) protector

Figure 5.14: Influence of the protector on the quality of the force data (please note that both force histories have been obtained from different experimental setups and do not compare directly)

Quasi-static beam bending was performed on a screw driven tension/compression testing machine which has already been described in Chapter 4. The experiment was recorded with a high resolution (5 megapixel) digital camera at a frame rate of 1 frame per second. The impact experiments were performed on the improved impact bending rig as described in the previous section. All impact experiments were recorded with a Phantom digital high speed camera at a frame rate of 30000-35000 frames per second. The specimen fixture was designed such that it could be applied in both experimental setups. The boundary conditions should therefore remain identical for both set of experiments.

The measured force-deflection curves for the impact experiments appear very noisy due to inertia effects. The impactor and specimen are initially not constantly in contact. The whole impact consists of a series of small impacts with the relative impact velocity decreasing. This behaviour is more pronounced at a span of 50 mm as the beam bending stiffness is lower and the specimen tends to vibrate more. As the vibration amplitude gets lower, it can be assumed that both, specimen and impactor, are in permanent contact and the displacement of the impactor corresponds to the deflection of the beam. This was confirmed by the use of image analysis. The displacement of impactor and specimen were tracked separately during the experiment. The relative displacement of impactor tip and beam and the measured contact force are plotted in Fig 5.15. The comparison shows that the oscillations in the force data coincide with a non-uniform displacement of impactor and beam.

5.3.2 Identification of failure modes

All experiments were recorded using digital photography. Each experiment has been analysed individually and the sequence of failure modes were identified. The visible failure modes are then correlated with the force deflection data which in turn allowed conclusions to be drawn concerning whether the first visible failure mode is also the first failure mode in general. In principle, four initial failure modes could be identified:

- *compressive fibre failure by fibre kinking*
- *compressive IFF (often in conjunction with kinking)*

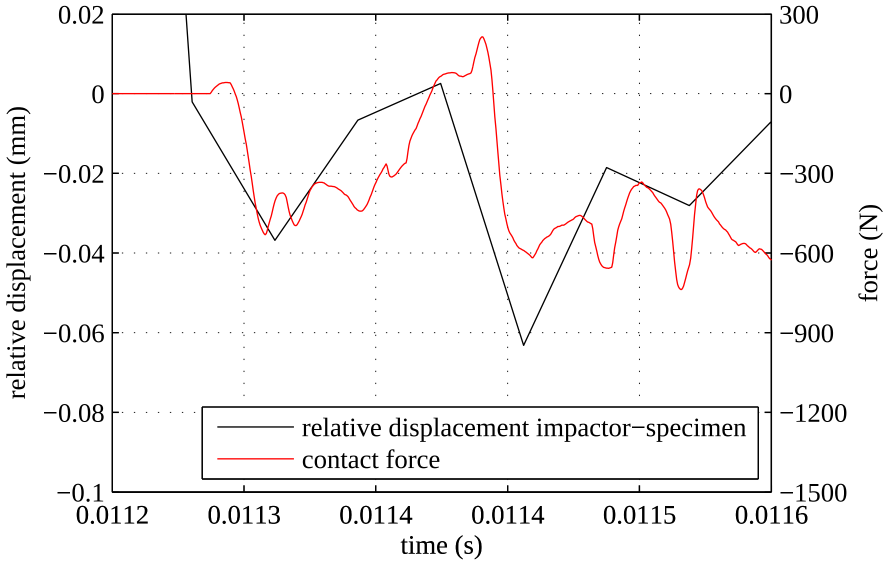

Figure 5.15: Investigation of the contact specimen-impactor directly after impact (rel. displacement > 0 - no contact, rel. displacement < 0 - impactor is pressed into specimen)

- *tensile IFF (often in conjunction with fibre rupture)*
- *delamination*

None of the tests failed by tensile fibre failure as a first failure mode. However, fibre rupture was observed in conjunction with tensile IFF. Typical initial failure modes for both, quasi-static and dynamic experimental setups, are displayed in Fig 5.16 and Fig 5.17.

5.3.3 Results and discussion

This section presents and discusses the results from the beam bending experiments.

The experiments with the $0°$ specimens and a span of 30 mm were designed for an interlaminar failure. Failure by delamination was observed in all specimens. However, failure in the quasi-statically tested specimens was initiated by a compressive fibre failure directly under the indenter and delamination formed only subsequently. The compressive failure mode occurred at a load of 1150 N while delamination was observed at a load of 1300 N. The impacted specimens failed due to fibre kinking in the surface ply directly under the

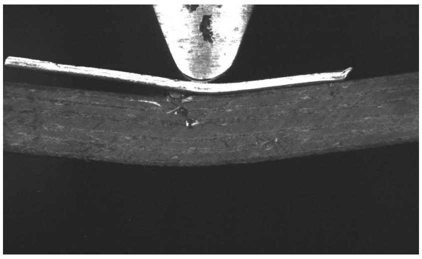

(a) fibre kinking/compressive IFF

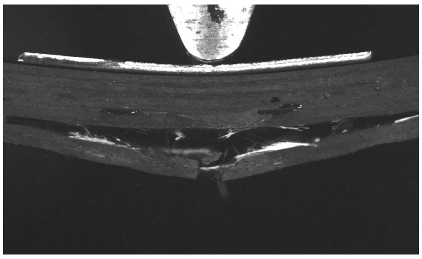

(b) tensile IFF and subsequent fibre rupture

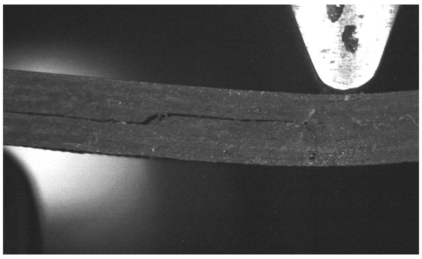

(c) delamination

Figure 5.16: Typical failure modes observed in quasi-static experiments

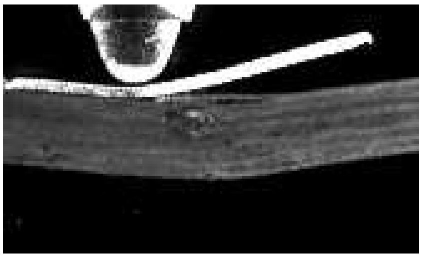

(a) fibre kinking/compressive IFF

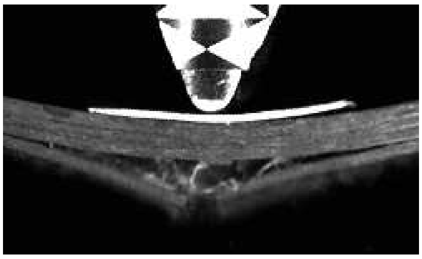

(b) tensile IFF and subsequent fibre rupture

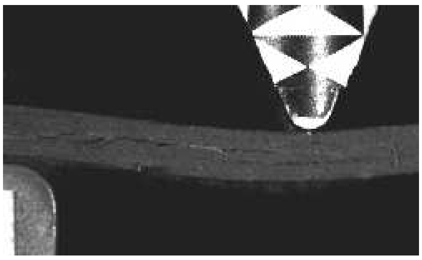

(c) delamination

Figure 5.17: Typical failure modes observed in dynamic experiments)

impactor followed by an IFF in the ply underneath. Subsequently, a delamination close to the neutral plane of the specimen formed. All impacted specimens failed at a load of approx. 1700 N. The force-deflection curves are presented in Fig. 5.18.

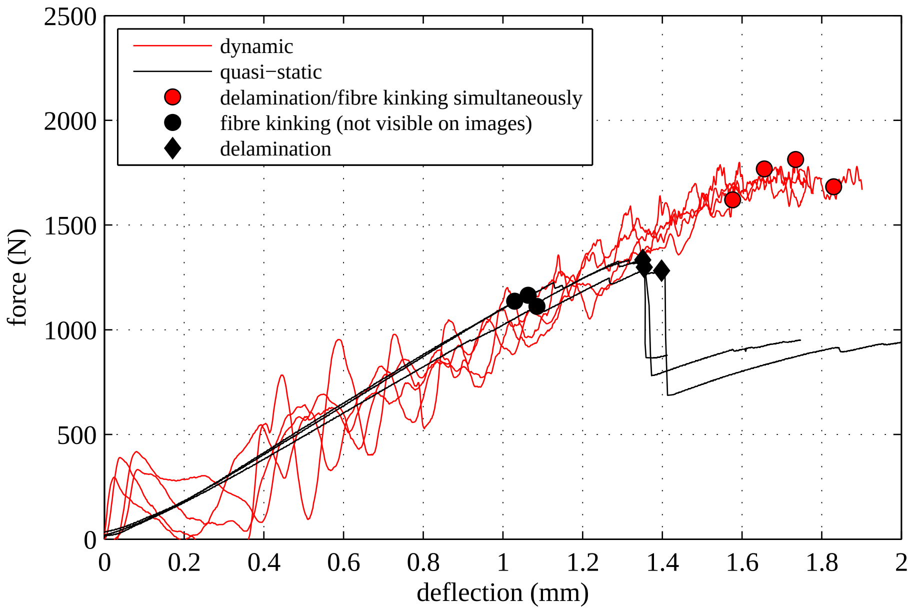

Figure 5.18: Force deflection data for 0° specimen tested with a span of 30 mm

The experiments with the 0° specimens at a span of 50 mm address the fibre failure modes. As the tensile strength of composites is usually significantly higher than the compressive strength, failure on the compressive side of the beam is expected. All specimens failed with a compressive failure as the first failure mode. The initial failure mode for the quasi-static experiments, however, was not visible on the images but clearly detectable as a small drop in force. The first visible failure usually coincided with the bigger drop of force after which the curve has been cut. The failure initiation in the impact experiments usually coincided with an observable drop in force as kinking initiated followed by a tensile IFF and fibre rupture on the tensile side. A significant increase of the force at failure compared to the quasi-static experiments was observed. The force rose by 56% from approx. 820 N to 1270 N. The corresponding force-deflection curves are presented in Fig 5.19.

The experimental setup of 90° specimen tested with a span of 30 mm aimed at an interlaminar failure mode (e.g. delamination) similar to the 0°-specimen tested at the same span.

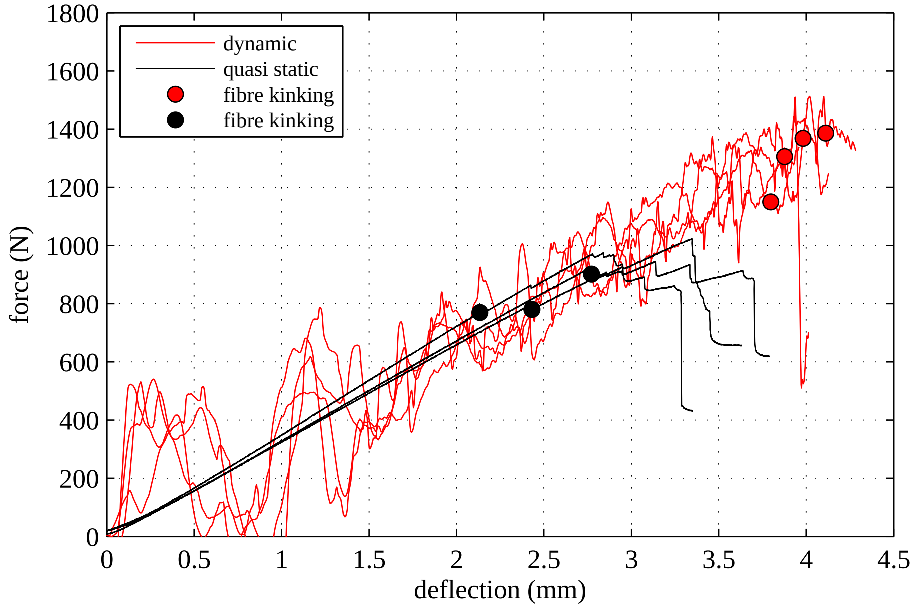

Figure 5.19: Force deflection data for 0° specimen tested with a span of 50 mm

However, the observed failure behaviour was more complex for this setup. At quasi-static loading velocities failure initiation was not visible on the recorded images. The initiation could only be detected by a slight drop of the recorded force. It is assumed that failure initiated by either compressive matrix failure under the indentor or fibre kinking in the ply below. The observed force at failure was quite low (650 N, 950 N). After failure initiation, the beams continued to bend at a slightly lower stiffness until the first visible failure mode occurred. All three beams failed by fibre kinking in the ply below the loaded surface at a load of approx 1200 N (one beam already showed a visible failure at approx. 1000 N). The impacted specimens failed by a simultaneous fibre kinking and fibre rupture/tensile IFF which in one case formed large scale delaminations. All failure modes occurred at very similar loads (approx. 1600 N). Damage progressed through the entire thickness of the beam specimen. The force-deflection curves are presented in Fig 5.20.

The matrix governed failure modes were addressed by the 90° specimens tested with a span of 50 mm. Two failure modes, fibre kinking and a combined tensile IFF with fibre rupture, were identified for quasi-static loading. Fibre kinking happens at a load approx. 900 N and the tensile IFF is reported at approx. 1100 N. The dynamic failure mode was clearly identified as tensile IFF and fibre rupture on the back face of the beam specimen at a load of approx 1150 N. As a consequence, large delaminations formed. The compressive failure was not observed in the dynamic loading regime. This might be caused by the complex stress state in the region where the impactor hits the beam specimen. The high compressive transverse stress σ_{22} and, resulting from the contact, a compressive through thickness stress σ_{33} seems to impede compressive failure. Surprisingly, no significant increase in force was observed between the tensile IFF at quasi-static loading and impact loading. The force-deflection curves are presented in Fig. 5.21.

In addition to the assessment of the sequence of failure modes for each setup, conclusions related to the delamination behaviour of the material may be drawn. After testing the material with beams oriented in 0° direction and 90° direction, the influence of ply orientation on the delamination behaviour was investigated. All specimen which showed delamination, where examined under a microscope to identify the preferred path of the delamination. The delamination in the 0° specimens initiated at the interface between the central plies and the adjacent plies of different orientation on the compressive side of the beam (the side where the indenter/impactor is in contact with the specimen). Initially, the delamination grows along this interface, but then forms a matrix crack through the two central plies to continue at the next interface between plies of different orientation.

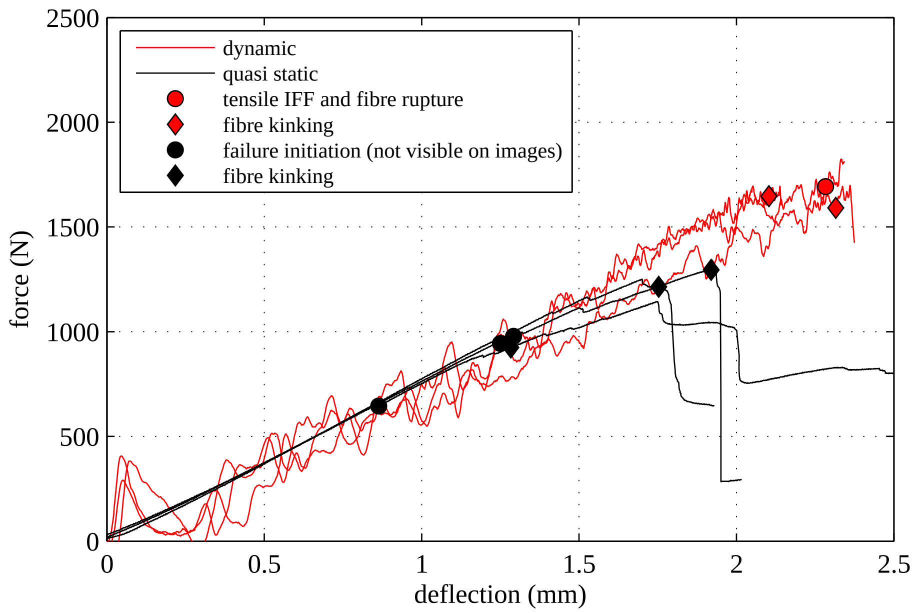

Figure 5.20: Force deflection data for 90° specimen tested with a span of 30 mm

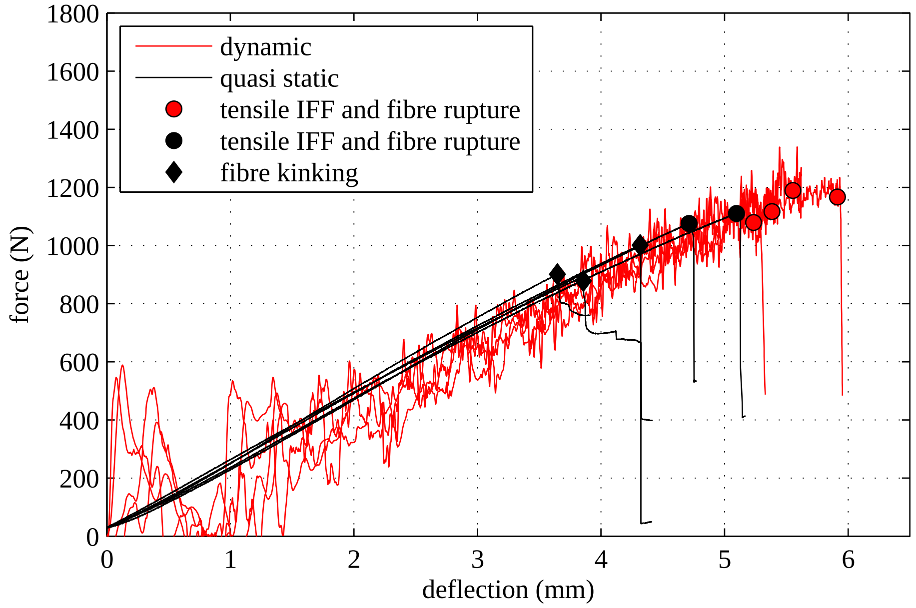

Figure 5.21: Force deflection data for 90° specimen tested with a span of 50 mm

The observed delamination pattern in 90° specimens was different to the 0° specimens. Two 0° plies are located in the centre of the beam. The delamination initiates, similar to the 0° specimens, but cannot break the central 0° plies as this would require breaking the fibres. Instead, in some cases, a second delamination formed on the other side of the central plies and continued growing along the path of maximum shear stress. In general, no evidence of delamination growing consistently between plies of the same orientation has been found in any of the tested specimens. This indicates that delamination tends to form and propagate between plies of different orientation. Resistance to delamination seems to be significantly lower between plies of different orientation. The different delamination patterns are shown in Fig 5.22.

The observed damage initiation as presented here is based mainly on identification by digital photography. For the quasi-static experiments, it has already been demonstrated that the first visible damage does not always coincide with the actual onset of damage. Therefore, it can be expected that similar difficulties exist in the impact experiments. However, the naturally very noisy impact force history does not allow for a detection similar to the quasi-static data. Especially for the compressive failure modes, the presented damage initiation force might be too high. The observation of damage initiation could be

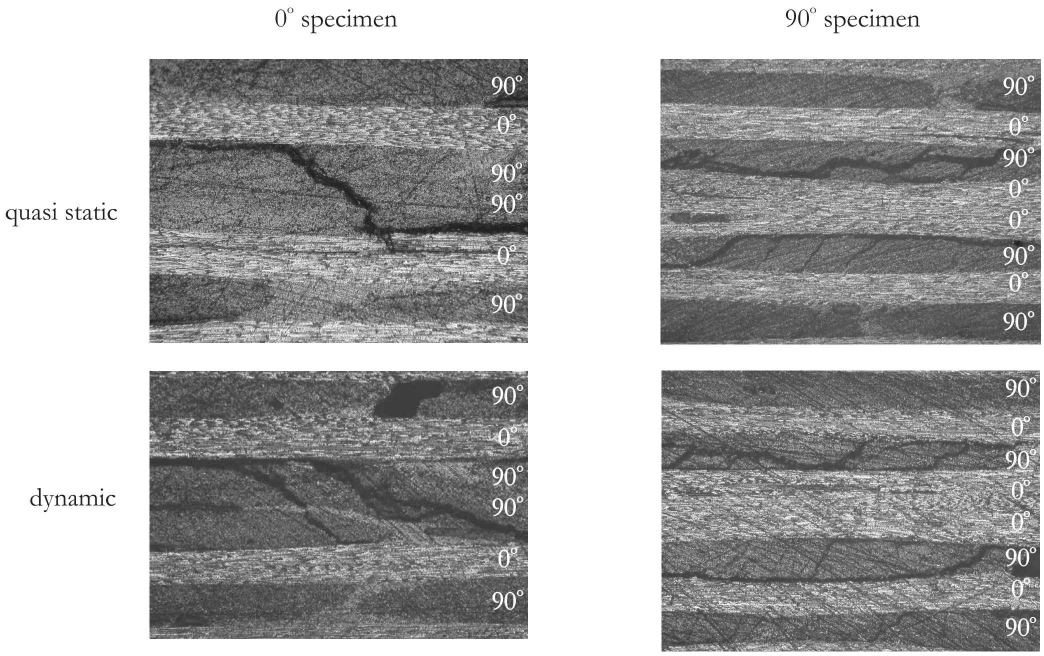

Figure 5.22: Experimentally observed delamination propagation

improved by higher resolution images thus enabling DSP on the beam which might reveal some localisation of deformation before the actual fracture is visible. Another key aspect of the investigation of damage initiation is a rigorous assessment of the initial damage state of the material after manufacturing. It is well know that many composite laminates have initial defects due to manufacturing. Non destructive inspection could be used to gain a better understanding of the relation between initial defects and damage initiation.

The nature of three point beam bending resulted in failure initiation by fibre kinking in many cases. The reason is that the region of high stresses due to bending coincided with the region where the force is transmitted into the specimen. This results in complex states of stress which often lead to failure by fibre kinking. If the experimental setup were to be further developed to enable four point beam bending experiments, then the load would not be transmitted in the region of maximum surface stress which would minimise the effect of contact stresses on failure initiation. This would allow for a better study of the failure modes independent from each other.

5.4 Summary

An improved method for impact bending experiments has been presented in this chapter. The experimental setup and subsequent data reduction has been verified both experimentally and numerically for three point beam bending. Optical measurement techniques like DSP were used to verify the deflection history as obtained from one dimensional wave analysis. Furthermore, DSP enabled a more accurate measurement of the impact velocity. It was demonstrated that accuracy improved significantly such that the data is suitable for constitutive model verification and validation.

The beam bending experiments demonstrated a wide range of different composite failure modes including fibre rupture, fibre kinking, IFF and delamination. Identical boundary conditions in quasi-static and impact experiments highlights the rate dependent material behaviour. A clear increase in force was observed for most configurations. This demonstrated the importance of incorporating strain rate dependent material behaviour into the constitutive equations.

The investigation of the influence of the ply orientation on the delamination behaviour concludes that delamination is very unlikely to initiate between plies of the same orientation. A more rigourous study, involving various ply orientations, should be undertaken to clarify what difference in angle would promote delamination and whether this changes due to loading rate.

The generated data will be used in the next chapter to demonstrate the model capabilities. The beam bending experiments will be modelled to verify the chosen failure model and the proposed damage model. Simulations will be performed for both, quasi-static experiments and impact experiments.

Chapter 6

Modelling of damage initiation and propagation in composite beams

In this chapter the proposed constitutive model is applied to simulate the performed three point bending experiment. The aim of the modelling exercise is the verification of the prediction of damage initiation and propagation.

6.1 The FE models

Two kinds of FE models have been created. First, the models for the quasi-static experiments and second, the models for the impact bending experiments. All models rely on a spatial discretisation by solid hexahedral elements with a single integration point. The link between the individual parts of the models is established by standard penalty method based contact available in LS-DYNA. The geometry of the bending rig has already been presented in Fig 5.12(c). The specimen in the FE model is 80 mm long, 9 mm wide and 3 mm thick. All layers of the composite beam specimen have been modelled explicitly using two elements per ply thickness. The interface is modelled with very thin solid elements. These elements are excluded from the time-step calculation as explained earlier (see Chapter 3) thus allowing for the simulations to be completed within a reasonable time. The intralaminar constitutive model (fibre rupture, fibre kinking, IFF) was used to simulate the ply behaviour, while the delamination model was applied to the interface elements. Four different configurations have been modelled, both, quasi-statically and dynamically. The beam specimen with the fibres in surface plies oriented along the beam axis (0° specimen) and the fibres oriented transverse to the beam axis in the surface plies (90° specimen). Bending with a span of 30 mm and 50 mm was modelled for each specimen type.

The indenter is simplified by only modelling the tip in the quasi static models. The support is modelled as rigid body. In order to solve the problem in a reasonable time, mass scaling has been used. Therefore, artificial mass is added to each element by LS-DYNA to obtain a longer time step. Mass scaling as widely used in explicit FE to simulate processes where the observed accelerations are very small and, consequently, inertia effects can be neglected. Mass scaling should always be used with care as it can result in contact instabilities due to large penetrations and unrealistic high inertia force if the density is increased too much. For the quasi-static simulations, the built in mass scaling option in LS-DYNA was used. The time step was forced to 0.002 s. The parts of the beam which extend beyond the support do not influence the quasi-static response of the beam and were therefore not modelled. As a result, the specimen in the models with a span of 30 mm is only 40 mm long and in the models with a span of 50 mm is only 60 mm long. The load was applied by a prescribed velocity to the nodes of the indenter. The FE meshes used for the quasi-static simulations are displayed in Fig 6.1(a) and Fig 6.1(b).

Modelling the impact experiments required an accurate representation of the interaction of impactor and beam. Therefore, the impactor and the beam specimen have been modelled in full detail. Inertia effects are important in dynamic simulations. Therefore, the correct density and specimen geometry is used in the simulations. The impact was simulated by prescribing an initial velocity to the impactor. The support is modelled as a rigid body. The two meshes are displayed in Fig 6.1(c) and Fig 6.1(d).

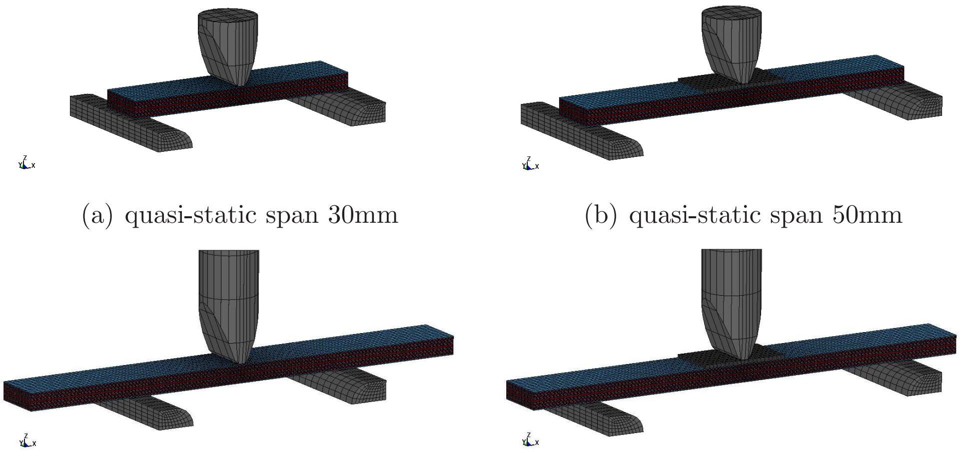

(a) quasi-static span 30mm (b) quasi-static span 50mm

(c) dynamic span 30mm (d) dynamic span 50mm

Figure 6.1: FE meshes used for the simulations

6.2 Material properties

The intrinsic properties of the UD ply could not be obtained experimentally because no UD laminate was available for this study. Therefore, the material properties needed to be estimated. The chosen estimation procedure relies on a theoretical prediction of material properties with a subsequent manual inverse modelling procedure of the experimentally investigated three point bending and uniaxial compression experiments. The theoretical prediction of properties was performed with the University of Twente Micromechanics Modeller (U20MM [47]). This open source tool allows calculation of theoretical material properties basing on the mechanical properties of the ingredients and the fibre volume fraction. The predictions were obtained by the Composite Cylinder Assemblage (CCA) model which was proposed by Hashin [123]. The fibre volume fraction was assumed to be 50%. The properties of fibre and matrix are displayed in 6.1. The Young's modulus

Table 6.1: Composite material properties used for deriving the properties of the T700/MTM44 composite

	E/E_1(GPa)	E_2(GPa)	ν
T700	230	10	0.3
MTM44	3.3	-	0.38

was adapted to the tangent modulus of the uniaxial compression experiments which were performed with the material. The initial tangent modulus of the whole cross ply laminate was obtained as 50.1 GPa. Using the rule of mixture and the theoretical prediction for the transverse plies, the Young's modulus in fibre direction was obtained as 94.23 GPa. The whole set of elastic properties is presented in Tab 6.2.

Table 6.2: Composite material properties used for the LS-DYNA analysis

E_1(MPa)	E_2(MPa)	E_3(MPa)	G_{12}(MPa)	G_{23}(MPa)	G_{13}(MPa)
94228	4800	4800	2.75	2.40	2.75
density(t/ mm^3)	ν_{12}	ν_{23}	ν_{13}		
15.58	0.42	0.247	0.42		

A comparison of the experimentally obtained force-deflection response with the numerically calculated behaviour shows a good agreement (see Fig 6.2). The oscillations on the numerical force deflection response are a consequence of the mass scaling. The immense inertia due to the artificially increased density results in unrealistically high contact forces when indenter and specimen get in contact. This effect is only observable in the early stage of the simulation when the beam is accelerated and is assumed not to affect the overall solution.

An initial guess of the strength properties was obtained from available experimental data and data sheets provided from the manufacturer (Advanced Composite Group - ACG MTM44 matrix resin). Subsequently, the properties were refined by a manual inverse procedure to represent the damage initiation as observed in the quasi-static experiments. The set of strength parameters used in the simulations is presented in Tab 6.3.

Table 6.3: Strength properties used for the LS-DYNA analysis (the values in brackets are the initial guesses where applicable)

X_t(MPa)	X_c(MPa)	Y_t(MPa)	Y_c(MPa)	S_{12}(MPa)
1900(1602)	1200(1036)	90(46.5)	250(215)	80(100)
S_f(MPa)	Z_t(MPa)	S_d(MPa)	θ^0_{fr} (°)	ψ (°)
130	70	40(63)	53	90

The curves which describe the rate dependent material properties are derived from the

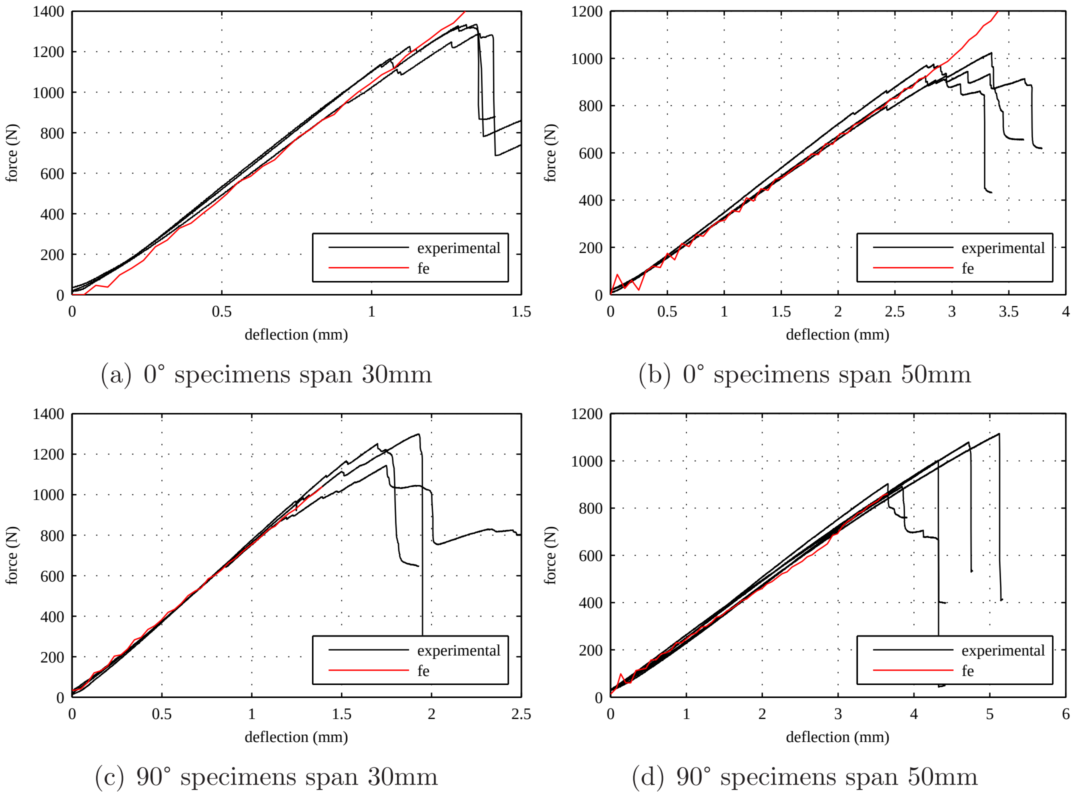

(a) 0° specimens span 30mm

(b) 0° specimens span 50mm

(c) 90° specimens span 30mm

(d) 90° specimens span 50mm

Figure 6.2: Verification of stiffness properties by comparison with experimental data

pure RTM6 data given in [49]. The data seems to fit the experimental data reasonably well (see Chapter 4) and seems to be a good approximation for the properties which could not be derived experimentally for this thesis. The following two rate dependency parameters are used

- *rate dependency of the stiffness* $K_1 = 0.0005$
- *rate dependency of the strength* $K_2 = 0.00035$

The curves defined by the above parameters are already illustrated in Chapter 2 (see Fig 2.29). The damage model has been calibrated according to the procedure as described in Chapter 3.7. The fracture energies were taken from [8] and are given in Table 6.4.

6.3 Quasi-static bending simulations

The purpose of the simulation of the quasi-static three point bending experiments was the verification of the model for the prediction of the onset of damage evolution. The proposed damage evolution algorithms could not be applied because of the mass scaling. When damage initiates, the problem does not remain quasi-static anymore as the energy release results in the sudden acceleration of certain sections of the beam. The artificially increased density would then result in unrealistically high inertia forces in the numerical simulation. The damage evolution could be modelled if the analysis would be restarted without mass scaling. As a consequence, the time step would be very small and the simulation could not be solved on a single cpu anymore. Therefore, only the analysis of damage initiation has been performed here. As already explained above, both stiffness and strength properties have been manually optimised to fit the experimental results. Therefore, the results as presented below suit the purpose of model verification but should not be seen as model validation.

6.3.1 0° specimens tested with span 30 mm

The quasi statically tested beams failed initially by local fibre kinking under the indenter. The FE model was able to predict the location of damage initiation correctly (see Fig 6.3 (b)). The Mohr Coulomb behaviour, which is built into the IFF model, results in prevention of IFF in that region despite the high local stresses arising from the contact with the indentor. This corresponds well with the experimental observations. The load at which kinking initiates, however, was underestimated in the simulation. One reason might be that the indentor tip is not modelled with sufficient accuracy and the contact induced

Table 6.4: Fracture energies for the calibration of the damage model (data taken from [8])

	fibre rupture	fibre kinking	IFF	delamination
G_{Ic} (N/mm)	91.6	79.9	0.22	0.258
G_{IIc} (N/mm)			1.108	1.108

stress state in the area is not very realistic.

The main mode of failure for this experimental setup was delamination. The numerical prediction of the deflection at delamination initiation corresponds well to the measured data. The force at delamination initiation cannot be directly compared as delamination initiated always after a fibre kinking failure and the damage evolution and subsequent stress redistribution was not modelled for the quasi-static cases. However, the improvements of the extended delamination initiation criterion could be demonstrated. Fig 6.3 (c) shows the exposure e_4 for both, tensile stress and compressive stress σ_{33}, at the onset of delamination and the exposure e_4 due to a negative stress σ_{33} only. Traditional delamination initiation criteria would not predict delamination under compressive normal stress in the delamination plane. A comparison with the experimental result, however, shows that the region with $-\sigma_{33}$ covers the observed initiation region. The ply of initiation is predicted slightly inaccurate as delamination would initiate above the central plies. It is assumed that this is caused by not considering the stress redistribution due to kinking.

The experimentally obtained force-deflection curves and observed damage initiation modes are compared with the numerical prediction in Fig 6.3 (a).

6.3.2 0° specimens tested with span 50 mm

The 0° specimens tested at a span of 50 mm all failed by fibre kinking. failure always initiated in the surface (0°) plies slightly outside of the region where the indentor was in contact with the specimen (see Fig 6.4 (b)).

The simulation accurately predicts the location of fibre kinking initiation. The maximum exposure is predicted in the surface ply in the immediate vicinity of the indentor's contact with the specimen. The very high through thickness stress under the indenter prevents the kink initiation due to the Mohr-Coulomb type of failure criterium. It should be noted that, theoretically, the fibre kinking should be predicted on both sides of the region where the indentor touches the specimen. However, in the presented simulations the kink

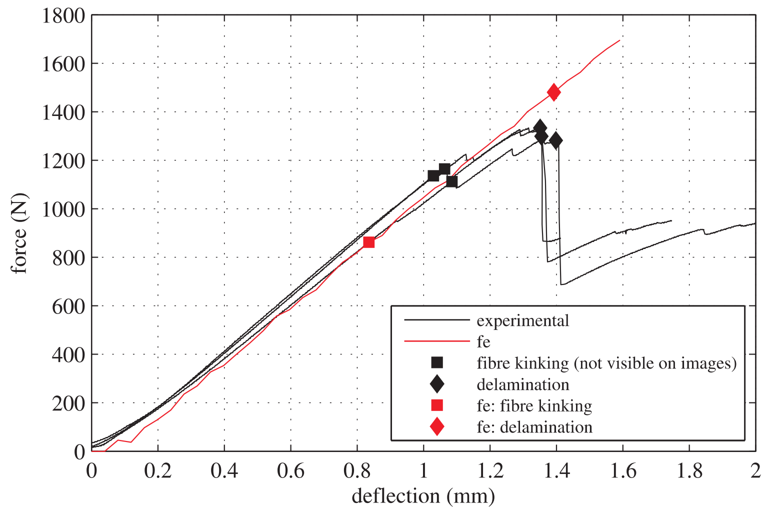

(a) comparison of force deflection curves from experiment and from the FE

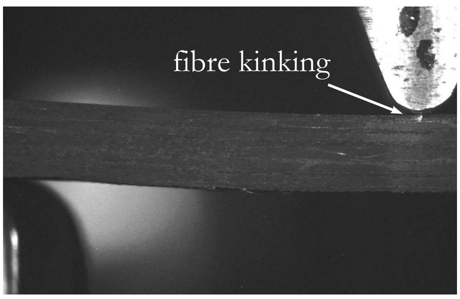

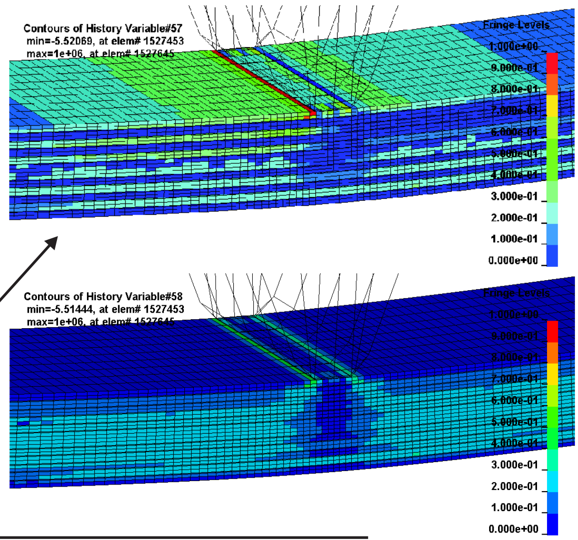

material exposure for fibre kinking

material exposure for IFF

(b) intralaminar damage initiation

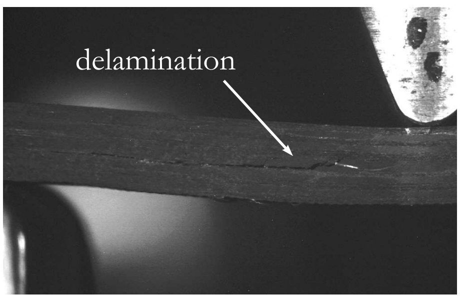

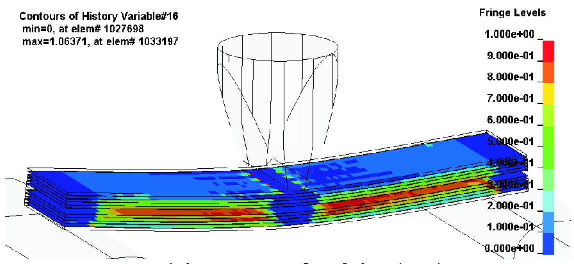

material exposure for delamination

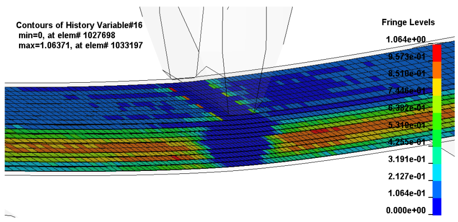

material exposure for delamination (magnified)

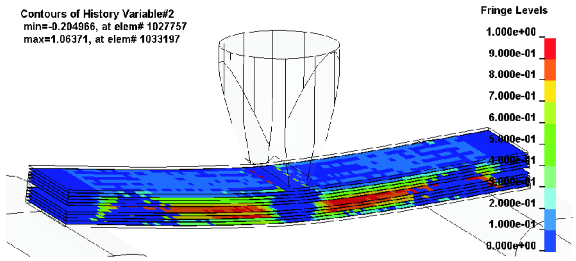

(c) interlaminar damage initiation

material exposure for delamination (for $-\sigma_{33}$ only)

Figure 6.3: Summary of FE results for the 0° specimen tested quasi-statically with a span of 30 mm

band angle ψ_k was set to a fixed value of $\psi_k = 90°$ (see Tab 6.3) while, theoretically, a kink band angle of $\psi_k = -90°$ would be possible too. The predicted load at kinking initiation was in good agreement with the experimental results.

The comparison of experimentally observed damage initiation and numerical representation is given in Fig 6.4 (b). The experimentally obtained force-deflection curves and observed damage initiation modes are compared with the numerical prediction in Fig 6.4 (a).

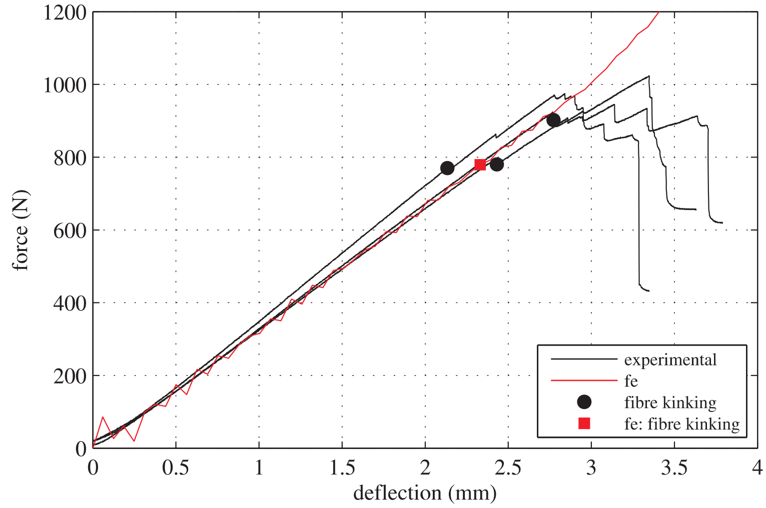

(a) comparison of force deflection curves from experiment and from the FE simulation

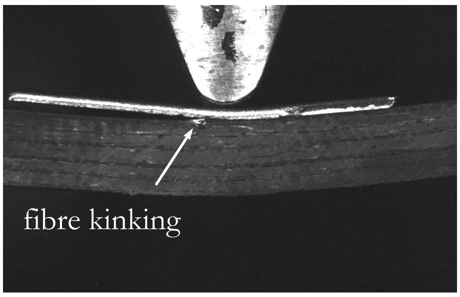

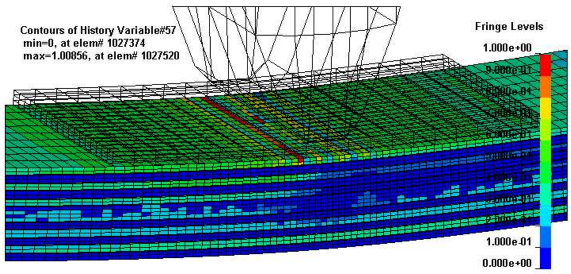

material exposure for fibre kinking

(b) intralaminar damage initiation

Figure 6.4: Summary of FE results for the 0° specimen tested quasi-statically with a span of 50 mm

6.3.3 90° specimens tested with span 30 mm

In the experiments damage initiation by fibre kinking was observed in the first subsurface ply (0°) on the side were beam and indentor are in contact (see Fig 6.5 (b)). Surprisingly, the surface ply with the highest strain along the beam axis and high contact stresses did not show any signs of damage initiation.

The model reproduced the same behaviour at matching load levels. The model prediction revealed the reason for damage initiation in the subsurface ply. The fibres are oriented transverse to the beam axis (90°) in the surface ply. The expected failure mode would therefore be IFF. The high compressive stresses in the contact region, however, prevent IFF due to the Mohr-Coulomb material behaviour and results in damage initiation by fibre kinking (see Fig 6.5 (b)). The Puck IFF model seems to be capable to correctly predict the failure mechanisms related to IFF.

The experimentally obtained force-deflection curves and observed damage initiation modes are compared with the numerical prediction in Fig 6.5 (a).

6.3.4 90° specimens tested with span 50 mm

The experiments resulted in two fundamentally different damage initiation modes. Some specimens failed due to fibre kinking in the subsurface 0° plies on the compressive side while others failed due to fibre rupture and tensile IFF on the tensile side of the beam at slightly higher load levels. The similar load and deflection at failure for both failure modes, again, underlines the Mohr-Coulomb material behaviour. In general, the compressive strength X_c in fibre direction is significantly lower than the tensile strength X_t. Compressive failure, however, is predicted using the Puck IFF model. The high compressive contact stresses in the area result in a higher load for compressive damage initiation and result in some cases in damage initiation by fibre rupture.

The model was able to predict both initiation modes. The kinking initiation starting in the second ply from the loaded surface (see Fig 6.6 (b)) and was predicted at similar

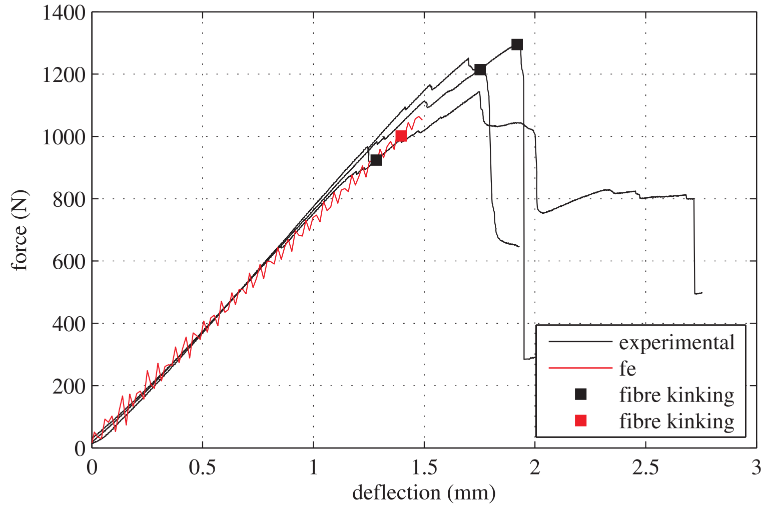

(a) comparison of force deflection curves from experiment and from the FE simulation

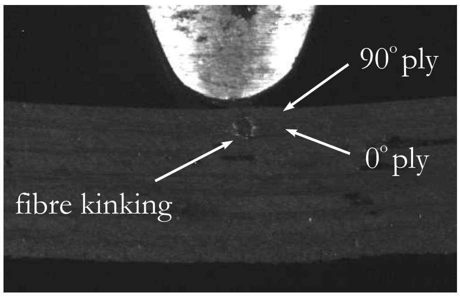

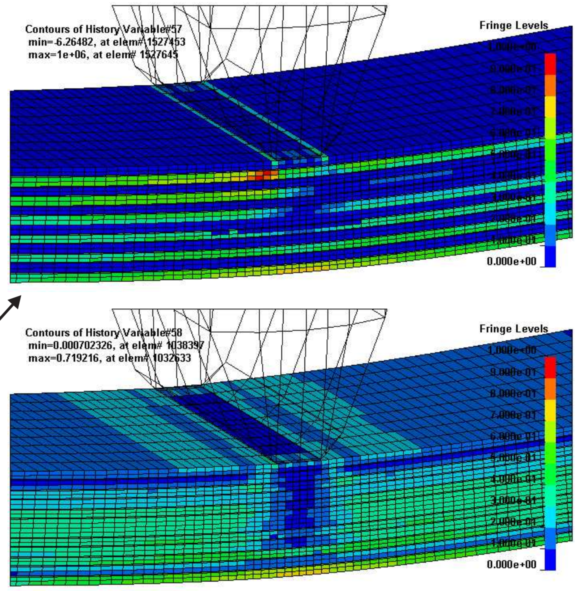

(b) intralaminar damage initiation

Figure 6.5: Summary of FE results for the 90° specimen tested quasi-statically with a span of 30 mm

load levels as observed experimentally (see Fig 6.6 (a)). The second predicted failure mode was fibre rupture/IFF (see Fig 6.6 (c)) which initiated at a slightly higher load as observed in the experiment. In general, a good agreement with the experiments was found. The prediction of the onset of compressive fibre failure by a simple maximum stress criterion or even some simple interaction criterion like the Hashin criterion, would not be able to predict this behaviour.

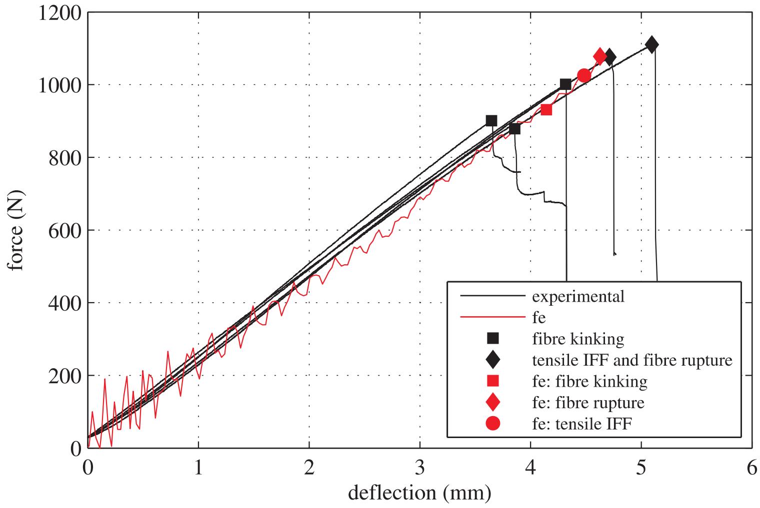

(a) comparison of force deflection curves from experiment and from the FE

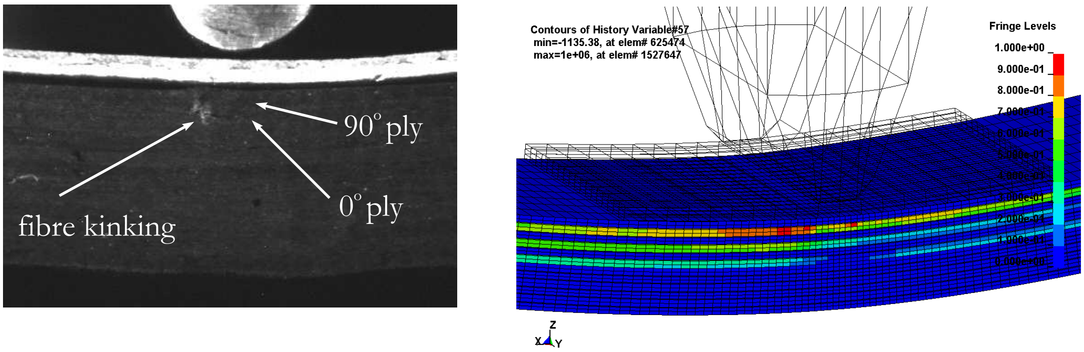

material exposure for fibre kinking

(b) compressive damage initiation

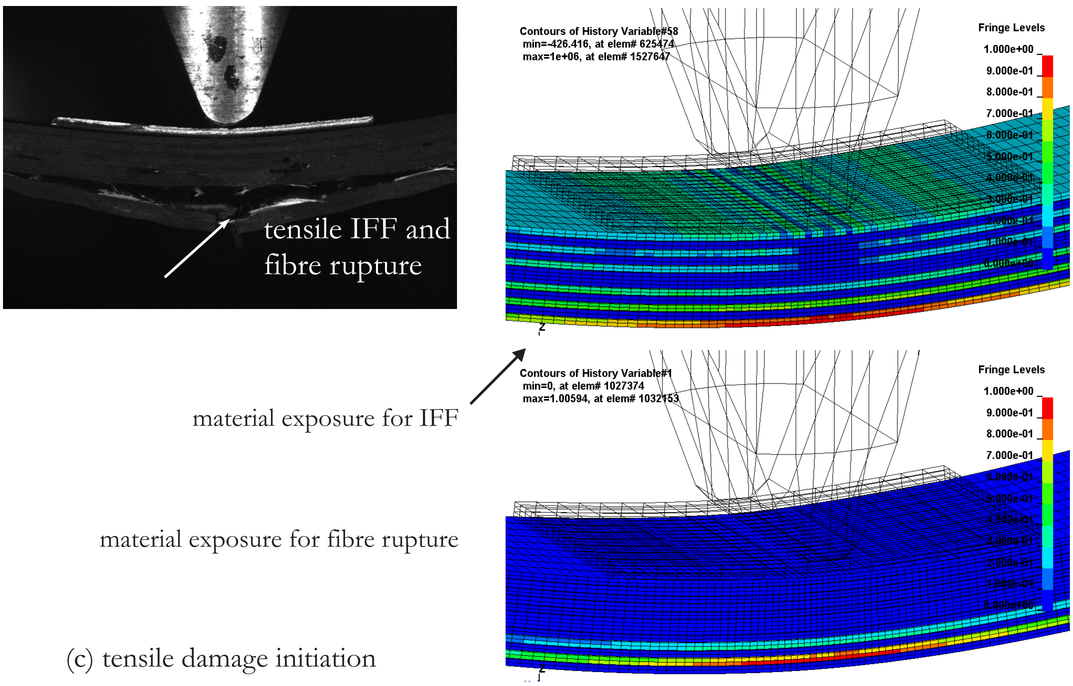

(c) tensile damage initiation

Figure 6.6: Summary of FE results for the 90° specimen tested quasi-statically with a span of 50 mm

6.4 Impact bending simulations

Selected impact bending experiments have been modelled in order to demonstrate the capability of the constitutive model for the prediction of damage evolution. The impactor bar is given the initial velocity as measured in the respective experiment and the experimental force deflection curves which are given for comparison here correspond to the experiment which was performed at the same impact velocity. The following section presents the obtained numerical predictions and compares them with the experimentally obtained results. The input properties are identical to the quasi static simulations. It should be noted that the presented numerical force data has been slightly filtered using a low-pass filter. The unfiltered response was very noisy due to the contact and would have made a direct comparison with the experiment difficult.

6.4.1 0° specimens tested with span 30 mm

The simulation was performed with an impact velocity of 5 m/s. The damage initiation was observed as fibre kinking in the ply closest to the impactor. IFF initiated on the compression side very shortly after the damage initiation by kinking. Subsequently, a large delamination formed close to the beam mid-plane.

The model correctly predicted damage initiation by fibre kinking, but at a lower deflection and force than in the experiment. The subsequent kinking evolution, however, did not seem to influence the overall stiffness response of the beam. In general, kink propagation evolved gradually and slowly rather then sudden as observed experimentally. One reason for that might be the chosen dissipation potential in the damage evolution equations for fibre kinking. The current formulation only relies in the shear stresses acting across the fibres for kink propagation. This might be too simple as it does potentially not include all stresses which contribute to fibre kink propagation. However, kink initiation in the experiments could have been detected at too high deflection. The resolution of the used high speed camera was not very high and the initial kinking might not have been identifiable on the images. Additionally, the penalty method used for the contact algorithms in the numerical model can result in unrealistic force peaks (which have been filtered out in Fig 6.7 (a) for clarity) which triggered initial kinking. Apparently, numerical kink propagation was really only predicted at a force which was very similar to the force at experimental kink initiation. The whole aspect of kink initiation will require more experimental investigation in the future.

Damage initiation by delamination with subsequent IFF and increased fibre kinking damage was predicted at a much higher deflection of approx. 1.4 mm. This correlates reasonably well with the experimental results. Unfortunately, the very thin delamination elements became unstable as delamination continued to grow. The extent of the final delamination could therefore not be modelled. Interestingly, IFF is predicted and propagated in the region where the delamination initiated to grow. The predicted fracture angle for IFF is scattering around 90° which would correspond to a failure in the delamination plane.

The total amount of predicted kinking damage is too high. The reason might be that underestimating delamination resulted in local stress too high in the kinking region. The initial loss of stiffness before the delamination formed in the experiments was captured well by the simulation. A summary of the simulation results is displayed in Fig 6.7.

6.4.2 0° specimens tested with span 50 mm

The simulation was performed with an impact velocity of 6.5 m/s. The specimen failed in the experiments in a sequence of fibre kinking on the compressive side of the beam followed by a tensile IFF and fibre rupture on the tensile side (see Fig 6.8 (b)).

The model predicts the sequence of failure modes accurately. Damage initiates by fibre kinking. The load and deflection at initiation was again lower than in the experiments. This probably due to the same reasons as described before. The initiation of kinking was predicted at a deflection which is too low. As the beam continues to deflect, however, the initial fibre kinking failure does not seem to progress. A significant growth of the kinking is

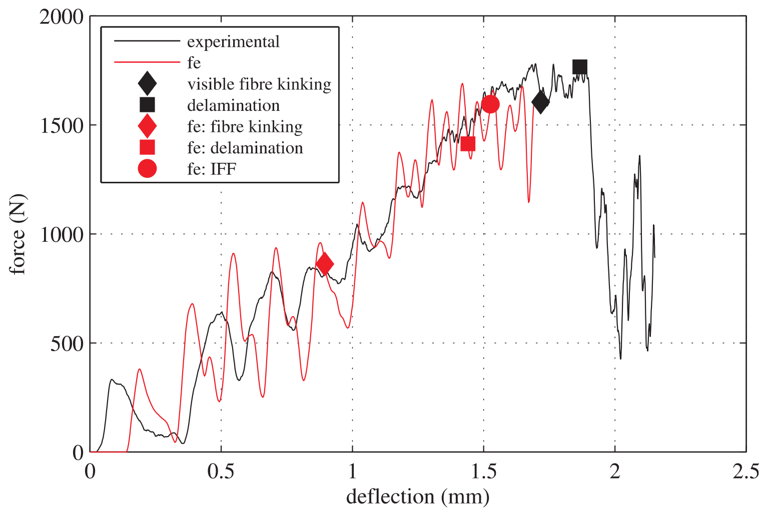

(a) comparison of force deflection curves from experiment and from the FE

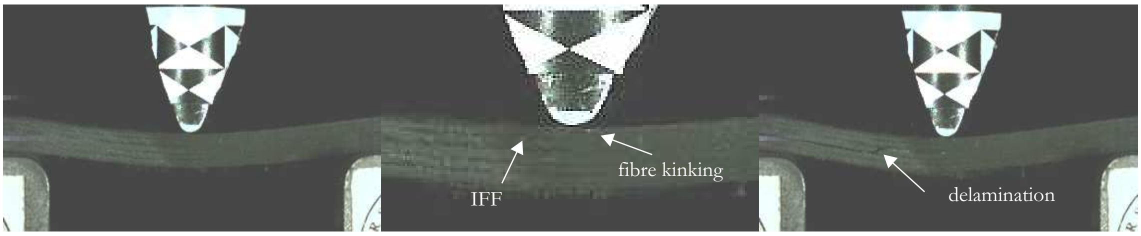

frame before damage initiation | fibre kinking and IFF under the impactor | delamination initiation

(b) experimentally observed damage evolution

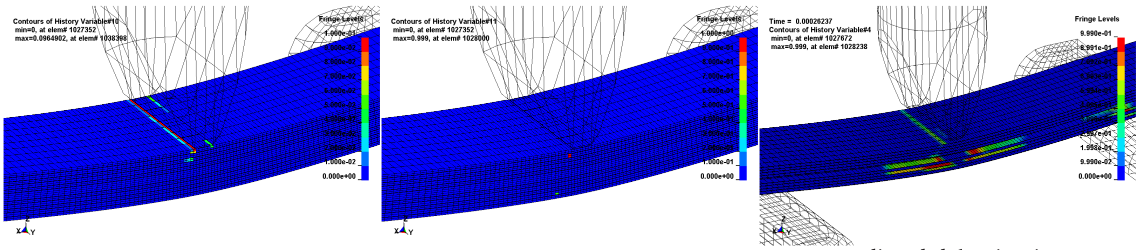

fibre kinking | IFF | predicted delamination propagation

(c) numerically predicted damage evolution

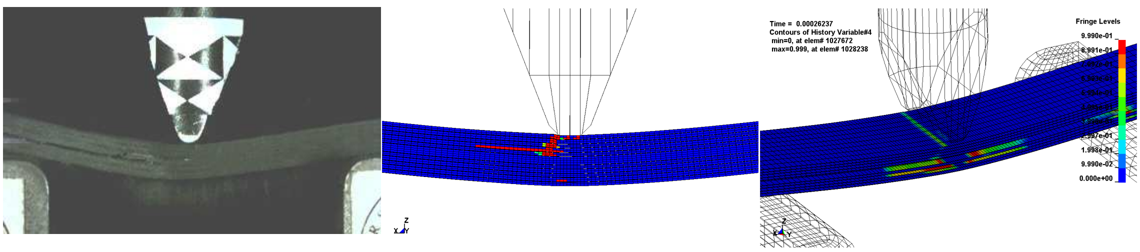

experimentally observed damage pattern | intralaminar damage state | interlaminar damage state

(d) final damage state (last state in numerical model)

Figure 6.7: Summary of FE results for the 0° specimen tested dynamically with a span of 30 mm

only observed at a deflection of approx. 3.4 mm which corresponds better to the experiment.

The next damage mode is a combined fibre rupture/tensile IFF on the tensile side of the beam (see Fig 6.8 (c))predicted after a slight drop of force similar to experimental observations. The final predicted state of damage is displayed in Fig 6.9 and shows good agreement between model and experiment. A similar amount of fibre kinking and fibre rupture is predicted. The area of predicted IFF covers some of the delaminations observed on the tensile side of the beam. Unfortunately, the thin delamination elements in the model became unstable so that not the entire force deflection behaviour could be predicted.

6.4.3 90° specimens tested with span 30 mm

The simulation was performed with an impact velocity of 5.45 m/s. The specimen failed by a simultaneous fibre kinking and fibre rupture/tensile IFF which subsequently formed large scale delaminations.

The position of damage initiation was predicted accurately by the model, but the model predicted the initiation as a sequence of failure modes rather than simultaneous initiation of all three damage modes (see Fig 6.10 (a) and Fig 6.10 (c)). The load and deflection at damage initiation were underestimated which might be caused by not correct data for the materials rate dependency. Small scale delamination initiation was predicted, but the growth of delamination could not be modelled because the simulation got unstable. The predicted final state of intralaminar damage, however, seems to agree reasonably well with the experimental observations (see Fig 6.10 (d)). The intralaminar damage propagated almost through the entire thickness of the beam similar to the experiment.

6.4.4 90° specimens tested with span 50 mm

The simulation was performed with an impact velocity of 6.5 m/s. The specimen failed by a simultaneous fibre rupture and tensile IFF which then resulted large scale delaminations.

The position of damage initiation was predicted accurately by the model. However,

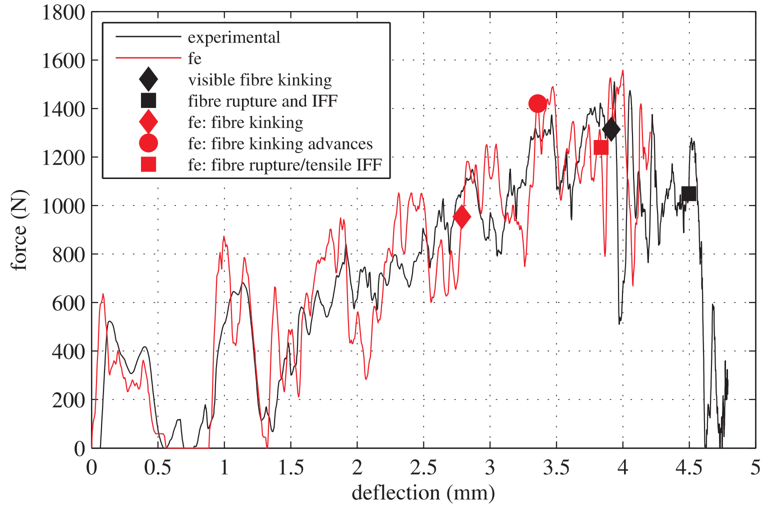

(a) comparison of force deflection curves from experiment and from the FE

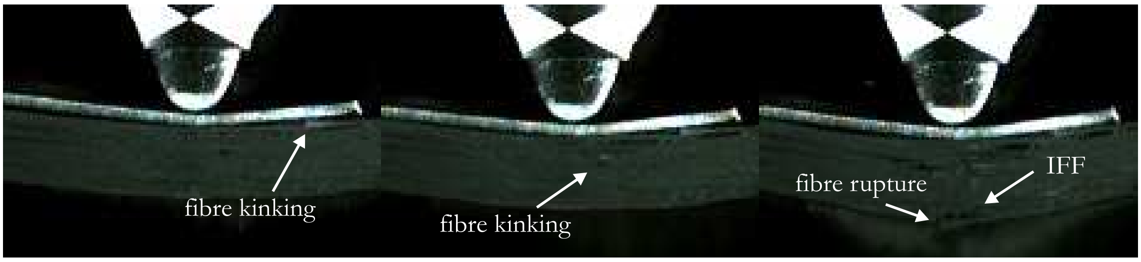

damage initiation by kinking | fibre kinking propagates | fibre rupture and IFF

(b) experimentally observed damage evolution

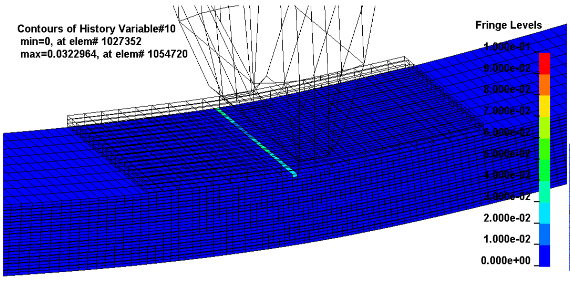

kink initiation

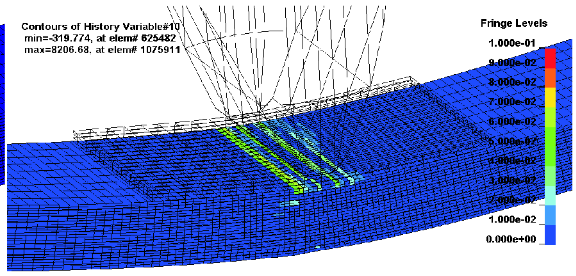

kink propagation

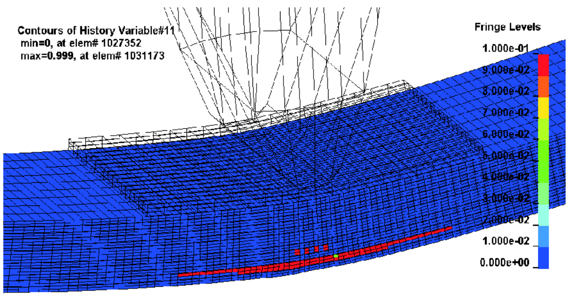

fibre rupture

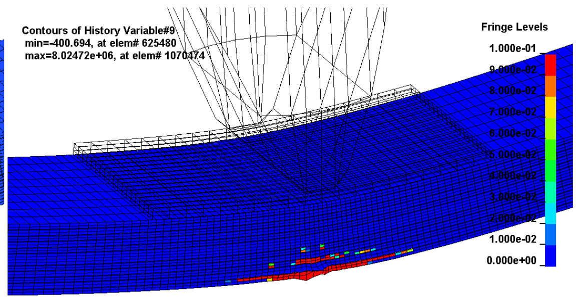

tensile IFF

(c) numerically predicted damage evolution

Figure 6.8: Summary of FE results for the 0° specimen tested dynamically with a span of 50 mm

(a) experimentally observed damage pattern

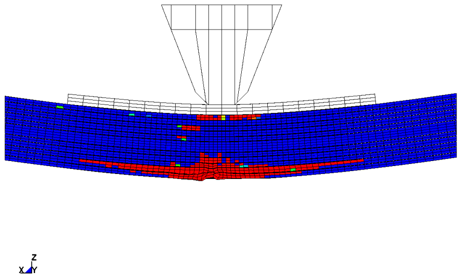

(b) numerically predicted damage pattern (all damage modes)

Figure 6.9: Comparison of the final amount of damage (last state in numerical simulation 0° span 50 mm)

the load and deflection at damage initiation were underestimated (see Fig 6.11 (a)). The initiation of fibre rupture and IFF was predicted almost simultaneously as observed experimentally. Due to the stability problems mentioned already earlier, the subsequent delamination propagation was not predicted by the model. Because the observed damage modes were tensile, entirely failed elements could be removed. The model with element erosion activated showed more realistic results. The delamination was partly predicted by IFF in the 90° plies. This behaviour was not observed in the simulation with deactivated element erosion. This indicates that an explicit representation of delamination by cohesive elements, contacts or element debonding techniques is necessary to represent delamination. The switch from fibre rupture and IFF as intralaminar failure modes to delamination as interlaminar failure mode was successfully modelled. The comparison is displayed in Fig 6.11 (b). Unfortunately, both models, with and without element erosion became unstable so that not the whole duration of the impact could be modelled.

6.5 Summary

In this chapter, the three point beam bending experiments, introduced in Chapter 5, were modelled using the proposed constitutive model. The simulations were performed in order to verify the constitutive model.

The simulations of the quasi-static simulations showed that the model is able to repre-

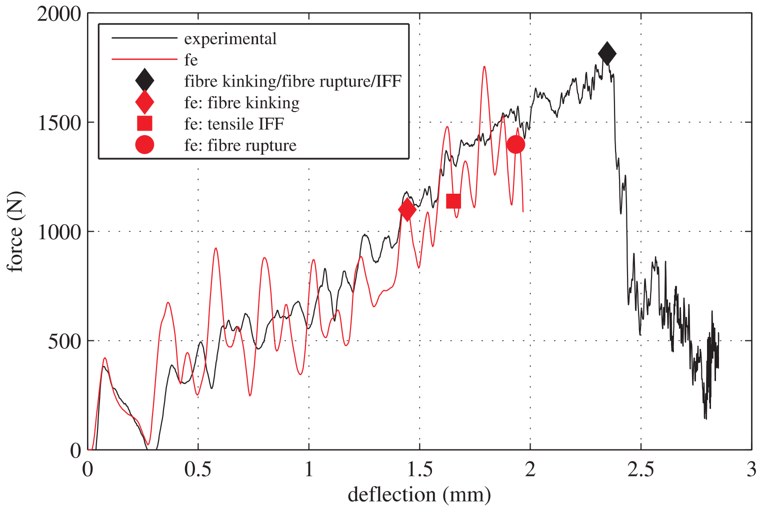

(a) comparison of force deflection curves from experiment and from the FE

damage initiation | damage propagation

(b) experimentally observed damage evolution

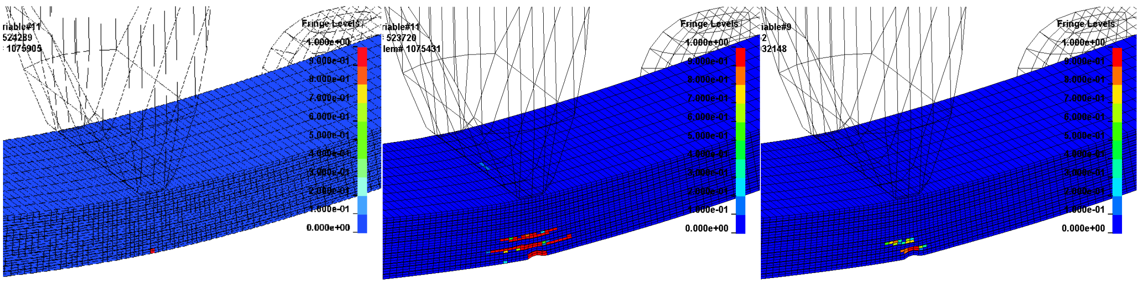

fibre kinking | IFF | fibre rupture

(c) numerically predicted damage evolution

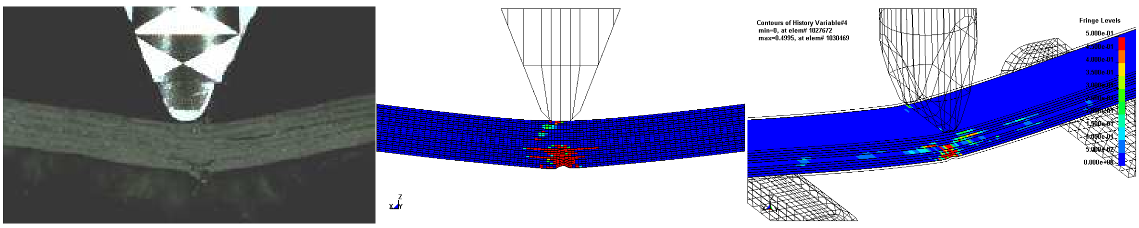

experimentally observed damage pattern | intralaminar damage state | interlaminar damage state

(d) final damage state (last state in numerical model)

Figure 6.10: Summary of FE results for the 90° specimen tested dynamically with a span of 30 mm

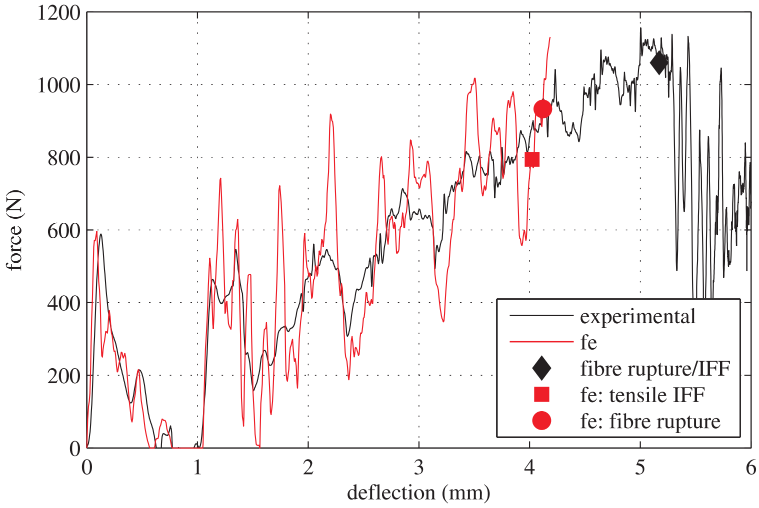

(a) comparison of force deflection curves from experiment and from the FE

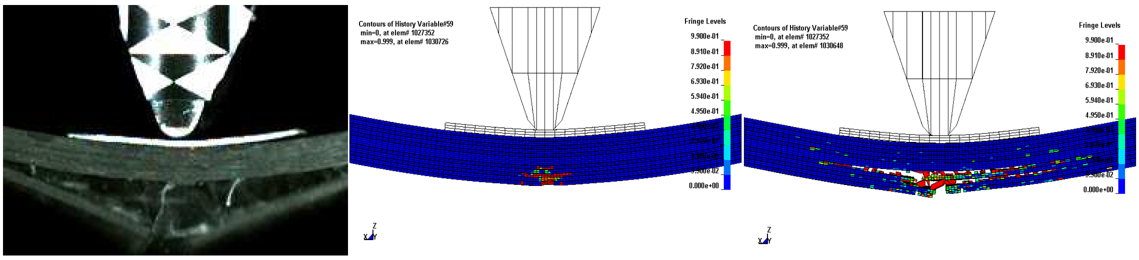

experimentally observed damage pattern | final damage state (no element erosion) | final damage state (element erosion)

(b) final damage state (last state in numerical model)

Figure 6.11: Summary of FE results for the 90° specimen tested dynamically with a span of 50 mm

sent the damage initiation correctly. The experimentally observed damage initiation modes, initiation location and load at initiation were correctly predicted by the FE simulations. The importance of incorporating Mohr-Coulomb material behaviour for the initiation of fibre kinking and IFF in the constitutive model was demonstrated. This enabled the prediction of failure initiation in subsurface plies away from the regions of highest stress and strain. Furthermore, the importance of the use of an extended delamination criterion was demonstrated. The experimentally observed initiation of delamination occurred in regions of negative through thickness stress. Commonly used delamination initiation criteria would not predict delamination under such conditions. Only the application of the extension of the criterion which is used here, enabled a correct prediction of the location of delamination initiation.

The simulation of the impact bending experiments demonstrated to capability of the model to predict the sequence of damage modes correctly. The three dimensional damage evolution algorithms on respective fracture planes enabled the prediction of damage evolution patterns which compared well to the experimental observed damage evolution. The predicted load at the onset of damage was conservative, especially for the 90° specimens. This might have been caused by the fact that the rate dependent input parameters were derived from a resin different to the one used in the beam specimens. Furthermore, the detection of the onset of damage in the experiments might have been inaccurate due to the relative low resolution of the available high speed images. The delamination propagation could not be modelled due to numerical instability of the very thin solid elements used for delamination modelling. However, for some cases the IFF model was able to predict delamination propagation as a matrix crack with a fracture angle of 90°. The use of element erosion demonstrated the need of an explicit representation of delamination.

A summary of the comparison of experiment and model is presented in Tab 6.5 and Tab 6.6. The following two chapters contain conclusions to be drawn from the presented study and suggestions for further development work.

Table 6.5: Conclusions on modelling of quasi-static beam bending - summary

	initiation load	initiation location
fibre rupture	good prediction	good agreement
fibre kinking	partly conservative	good agreement
IFF	good prediction	good agreement
delamination	good prediction	good agreement

Table 6.6: Conclusions on modelling of dynamic beam bending - summary

	damage initiation	damage propagation
fibre rupture	slightly conservative	good agreement
fibre kinking	conservative	realistic propagation prediction good prediction of kink propagation angle
IFF	slightly conservative	good agreement switch of IFF/delamination predicted
delamination	conservative	delamination propagation is numerically unstable, no propagation prediction

Chapter 7

Conclusions

7.1 Prediction of the onset of damage

A three dimensional model for the prediction of the initiation of damage in UD composites has been proposed. The model builds on physically based failure criteria which have been selected to predict fibre rupture, fibre kinking, IFF and delamination as the main failure mechanisms in laminates consisting of UD plies. The selected failure criteria predict the onset of damage by assessing the tractions acting on potential fracture planes. For fibre kinking and IFF these fracture planes are usually not aligned with the material coordinate system. Novel computational efficient algorithms have been proposed for finding critical orientation of potential fracture planes in three dimensions. This enabled the application of the model within the framework of explicit FE. The consistent assessment of all damage initiation modes on fracture planes enables a physically based representation of the underlying failure mechanisms as only stresses which contribute to damage initiation are considered. This improves the accuracy of the prediction of the onset of damage evolution. Furthermore, the knowledge of the fracture plane enabled the use of the local strain rate on the plane where fracture occurs for the incorporation of rate effects into the constitutive model. This novel approach should yield considerable more accuracy for the modelling of impact events. The application of the constitutive model to the quasi static beam experiments has demonstrated the importance of the consideration of Mohr-Coulomb material behaviour for the prediction of the damage initiation. It has been found to be essential for the correct prediction of fibre kinking and IFF in zones of three dimensional mainly compressive stress. Furthermore, the beam bending simulations demonstrated the necessity of delamination prediction under compressive through thickness stress.

The proposed model for damage initiation uses an original approach for strength prediction. All selected failure criteria are homogeneous in their stress terms and allow the calculation of the material exposure e as a measure for damage initiation and subsequently, for damage evolution. This enables the consistent representation of the underlying failure mechanisms in the constitutive model.

7.2 Prediction of damage evolution

The proposed model for damage evolution builds on the physically sound model for the prediction of damage initiation. The failure criteria are used as the dissipation potentials which define the damage evolution. The dissipation potentials are physically based as they only comprise stresses which contribute to damage evolution of a particular failure mode. Furthermore, a novel dissipation potential has been suggested for fibre kinking. The damage evolution algorithms use a simple damage evolution law which does not rely on a prescribed damage evolution function. The amount of damage per increment of load, and subsequently the resulting energy dissipation, is given by the dissipation potential while the direction of damage evolution is given by the respective fracture plane. Therefore, the predicted orientations of fracture planes are used to enable a physically correct material degradation. Inadmissable stress states are returned to damaged failure surfaces which are defined on the respective fracture plane. Consequently, only the relevant components of stress are reduced as damage propagates. The stress return relies entirely on numerical efficient single step stress return algorithms. This has successfully demonstrated to represent localisation phenomena for fibre kinking and IFF in the beam bending simulations.

CDM models usually suffer from mesh dependent energy dissipation. This has been addressed by the introduction of an element size dependent parameter into the damage evolution laws. An algorithm has been developed within this study which estimates the area of a potential crack by the projection of space diagonals on the respective fracture plane. This has been demonstrated to significantly reduce mesh dependent energy dissipation.

The simulation of impact beam experiments showed promising results for the prediction of fibre rupture, fibre kinking and IFF. The propagation of those damage modes could be predicted well. The chosen approach for delamination propagation, however, did not seem to suitable at the meso scale. Interestingly, some of the delamination growth was predicted by the IFF model where the fracture angle was correctly predicted as 90°.

The constitutive model development was inspired by the need for more sophisticated numerical modelling tools for the development of aircraft engine components. Within this study, the model has already successfully been applied in an industrial environment to support the development of a composite fan blade.

7.3 Characterisation of strain rate dependent material behaviour

An extensive literature review of available data for rate dependent composite material behaviour established the general trends and identified the need of further characterisation of rate dependent material behaviour in compression. Especially, the investigation of failure initiation modes was not sufficiently studied in the past.

In the performed experiments a special focus was given to the development of an experimental setup which results in a valid failure mode. Furthermore, digital image analysis has proven very useful in the analysis and verification of experimental results. Especially, Digital Speckle Photography enabled a comparable measurement of deformation across all strain rates and experimental rigs. The focus was on strain measurement in the specimens gauge section thus canceling out any effects of fixture compliance on the results. This yields in a significantly more accurate assessment of strain rate dependent material behaviour.

The compressive material behaviour transverse to the fibre of a UD reinforced material was investigated to establish the rate dependency of the Puck failure model for failure transverse to the reinforcement direction. Therefore, the orientation of the fracture plane was studied. The experiments suggest a constant fracture plane inclination at all applied loading rates. Furthermore, a clear increase in strength was observed. The results should encourage an additional experimental study which investigates the scatter of observed fracture angles as the current results base only on a small number of experiments.

A cross ply laminate was investigated under uniaxial compression. Special emphasis was given to the failure initiation. Digital photography was utilised to monitor the damage initiation at all strain rates. Different specimen geometries were investigated towards the failure initiation. A specimen clamping approach and specimen geometry was developed allowing for a comparable failure mode in the gauge section at all loading rates. The observed failure mode and damage propagation remained similar for all tested strain rates and clear increased rise in strength was observed.

7.4 Improved experimental method for impact beam bending

An improved method for impact bending experiments has been developed in this thesis. The experimental setup and subsequent data reduction has been verified both experimentally and numerically for three point beam bending. Optical measurement techniques like DSP have therefore been used for experimental verification. Furthermore, the optical measurement enabled a better estimation of the impact velocity of the impactor bar which further increases accuracy. The proposed method relies entirely on the measurement of the experimental boundary conditions and does not require instrumentation of the specimens. This, in turn, enables inexpensive and fast characterisation of composite materials regarding their performance under low velocity impacts. It was demonstrated that the accuracy improved significantly such that the data is suitable for constitutive model verification and validation.

The beam bending experiments demonstrated a wide range of different composite failure modes including fibre rupture, fibre kinking, IFF and delamination. Identical boundary conditions in quasi-static and impact experiments highlights the rate dependent material behaviour. A clear increase in force was observed for most configurations. The investigation of the influence of the ply orientation on the delamination behaviour concludes that delamination is very unlikely to initiate between plies of the same orientation. A more rigourous study, involving various ply orientations, should be undertaken to clarify what difference in angle would promote delamination and whether this changes due to loading rate.

People often refer to a thesis as describing a piece of research which has not been finished, but has just been abandoned somewhere along the way. This thesis is no different! Despite the efforts in characterising composites and simulating their behaviour, this thesis left many aspects unanswered and opened new sets of challenges to be addressed in future research. The following chapter will close the thesis with a number of suggestions for exciting future research to further enhance the understanding of composites and to improve design methods thus enabling a better application of these high potential materials.

Chapter 8

Future work

8.1 Numerical

This study demonstrated that three dimensional theories are needed for the prediction of damage initiation. More experimental data is necessary to verify available failure criteria, especially for multi axial stress states. This should be addressed in extensive material characterisation programs at quasi-static loading. However, off-axis data could be generated at high strain rates. Such experiments have already been performed, but more effort is needed and improved optical measurement, as introduced in this study, should be used. The outcome of the next round of the World Wide Failure Exercise which is focused on three-dimensional failure theories, is eagerly expected, as it should inspire further improvements for the composite strength prediction

The non-linear shear behaviour of composites plays an important role in the failure behaviour and is currently not included in the constitutive model. Especially for the compressive fibre failure by kinking the significance of non-linear shear has already been demonstrated [8]. It was shown that due to shear nonlinearity the compressive failure mode might switch from kinking to an instability mode. This is not considered in the current model. Current research at the University of Oxford focuses on deriving the non-linear composite behaviour by micro mechanical models which consider the behaviour of the composite ingredients to predict the behaviour for the composite itself [48]. This methodology should be included into the constitutive equations thus enabling a physically sound modelling of non linear material behaviour.

Another important aspect of composite behaviour is the so called in-situ strength. Depending on whether a composite ply is embedded in other plies or it is on the surface of a laminate, the strength properties are different. Also, the general configuration of the laminate can influence the strength of the single ply. The theoretical background for the prediction of the change has already been well established. However, a reasonable numerical implementation would require knowledge of the position of the element within the laminate (element has an outside surface or not). Unfortunately, this is currently not possible in many commercial FE solvers and should be addressed in the future.

The delamination modelling strategy chosen in this study was not entirely satisfying for the scale at which the constitutive model operates. The current delamination model should be implemented into an interface element which is now available in LS-DYNA. This will enhance the performance of the delamination prediction. On the longer run, however, the author believes that element debonding and element splitting algorithms will prove more efficient for the modelling of fracture in general. The energy dissipation would then be represented by a spring damper model which is placed on the newly created interface between elements. This would overcome many problems related to CDM as energy dissipation would be related to the area of the newly created interface and not the volume of the element. The calculated orientation of certain fracture planes could be used to create the new interfaces. Initial attempts for three dimensional element splitting algorithms have already been made in Oxford [124].

It is well known that the mechanisms for crack initiation are different from the mechanisms for crack propagation. In the constitutive model, as proposed in this study, a 'new' crack is generated in each element. The reason is that no information of neighbouring elements is available. Incorporating this information would be essential to distinguish initiation and propagation. Especially for delamination this could improve the accuracy of the prediction of delamination propagation.

8.2 Experimental

Because of the limited availability of material within this study, no full material characterisation was performed. Future research should rely on an extensive material characterisation program. This would enable a further verification and validation of the proposed constitutive model. Furthermore, the statistical distribution of fracture plane angles could be established. In conjunction with higher quality ultra high speed photography, the transverse compression experiments could be repeated to investigate the highly non-linear material behaviour before failure at high strain rates. Full field strain measurements basing on DSP would give useful information about potential inelastic deformation and localisation before a visible fracture plane forms.

The nature of three point beam bending resulted in failure initiation by fibre kinking or compressive IFF in many cases. The reason is that the region of high stresses due to bending coincided with the region where the force is transmitted into the specimen. This results in complex states of stress which often lead to failure by fibre kinking. If the experimental setup were to be further developed to enable four point beam bending experiments, then the load would not be transmitted in the region of maximum surface stress which would minimise the effect of contact stresses on failure initiation. This would allow for a better study of the failure modes independent from each other.

Another important aspect which has not been addressed sufficiently within this study, and in research in general, is the rate dependency of the critical energy release rates. Currently, only little is know about possible changes of fracture toughness due to changes in strain rate. Future research efforts should clearly address this aspect of composite damage evolution.

8.3 Combining experimental work and numerical interpretation

The increasingly complex constitutive models require a growing number of parameters, many of which are very difficult or sometimes impossible to obtain experimentally. Novel techniques like inverse modelling should be able to bridge this gap. It has already been demonstrated for metals [81] that inverse modelling can help to obtain more representative sets of input properties. Furthermore, this technique allows to grow confidence in the available constitutive models by investigating the sensitivity and physical meaning of certain constitutive parameters. It was also demonstrated that inverse modelling helps to design experimental setups to give the relevant information for a given constitutive model. Inverse modelling should therefore help to improve the predictive numerical modelling capabilities in the future.

Up to date, numerical models build on many approximations regarding the architecture of the composite (fibre volume fraction, fibre orientations, etc.) and initial state of the material (initial defects, residual stresses). In the future, non destructive inspection tools like computer tomography should be used more intensively to obtain a more accurate representation of the material which can then be used in FE models. This will help to identify the source of the often significant scatter in the experimental results and enable to consider these stochastic effects in constitutive models.

Bibliography

[1] G. C. Davila and P. P. Camanho. Failure criteria for FRP laminates in plane stress. *Tech. Rep.*, NASA-TM-2003-212663, 2003.

[2] P. D. Soden, M. J. Hinton, and A. S. Kaddour. Biaxial test results for strength and deformation of a range of e-glass and carbon fibre reinforced composite laminates: failure exercise benchmark data. *Composites Science and Technology*, 62(12-13):1489–1514, 2002.

[3] R. G. Cuntze, R. Deska, B. Szelinski, R. JeltschFricker, S. Meckbach, D. Huybrechts, J. Kopp, L. Kroll, S. Gollwitzer, and R. Rackwitz. *Neue Bruchkriterien und Festigkeitsnachweise fuer unidirektionalen Faserkunststoffverbund unter mehrachsiger Beanspruchung -Modellbildung und Experimente*, volume Reihe 5 Nr 506 of *VDI Fortschritt-Berichte*. VDI Verlag, Duesseldorf, 1997.

[4] S. T. Pinho, L. Iannucci, and P. Robinson. Physically based failure models and criteria for laminated fibre-reinforced composites with emphasis on fibre kinking. part II: Fe implementation. *Composites Part A-Applied Science and Manufacturing*, 37(5):766–777, 2006.

[5] P. M. Jelf and N. A. Fleck. The failure of composite tubes due to combined compression and torsion. *Journal of Materials Science*, 29(11):3080–3084, 1994.

[6] T. J. Vogler and S. Kyriakides. On the initiation and growth of kink bands in fiber composites: Part I. experiments. *International Journal of Solids and Structures*, 38(15):2639–2651, 2001.

[7] P. D. Soden, M. J. Hinton, and A. S. Kaddour. Lamina properties, lay-up configurations and loading conditions for a range of fibre-reinforced composite laminates. *Composites Science and Technology*, 58(7):1011–1022, 1998.

[8] S. T. Pinho. *Modelling failure of laminated composites using physically-based failure models*. PhD thesis, Imperial college, 2005.

[9] O. Hoffman. The brittle strength of orthotropic materials. *Journal of Composite Materials*, 1:200–206, 1967.

[10] S. W. Tsai and E. M. Wu. A general theory of strength for anisotropic materials. *Journal of Composite Materials*, 5:58–80, 1971.

[11] A. Puck. *Festigkeitsanalyse von Faserverbundlaminaten*. Carl Hanser Verlag, Muenchen, 1996.

[12] Z. Hashin and A. Rotem. Fatigue failure criterion for fiber reinforced materials. *Journal of Composite Materials*, 7(Oct):448–464, 1973.

[13] Z. Hashin. Failure criteria for unidirectional fibre composites. *Journal of Applied Mechanics*, 47:329–334, 1980.

[14] T. J. Juhsz. *Ein neues physikalisch basiertes Versagenskriterium fuer schwach 3D verstaerkte Faserverbundlaminate*. PhD thesis, Technische Universitaet Carolo-Wilhemina zu Braunschweig, 2003.

[15] L. J. Hartsmith. The difference between real and imaginary interactions in composite failure predictions - a reply. *Composites*, 25(2):161–164, 1994.

[16] E. C. Edge. Does transverse and shear loading affect the compression strength of unidirectional CFC - a reply. *Composites*, 25(2):159–161, 1994.

[17] M. J. Hinton and P. D. Soden. Predicting failure in composite laminates: The background to the exercise. *Composites Science and Technology*, 58:1001–1010, 1998.

[18] M. J. Hinton, A. S. Kaddour, and P. D. Soden. A comparison of the predictive capabilities of current failure theories for composite laminates, judged against experimental evidence. *Composites Science and Technology*, 62(12-13):1725–1797, 2002.

[19] M. J. Hinton, A. S. Kaddour, and P. D. Soden. A further assessment of the predictive capabilities of current failure theories for composite laminates: comparison with experimental evidence. *Composites Science and Technology*, 64(3-4):549–588, 2004.

[20] P. D. Soden, A. S. Kaddour, and M. J. Hinton. Recommendations for designers and researchers resulting from the world-wide failure exercise. *Composites Science and Technology*, 64(3-4):589–604, 2004.

[21] A. Puck and H. Schuermann. Failure analysis of FRP laminates by means of physically based phenomenological models. *Composites Science and Technology*, 58:1045–1067, 1998.

[22] R. G. Cuntze and A. Freund. The predictive capability of failure mode concept-based strength criteria for multidirectional laminates. *Composites Science and Technology*, 64:343–377, 2004.

[23] O. Mohr. Welche Umstaende bedingen die Elastizitaetsgrenze und den Bruch eines Materials? *Z. d. VDI*, 45:1524–1530, 1900.

[24] A. Puck, J. Kopp, and M. Knops. Guidelines for the determination of the parameters in puck's action plane strength criterion. *Composites Science and Technology*, 62(3):371–378, 2002.

[25] U. Icardi, S. Locatto, and A. Longo. Assessment of recent theories for predicting failure of composite laminates. *Applied Mechanics Reviews*, 60(1-6):76–86, 2007.

[26] S. T. Pinho, C. G. Dvila, P. P. Camanho, L. Iannucci, and P. Robinson. Failure models and criteria for FRP under in-plane or three-dimensional stress including shear non-linearity. Technical Report 213530, Imperial College, 2005.

[27] C. Gonzalez and J. Llorca. Mechanical behavior of unidirectional fiber-reinforced polymers under transverse compression: Microscopic mechanisms and modeling. *Composites Science and Technology*, 67(13):2795–2806, 2007.

[28] N. A. Fleck. Compressive failure of fiber composites. In *Advances in Applied Mechanics, Vol 33*, pages 43–117. 1997.

[29] B. W. Rosen. *Mechanics of Composite Strengthening.* Fibre Composites Materials. American Society of Metals, 1965.

[30] A. S. Argon. *Fracture of composites*, volume 1 of *Treatise on Material Science and Technology.* Academic Press, New York, 1972.

[31] B. Budiansky. Micromechanics. *Computers and Structures*, 16(1-4):3–12, 1983.

[32] S. W. Yurgartis. Measurement of small-angle fiber misalignments in continuous fiber composites. *Composites Science and Technology*, 30(4):279–293, 1987.

[33] G. M. Martinez, M. R. Piggott, D. M. R. Bainbridge, and B. Harris. The compression strength of composites with kinked, misaligned and poorly adhering fibers. *Journal of Materials Science*, 16(10):2831–2836, 1981.

[34] S. Kyriakides, R. Arseculeratne, E. J. Perry, and K. M. Liechti. On the compressive failure of fiber-reinforced composites. *International Journal of Solids and Structures*, 32(6-7):689–738, 1995.

[35] T. V. Parry and A. S. Wronski. Kinking and compressive failure in uniaxially aligned carbon-fiber composite tested under superposed hydrostatic-pressure. *Journal of Materials Science*, 17(3):893–900, 1982.

[36] S. T. Pinho, L. Iannucci, and P. Robinson. Physically-based failure models and criteria for laminated fibre-reinforced composites with emphasis on fibre kinking: Part I: Development. *Composites Part A-Applied Science and Manufacturing*, 37(1):63–73, 2006.

[37] W. C. Cui, M. R. Wisnom, and M. Jones. A comparison of failure criteria to predict delamination of unidirectional glass epoxy specimens waisted through the thickness. *Composites*, 23(3):158–166, 1992.

[38] J. M. Whitney and R. J. Nuismer. Stress fracture criteria for laminated composites containing stress-concentrations. *Journal of Composite Materials*, 8(JUL):253–265, 1974.

[39] J. C. Brewer and P. A. Lagace. Quadratic stress criterion for initiation of delamination. *Journal of Composite Materials*, 22(12):1141–1155, 1988.

[40] P. P. Camanho, C. G. Davila, and M. F. de Moura. Numerical simulation of mixed-mode progressive delamination in composite materials. *Journal of Composite Materials*, 37(16):1415–1438, 2003.

[41] J. P. Hou, N. Petrinic, and C. Ruiz. A delamination criterion for laminated composites under low-velocity impact. *Composites Science and Technology*, 61:2069–2074, 2001.

[42] T. K O'Brien. *Characterisation of Delamination Onset and Growth in a Composite Laminate*, ASTM STP 775 *Damage in Composite Materials*. American Society for Testing and Materials, 1982.

[43] W. C. Cui and M. R. Wisnom. A combined stress-based and fracture-mechanics-based model for predicting delamination in composites. *Composites*, 24(6):467–474, 1993.

[44] W. H. Press, S. A. Teukolsky, W. T. Vetterling, and B. P. Flannery. *Numerical Recipes in C*. Cambridge University Press, New York, 2 edition, 1992.

[45] J. Wiegand, N. Petrinic, and B. Elliott. An algorithm for determination of the fracture angle for the three-dimensional Puck matrix failure criterion for UD composites. *Composites Science and Technology*, In Press, Corrected Proof, 2008.

[46] J. X. Tao and C. T. Sun. Influence of ply orientation on delamination in composite laminates. *Journal of Composite Materials*, 32(21):1933–1947, 1998.

[47] R. de Vries, E. Lamers, S. Wijskamp, B. Villa Rodriguez and R. Akkerman. U20MM: The University of Twente Micromechanics Modeller. *Available: http://www.pt.ctw.utwente.nl/organisation/tools/*, 2008.

[48] R. Gerlach. Characterisation of the strain rate dependent behaviour of 3-D composites using a meso mechanics approach. *Transfer-Report*, University of Oxford, 2007.

[49] Robert Gerlach, Clive R. Siviour, Nik Petrinic, and Jens Wiegand. Experimental characterisation and constitutive modelling of RTM-6 resin under impact loading. *Polymer*, 49(11):2728–2737, 2008.

[50] B. Bouette, C. Cazeneuve, and C. Oytana. Effect of strain rate on interlaminar shear properties of carbon epoxy composites. *Composites Science and Technology*, 45(4):313–321, 1992.

[51] L. Dong and J. Harding. A single-lap shear specimen for determining the effect of strain-rate on the interlaminar shear-strength of carbon-fiber-reinforced laminates. *Composites*, 25(2):129–138, 1994.

[52] T. Yokoyama and K. Nakai. Evaluation of interlaminar shear strength of a unidirectional carbon/epoxy laminated composite under impact loading. *Journal De Physique IV*, 134:797–804, 2006.

[53] R. Talreja. *Damage Mechanics of Composite Materials.* Elsevier, 1994.

[54] O. Allix. A composite damage meso-model for impact problems. *Composites Science and Technology*, 61(15):2193–2205, 2001.

[55] K. V. Williams, R. Vaziri, and A. Poursartip. A physically based continuum damage mechanics model for thin laminated composite structures. *International Journal of Solids and Structures*, 40(9):2267–2300, 2003.

[56] L. M. Kachanov. *On the creep rupture time*, volume 8 of *Izv AN SSSR Otd Tekhn Nauk*. 1958.

[57] Y. N. Rabotnov. *Creep problems of structural members*. North Holland, Amsterdam, 1969.

[58] S. Murakami and N. Ohno. *A continuum theory of creep and creep damage*. Creep in Structures. Springer-Verlag, Berlin, 1981.

[59] J. Lemaitre and J. L. Chaboche. Phenomenological approach of damage rupture. *Journal De Mecanique Appliquee*, 2(3):317–365, 1978.

[60] F. K. Chang and K. Y. Chang. A progressive damage model for laminated composites containing stress concentrations. *Journal of Composite Materials*, 21(9):834–855, 1986.

[61] P. Ladeveze and E. LeDantec. Damage modelling of the elementary ply for laminated composites. *Composites Science and Technology*, 43(3):257–267, 1992.

[62] A. Matzenmiller, J. Lubliner, and R. L. Taylor. A constitutive model for anisotropic damage in fibre-composites. *Mechanics of Materials*, 20:125–152, 1995.

[63] A. F Johnson, A. K. Pickett, and P. Rozycki. Computational methods for predicting impact damage in composite structures. *Composites Science and Technology*, 61:2183–2192, 2001.

[64] L. Greve and A. K. Pickett. Modelling damage and failure in carbon/epoxy non-crimp fabric composites including effects of fabric pre-shear. *Composites Part A-Applied Science and Manufacturing*, 37(11):1983–2001, 2006.

[65] J. L. Curiel Sosa, N. Petrinic, and J. Wiegand. A three-dimensional progressive damage model for fibre-composite materials. *Mechanics Research Communications*, 35(4):219–221, 2008.

[66] K. V. Williams and R. Vaziri. Application of a damage mechanics model for predicting the impact response of composite materials. *Computers and Structures*, 79:997–1–11, 2001.

[67] P. Maimi, P. P. Camanho, J. A. Mayugo, and C. G. Davila. A continuum damage model for composite laminates: Part I - constitutive model. *Mechanics of Materials*, 39(10):897–908, 2007.

[68] P. Maimi, P. P. Camanho, J. A. Mayugo, and C. G. Davila. A continuum damage model for composite laminates: Part II - computational implementation and validation. *Mechanics of Materials*, 39(10):909–919, 2007.

[69] W. Hufenbach, R. Bohm, L. Kroll, and A. Langkamp. Theoretical and experimental investigation of anisotropic damage in textile-reinforced composite structures. *Mechanics of Composite Materials*, 40(6):519–532, 2004.

[70] M. A. Crisfeld, Y. Mi, G. A.O. Davies, and H. B. Hellweg. Finite element methods and the progressive failure modelling of composite structures. In D.R.J. Owen, editor, *Computational Plasticity Fundamentals and Applications*, volume Part1, pages 239–254, CIMNE Barcelona, 1997.

[71] D. J. Elder, R. S. Thomson, M. Q. Nguyen, and M. L. Scott. Review of delamination predictive methods for low speed impact of composite laminates. *Composite Structures*, 66(1-4):677–683, 2004.

[72] O. Allix and P. Ladeveze. Interlaminar interface modeling for the prediction of delamination. *Composite Structures*, 22(4):235–242, 1992.

[73] S. T. Pinho, L. Iannucci, and P. Robinson. Formulation and implementation of decohesion elements in an explicit finite element code. *Composites Part A-Applied Science and Manufacturing*, 37(5):778–789, 2006.

[74] W. G. Jiang, S. R. Hallett, B. G. Green, and M. R. Wisnom. A concise interface constitutive law for analysis of delamination and splitting in composite materials

and its application to scaled notched tensile specimens. *International Journal for Numerical Methods in Engineering*, 69(9):1982–1995, 2007.

[75] J.O. Hallquist. *LS-DYNA3D Keyword manual.* Livermore Software Technology Corporation, 2007.

[76] B. Budiansky, N. A. Fleck, and J. C. Amazigo. On kink-band propagation in fiber composites. *Journal of the Mechanics and Physics of Solids*, 46(9):1637–1653, 1998.

[77] M. P. F. Sutcliffe and N. A. Fleck. Microbuckle propagation in carbon fiber-epoxy composites. *Acta Metallurgica et Materialia*, 42(7):2219–2231, 1994.

[78] M. P. F. Sutcliffe and N. A. Fleck. Microbuckle propagation in fibre composites. *Acta Materialia*, 45(3):921–932, 1997.

[79] ASTM D5528. Mode I interlaminar fracture toughness of unidirectional fibre-reinforced polymer matrix composites. 2001.

[80] ASTM D6671/D6671M. Mixed mode I-mode II interlaminar fracture toughness of unidirectional fibre-reinforced polymer matrix composites. 2004.

[81] B. Elliott and N. Petrinic. *Strategies for efficiency in inverse modelling of material parameters for predictive modelling of aerospace alloys.* Compututional Fluid and Solid Mechanics. Elsevier LTd., 2005.

[82] Z. P. Bazant and B. H. Oh. Crack band theory for fracture of concrete. *Materials and structures*, 16:155–177, 1983.

[83] F. Dunne and N. Petrinic. Introduction to Computational Plasticity. Oxford University Press, Oxford, 2005.

[84] W. J. Cantwell and J. Morton. The impact resistance of composite-materials - a review. *Composites*, 22(5):347–362, 1991.

[85] S. T. S. Al-Hassani and A. S. Kaddour. Strain rate effects on grp, krp and cfrp composite laminates. In *Impact Response and Dynamic Failure of Composites and*

Laminate Materials, Pts 1 and 2, volume 141-1 of *Key Engineering Materials*, pages 427–451. 1998.

[86] G. C. Jacob, J. M. Starbuck, J. F. Fellers, S. Simunovic, and R. G. Boeman. Strain rate effects on the mechanical properties of polymer composite materials. *Journal of Applied Polymer Science*, 94(1):296–301, 2004.

[87] J. E. Field, S. M. Walley, W. G. Proud, H. T. Goldrein, and C. R. Siviour. Review of experimental techniques for high rate deformation and shock studies. *International Journal of Impact Engineering*, 30(7):725–775, 2004.

[88] Z. H. Li and J. Lambros. Determination of the dynamic response of brittle composites by the use of the split hopkinson pressure bar. *Composites Science and Technology*, 59(7):1097–1107, 1999.

[89] I. M. Daniel, H. M. Hsiao, and R. D. Cordes. *Dynamic Response of Carbon/Epoxy Composites*. High Strain Rate Effects on Polymer, Metal and Ceramic Matrix Composites and Other Advanced Materials. ASME, 1995.

[90] N. Almaliky and D. J. Parry. Measurements of high-strain rate properties of polymers using an expanding ring method. *Journal De Physique IV*, 4(C8):71–76, 1994.

[91] C. P. Buckley, J. Harding, J. P. Hou, C. Ruiz, and A. Trojanowski. Deformation of thermosetting resins at impact rates of strain. part i: Experimental study. *Journal of the Mechanics and Physics of Solids*, 49(7):1517–1538, 2001.

[92] I. M. Daniel and T. Liber. Strain rate effects on the mechanical properties of fibre composites part 3. Technical Report NASA-CR-135087, 1976.

[93] I. M. Daniel, R. H. Labedz, and T. Liber. New method for testing composites at very high-strain rates. *Experimental Mechanics*, 21(2):71–77, 1981.

[94] J. Harding and L. M. Welsh. A tensile testing technique for fiber-reinforced composites at impact rates of strain. *Journal of Materials Science*, 18(6):1810–1826, 1983.

[95] J. Harding. High rate test data on materials 1 and 2. Technical Report HICAS D.1.3.4, Department of Engineering Science University of Oxford, 1999.

[96] C. Cazeneuve and J. C. Maile. Behavioral-study of carbon-fiber composites at different rates of deformation. *Journal De Physique IV*, 46(NC-5):551–556, 1985.

[97] I. W. Hall and M. Guden. High strain rate testing of a unidirectionally reinforced graphite epoxy composite. *Journal of Materials Science Letters*, 20(10):897–899, 2001.

[98] M. V. Hosur, J. Alexander, U. K. Vaidya, and S. Jeelani. High strain rate compression response of carbon/epoxy laminate composites. *Composite Structures*, 52(3-4):405–417, 2001.

[99] D. J. Parry and F. S. Al-Hazmi. Stress-strain behaviour of IM7/977-2 and IM7/APC2 carbon fibre composites at low and high strain rates. *Journal De Physique IV*, 110:57–62, 2003.

[100] Q. D. Bing and C. T. Sun. Modeling and testing strain rate-dependent compressive strength of carbon/epoxy composites. *Composites Science and Technology*, 65(15-16):2481–2491, 2005.

[101] L. G. Melin and L. E. Asp. Effects of strain rate on transverse tension properties of a carbon/epoxy composite: studied by moire photography. *Composites Part A-Applied Science and Manufacturing*, 30(3):305–316, 1999.

[102] A. Gilat, R. K. Goldberg, and G. D. Roberts. Experimental study of strain-rate-dependent behavior of carbon/epoxy composite. *Composites Science and Technology*, 62(10-11):1469–1476, 2002.

[103] N. Taniguchi, T. Nishiwaki, and H. Kawada. Tensile strength of unidirectional CFRP laminate under high strain rate. *Advanced Composite Materials*, 16(2):167–180, 2007.

[104] T. G. Rio, E. Barbero, R. Zaera, and C. Navarro. Dynamic tensile behaviour at low temperature of CFRP using a split hopkinson pressure bar. *Composites Science and Technology*, 65(1):61–71, 2005.

[105] C. Baley, P. Davies, Y. Grohens, and G. Dolto. Application of interlaminar tests to marine composites. a literature review. *Applied Composite Materials*, 11(2):99–126, 2004.

[106] B. Hopkinson. A method of measuring the pressure produced in the detonation of high explosives or by the impact of bullets. *Philosophical Transactions of the Royal Society London A*, 213:437–456, 1914.

[107] R. M. Davies. A critical study of the hopkinson pressure bar. *Philosophical Transactions of the Royal Society of London. Series A, Mathematical and Physical Sciences*, 240(821):375–457, 1948.

[108] H. Kolsky. An investigation of the mechanical properties of materials at very high rates of loading. *Proceedings of the Physical Society of London B*, 62:676–700, 1949.

[109] G. T. Gray. *Classical split-Hopkinson pressure bar testing*, volume 8 of *ASM handbook: Mechanical Testing and Evaluation*. 2000.

[110] L. M. Yang and V. P. W. Shim. An analysis of stress uniformity in split hopkinson bar test specimens. *International Journal of Impact Engineering*, 31(2):129–150, 2005.

[111] D. J. White, W. A. Take, and M. D. Bolton. Soil deformation measurement using particle image velocimetry (PIV) and photogrammetry. *Geotechnique*, 53(7):619–631, 2003.

[112] A. Jumpasut, N. Petrinic, B. C.F. Elliott, C. R. Siviour, and M. R. Arthington. An error analysis into the use of regular targets and target detection in image analysis for impact engineering. *Applied Mechanics and Materials*, 13-14:203–210, 2008.

[113] ASTM D3410/D3410M-03. Standard test method for compressive properties of polymer matrix composite materials with unsupported gage section by shear loading. 2003.

[114] O. Allix, P. Ladeveze, and E. Vittecoq. Modeling and identification of the mechanical-behavior of composite laminates in compression. *Composites Science and Technology*, 51(1):35–42, 1994.

[115] EN-ISO 14125. Determination of flexural properties. 1998.

[116] J. M. Lifshitz, F. Gov, and M. Gandelsman. Instrumented low-velocity impact of cfrp beams. *Int. Journal of Impact Engineering*, 16(2):201–215, 1995.

[117] ASTM D7136/D7136M. Measuring the damage resistance of a fibre-reinforced polymer matrix composite to a drop-weight impact event. 2005.

[118] M. S. Found, I. C. Howard, and A. P. Paran. Interpretation of signals from dropweight impact tests. *Composite Structures*, 42(4):353–363, 1998.

[119] B. Galpin, V. Grolleau, S. Umiastowski, G. Rio, and L. Maheo. Design and application of an instrumented projectile for load measurements during impact. *International Journal of Crashworthiness*, 13(2):139–148, 2008.

[120] Y. Chuman, K. Mimura, K. Kaizu, and S. Tanimura. A sensing block method for measuring impact force generated at a contact part. *International Journal of Impact Engineering*, 19(2):165–174, 1997.

[121] S. R. Hallett. Three-point beam impact tests on T300/914 carbon-fibre composites. *Composites Science and Technology*, 60(1):115–124, 2000.

[122] H. Kolsky. *Stress waves in solids.* Dover Publications, INC, New York, 1963.

[123] Z. Hashin. Theory of fibre reinforced materials. *NASA CR-1974*, 1972.

[124] P. R. Johnson, N. Petrinic, and E. Sueli. Element - splitting for simulation of fracture in 3D solid continua. *COMPLAS VIII International Conference on Computational Plasticity*, 2005.

[125] K. S. Liu and S. W. Tsai. A progressive quadratic failure criterion for a Laminate. *Composites Science and Technology*, 58(7):1023–1032, 1998.

[126] P. A. Zinoviev, S. V. Grigoriev, O. V. Lebedeva and L. P. Tairova. The strength of multilayered composites under a plane-stress state. *Composites Science and Technology*, 58(7):1209–1223, 1998.

[127] T. A. Bogetti, C. P.R. Hoppel, V. M. Harik, J. F. Newill and B. P. Burns. Predicting the nonlinear response and progressive failure of composite laminates. *Composites Science and Technology*, 64(3):329–342, 2004.